TRINITY COLLEGE DUBLIN

SCHOOL OF PHYSICS

Molecular Electronics: First Principles and Model Approaches

by

Amaury de Melo Souza

A thesis submitted for the degree of

Doctor of Philosophy

March 2015

Declaration

I, Amaury de Melo Souza, hereby declare that this thesis has not been submitted as an exercise for a degree at this or any other University. It comprises work performed entirely by myself during the course of my Ph.D. studies at Trinity College Dublin. I was involved in a number of collaborations, and where it is appropriate my collaborators are acknowledged for their contributions. I agree that the Library may lend or copy this thesis upon request.

Amaury de Melo Souza

Have not I commanded thee? Be strong and of a good courage; be not afraid, neither be thou dismayed: for the Lord thy God is with thee whithersoever thou goest.

Joshua 1:9. (The Bible, King James Version)

Abstract

This thesis deals with the application and the development of computational tools for the study of ground state and electronic transport properties of molecular junctions. The calculations can be divided in two main categories, depending on whether they are based on first-principles or model Hamiltonians, respectively. From the point of view of first-principles calculations, the ground state properties are studied within density functional theory (DFT) and the electronic transport within the non-equilibrium Green's functions (NEGF) formalism. From the point of view of model Hamiltonians, the electronic transport is calculated by means of the density matrix formalism by solving master equations (ME), where all the parameters can be obtained from first-principles calculations. These approaches allow us to study the electronic transport in different regimes: for strong electrode-molecule coupling, where tunneling is the doming mechanism, as well as for weak electronic coupling, where Coulomb blockade dominates.

For a quantitative description of the electronic transport across molecular junctions it is key to account for renormalization of the energy levels when the organic/inorganic interfaces are formed. We show how DFT within local and semi-local exchange correlation functionals does not capture this effect. We apply a constrained-DFT approach to study the energy level alignment of a benzene/Lithium(100) interface, and we find that the quasi-particle energy gap of the molecule is reduced by $\sim$2.5 eV due to image charge effect.

We present a thorough study of Au/benzene-dithiol/Au molecular junctions. Firstly, we perform ground state DFT calculations in order to study the stability of this system with respect to the adsorption of the molecule on surfaces as well as when the molecule is in a junction, and we find that the thiol junctions are energetically more stable than their thiolate counterparts. We present a detailed discussion on the energy level alignment of these junctions, and present different methods to account for the energy level renormalization. By means of DFT-NEGF we perform quantum transport calculations for these junctions under stretching and compare the results for both thiol and thiolate terminations. We find that the conductance of the thiol junctions is reduced as the electrodes separation increases, whereas the thiolate junctions the conductance increases. Finally, we perform calculations by using a combined approach of molecular dynamics and Monte Carlo simulations in order to account for effects of temperature and the statistical as-

pects of the experiments, namely the possibility of having many different geometries and therefore different conductance values.

We use the computationally efficient master equation approach to study the transport properties of molecular junctions, where all the parameters for the model Hamiltonian can be obtained from first-principles calculations. We show that the master equation approach can describe the transport properties of molecular junctions in the Coulomb blockade regime, where the NEGF within DFT-LDA fails due to the lack of the derivative discontinuity in the local density approximation (LDA). We have applied this method to reproduce experimental data for porphyrin-Zn-gold molecular junctions in the weak coupling limit. Within the model, we include temperature effects by considering an effective single vibron-mode, and demonstrate that vibration excitations can be responsible for the linear-like current increase observed in the experiments.

Finally, we study light-induced charge transfer and conductance enhancement due to the interaction of charge carriers with light. We show how the transport properties of molecular junctions with donor-acceptor structures change depending on the charge state of the molecule. This is accomplished by combining CDFT with the NEGF formalism. Furthermore, within the ME approach, we study the effect of light in simple models of one and two levels and show the results when one considers higher-order contributions, such as cotunneling. We then discuss the interplay between vibrons and light-induced effects and show how light can be used to control the conductance of molecular junctions in the strong electron-vibron coupling limit.

In summary, we present two main sets of approaches to electronic quantum transport in molecular junctions: DFT-NEGF, and model Hamiltonians and ME's. By applying these methods to molecular junctions of current interest, we address key aspects of quantum transport. These are the problem of energy level renormalization due to image charge effect, different transport regimes (tunneling, Coulomb blockade and Franck-Condon blockade), temperature effects, light induced tunneling as well as the statistical aspect of conductance measurements.

Acknowledgments

I am grateful and indebted to many people for their help, guidance, support, friendship and love. Certainly, I would have not been able to finish this thesis without them.

I would like to start with a big thanks to my supervisor Prof. Stefano Sanvito and my co-supervisor Dr. Ivan Rungger for their incredible capacity of leadership, insight, vision and deep knowledge. Their dedication and how they treat each member of our group have been really inspiring to me in pursuing my academic career. Many other members and former members of the group contributed in different important ways. A special thanks to Dr. Tom Archer, Dr. Andrea Droghetti, Dr. Awadhesh Narayan, Dr. Sandip Bhattacharya and Dr. Das Pemmaraju for their valuable discussions, suggestions and technical support. My gratitude to all the other members of the Computational Spintronics group who, with a simple smile or a corridor conversation, have made of my days here much more pleasant. All the colleagues that I had the privilege to share the office with for the last four years, Paul Gorman and John Duffy, thanks for valuable discussions about different subjects that in a way or another have contributed to built up our character. I am confident that many of you have become lifetime friends! I would like to thank Stefania Negro for her administrative support, always kind and really helpful. The computational resources were provided by the TCHPC of Trinity College, thus a special thanks to all the stuff members who have always been willing to help.

I would like to express my gratitude to my friends from Brazil, Prof. Alexandre Reily Rocha, Prof. Renato Borges Pontes and Prof. Antonio Jose Roque da Silva, who have participated also as collaborators in the present thesis. Our collaborator in Saudi Arabia, Prof. Udo Schwingenschlögl and Dr. William French in the USA. My special thanks to my dear friends and colleagues in this project, Obodo Joshua, Chengjun Jin, Enrique Montes and Altynbek Murat (based in KAUST) for their friendship and enjoyable moments spent in Dublin and in Saudi Arabia. Thanks to KAUST University for the financial support through the ACRAB project.

During these years in Trinity and in Ireland, I had the privilege to meet and become friends with really wonderful people and their love and kindness were essentially emotional fuel to me. All the brothers and sisters from the Maranatha Christian Church in Belfast, especially Pr. Andrew and his family, Rovena and Richard, Rasa and Janmark, Brian, Gustavo Pirola, Paul and many others, my eternal gratitude for your prayers, kindness

and friendship. A huge thanks to my dear friends in Sao Paulo (Maranatha Church, Sumaré), I am aware of your prayers and love during my stay in Ireland. I love you all!!!

My warmth gratitude to my new brothers Vilmar Banderó, Prof. Mauro Ferreira, Prof. Claudionor Bezerra, my Canadian friend/sister Leanna Kohnke and the 'baianas' Luana Martins, Isadora and Bruna for all the happy hours we spent together, from whom I could always find support and help. Without words to describe her kindness and friendship, I want to thank Luz Adriana Leon, my Colombian special friend and one of the most incredible person I have ever met. Thank you all for everything you have done for me, I will never be able to pay it back.

During the past months, I had the privilege to meet the members of the Selah Church in Dublin. Thanks to Peter whose love and fragrance of Christ is so strong and contagious. Thanks to the members of the worship team (Roger Santana, Carol Fukushima, Michelle Eloi, Simone Cristtina, Tiago Silva, Polyana Fernandes, Laura Ceregatti, Lucas Cirino and Miuna Ferreira) with whom I spent most of my best last moments in Dublin. To all the brothers that became really good friends and supporters in prayers and coffee breaks. Thanks for your love and fellowship in all times, I love you all.

Finally, I want to thank those who will always be there for me, my beloved family. A huge thanks to my father Juanil Santos de Souza and to my mother Odete Alves de Melo Souza, for every word, every tear, every prayer, every hug, every kiss and every penny spent with me, my sincere love. To my brother Daniel de Melo Souza, my big sister Aelbany Karla de Melo Souza and her beautiful family (Kayo, Kaua, Washington) and my little sister Flavia Karlayne de Melo. To my second mother Tia Arlete and her family (Tain e Talisson), your love and prayers have made the difference in my life. To my best friend Denise Santana and her family (Marcinho and Luiz Felipe), who always made me laugh in the midst of any circumstances and times. To Daniele Ferreira and her family for their love and the wonderful time we always spent together. With all my heart and sincerity, I dedicate this thesis to all of you!

At the beginning of my Ph.D. I held on this

Have I not commanded you? Be strong and courageous. Do not be afraid; do not be discouraged, for the Lord your God will be with you wherever you go.

Joshua 1:9.

Now, in the end of this period, I can really say that

I have fought the good fight, I have finished the race, I have kept the faith.

2 Timothy 4:7

and

The Lord has done great things for us, and we are filled with joy.

Psalms 126:3.

Contents

List of Figures

List of Tables

Constants and Nomenclature

Constants

Symbol	Value/Units	Description
e	1.6022×10^{-19} C	Elementary electron charge
ϵ_0	8.8541×10^{-12} F m^{-1}	Electric permittivity
G_0	$2e^2/h = 7.7480 \times 10^{-5}$ S	Quantum of conductance
h	6.6260×10^{-34} J s	Planck's constant
$\hbar = h/2\pi$	1.0546×10^{-34} J s	Planck's constant
k_B	1.3806×10^{-23} m^2 kg s^{-2} K^{-1}	Boltzmann constant
m	9.1093×10^{-31} kg	Electron mass

Nomenclature

Chapter 1

Symbol	Description
E^{A}	Electron affinity
$E_{\mathrm{QP}}^{\mathrm{gap}}$	Quasi-particle energy gap
E_{F}	Fermi energy
G	Conductance
$\hbar\omega$	Photon energy
I^{P}	Ionization potential
N	Number of particles in the system
$\mathcal{U}$	Charging energy parameter
W_{F}	Work function

Chapter 2

Symbol	Description
Δ	Fundamental energy gap
Δ_{xc}	Derivative discontinuity in the exchange-correlation energy
Δ_{KS}	Kohn-Sham single-particle energy gap
E	Total energy
E_0	Ground-state total energy for the Kohn-Sham system
E_{xc}	Exchange-correlation energy
$E_{\mathrm{xc}}^{\mathrm{LDA}}$	Exchange-correlation energy within the LDA approximation

ϵ_{N}	N'th Kohn-Sham eigenvalue
ε_{x}	Exchange energy density
$\tilde{\Psi}$	Total wave-function
ϕ_i	Kohn-Sham orbitals
Φ	Nuclear wave-function
Ψ	Electronic wave-function
ψ_i	Single-particle wave-function
ρ	Electronic charge density
ρ_0	Ground-state electronic charge density
$\sigma = \uparrow, \downarrow$	Index of spin
t^{hom}	Kinetic energy density of a homogeneous system
t	Time
U_{H}	Hartree energy
$\hat{U}$	Electron-electron Coulomb interaction operator
$\hat{V}_{\mathrm{ext}}$	Electron-nuclei interaction operator
$V_{\mathrm{c}}^{\sigma} w_{\mathrm{c}}^{\sigma}$	Constrained-DFT auxiliary potential for spin σ

Chapter 3

Symbol	**Description**
A	Spectral function
f	Fermi-Dirac distribution function
$\mathcal{G}$	Total Green's function
$\mathcal{G}^{-}$	Advanced Green's function
$\mathcal{G}^{+}$	Retarded Green's function
$\mathcal{G}_0^{-}$	Unperturbed advanced Green's function
$\mathcal{G}_0^{+}$	Unperturbed retarded Green's function
$g_{\mathrm{L,R}}$	Green's function for the isolated left/right electrodes
Γ_{L}	Electronic coupling to the left electrode
Γ_{R}	Electronic coupling to the right electrode
$\mathcal{G}^{<}$	Lesser Green's function
$\hat{H}$	Hamiltonian operator
$\hat{H}_0$	Unperturbed Hamiltonian operator
$\mathcal{H}$	Hamiltonian matrix for the whole system
$I^{\mathrm{L,R}}$	Electrical current through the left/right contacts
$\mathbf{k}$	Wave-vector
ν	Density of states
μ	Electrochemical potential
q_{D}	Charge in the device region
Σ	Self-energy operator
S	Overlap Matrix

Θ	Temperature
T	Transmission function
$\hat{U}$	Time evolution operator

Chapter 4

Symbol	**Description**
ϵ_m	Eigenvalue for the charge state $\|m\rangle$
Γ^{if}	Transition rates from the initial state i to the final state f
$\hbar\omega_{mn} = \epsilon_m - \epsilon_n$	Total energy differences between the two charge states $\|m\rangle$ and $\|n\rangle$
$\hat{r}$	Interaction operator acting in the reservoirs subspace
$\|\mathcal{R}\rangle$	State vector for the reservoirs subspace
$\hat{\rho}_I$	Reduced-density matrix operator in the interaction picture
$\hat{s}$	Interaction operator acting in the small quantum system subspace
$\|\mathcal{S}\rangle$	State vector for the small quantum system subspace
$\mathcal{T}$	Transfer Matrix operator
$\hat{U}_I$	Time evolution operator in the interaction picture
$\hat{\chi}_I$	Full density matrix operator in the interaction picture
ζ	Parameter for the light intensity

Chapter 5

Symbol	**Description**
E_{CT}^{+}	Charge-transfer energy to add one electron
E_{CT}^{-}	Charge-transfer energy to remove one electron
$E_{\mathrm{CT}}^{\mathrm{gap}}$	Charge-transfer energy gap
d_0	Image charge plane height
d_0^{+}	Image charge plane height for adding one electron to the molecule
d_0^{-}	Image charge plane height for removing one electron from the molecule
$\Delta\rho$	Charge-density differences
q	Point charge
U	Classical image charge for a point charge interacting with two flat surfaces
V	Classical image charge for a point charge interacting with one flat surface

Chapter 6

Symbol	**Description**
α	Scaling parameter for atomic-self interaction correction
$E_{\mathrm{LDA}}^{\mathrm{gap}}$	LDA HOMO-LUMO energy gap
ϵ_{LDA}	Kohn-Sham eigenvalue within the LDA approximation
L	Electrodes separation
Σ_{o}	Shift to the occupied Kohn-Sham levels

Σ_{u}	Shift to the unoccupied Kohn-Sham levels

Chapter 7

Symbol	**Description**
$\hat{b}$	Single-particle annihilation bosonic operator for the vibrons
$\hat{b}^{\dagger}$	Single-particle creation bosonic operator for the vibrons
$\hat{c}$	Single-particle annihilation fermionic operator acting on the molecule
$\hat{c}^{\dagger}$	Single-particle creation fermionic operator acting on the molecule
$\hat{d}_{\alpha\mathbf{k}}$	Single-particle annihilation fermionic operator acting on the electrode α
$\hat{d}^{\dagger}_{\alpha\mathbf{k}}$	Single-particle creation fermionic operator acting on the electrode α
ϵ_i	Single-particle energy of electrons in the molecule
$\epsilon_{\alpha\mathbf{k}}$	Single-particle energy for electrons in the electrode α
γ_{α}	Hopping parameter
Γ_{α}	Electronic coupling to the electrode α
$\Gamma_{\alpha}^{nm;q'q}$	Sequential tunneling transition rates from state $\|n,q'\rangle \rightarrow \|m,q\rangle$ through electrode α
$\Gamma_{\alpha\alpha'}^{nm;q'q}$	Cotunneling transition rates from state $\|n,q'\rangle \rightarrow \|m,q\rangle$
$\hbar\omega_{\mathrm{q}}$	Phonon energy
λ	Electron-vibron coupling strength
$\hat{n}$	Number operator
$\rho_n^{q'}$	Occupation of charge state n and vibronic state q'
τ	Phonon relaxation time

Chapter 8

Symbol	**Description**
Γ_{α}^{+}	Sequential tunneling transition rates for adding one electron to the molecule through electrode α
Γ_{α}^{-}	Sequential tunneling transition rates for removing one electron from the molecule through electrode α
$\Gamma_{\alpha}^{+,qq'}$	Sequential tunneling transition rates for adding one electron to the molecule through electrode α and changing the vibron state $q \rightarrow q'$
$\Gamma_{\alpha}^{-,qq'}$	Sequential tunneling transition rates for removing one electron from the molecule through electrode α and changing the vibron state $q \rightarrow q'$
J_{ν}	Bessel's function of first kind for order ν
$\nu\hbar\omega$	Energy of ν photons
$\hbar\omega$	Photon energy

Chapter 1

General Introduction

1.1 Molecular Electronics

Molecular electronics consists of using single molecules as active components of electronic devices, such as in molecular diodes, transistors and integrated circuits [1]. Single molecules can offer several unique properties to electronics. The size of simple molecules is within several nanometers and hence the electronic spectrum is quantized with the typical energy scale of ∼eV. They also allow self-assembly, *i.e.* the spontaneous and reversible organization of molecular units into ordered structures by non-covalent interactions. This is very useful in fabricating electronic devices at such a small length scale. The large number of chemicals and their different chemical and electrical functions can open up many new possibilities to engineering a molecule to perform different tasks in different conditions.

Molecules were first proposed as an active electronic unit by Aviram and Ratner in the 1970s [2]. They proposed that certain types of molecules can yield current rectifying behavior. These are $D-\sigma-A$ molecules, where D is an electron-donor moiety and A is an electron-acceptor moiety. Then, σ is called the "bridge" and it is a conducting molecule that connects the donor to the acceptor. In these molecules, the state $D^- - \sigma - A^+$ is expected to be energetically more accessible than the $D^+ - \sigma - A^-$ state, therefore, leading to an asymmetric current versus bias voltage curve, *i.e.* to rectification.

Due to recent advancements in experimental techniques, electronic transport measurements through a single molecule are now realized routinely. In general, the possible experimental setups can be divided into two main categories, namely, scanning tunneling microscopy (STM) [3, 4, 5, 6, 7, 8, 9, 10, 11, 12, 13] and mechanically controlled break-junctions (MCBJs) experiments [14, 15, 16, 17, 18, 19, 20, 21, 22, 23]. In the first, the target molecules are deposited onto a metallic surface, forming a self-assembly monolayer (SAM), and a STM tip is brought into contact to form the molecular junction. Then a bias is applied between the tip and the metallic substrate and the electrical current through

the molecule is measured. In the second, a metallic nanocontact is created by stretching a metal wire and, just before rupture, a solution containing the target molecules is added to the system. Subsequently, the metallic contact is further stretched until rupture. In some cases a molecule gets trapped between the metallic tips forming the molecular junctions (MJ). Likewise, a bias is applied between the two electrodes and the electrical current through the molecule is measured. Both experimental setups are schematically shown in Fig. 1.1.

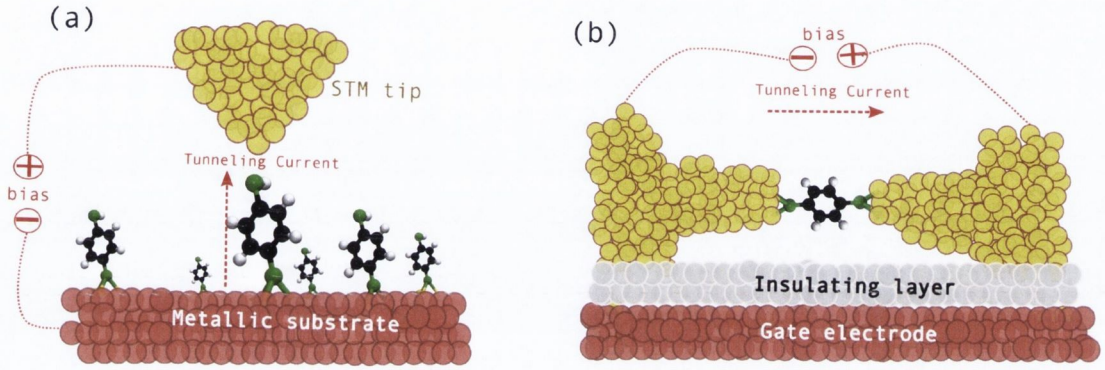

Figure 1.1: Cartoon showing at the atomic scale the formation of molecular junctions. (a) A STM tip is put in contact with a benzene-1,4-dithiol (BDT) molecule previously adsorbed onto the metallic surface. A voltage is applied between the tip and the substrate and a tunneling current is established. (b) MCBJ setup after the metallic nanowire has been broken and a molecule has been trapped in the nanogap. A voltage is applied between the two electrodes and an electrical current is established. A gate voltage can be applied by means of a third electrode, which shifts the energy levels of the molecule.

1.2 Statistical aspect of molecular junction measurements

A long-standing problem in the area of molecular electronics is the difficulty of finding quantitative agreement between theory and experiments in some cases. This makes it difficult to design and build functioning devices based on molecules. More than a decade has passed since the pioneering experiment by Reed *et al.* [14], and yet the well-known prototype molecular junction that consists of a benzene-1,4-dithiol molecule inserted between two gold electrodes (Au-BDT-Au) is still not fully understood. Numerous experimental [22, 21, 20, 12, 18, 5, 15, 5, 17] and theoretical [24, 25, 26, 27, 28, 29, 30] works have been reported, with both experimental and theoretical results varying over a large range. Due to the nature of the experiments, several different geometrical contacts can be accessed during the stretching process of the junction, which leads to a statistical character of the experimental analysis. In fact, in a single experiment, a broad range of values for the conductance, G, is observed, and in some cases even very different average G values

between experiments [22, 17, 26]. Yet, recent independent measurements [12, 4, 7, 23] agree on an average value of G of about $0.01G_0$ for Au-BDT-Au, where $G_0 = 2e^2/h$ is the quantum conductance (e is the electron charge and h is the Planck's constant).

1.3 Molecular junctions: strong and weak coupling limits

In all these junctions, the understanding of the details of the organic/inorganic interface is crucial to interpret the experimental data [31, 29, 30]. For instance, depending on how the molecule connects to the electrodes, two main regimes of transport can take place. First, for strong coupling, where the dominant energy scale is the bonding energy, fractional charge transfer can occur through the device. This regime manifests, for instance, in the Au-BDT-Au junction where the tunneling of electrons through the MJ is the dominant mechanism of charge transfer. In contrast, if the molecule is weakly coupled to the electrodes, when an electron has been transferred to the molecule, due to the Coulomb repulsion, a second electron is blocked to hop in until its energy overcomes the single-electron charging energy, $\mathcal{U}$. In this case, the system is in the Coulomb blockade (CB) regime (see Chapter 2 of Ref. [32] for a detailed description of CB), characterized by tunneling of integer number of electrons. Fig. 1.2(a) shows schematically the typical current versus voltage for the two regimes and how the electronic coupling strength affects the shape of the curve. Fig. 1.2(b) shows a stability diagram or Coulomb diamond for a two level model system where the transfer of integer number of electrons takes place. The charge state of the molecule is easily identified for different blockaded regions. The value of $\mathcal{U}$ can also be easily extracted from such plots.

1.4 Energy level alignment at the interface

In addition to the possibility of different transport regimes, another important issue in molecular electronics is the energy level alignment at the interface and the renormalization of the molecular energy levels when the interface is formed. It has been demonstrated experimentally [33, 34, 35, 36] that the quasi-particle energy gap, $E_{\mathrm{QP}}^{\mathrm{gap}}$, of a molecule, defined as the difference between its ionization potential, I^{P}, and its electron affinity, E^{A}, is reduced with respect to that of the gas phase by adsorbing the molecule on a polarizable substrate. In a non-interacting quasi-particle picture, the I^{P} is the negative of the highest occupied molecular orbital (HOMO) energy, while the E^{A} corresponds to the energy of the lowest unoccupied molecular orbital (LUMO). The reduction of the I^{P} and E^{A} of a molecule adsorbed on a metallic surface is mainly due to the Coulomb interaction between the added/subtracted charge on the molecule and the screening electrons in

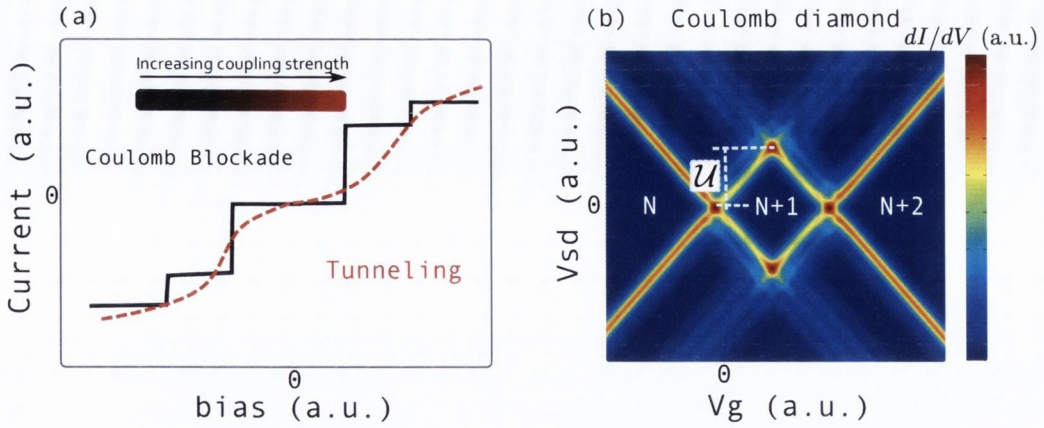

Figure 1.2: (a) Schematic representation of a typical current versus voltage curve for a two-level system and how the shape of the current changes with respect to the electronic coupling strength. For weak coupling, integer number of electrons is transferred and the current shows a step-like behavior. For strong coupling, fractional charge transfer can take place and the current is smoothed out due to electron tunneling. (b) An example of a Coulomb diamond or stability diagram for a two level system in the Coulomb blockage regime. The charge state of the molecule for different blockaded region is shown. Also the single-electron charging energy, $\mathcal{U}$, can be identified.

the substrate. This interaction leads to a polarization of the surface, so that a surface charge with opposite sign with respect to the charge state of the molecule is formed, as schematically shown in Fig. 1.3(a-b). This non-local feature, called image-charge effect, becomes more relevant as the molecule approaches the metallic surface. As a consequence, the reduction of the I^{P} and the E^{A}, hence of the $E_{\mathrm{QP}}^{\mathrm{gap}}$, becomes more prominent with the molecule approaching the surface, as illustrated in Fig. 1.4.

Although this effect is known to be present in all the transport measurements of molecular junctions, it was only recently that it could be quantified. Perrin *et al.* [37] using a MCBJ were able to observe the energy level renormalization of a zinc-porphyrin molecule [Zn(5,15-di(p-thiolphenyl)-10,20-di(p-tolyl)porphyrin)], abbreviated ZnTPPdT, where the molecule is weakly coupled to two gold electrodes. In Chapter 5 we discuss in detail this problem and we show our approach to quantify the molecular energy level renormalization. We then apply this method in Chapter 6 and Chapter 7.

1.5 Interaction of light with molecular junctions

The underlying processes of the interaction of light with molecular junctions are attracting great attention as a challenging theoretical and experimental problem and because of their potential application as a characterization and control tool [38, 39, 40, 41, 42]. This area of research is at the interface between two other important areas, namely, molecular electronics and molecular plasmonics and it is seen as having important technological implications. Advances in optical microscopy techniques have made of optical

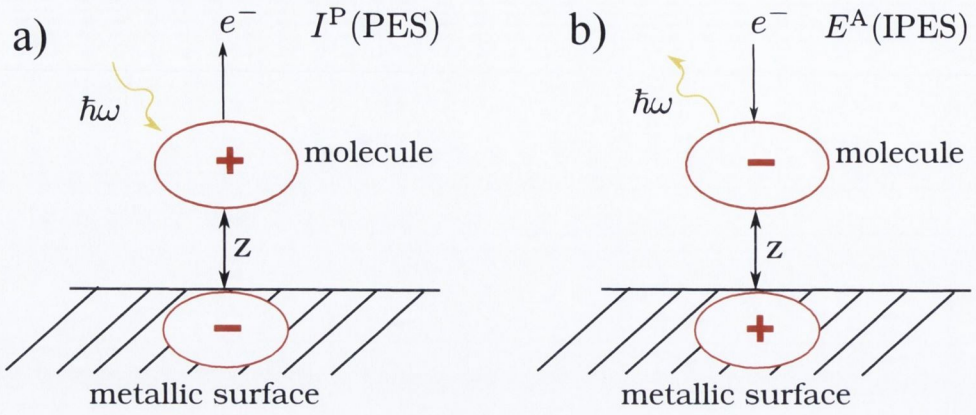

Figure 1.3: Illustration of the surface polarization effect due to a charged molecule in the vicinity of the metallic surface at a distance z. (a) Photo-emission spectroscopy (PES) used to measure the I^P where one electron is taken from the molecule after absorbing a photon of energy $\hbar\omega$. (b) Inverse photo-emission spectroscopy (IPES) used to measure the E^A. One electron is added to the molecule and the energy of the emitted photon is measured.

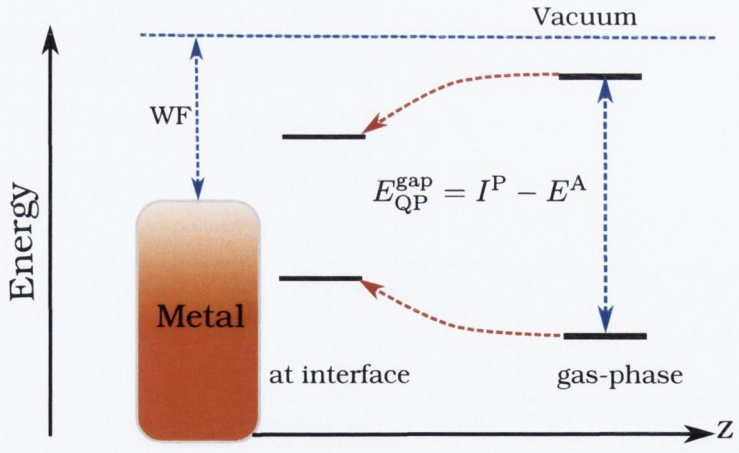

Figure 1.4: (a) Schematic energy level diagram of the frontier orbitals of a molecule approaching a metallic surface. Due to the interaction with the screening charge formed at the surface, the system is further stabilized and the E_{QP}^{gap} is reduced with respect to its gas phase value as z is reduced. W_F is the work function of the metal.

spectroscopy an important observation and diagnostic tool for molecular junctions.

Historically, the first experiments of ac-bias driven tunneling are due to Dayem and Martin [43] who studied photon-assisted tunneling (PAT) in superconductor-insulator-superconductor hybrid structures. Tien and Gordon were the first ones to propose a simple model to explain PAT in terms of ac- induced sidebands [44]. The well-known Tien-Gordon model has shown to account for the main qualitative physics of PAT through different nanostructure and mesoscopic devices.

An example of the importance of studying light induced effects in molecular junctions is the one applied to photovoltaic devices. Organic solar cells (OSCs), which lie within the class of third generation solar cells, are considered as one of the most promising systems to enhance efficiency and to reduce the cost of power-to-energy conversion, when compared to silicon based devices. OSCs materials can be organized in different categories ranging from the crystalline small molecules [45], dye-sensitized solar cells (DSSCs) [46, 47] to amorphous polymers (plastics). More recently, another class of solar cells have shown great potential, the perovskites solar cells that consist of an organic molecule inside an inorganic crystalline structure [48].

The theoretical approaches to PAT in molecular junctions can be divided into two main categories: (i) methods based on the framework of scattering theory, sometimes within the non-equilibrium Green's function (NEGF) formalism, extended to account for the presence of an external electromagnetic field and (ii) those based on master equation (ME) approach or similar kinetic descriptions of transport, again generalized to take into account external oscillating field. For instance, Foden and Whittaker [49] extended the Tien-Gordon model by given a quantum electrodynamics treatment to the photon field. Later, Park *et al.* [50] by means of the Keldysh formalism, equivalent to the NEGF formalism, generalized this model for adiabatic PAT in order to account for non-adiabatic processes, *i.e.* for interference between the different transport channels. Galperim *et al.* [51, 52, 53], within the Keldysh formalism, studied light-induced charge transport in molecular junctions presenting strong charge-transfer transition into their excited states. Their model consists of a two-level (HOMO and LUMO levels) for the molecule strongly coupled to the electrodes. The molecules studied present dipole moments that changes considerably upon excitation leading to a strong shift of the electronic charge distribution. In other words, one of the energy levels, either the HOMO or the LUMO, is stronger coupled to one contact than to the other. When an optical excitation from the HOMO level to the LUMO occur, due to the asymmetry in the contact couplings, a current is established even without applied bias. Within the same approach, they could also study current-induced light emission, where by applying bias, electroluminescence can be observed [54]. Tian *et al.* have also studied electroluminescence in molecular junctions within the density matrix formalism (ME approach) [55]. Fainberg *et al.* [56] generalized the approach of Galperim *et al.* [51, 52, 53] in order to account for

different laser pulse shapes. By means of the density matrix formalism, they could derive a set of closed MEs to compute the observables.

1.6 Theoretical point of view on molecular junctions

From the theoretical point of view, the study of charge transport in molecular junctions in general is very challenging for several reasons: (i) an electronic structure theory able to give a correct description of the excited states and the energy level position of the molecules is needed. Moreover, this can not be so computationally demanding due to the necessity of, very often, describing very large systems. (ii) The energy levels alignment of organic/inorganic interfaces has to be well described, *i.e.* the position of the frontier molecular orbitals of the organic light-harvesting material with respect to the electrode bands need to be computed correctly, since it determines the rates at which charges are injected or recombined. Moreover, this is a key design quantity for engineering materials combinations with enhanced light-to-current conversion. (iii) Different electronic transport regimes can take place. For instance, Coulomb blockade, sequential tunneling, inelastic cotunneling, light-induced vibration, current-induced light emission could take place in a molecular junction; (iv) Effects of temperature on the transport properties of MJs, even without light effects, have been studied and shown to play an important role when comparing to experimental data both, in the strong coupling limit [29, 30] and in the weak one [57, 58]. Furthermore, as far as illumination of the junction is concerned, the issue of heating can not be avoided [59, 60, 61, 62].

In regards to electronic transport calculations, there are two main approaches, namely, the ones based on the non-equilibrium Green's functions (NEGF) formalism [63] and the ones based on the density matrix formalism that leads to solving master equations (ME) [64]. The former is often combined with density functional theory (DFT) [65, 66] in order to describe the electronic structure of the system. The later is usually associated with a model Hamiltonian that captures the physics of interest. In the present work we intend to explore both methodologies applied to the study of molecular junctions. We address the limitations of these approaches and discuss in which case one is more appropriated than the other.

1.7 Dissertation Layout

In Chapter 2 we present an introduction to DFT, the electronic structure method used throughout the present work. We discuss its advantages and most importantly its limitations when a quantitative description of electronic transport properties of molecular junctions is required. For instance, in Sec. 2.5.2 we discuss the problem of the lack of

the derivative discontinuity in local and semi-local approximations of the DFT exchange-correlation functional and in Sec. 2.5.3 the problem of the self-interaction error in DFT.

In Chapter 3 we present a general overview of quantum transport through nanoscale systems and we discuss the Landauer-Büttiker approach in Sec. 3.1. In Sec. 3.3 we present the formalism to first-principles based quantum transport used in this dissertation, namely the NEGF. This approach is combined throughout with DFT as the method of choice to describe the electronic structure of nanoscale systems. In Sec. 3.5 we discuss some particularities of this combination.

In Chapter 4 we present the density matrix formalism by which we can derive MEs combined with model Hamiltonians. The ME is a different approach to the quantum transport, where the key quantity is the reduced density matrix. The transition rates are treated within time-dependent perturbation theory and the full derivation of these quantities are presented in Appendix B and Appendix C. By solving a simple set of linear equations, one can evaluate the electrical current through molecular systems including different effects, such as, temperature and light-induced tunneling.

In Chapter 5 we start by presenting a discussion on the energy level alignment of organic/inorganic interfaces and our approach to its calculation, namely, a constrained-DFT (CDFT) method by which one can evaluate the molecular energy levels renormalization when an interface is formed. The theoretical background of this method is given in Sec. 2.6 and the details of its implementation are given in Appendix E.

In Chapter 6 we present a thorough study of the Au-BDT-Au molecular junction. In Sec. 6.1.1 we discuss the stability of this system with respect to the adsorption of the molecule on surfaces as well as when the molecule is in a junction. In Sec. 6.1.2 we discuss the energy level alignment of these junctions and present different methods to account for energy level renormalization. In Sec. 6.1.4 we present our results of the quantum transport of these molecular junctions under stretching and compare the results for both thiol and thiolate junctions. Finally, in Sec. 6.1.6 we present a combined molecular dynamics and Monte Carlo approach in order to account for effects of temperature and the statistical aspect of the experiments, namely, the possibility of having many different geometries and, therefore, different conductance values.

In Chapter 7 we apply the ME formalism presented in Chapter 4 to the electron transport in the weak coupling limit, *i.e.* in the CB regime. We apply this approach and compare our results to available experimental data of energy level renormalization in molecular junctions as a function of the electrodes separation. We show how the energy level alignment of the junction plays a crucial role in determining the electronic transport. Moreover, by including vibronic degrees of freedom we show that our theoretical results are in good agreement with the experimental data.

Finally, in Chapter 8 we discuss light-induced charge transfer and conductance enhancement due to the interaction of charge carries with light. Within the ME approach,

in Sec. 8.1.1, we study the effect of light in simple models of one and two levels and show the results when one considers higher-order contributions, such as cotunneling. In Sec. 8.2 we discuss the interplay between phonons and light-induced effects and show how light can be used to control the conductance of molecular junctions in the strong electron-vibron coupling limit. In Sec. 8.3.1 we show how the transport properties of molecular junctions with donor-acceptor structure change depending on the charge state of the molecule. This is accomplished by combining CDFT with the NEGF method.

Chapter 2

Density Functional Theory

2.1 Introduction

In quantum mechanics, all the information concerning the system is contained in the so-called total wave function, $\tilde{\Psi}(\mathbf{R}, \mathbf{r})$, where $\mathbf{R}$ and $\mathbf{r}$ represent a set of nuclei and electrons coordinates, respectively. We omit the spin degrees of freedom for the sake of simplicity. Our aim is to understand how density functional theory (DFT) can be applied to the study of the electronic structure of atoms, molecules and solids. Since we are concerned exclusively on the electronic structure, the nuclear degrees of freedom (*e.g.* the crystal lattice in a solid) appear only in the form of a potential $v(\mathbf{r})$ acting on the electrons. This is the *Born-Oppenheimer approximation*, so that the wave function can be rewritten as $\tilde{\Psi} = \Phi(\mathbf{R})\Psi(\mathbf{r}; \mathbf{R})$, *i.e.* as a product of the electronic and nuclear degrees of freedom and with the electronic part $[\Psi(\mathbf{r}; \mathbf{R})]$ parameterized by the nuclear coordinates. For non-relativistic electrons, this wave function is calculated by solving the Schrödinger's equation, which for a single electron moving under the effect of an external potential $v(\mathbf{r})$ reads [1]

$$\left[-\frac{\hbar^2 \nabla^2}{2m} + v(\mathbf{r}) \right] \Psi(\mathbf{r}) = \epsilon \Psi(\mathbf{r}). \tag{2.1.1}$$

For a multi-electron system, *i.e.* for a many-body problem, the Schrödinger's equation becomes

$$\left[-\frac{\hbar^2 \nabla^2}{2m} + v(\mathbf{r}_i) + \sum_{i<j} U(\mathbf{r}_i, \mathbf{r}_j) \right] \Psi(\mathbf{r}_1, \mathbf{r}_2 \ldots, \mathbf{r}_N) = E\Psi(\mathbf{r}_1, \mathbf{r}_2 \ldots, \mathbf{r}_N), \tag{2.1.2}$$

where N is the number of electrons in the system and $U(\mathbf{r}_i, \mathbf{r}_j)$ describes the electron-electron interaction term. For a Coulomb system, the interaction term is given by the

[1] We omit the coordinate $\mathbf{R}$ in order to simplify the notation.

following operator

$$\hat{U} = \sum_{i<j} U(\mathbf{r}_i, \mathbf{r}_j) = \frac{1}{4\pi\epsilon_0} \sum_{i<j} \frac{e^2}{|\mathbf{r}_i - \mathbf{r}_j|}, \tag{2.1.3}$$

which is the same for any system of particles interacting via Coulomb interaction. In the same way, the kinetic energy operator given by

$$\hat{T} = \sum_i -\frac{\hbar^2 \nabla_i^2}{2m} \tag{2.1.4}$$

is the same for any non-relativistic electron. Note that for materials containing atoms with large atomic numbers (Z), the electrons are accelerated to relativistic velocities, therefore, one must include relativistic effects by solving Dirac's equation and the kinetic operator takes a different form. In the absence of external perturbations, *e.g.* and electric field, $v(\mathbf{r})$ is given by the electron-nuclei interaction

$$\hat{V}_{ext} = \sum_i v(\mathbf{r}_i) = \frac{1}{4\pi\epsilon_0} \sum_{ik} \frac{Z_k e^2}{|\mathbf{r}_i - \mathbf{R}_k|}, \tag{2.1.5}$$

where the sum extends over all nuclei, each with charge $Q_k = Z_k e$ and coordinates $\mathbf{R}_k$. Note that it is only the spatial arrangement of the atoms (apart from the corresponding boundary conditions) that distinguishes a molecule from a solid. For this reason, the operators $\hat{U}$ and $\hat{T}$ are often called "universal" whereas $\hat{V}_{ext}$ is system-dependent. Similarly, it is only through the term $\hat{U}$ that the single-body quantum mechanics of Eq. (2.1.1) differs from the complex many-body problem posed by Eq. (2.1.2). The natural way to solve the problem is by specifying the external potential $\hat{V}_{ext}$, so that the system of interest is defined, and introducing it into the Schrödinger's equation in order to obtain the wave function Ψ. All the properties of the system are then calculated by evaluating the expectation values of the operators that represent the properties of interest, *i.e.* $\langle\Psi|\ldots|\Psi\rangle$. One important observable is the electronic density given by

$$\rho(\mathbf{r}) = N \int d^3r_2 \int d^3r_3 \ldots \int d^3r_N \Psi^*(\mathbf{r}, \mathbf{r}_2 \ldots, \mathbf{r}_N)\Psi(\mathbf{r}, \mathbf{r}_2 \ldots, \mathbf{r}_N). \tag{2.1.6}$$

DFT recognizes that non-relativistic Coulomb systems differ only by their potential $v(\mathbf{r})$, and gives a prescription for dealing with the universal operators $\hat{U}$ and $\hat{T}$. Furthermore, DFT provides a way to systematically map the many-body problem, with the interaction term $\hat{U}$ onto a single-body problem, without $\hat{U}$. All this is done by promoting the particle density $\rho(\mathbf{r})$ from just one among many observables to the key variable, on which the calculation of all other observables can be based.

2.2 Hohenberg-Kohn theorems

This insight is due to Hohenberg and Kohn [65], who in 1964 set the foundation of DFT by treating the electron charge density as the fundamental variable in the N-body problem. By doing so, the scheme to solve the electronic system can be summarized as

$$\rho(\mathbf{r}) \Longrightarrow \Psi(\mathbf{r}, \mathbf{r}_2 \ldots, \mathbf{r}_N) \Longrightarrow v(\mathbf{r}) \tag{2.2.1}$$

i.e. knowledge of $\rho(\mathbf{r})$ implies knowledge of the wave function and the potential, and hence of all other observables. The DFT is based on two theorems, the Hohenberg-Kohn theorems (HKTs). Here we present the derivation of the HKTs as given originally by Hohenberg-Kohn in Ref. [65]. Other demonstrations can be found in Ref. [67]. The first theorem presents the relation of uniqueness between the ground state electronic charge density, *i.e.* $\rho_0(\mathbf{r})$, and the external potential $v(\mathbf{r})$:

> **Theorem I:** *The ground state charge density $\rho_0(\mathbf{r})$ of a system of interacting electrons under the influence of the external potential $V_{ext}(\mathbf{r})$ determines uniquely that potential.*

In other words, for every potential (or arrangement of atoms) there is only one representation of the ground state electronic charge density and vice-versa. Moreover, if the ground state is degenerate, Theorem I refers to the density of any of those states. As a consequence of Theorem I:

> **Corollary:** If the external potential $V_{ext}(\mathbf{r})$ is determined, then also the Hamiltonian is so. Consequently, the wave functions of each electron for the ground state, are also determined. Therefore, once the ground state charge density $\rho_0(\mathbf{r})$ is known, all the ground state properties of the system are determined.

Proof of Theorem I: The demonstration is as follows. Assuming that the ground state of a system can be characterized by the Hamiltonian $\hat{H}$ containing the potential $v(\mathbf{r})$, the Schrödinger's equation is given by:

$$(\hat{T} + \hat{U} + \hat{V}_{ext})\Psi = E\Psi, \tag{2.2.2}$$

where $\hat{T}$, $\hat{U}$ and $\hat{V}_{ext}$ represent the kinetic, electron-electron interaction and external potential operators, respectively. If we assume the existence of another potential $\hat{V'}_{ext}$ we can write the corresponding Hamiltonian $\hat{H}'$. The Schrödinger's equation solution can be written in a simplified form as Ψ' ($\hat{H}'\Psi' = E'\Psi'$), which yields the same electronic charge density $\rho(\mathbf{r})$. By applying the variational principle, we obtain

$$E = \langle\Psi|\hat{T} + \hat{V}_{ext} + \hat{U}|\Psi\rangle < \langle\Psi'|\hat{T} + \hat{V}_{ext} + \hat{U}|\Psi'\rangle, \tag{2.2.3}$$

$$E' = \langle\Psi'|\hat{T} + \hat{V'}_{ext} + \hat{U}|\Psi'\rangle < \langle\Psi|\hat{T} + \hat{V'}_{ext} + \hat{U}|\Psi\rangle. \tag{2.2.4}$$

Therefore,

$$E < \langle \Psi' | \hat{H} | \Psi' \rangle = \langle \Psi' | \hat{H}' | \Psi' \rangle + \langle \Psi' | \hat{V}_{ext} - \hat{V}'_{ext} | \Psi' \rangle \tag{2.2.5}$$

$$E < E' + \int \rho(\mathbf{r})[v'(\mathbf{r}) - v(\mathbf{r})]d^3r. \tag{2.2.6}$$

This leads to the following equations

$$E < E' + \int \rho(\mathbf{r})[v(\mathbf{r}) - v'(\mathbf{r})]d^3r, \tag{2.2.7}$$

$$E' < E + \int \rho(\mathbf{r})[v'(\mathbf{r}) - v(\mathbf{r})]d^3r, \tag{2.2.8}$$

and finally we obtain the inconsistency

$$E + E' < E' + E. \tag{2.2.9}$$

Thus, we verify that there is only one electronic charge density that corresponds to the ground state charge density for the specified potential. In other words, for a certain atomic arrangement, the ground state charge density can be uniquely defined.

Theorem II is stated as

> **Theorem II:** *There exist an universal functional of the electronic density for the total energy, $E[\rho(\mathbf{r})]$. The functional is minimized at the ground state charge density. The value of the functional at the minimum is the ground state total energy.*

Proof of Theorem II: Theorem II establishes that $E[\rho]$ is a functional of $\rho(\mathbf{r})$ and that

$$E[\rho_0] \leq E[\rho], \tag{2.2.10}$$

where ρ_0 is the ground state density. As a consequence, any ground state observable of the system is an unique functional of the electronic density. The total energy for a given density $\rho(\mathbf{r})$ is given by

$$E[\rho] = \langle \Psi[\rho] | \hat{T} + \hat{U} | \Psi[\rho] \rangle + \langle \Psi[\rho] | \hat{V} | \Psi[\rho], \rangle \tag{2.2.11}$$

$$E[\rho] = F[\rho] + \langle \Psi[\rho] | \hat{V} | \Psi[\rho] \rangle, \tag{2.2.12}$$

and for the ground state,

$$E[\rho_0] = F[\rho_0] + \langle \Psi[\rho_0] | \hat{V} \, | \Psi[\rho_0] \rangle \, . \tag{2.2.13}$$

The functional $F[\rho]$ is universal and it is valid for any N-electrons system. The total

energy of the ground state is given by

$$E[\rho_0] = F[\rho_0] + \langle \Psi_0 | \hat{V} | \Psi_0 \rangle, \tag{2.2.14}$$

where $|\Psi_0\rangle$ is the ground state wave function. By applying the variational principle we obtain

$$E[\Psi_0] < E[\Psi], \tag{2.2.15}$$

$$\langle \Psi_0 | \hat{T} + \hat{U} | \Psi_0 \rangle + \langle \Psi_0 | \hat{V} | \Psi_0 \rangle < \langle \Psi | \hat{T} + \hat{U} | \Psi \rangle + \langle \Psi | \hat{V} | \Psi \rangle, \tag{2.2.16}$$

$$F[\rho_0] + \langle \Psi_0 | \hat{V} | \Psi_0 \rangle < F[\rho] + \langle \Psi | \hat{V} | \Psi \rangle, \tag{2.2.17}$$

$$E[\rho_0] < E[\rho]. \tag{2.2.18}$$

Both the HKTs show that it is possible, from the electronic density, to obtain all the ground state properties of interest of the system. However, they do not discuss how to perform this task, namely they do not provide an expression for the functional. This is what we will look at in the next sections.

2.3 Thomas-Fermi approximation

An important problem in solid-state theory and quantum chemistry is to understand how a many-electron system behaves due to Coulomb interaction. The *Thomas-Fermi approximation* [68, 69] assumes that the functional for the electron-electron interaction energy is approximately equal to the Coulomb term, or *Hartree*, and can be stated as

$$U[\rho] \approx U_H[\rho] = \frac{e^2}{4\pi\epsilon_0} \int d\mathbf{r} \int d\mathbf{r}' \frac{\rho(\mathbf{r})\rho(\mathbf{r}')}{|\mathbf{r} - \mathbf{r}'|}, \tag{2.3.1}$$

where e is the electron charge. Another approximation is to assume that the kinetic energy of a system of interacting electrons is the same as that of a system of interacting electrons of constant electronic charge density,

$$T[\rho] \approx T^{\mathrm{LDA}}[\rho] = \int d^3\mathbf{r}\; t^{\mathrm{hom}}(\rho(\mathbf{r})), \tag{2.3.2}$$

where $t^{hom}(\rho)$ is the kinetic-energy density of a homogeneous interacting system with (constant) density ρ. Since it refers to interacting electrons, $t^{hom}(\rho)$ is not known explicitly and further approximations are needed. As it stands, Eq. (2.3.2) is already a first example of a local-density approximation (LDA). In this approximation, it is assumed that the real inhomogeneous system with density $\rho(\mathbf{r})$ in potential $v(\mathbf{r})$ can be divided into smaller systems. In each of these subsystems $\rho(\mathbf{r})$ are $v(\mathbf{r})$ approximately constant. In each cell (*i.e.* locally) one can then use the per-volume energy of a homogeneous system to

approximate the contribution of the cell to the real inhomogeneous one. By making these cells infinitesimally small and summing over all of them, one obtain Eq. (2.3.2). For a homogeneous non-interacting system, however, the density functional form of the kinetic energy term is known and it is given by

$$\rho = \frac{1}{3\pi^2}\left(\frac{2m}{\hbar^2}\right)^{\frac{3}{2}} E_{\mathrm{F}}^{3/2}, \tag{2.3.3}$$

where E_{F} is the Fermi energy. The kinetic energy is $T = 3\rho E_{\mathrm{F}}/5$. Thus, the kinetic energy density, T/N, is

$$t_{\mathrm{s}}^{\mathrm{hom}}[\rho] = \frac{3}{5}\frac{\hbar^2}{2m}\left(3\pi^2\right)^{2/3}\rho^{2/3}, \tag{2.3.4}$$

where the subscript "s" specifies that we are dealing with a non-interacting system or a system of "single-particles". Thus, the approximations can then be summarized as

$$T[\rho] \approx T^{\mathrm{LDA}}[\rho] \approx T_{\mathrm{s}}^{\mathrm{LDA}}[\rho] = \int d^3\mathbf{r}\; t_{\mathrm{s}}^{\mathrm{hom}}(\rho(\mathbf{r})), \tag{2.3.5}$$

where $T_{\mathrm{s}}^{\mathrm{LDA}}[\rho]$ is the local-density approximation to $T_{\mathrm{s}}[\rho]$, the kinetic energy of non-interacting electrons of density ρ. One can further improve the Thomas-Fermi approximation by including the quantum mechanics effects due exchange, *i.e.* the Pauli's principle. In the LDA, the functional for the exchange energy is known for an electron gas system and it is given by

$$E_{\mathrm{x}}^{\mathrm{LDA}}[\rho] = \int \rho(\mathbf{r})\varepsilon_{\mathrm{x}}\rho(\mathbf{r})d\mathbf{r}, \tag{2.3.6}$$

where the exchange energy density is

$$\varepsilon_{\mathrm{x}}(\rho) = -\frac{3}{4}e^2\left(\frac{3}{\pi}\right)^{\frac{1}{3}}\rho^{\frac{1}{3}}. \tag{2.3.7}$$

This approximation is known as Thomas-Fermi-Dirac [70]. The functional for the total energy can then be written as

$$E_{\mathrm{TFD}}[\rho] = T_{\mathrm{s}}^{\mathrm{LDA}}[\rho] + U_{\mathrm{H}}[\rho] + V[\rho] + E_{\mathrm{x}}^{\mathrm{LDA}}[\rho] \tag{2.3.8}$$

Moreover, terms that account for variations in the charge density for the kinetic energy can be added to the Thomas-Fermi-Dirac approximation, *e.g.* the *von Weizäcker* term. Yet, the Thomas-Fermi-Dirac approximation does not give satisfactory results. A major deficiency is that when applied to molecular systems, the molecules are unstable, *i.e.* the energy of a set of isolated atoms is lower than that of the bound molecule [71]. This is directly related to the fact that correlation effects are neglected in the electron-electron interaction energy and also because of the local approximation for the kinetic energy.

2.4 Kohn-Sham equations

DFT can be implemented in many ways and usually the minimization of an explicit energy functional is normally not the most efficient one. Kohn and Sham [66] proposed a new root to circumvent the problem. Their insight consists in replacing the real and complicated many-body problem of interacting electrons by an equivalent problem of non-interacting particles. It is assumed that the ground state density of the many-body problem is the same of an auxiliary system of non-interacting electrons. This leads to a set of single-particle equations.

The approximation presented in Eq. (2.3.5) for the kinetic energy is not enough. A more accurate way to treat the kinetic energy of interacting particles, $T[\rho]$, is based on decomposing this term into two contributions. The first part, $T_{\rm s}[\rho]$ (again the "s" subscript stands for single-particle), corresponds to the kinetic energy of the non-interacting particles and the second part contains the correlation effects $T_{\rm c}[\rho]$ (the "c" subscript stands for correlation),

$$T[\rho] = T_{\rm s}[\rho] + T_{\rm c}[\rho]. \tag{2.4.1}$$

Unfortunately, the term $T_{\rm s}[\rho]$ does not have a known functional form and we need to use approximations to treat this contribution. In contrast, the kinetic energy functional for non-interacting particles is known

$$T_s[\rho] = -\frac{\hbar^2}{2m}\sum_i \int d\mathbf{r}\psi_i^*(\mathbf{r})\nabla^2\psi_i(\mathbf{r}), \tag{2.4.2}$$

where the sum is over all the individual contributions of the non-interacting wave function ψ_i. Since all ψ_i are functionals of the density (Theorem I), $T_{\rm s}[\rho]$ is explicitly a functional of the orbitals but implicitly a functional of the electronic charge density, $T_{\rm s}[\rho] = T_{\rm s}[\{\psi_i[\rho]\}]$. In other words, $T_{\rm s}$ depends on the full set of occupied orbitals ψ_i, each of which is a functional of $[\rho]$.

The potential energy is given by the sum of three contributions: the first is the Hartree energy, $U_{\rm H}[\rho]$, the second is the exchange term due to the Pauli's principle, $U_{\rm x}[\rho]$. The last term is the contribution due to correlation, $U_{\rm c}[\rho]$. The total energy can then be written as

$$E[\rho] = T_{\rm s}[\rho] + U_{\rm H}[\rho] + V[\rho] + E_{\rm xc}, \tag{2.4.3}$$

$$V[\rho] = \int \rho(\mathbf{r})v(\mathbf{r})d^3r, \tag{2.4.4}$$

$$E_{\rm xc} = U[\rho] - U_{\rm H}[\rho] + T[\rho] - T_{\rm s}[\rho]. \tag{2.4.5}$$

All the contributions due to exchange and correlation from both the kinetic and the potential energy terms ($T_{\rm c}[\rho]$, $U_{\rm x}[\rho]$ and $U_{\rm c}[\rho]$) are put together in a single term called

the exchange-correlation (XC) term, $E_{\rm xc}$. This way, DFT looks formally like a single-particle theory, where many-body effects are still included via the XC functional. In order to calculate the total energy of the system, the functional $E[\rho]$ has to be minimized following the variational principle where the constraint is the total number of electrons. With the Lagrange multipliers technique one define a new function $F(\lambda, \mathbf{r}) = f(\mathbf{r}) - \lambda g(\mathbf{r})$, where λ is identified as the chemical potential. We need to compute

$$\frac{\delta}{\delta\rho}\left(E[\rho] - \lambda\left[\int \rho(\mathbf{r})d^3r - N\right]\right) = 0 \tag{2.4.6}$$

so that

$$\begin{aligned}\frac{\delta T_{\rm s}[\rho]}{\delta\rho} + \frac{\delta U_{\rm H}[\rho]}{\delta\rho} + \frac{\delta V_{\rm s}[\rho]}{\delta\rho} + \frac{\delta E_{\rm xc}[\rho]}{\delta\rho} - \lambda = 0 \\ \frac{\delta T_{\rm s}[\rho]}{\delta\rho} + v_{\rm H}[\rho](\mathbf{r}) + v[\rho](\mathbf{r}) + v_{\rm xc}[\rho](\mathbf{r}) - \lambda = 0.\end{aligned} \tag{2.4.7}$$

Considering an auxiliary system of non-interacting particles subject to the potential $v_{\rm s}(\mathbf{r})$, then applying the variational principle one has

$$\frac{\delta T_{\rm s}[\rho]}{\delta\rho} + v_{\rm s}[\rho](\mathbf{r}) - \lambda = 0. \tag{2.4.8}$$

Since for the non-interacting particles system there is neither exchange, nor correlation nor electrostatic interaction, the charge density that minimizes Eq. (2.4.8) is $\rho_{\rm s}(\mathbf{r})$. By comparing Eq. (2.4.8) with Eq. (2.4.7), we see that in order to have both equations satisfied $[\rho_{\rm s}(\mathbf{r}) \equiv \rho(\mathbf{r})]$ we need

$$v_{\rm s}[\rho](\mathbf{r}) = v_{\rm H}[\rho](\mathbf{r}) + v[\rho](\mathbf{r}) + v_{\rm xc}[\rho](\mathbf{r}). \tag{2.4.9}$$

This shows that it is possible to calculate the electronic density of the interacting particles system subject to the potential $v(\mathbf{r})$, by solving single-particle equations of the non-interacting system subject to the potential $v_{\rm s}(\mathbf{r}) = v_{\rm eff}(\mathbf{r})$. In particular, the single-particle Schrödinger's equation of the auxiliary system is given by

$$\left[\frac{-\hbar^2}{2m}\nabla^2 + v_{\rm eff}(\mathbf{r})\right]\phi_i = \epsilon_i\phi_i, \tag{2.4.10}$$

where the solutions are the so-called Kohn-Sham (KS) orbitals that reproduce the charge density $\rho(\mathbf{r})$ of the original system,

$$\rho(\mathbf{r}) = \sum_{\rm occup} \phi_i^*\phi_i. \tag{2.4.11}$$

In other words, the KS procedure assumes that there is a Hamiltonian that describes a

system of non-interacting particles subject to an effective potential that generates the same charge density of the interacting system. Since the potential $v_{\text{eff}}(\mathbf{r})$ depends on $\rho(\mathbf{r})$ and vice-versa, the solution can be obtained through a self-consistent procedure. It starts with a "guess" density. From this density one calculates $v_{\text{s}}(\mathbf{r})$. Eq. (2.4.10) is then solved and the functions ϕ_i are determined. Finally from Eq. (2.4.11) a new charge density is computed. The procedure is repeated self-consistently until the criterion of convergence is satisfied, *i.e.* until the input charge density is the same as the output one within a specified tolerance.

The set of Eq. (2.4.9), Eq. (2.4.10) and Eq. (2.4.11) is known as the KS equations. From the solution of these equations, a final expression for the ground state total energy can be obtained

$$E_0 = \sum_i^N \epsilon_i - \frac{q^2}{4\pi\epsilon_0} \int d^3r \int d^3r' \frac{\rho_0(\mathbf{r})\rho_0(\mathbf{r}')}{|\mathbf{r}-\mathbf{r}'|} - \int d^3r v\rho_0(\mathbf{r}) + E_{\text{xc}}[\rho_0]. \tag{2.4.12}$$

One major advantage of the KS scheme is that the term for the kinetic energy is solved exactly (for the non-interacting electron system), nevertheless, it requires solving N single-particle equations instead of minimizing the functional of the total energy with respect to the charge density.

2.5 Local density approximation

Eq. (2.4.12) allows us to calculate the ground state total energy of a system of interacting electrons. However, there is still an important part missing, *i.e.* the functional form of the E_{xc} is unknown! Therefore, approximations have to be made for a practical use of the KS scheme. There are three main sets of approximations to the XC functional, namely, local [72], semi-local [73] and hybrids [74, 75]. In the present work, we widely use the LDA [66, 72, 76]. Therefore, we focus our attention on this approximation and discuss its limitations and problems. In the LDA, the XC energy can be written as

$$E_{\text{xc}}^{\text{LDA}}[\rho] = \int \varepsilon_{\text{xc}}^{\text{LDA}}(\rho(\mathbf{r}))\rho(\mathbf{r})d\mathbf{r}. \tag{2.5.1}$$

where $\varepsilon_{\text{xc}}^{\text{LDA}}$ is XC energy density of an homogeneous electron gas with density $\rho(\mathbf{r})$. The exact functional form for the exchange part of E_{xc} is known from Eq. (2.3.7). The correlation contribution, $\varepsilon_{\text{c}}^{\text{LDA}}$, instead can be obtained with accuracy through quantum monte carlo simulations (QMC) [72]. From these, an analytic expression for $\varepsilon_{\text{c}}^{\text{LDA}}$ is determined as a function of the density, which is a requirement since the energy is a *continuous function of the density.* By construction, a LDA functional is purely local, therefore it is expected to lead to very good results for systems where the charge density varies slowly in space. That is the primarily reason why DFT-LDA describes with good

success the properties of metallic solids but it does not perform well for non-homogeneous systems, such as molecules and atoms.

2.5.1 Interpreting the Kohn-Sham eigenvalues

The ground state total energy given in Eq. (2.4.12) shows that E_0 is not simply the sum of all the ε_i, *i.e.* of the KS eigenvalues. The KS eigenvalues simply represent the eigenvalues of an auxiliary single-particle equation of which the eigenvectors give the correct charge density. In this framework, the charge density is the quantity with physical meaning. Since the KS eigenvalues do not represent the true energy spectrum, they are not to be trusted quantitatively. An important exception to this is the highest occupied KS eigenvalue. Denoting by $\varepsilon_{\mathrm{N}}(\mathrm{M})$ the N'th eigenvalue of a system with M electrons one can show that $I^{\mathrm{P}} = -\varepsilon_{\mathrm{N}}(\mathrm{N})$, where I^{P} is the ionization potential of the N-body system. Likewise, $E^{\mathrm{A}} = -\varepsilon_{\mathrm{N}+1}(\mathrm{N}+1)$ where E^{A} is the electron affinity of the N-particle system [77, 78]. Nevertheless, these relations are valid only when dealing with the exact functional for the total energy. When calculated with an approximated functional such as LDA, the highest occupied and the lowest unoccupied orbitals do not offer good results when compared to experimental data for I^{P} and E^{A}, respectively.

2.5.2 The lack of the derivative discontinuity

An important property of the exact DFT functional is the derivative discontinuity of the XC functional with respect to the particle number [79, 77, 80]. This is given by

$$\left.\frac{\delta E_{\mathrm{xc}}[n]}{\delta\rho(\mathbf{r})}\right|_{N+\delta} - \left.\frac{\delta E_{\mathrm{xc}}[n]}{\delta\rho(\mathbf{r})}\right|_{N-\delta} = v_{\mathrm{xc}}^{+(\mathbf{r})} - v_{\mathrm{xc}}^{-(\mathbf{r})} = \Delta_{\mathrm{xc}}, \tag{2.5.2}$$

where δ is an infinitesimal electron number and Δ_{xc} is a shift of the $v_{\mathrm{xc}(\mathbf{r})}$ when the system passes from electron-poor, $N-\delta$, to electron-rich, $N+\delta$. It is a system-dependent quantity. Likewise, the non-interacting kinetic energy functional has a similar discontinuity that can be represented by

$$\left.\frac{\delta T_{\mathrm{s}}[n]}{\delta\rho(\mathbf{r})}\right|_{N+\delta} - \left.\frac{\delta T_{\mathrm{s}}[n]}{\delta\rho(\mathbf{r})}\right|_{N-\delta} = \varepsilon_{\mathrm{N}+1} - \varepsilon_{\mathrm{N}} = \Delta_{\mathrm{KS}}, \tag{2.5.3}$$

i.e. the difference between the highest occupied and lowest unoccupied KS single-particle eigenvalues. The discontinuity in the non-interacting kinetic energy is therefore the KS single-particle gap, Δ_{KS}, whereas the discontinuity in the XC correlation energy (Δ_{xc}) is a many-body effect. The true fundamental gap given by

$$\Delta = I^{\mathrm{P}} - E^{\mathrm{A}} = E(N+1) + E(N-1) - 2E(N), \tag{2.5.4}$$

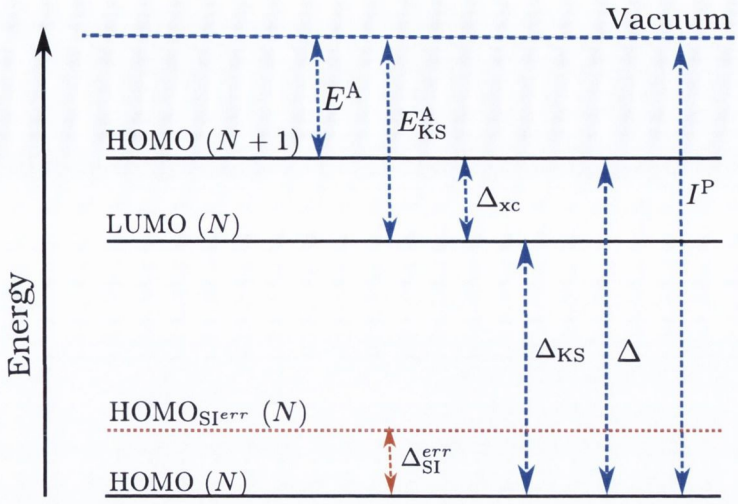

Figure 2.1: Energy level diagram of the KS eigenvalues and their relationship to the ionization potential (I^{P}) and electron affinity (E^{A}). $E^{\mathrm{A}}_{\mathrm{KS}}$ is the KS electron affinity, Δ_{xc} is the derivative discontinuity in the XC energy, Δ_{KS} and Δ are the KS gap and the fundamental gap, respectively. Finally, $\Delta^{err}_{\mathrm{SI}}$ is the shift of the occupied orbitals due to the self-interaction error in DFT.

is the discontinuity of the total ground-state energy functional [79, 77, 80], *i.e.*

$$\left.\frac{\delta E[n]}{\delta\rho(\mathbf{r})}\right|_{N+\delta} - \left.\frac{\delta E[n]}{\delta\rho(\mathbf{r})}\right|_{N-\delta} = \Delta_{\mathrm{KS}} + \Delta_{\mathrm{xc}} = \Delta. \tag{2.5.5}$$

Since all the terms other than E_{xc} and T_{s} in the total energy functional, Eq. (2.4.12), are continuous functionals of the charge density, the fundamental gap is the sum of the KS gap and the XC discontinuity. As discussed in Sec. 2.5, the LDA functional is a continuous function of the charge density [Eq. (2.5.1)], therefore it predicts $\Delta_{\mathrm{xc}} = 0$ leading to a underestimated fundamental gap. All these quantities along with the KS eigenvalues and their relation to observables are schematically shown in the energy diagram of Fig. 2.1. For molecules, HOMO(N) is the highest occupied molecular orbital of the N-electron system, HOMO($N+1$) the same for the $(N+1)$-electron system, and LUMO(N) the lowest unoccupied orbital of the N-electron system. In solids presenting an energy gap, *e.g.* semiconductors, the HOMO and LUMO are referred as the top of the valence band and the bottom of the conduction band, respectively. In metals, where there is no energy gap, HOMO and LUMO coincide and equal to the E_{F} of the material. The vertical arrows in Fig. 2.1 show the fundamental gap within DFT (with the exact functional), Δ, the KS single particle gap, Δ_{KS}, and the derivative discontinuity in the exchange correlation potential, Δ_{xc}; also the ionization potential of the N-interacting system, I^{P}, which is equal to the ionization potential of the KS system, $I^{\mathrm{P}}_{\mathrm{KS}}$; the electron affinity of the N-interacting electron system, E^{A}, and the KS electron affinity $E^{\mathrm{A}}_{\mathrm{KS}} = -\varepsilon_{\mathrm{N+1}}(\mathrm{N})$. Note that Δ_{KS} is reduced compared to the fundamental gap due to the lack of the derivative

discontinuity in the exchange correlation potential within the KS scheme.

Despite all the interpretative problems with the KS eigenvalues, it is a fortunate surprise that in many situations they do empirically provide a very good first approximation to the real spectrum of extended systems. For example, usually band-structure calculations in solid-state physics show good agreement with experimental photo-emission data and inverse photo-emission spectroscopy. Nonetheless, in molecular systems, the HOMO-LUMO gap is hugely underestimated, typically by about 50%, when compared to $I^{\mathrm{P}} - E^{\mathrm{A}}$. This is also related to another problem, namely, the self-interaction (SI) problem in DFT that we shall discuss in the next section.

2.5.3 The self-interaction problem: ASIC method

In Sec. 2.3 we presented the Thomas-Fermi approximation, which consists of replacing the expectation value of the electron-electron interaction (given by the Coulomb's law) by a functional of the electronic density, Eq. (2.3.1). However, already in 1934, Fermi and Amaldi observed a failure of this approximation in the limit of one electron system, *i.e.* there is a non-vanishing contribution from the interaction of the electron with itself known as the self-interaction (SI) error [81]. This is not the case of the well-known wave function based mean-field Hartree-Fock (HF) method. In HF, the total electronic energy is given by the sum of the Hartree and the exchange contributions. The exchange energy is given by

$$E_{\mathrm{x}}^{\mathrm{HF}} = -\frac{1}{4\pi\epsilon_0}\sum_{\sigma}\sum_{\alpha,\alpha'} f_{\sigma\alpha}f_{\sigma\alpha'}\int d^3r\int d^3r'\frac{\psi^*_{\sigma\alpha}(\mathbf{r})\psi^*_{\sigma\alpha'}(\mathbf{r}')\psi^*_{\sigma\alpha'}(\mathbf{r})\psi_{\sigma\alpha}(\mathbf{r}')}{|\mathbf{r}-\mathbf{r}'|}. \tag{2.5.6}$$

Here the $\psi_\sigma(\mathbf{r})$'s are the Slater determinants for spin σ with occupation numbers $f_{\alpha\sigma}$. When the $\alpha = \alpha'$, this term constitutes a self-exchange energy that exactly cancels out the self-Hartree energy of Eq. (2.3.1) on an orbital-by-orbital basis so that HF is free of SI errors. Although HF does not contain SI errors, it totally neglects correlation effects, which limits its application to many systems. Within DFT, however, when using local or semi-local functionals, the spurious SI error is only partially canceled. In other words, the condition for KS-DFT

$$U[\rho^\sigma_\alpha] + E_{\mathrm{xc}}[\rho^\sigma_\alpha, 0] = 0, \tag{2.5.7}$$

for the orbital density $\rho^\sigma_\alpha = |\psi^\sigma_\alpha|^2$ of the fully occupied KS orbital ψ^σ_α is not satisfied. As a consequence, the KS potential becomes too repulsive and this leads to a series of failures in describing fundamental properties. For instance, negatively charged ions (H^-, O^-, F^-) are predicted to be unstable within LDA [82], the energy gap of transition metal oxides (MnO, NiO) are predicted too small [83] when compared to experimental data. Moreover, the KS HOMO that is rigorously associated to the $-I^{\mathrm{P}}$, as discussed in Fig. 2.1, is very often found to be several eV higher in energy, specially for molecules, when compared to

experimental data.

The modern theory of self-interaction correction (SIC) was proposed in the 80's by Perdew and Zunger [76] (PZ). The idea consists of removing directly the self-Hartree and self-XC energy of all the occupied KS orbitals from the approximated XC functional. For instance, for the LDA one has

$$E_{\rm xc}^{\rm SIC}[\rho^{\uparrow},\rho^{\downarrow}] = E_{\rm xc}^{\rm LDA}[\rho^{\uparrow},\rho^{\downarrow}] - \sum_{\alpha\sigma}^{occup.} \delta_{\alpha\sigma}, \tag{2.5.8}$$

where

$$\delta_{\alpha\sigma} = U[\rho_{\alpha}^{\sigma}] + E_{\rm xc}^{\rm LDA}[\rho_{\alpha}^{\sigma},0] \tag{2.5.9}$$

is the self-interaction of orbital $\alpha\sigma$. In other words, one subtracts, orbital by orbital, the contribution that the Hartree and XC functionals would make if there was only one electron in the system. This correction can be applied to any approximate density functional, and it ensures that the resulting corrected functional satisfies

$$E_{\rm xc}^{\rm SIC}[\rho^{(1)},0] = -U[\rho^{(1)},0], \tag{2.5.10}$$

i.e. for a single electron, the self-interaction comes only from the Hartree term. The PZ-SIC approach can be applied to any spin-density functional for the $E_{\rm xc}$ and when applied to the exact functional, the correction vanishes.

For a completely uniform system, the LDA approximation is exact. Therefore, in this limit, it is self-interaction free. However, for many realistic systems of interest, they show very strong localized states, such as d states in transition-metal oxides, and the SI becomes really important. Unfortunately the PZ-SIC, which minimizes the corrected energy functional with respect to the orbitals, does not lead to usual KS equations since the effective potential is different for each orbital. In order words, the XC functional within the PZ-SIC is orbital dependent, therefore, one cannot define a kinetic energy functional independently from the choice of the XC functional [76]. As a consequence, the KS orbitals are not orthogonal and the KS equation is not invariant when making a unitary transformation of the occupied orbitals. Therefore, the effect of SIC will depend on the difference in occupied orbitals before and after the unitary transformation. To circumvent this, elaborated schemes of minimization and several developments have been made [81, 84].

In the present work we explore an approximated method by considering only the atomic contributions to SIC, the ASIC method [85, 86, 87, 88]. The method is applied to the LDA which has the benefit of preserving the local aspect of the LDA potential. A first step of the ASIC method is to incorporate part of the SIC into the definition of the pseudopotentials [89]. The idea consists in subtracting the atomic SI from the free atom,

and then transferring the resulting electronic structure to the definition of a standard norm-conserving pseudopotential. By doing so, the SIC contribution to the total energy can be separated into the contributions from the core electrons and the valence electrons. A further approximation is to assume that the SIC contributions for the valence electrons are also atomic-like. Although this approximation sounds drastic, the orbitals that present more SI are those more localized, *e.g.* *d* orbitals, therefore the atomic-like approximation looks appropriate. In Chapter 6 we will show how the lack of derivative discontinuity and the problem of self-interaction can lead to wrong predictions of transport properties of molecular junctions.

2.6 Constrained density functional theory

Among the various possibilities used to obtain improved results within DFT, constrained DFT (CDFT) represents a conceptually different approach to the problem. The idea behind CDFT is that one can always define an appropriate density functional, implementing a given desired constraint on the charge density [90] (*e.g.* one can demand that an electron is localized on a particular group of atoms in a molecule). This is obtained by introducing an appropriate external potential in the KS equations. The crucial point is that the approach is fully variational, meaning that the energy minimum of the constrained functional represents the ground state of the system under that particular constraint [91, 92, 93]. The method allows, for example, to access energies and electron density distributions of charge transfer states of a given system, and has been successfully applied to the study of long-range charge transfer excitations between molecules [91, 94, 95]. In Chapter 5 we apply CDFT to the investigation of the energy level alignment of metal/molecule interfaces. In relation to this problem CDFT has two main advantages. Firstly, since CDFT is based on total energy differences it does not present the conceptual problems of interpreting the KS eigenvalues as a true quasiparticle spectrum. Secondly, one has to note that the total energy, even in the case of local functionals, is a rather accurate quantity, in contrast to the charge density that local functionals usually tend to over-delocalize. This means that a theory that improves the charge density but that relies on the total energy is expected to be accurate.

In the KS framework [66] the total energy (in atomic units) is given by

$$E[\rho] = \sum_{\sigma}^{\alpha,\beta} \sum_{i}^{N_\sigma} \langle \phi_{i\sigma} | -\frac{1}{2}\nabla^2 | \phi_{i\sigma} \rangle + \int d\mathbf{r}\, v(\mathbf{r})\rho(\mathbf{r}) + U_{\mathrm{H}}[\rho] + E_{\mathrm{xc}}[\rho^\alpha, \rho^\beta], \tag{2.6.1}$$

where U_{H} is the Hartree energy, E_{xc} is the exchange-correlation energy, $v(\mathbf{r})$ is the external potential, $\rho^\sigma(\mathbf{r})$ is the electronic density for spin $\sigma = \uparrow, \downarrow$ of N_σ electrons ($\rho = \rho^\uparrow + \rho^\downarrow$) and the set $\{|\phi_{i\sigma}\rangle\}$ contains the KS wavefunctions that minimize the energy. A generic

constraint on the charge density is that there is a specified number of electrons for each spin, N_c^σ, within a certain region of space. This can be written as

$$\int w_c^\sigma(\mathbf{r})\rho^\sigma(\mathbf{r})\,d\mathbf{r} = N_c^\sigma\,, \tag{2.6.2}$$

where $w_c^\sigma(\mathbf{r})$ is a weighting function that describes the spatial extension of the constraining region. In the simplest case $w_c^\sigma(\mathbf{r})$ can be chosen to be equal to 1 within a certain volume and 0 elsewhere. In order to minimize the KS total energy of Eq. (2.6.1) subject to the constraint of Eq. (2.6.2), an additional spin-dependent term, proportional to the Lagrange multiplier, V_c^σ, is added to the energy. A new functional is thus defined to be

$$W[\rho, V_c] = E[\rho] + \sum_\sigma V_c^\sigma \left(\int w_c^\sigma(\mathbf{r})\rho^\sigma(\mathbf{r})\,d\mathbf{r} - N_c^\sigma \right)\,. \tag{2.6.3}$$

When ρ satisfies the constraint in Eq. (2.6.2) then $E[\rho] = W[\rho, V_c]$ by construction. Up to the ρ independent term $\sum_\sigma V_c^\sigma N_c^\sigma$, $W[\rho, V_c]$ is the ground state energy of a system with an additional spin-dependent external potential $V_c^\sigma w_c^\sigma(\mathbf{r})$. The KS equations with this additional potential are then given by

$$\left[-\frac{1}{2}\nabla^2 + v(\mathbf{r}) + v_{xc}^\sigma(\mathbf{r}) + V_c^\sigma w_c^\sigma(\mathbf{r}) + \int \frac{\rho(\mathbf{r}')}{|\mathbf{r}-\mathbf{r}'|}\,d\mathbf{r}' \right] \phi_i^\sigma(\mathbf{r}) = \epsilon_i \phi_i^\sigma(\mathbf{r})\,, \tag{2.6.4}$$

where v_{xc}^σ is the exchange and correlation potential. As in standard KS DFT the electron density is constructed from the occupied KS eigenvectors, $\{\phi_i^\sigma(\mathbf{r})\}$, until self-consistency is achieved. In this particular case, the self-consistency has also to guarantee that the constraint set by Eq. (2.6.2) is satisfied. The minimization then proceeds as follows. Firstly, as in the standard KS scheme, an initial charge density is defined and then updated until the KS equations are satisfied self-consistently. Secondly, at every self-consistent step in this update of the charge density a second self-consistent loop is performed, where for a given input density, $\rho(\mathbf{r})$, the value of V_c^σ is updated until the output charge density obtained via solution of Eq. (2.6.4) satisfies the constraint of Eq. (2.6.2). This second step is performed following an optimization scheme suggested in Ref. [92]. Updating V_c^σ in this way ensures that at each self-consistent step and therefore also at convergence the constraint is fulfilled.

This methodology was implemented in the DFT package SIESTA [96]. SIESTA uses a linear combination of atomic orbitals (LCAO) basis set, so that, instead of defining the constraining region in real space via the function $w_c^\sigma(\mathbf{r})$, we define it over the LCAO space. This requires that the total charge projected onto a given set of basis orbitals is equal to N_c^σ. For this aim we have implemented both the Löwdin [97, 93] and the Mülliken [98] projection schemes. A detailed description of the implementation is given in Appendix E.

Chapter 3

Quantum Transport at the Nanoscale

In the past decades, important advances in the area of semiconductors have led to the miniaturization of electronic devices to the nanoscale. In this limit, quantum effects such as conductance quantization and quantum Hall effect can be observed by electron transport measurements. However, these bring other challenges that have to be tackled. For instance, the density increase of the active components of the devices leads to problems such as power dissipation and undesirable quantum tunneling, which reduces the efficiency of logical devices. Therefore, understanding the influence of these effects over the device performance is key for the development of novel and more efficient electronics. In particular, understanding the electronic transport properties of such systems is crucial and challenging.

Electronic transport in nanostructures is essentially a many-body non-equilibrium statistical problem, where the conducting electrons and the background ionic structure are in a state of non-equilibrium, whose properties can be known only statistically. Therefore, important approximations and assumptions are usually at hand in order to transform the many-body problem into a tractable one that still captures most of the relevant physics. The first steps towards the development of a quantum transport theory are due to Landauer [99, 100]. Other important contributions are due to Büttiker [101, 102] who extended the Landauer's ideas to systems consisting of many contacts. This is nowadays known as the Landauer-Büttiker approach to quantum transport.

In this chapter we present the basic ideas behind the Landauer-Büttiker approach and the well known non-equilibrium Greens' function formalism (NEGF) used to study coherent electronic quantum transport in nanostructures. We end the chapter with a discussion on the limitations of the NEGF approach as well as when combined with DFT.

3.1 Landauer-Büttiker approach

In this section we present the Landauer-Büttiker approach [103] to quantum transport and how the quantization of conductance appears in nanoscale systems. There are several importance approximations, which we will present when needed. The basic idea behind this approach is that the electrical current flowing through a quantum system is expressed in terms of the probability of electrons to be transmitted across the device. For instance, when an external potential is applied between the two electrodes connected to a ballistic nanostructure the probability of transmitting the incoming electrons through the device is equal to unity, *i.e.* for a ballistic conductor [1], the electrical current obtained is finite indicating that there is still an observable resistance in the system.

Let us consider a quantum system or nanostructure connected to the two electrodes with a cross section W and length l. If the dimensions of the nanostructure are of the order of the dimensions of the electrodes, *i.e.* micrometers, the conductance is given by $G = \sigma W/l$ (Ohm's law), where the conductivity σ is an intrinsic property of the material. Ohm's law predicts that if one reduces the length of the nanostructure, the conductance should increase towards infinite values. However, this is not observed in experiments, and the conductance eventually tends to reach a limiting value when the device is much smaller than the electronic mean free path. This resistance appears at the interface between the nanostructure and the electrodes. A very simplistic explanation is that, while in the electrodes there are infinite sub-bands or normal modes that contribute to the current, in the nanostructure they are very few, so that the current has to be redistributed at the interface and this leads to the finite resistance observed.

Approximation 1: The first assumption in the Landauer-Büttiker approach is to replace the closed system (composed of the electrodes, nanostructure and an external battery) by an open quantum system, where the battery is removed since it is a too complicated object to be treated quantum mechanically. Therefore, we assume that the electrodes are metallic and infinite so that they are unperturbed due to the addition or the removal of electrons, *i.e.* the electrodes are considered as electron reservoirs and they can be characterized by their chemical potentials, μ. The battery then is just an external potential difference applied between the two electrodes shifting their chemical potentials.

Approximation 2: The next step is to assume the *mean-field approximation* where the electrons move under the influence of a mean-field created by the other electrons, *i.e.* we transform the complicated many-body problem into a single-particle picture much easier to deal with. Any mean-field Hamiltonian is appropriate for this task and so is the DFT KS Hamiltonian, as presented in Sec. 2.4. Without this approximation, one should in principle, determine the full many-body statistical operator, from which one can compute

[1] A ballistic conductor is defined as a conductor in which the electronic mean free path is much larger than the dimensions of the conductor itself so that no scattering events occur.

the expectation value of the current. The problem is, if we were dealing with interacting electrons, also for the electrons on the electrodes far away from the nanostructure attached to them, we would need to describe how they evolve in time even before being scattered at the nanostructure. This leads to a nested infinite number of equations, which prevents us to obtain a closed set of equations to compute the current [63]. Within the mean-field approximation, one can describe the electronic structure of the full system in terms of independent single-particle bands or channels. The assumption here, besides the mean-field approximation, is that the off-diagonal elements of the density matrix that describe the coherences between the state vectors are exactly zero. In other words, we assume that the system has somehow evolved to a totally incoherent (independent) set of (single-particle) channels rapidly after interacting with an environment. Having said that, for each sub-band of the quantum system we can associate a dispersion relation as given by $E(N, \mathbf{k})$, where N is the sub-band index and $\mathbf{k}$ is the wave-vector. Moreover, $\epsilon_N = E(N, \mathbf{k} = 0)$ is the cutoff energy for the sub-band N, *i.e.* electrons with energy lower than ϵ_N are not able to tunnel through the device since there is no available states in this range of energy. The total number of sub-bands for a given energy E can be obtained by adding up the number of sub-bands with cutoff energy smaller than E as

$$M(E) = \sum_N \vartheta(E - \epsilon_N). \tag{3.1.1}$$

In order to simplify the arguments to come, we adopt for the moment zero temperature, so that there is current flow just for the range of energy $\mu_{\mathrm{L}} > E > \mu_{\mathrm{R}}$, where $\mu_{\mathrm{L(R)}}$ is the chemical potential of the left (right) electrodes. ϑ is the Heaviside step function given by

$$\vartheta(E - \epsilon_N) = \begin{cases} 1\ , & \text{if} \quad E - \epsilon_N \geq 0 \\ 0\ , & \text{if} \quad E - \epsilon_N < 0 \end{cases}. \tag{3.1.2}$$

Let us consider one single sub-band, where all the state vectors $\mathbf{k}$ are occupied following the Fermi-Dirac distribution function,

$$f(E, \mu_{\mathrm{L,R}}) = \frac{1}{e^{-\frac{E-\mu_{\mathrm{L,R}}}{k_{\mathrm{B}}\Theta}} + 1}, \tag{3.1.3}$$

where Θ is the temperature and k_{B} is the Boltzmann constant. For a uniform electron gas with electronic density n, moving with velocity v, the electrical current is given by $I = envA$. Therefore, the current through all the states $\mathbf{k}$ is given by

$$I = \frac{e}{l} \sum_{\mathbf{k}} v f(E) = \frac{e}{l} \sum_{\mathbf{k}} \frac{1}{\hbar} \frac{\partial E}{\partial \mathbf{k}} f(E). \tag{3.1.4}$$

By transforming the sum into an integral over the wave vectors

$$\sum_{\mathbf{k}} \rightarrow 2(spin) \times \frac{l}{2\pi} \int d\mathbf{k}, \tag{3.1.5}$$

we can rewrite the electrical current as

$$I = \frac{2e}{h} \int_{-\infty}^{\infty} f(E) dE. \tag{3.1.6}$$

The total current is then given by the sum of all the sub-bands as,

$$I = \frac{2e}{h} \int_{-\infty}^{\infty} M(E) f(E) dE. \tag{3.1.7}$$

This formula does not tell us anything about a quantum state of the system. In fact, the current is a statistical quantity averaged out in time and implicitly assumed to be stationary. The ideally stationary current is obtained because we assumed that the electrodes are simply reservoirs of electrons, *i.e.* they continually feed electrons in the distant past, and far away from the nanoscale junction, into wave-packets which move towards or away from the junction, without changing the current in time. Therefore, one can replace the open boundary condition problem to a periodic boundary condition problem. In other words, the electrons come from a distant past and far away from the junction towards the junction where they are scattered due to the broken periodicity caused by the device region, and subsequently move far away from it and keep propagating as different wave-packets to a distant future.

If we assume that the number of sub-bands M is energy independent for the range $\mu_{\mathrm{L}} > E > \mu_{\mathrm{R}}$, the Fermi-Dirac function becomes a step function [$f(E) = 1$ for $\Theta = 0\ K$] and we obtain

$$I = \frac{2e^2}{h} M \frac{(\mu_{\mathrm{L}} - \mu_{\mathrm{R}})}{e}, \tag{3.1.8}$$

$$G_{\mathrm{c}}^{-1} \equiv \frac{(\mu_{\mathrm{L}} - \mu_{\mathrm{R}})/e}{I} \approx \frac{12.8k\Omega}{M}, \tag{3.1.9}$$

where G_{c}^{-1} is the electrical resistance between the electrodes and the quantum system (contact resistance) and $(\mu_{\mathrm{L}} - \mu_{\mathrm{R}})/e$ is the bias applied to the electrodes. We assume that the applied bias, V, modify the electrodes chemical potential symmetrically as

$$\mu_{\mathrm{L}} = \mu_0 + \frac{eV}{2} \tag{3.1.10}$$

and

$$\mu_{\mathrm{R}} = \mu_0 - \frac{eV}{2}, \tag{3.1.11}$$

respectively, where μ_0 is the common equilibrium chemical potential.

The discussion so far has been based on the assumption that we are dealing with a ballistic quantum system with probability of transmitting the incoming electron equal to unity. For a ballistic system with probability less than unity, we include a factor in Eq. (3.1.9), which gives the average probability, T, to transmit one electron through the quantum device. The transmission coefficients, T, will be formally defined in Sec. 3.3. Then, Eq. (3.1.9) can be rewritten as [2]

$$G_c = \frac{2e^2}{h} MT, \tag{3.1.12}$$

which is known as the *Fisher-Lee formula* [104]. Note that conductance quantization is given in steps of the quantum conductance, $G_0 \equiv 2e^2/h$. In summary, while systems at the macroscopic scale obey the Ohm's law, at the nanoscale, important differences can be observed: (i) the contact resistance at the interface between the electrodes and the device is independent on the length of the device. (ii) The conductance do not decrease linearly with the cross section of the device, in fact, it changes discretely with the number of sub-bands available for conductance in the range of energy given by the external applied bias. (iii) The conductance depends linearly on the transmission probability of the device.

At $\Theta = 0$, incoming electrons from the left electrode with energy $\mu_L > E > \mu_R$ can tunnel through the device and occupy empty states on the right electrode. However, electrons from the right electrode can not be transmitted to the left electrode since all the states are already occupied at 0 K. Nevertheless, for temperatures different from 0 K, we need to take into account the Fermi-Dirac distribution functions of each electrode so that Eq. (3.1.7) becomes

$$I = \frac{2e}{h} \int_{-\infty}^{+\infty} \tilde{T}(E)(f_L(E) - f_R(E))dE, \tag{3.1.13}$$

where $\tilde{T}(E) = M(E)T(E)$.

3.1.1 Conductance linear regime

In equilibrium, *i.e.* for no external applied bias, $I = 0$ for

$$\begin{cases} \mu_L \to \mu_R \,, & \text{for } \Theta = 0 \\ f_L(E) \to f_R(E) \,, & \text{for } \Theta > 0. \end{cases}$$

[2] In this simple derivation, we assume that T is the same for all the sub-bands, which can be easily generalized if we consider that $MT = \sum_{i=1}^{M} T_i$.

If we consider small fluctuations around the equilibrium, the current is proportional to the applied bias

$$dI = \frac{2e}{h}\int \left\{ [\tilde{T}(E)]_{eq} d[(f_{\mathrm{L}}(E) - f_{\mathrm{R}}(E))] + \cancelto{0}{[(f_{\mathrm{L}}(E) - f_{\mathrm{R}}(E)]_{eq} d[\tilde{T}(E))_{eq}]} \right\}, \quad (3.1.14)$$

where the second term vanishes since the two electrodes have the same Fermi-Dirac function at equilibrium. Expanding the first term of Eq. (3.1.14), we obtain

$$\begin{aligned} df_{\mu_i} &\approx (\frac{\partial f_{\mu_i}}{\partial \mu_i})_{\mu_i=\mu_0} d\mu_i \ , \quad \text{with} \quad d\mu_i = \mu_i - \mu_0 \\ d[f_{\mathrm{L}} - f_{\mathrm{R}}] &\approx (\frac{\partial f_{\mu}}{\partial \mu})_{\mu=\mu_{eq}} [\mu_{\mathrm{L}} - \mu_{\mathrm{R}}] \quad = \quad (-\frac{\partial f_0}{\partial E})_{\mu=\mu_{eq}} [\mu_{\mathrm{L}} - \mu_{\mathrm{R}}] \end{aligned} \quad (3.1.15)$$

where f_0 is the Fermi-Dirac function at equilibrium ($\mu = E_f$). Therefore,

$$G = \frac{dI}{(\mu_{\mathrm{L}} - \mu_{\mathrm{R}})/e} = \frac{2e^2}{h}\int \tilde{T}(E)(-\frac{\partial f_0}{\partial E})dE. \quad (3.1.16)$$

For low temperatures, we have the following

$$f_0 \approx \vartheta(E_f - E) \quad \Longrightarrow \quad -\frac{\partial f_0}{\partial E} \approx \delta(E_f - E) \quad (3.1.17)$$

and

$$\vartheta(E_f - E) = \begin{cases} 1 \ , & \text{if} \quad E_f - E \geq 0 \\ 0 \ , & \text{if} \quad E_f - E < 0 \end{cases} \ , \quad \delta(E_f - E) = \begin{cases} 1 \ , & \text{if} \quad E_f = E \\ 0 \ , & \text{if} \quad E_f \neq E \end{cases} \quad (3.1.18)$$

where $\vartheta(E_f - E)$ and $\delta(E_f - E)$ are the Heaviside and Delta-Dirac functions, respectively. Finally, by inserting this result into Eq. (3.1.16), we have the conductance in the linear regime given by

$$G = \frac{2e^2}{h}\int \tilde{T}(E)\delta(E_f - E)dE \quad \Longrightarrow \quad G = \frac{2e^2}{h}\tilde{T}(E_f). \quad (3.1.19)$$

Note that this formula is valid for applied bias $(\mu_L - \mu_R)$ much smaller than $k_{\mathrm{B}}\Theta$, so that the first order expansion used in Eq. (3.1.15) can be justified.

3.2 Lippmann-Schwinger equation

Let us consider a single-particle Hamiltonian for our entire system, such as

$$\hat{H} = \hat{H}_0 + \hat{V}(\mathbf{r}), \quad (3.2.1)$$

where the first term corresponds to the free unperturbed electrons and the second contains the scattering potential due to the nanoscale junction. This is assumed to be time-independent. We can solve the Schrödinger equation for the full Hamiltonian and as well as only for $\hat{H}_0$, *i.e.* in absence of the scattering potential, so that

$$i\hbar\frac{\partial}{\partial t}\left|\psi(t)\right\rangle = \hat{H}(t)\left|\psi(t)\right\rangle \tag{3.2.2}$$

and

$$i\hbar\frac{\partial}{\partial t}\left|\psi_0(t)\right\rangle = \hat{H}_0(t)\left|\psi_0(t)\right\rangle, \tag{3.2.3}$$

where $|\psi(t)\rangle$ and $|\psi_0(t)\rangle$ are the perturbed and the unperturbed state vector, respectively. These equations can be written in a more compact form as

$$\hat{\mathcal{L}}\left|\psi(t)\right\rangle = 0, \tag{3.2.4}$$

where $\hat{\mathcal{L}} = i\hbar\frac{\partial}{\partial t} - \hat{H}$ or $\hat{\mathcal{L}} = i\hbar\frac{\partial}{\partial t} - \hat{H}_0$, is a linear differential operator. From the general theory of differential equations, one can rewrite Eq. (3.2.4) in terms of *Green's functions or propagator*, $\mathcal{G}(t)$, as

$$\hat{\mathcal{L}}\mathcal{G}(t) = \mathbb{1}\delta(r - r')\delta(t - t'). \tag{3.2.5}$$

In fact, Eq. (3.2.2) can be solved with two types of Green's functions

$$\left(i\hbar\frac{\partial}{\partial t} - \hat{H}\right)\mathcal{G}^{\pm}(t) = \mathbb{1}\delta(t). \tag{3.2.6}$$

Eq. (3.2.6) represents two equations of motion for the Green's functions $\mathcal{G}^+$ and $\mathcal{G}^-$ with the boundary conditions

$$\begin{aligned}
&\mathcal{G}^+(t) = 0 \quad \text{for } t < 0, \text{ retarded} \\
&\text{and} \\
&\mathcal{G}^-(t) = 0 \quad \text{for } t > 0, \text{ advanced.}
\end{aligned}$$

These boundary conditions lead to the two formal solutions of Eq. (3.2.6) as

$$\mathcal{G}^+(t) = \begin{cases} -\frac{i}{\hbar}e^{-\frac{i}{\hbar}\hat{H}t} & t > 0 \\ 0 & t < 0 \end{cases} \quad \text{and} \quad \mathcal{G}^-(t) = \begin{cases} 0 & t > 0 \\ \frac{i}{\hbar}e^{-\frac{i}{\hbar}\hat{H}t} & t < 0 \end{cases}. \tag{3.2.7}$$

The propagator $\mathcal{G}^+(t)$ (for $t > 0$) is proportional to the time-evolution operator given by

$$\hat{\mathcal{U}}(t, 0) = e^{-\frac{i}{\hbar}\hat{H}t}, \tag{3.2.8}$$

for a time-independent Hamiltonian. Similarly, one can describe the time-evolution of a state vector using the Green's function as

$$|\psi(t)\rangle = i\hbar\mathcal{G}^{+}(t-t_0)\,|\psi(t_0)\rangle\,, \quad \text{for } t > t_0, \tag{3.2.9}$$

i.e. $\mathcal{G}^{+}$ propagates the state vector and contains the history of its time evolution. For this reason, $\mathcal{G}^{+}$ is called *retarded Green's function.* Similarly, $\mathcal{G}^{-}$ can be used to define the time-evolution of a state vector to *past* times as

$$|\psi(t)\rangle = -i\hbar\mathcal{G}^{-}(t-t_0)\,|\psi(t_0)\rangle\,, \quad \text{for } t < t_0, \tag{3.2.10}$$

in other words, $\mathcal{G}^{-}$ carries information about the history of the time evolution from the present to a past time. Therefore, $\mathcal{G}^{-}$ is called the *advanced Green's function.* If instead of dealing with the full Hamiltonian $\hat{H}$ we use the unperturbed Hamiltonian, $\hat{H}_0$, we obtain

$$\mathcal{G}_0^{+}(t) = \begin{cases} -\frac{i}{\hbar}e^{-\frac{i}{\hbar}\hat{H}_0 t} & t > 0 \\ 0 & t < 0 \end{cases} \quad \text{and} \quad \mathcal{G}_0^{-}(t) = \begin{cases} 0 & t > 0 \\ \frac{i}{\hbar}e^{-\frac{i}{\hbar}\hat{H}_0 t} & t < 0, \end{cases} \tag{3.2.11}$$

to which we shall refer as "free" retarded and advanced Green's functions, respectively.

We now want to relate the Green's functions for the full Hamiltonian, $\hat{H}$, with the Green's functions of the unperturbed Hamiltonian, $\hat{H}_0$. For instance, we can write

$$\left(i\hbar\frac{\partial}{\partial t} - \hat{H}_0\right) = \mathbb{1}\delta(t)\left[\mathcal{G}_0^{\pm}(t)\right]^{-1}, \tag{3.2.12}$$

which can be inserted into Eq. (3.2.6) to yield

$$\mathbb{1}\delta(t)\mathcal{G}^{\pm}(t) = \mathbb{1}\delta(t)\mathcal{G}_0^{\pm}(t) + \mathcal{G}^{\pm}(t)\hat{V}\mathcal{G}_0^{\pm}(t). \tag{3.2.13}$$

If we integrate this equation for $\mathcal{G}^{+}$ from t_0 to $t > t_0$ we finally obtain the *Lippmann-Schwinger equation* which relates the full retarded Green's function to the free retarded Green's function

$$\mathcal{G}^{+}(t-t_0) = \mathcal{G}_0^{+}(t-t_0) + \int_{t_0}^{t} dt'\mathcal{G}^{+}(t-t')\hat{V}\mathcal{G}_0^{+}(t'-t_0). \tag{3.2.14}$$

Likewise, if we perform the integration for $\mathcal{G}^{-}$ from $t < t_0$ to t_0 we obtain similar relation for the advanced Green's function as

$$\mathcal{G}^{-}(t-t_0) = \mathcal{G}_0^{-}(t-t_0) + \int_{t_0}^{t} dt'\mathcal{G}^{-}(t-t')\hat{V}\mathcal{G}_0^{-}(t'-t_0). \tag{3.2.15}$$

Eq. (3.2.14) and Eq. (3.2.15) can be rewritten in a different way where one can iteratively replace the full Green's function inside the integral by its own value, which leads to an

infinite series expansion. This is the basis for a perturbative expansion, and one obtains

$$\begin{aligned}\mathcal{G}^{+}(t-t_0) =& \mathcal{G}_0^{+}(t-t_0) + \int_{t_0}^{t} dt' \mathcal{G}^{+}(t-t')\hat{V}\mathcal{G}_0^{+}(t'-t_0) \\ &+ \int_{t_0}^{t} dt' \int_{t_0}^{t'} dt'' \mathcal{G}^{+}(t-t')\hat{V}\mathcal{G}_0^{+}(t'-t'')\hat{V}\mathcal{G}_0^{+}(t''-t_0) + \dots \end{aligned} \tag{3.2.16}$$

and

$$\begin{aligned}\mathcal{G}^{-}(t-t_0) =& \mathcal{G}_0^{-}(t-t_0) + \int_{t_0}^{t} dt' \mathcal{G}^{-}(t-t')\hat{V}\mathcal{G}_0^{-}(t'-t_0) \\ &+ \int_{t_0}^{t} dt' \int_{t_0}^{t'} dt'' \mathcal{G}^{-}(t-t')\hat{V}\mathcal{G}_0^{-}(t'-t'')\hat{V}\mathcal{G}_0^{-}(t''-t_0) + \dots \end{aligned} \tag{3.2.17}$$

If the series expansion converges, one can write the effect of all the scattering events into a single quantity called *self-energy*, $\Sigma^{\pm}$, and Eq. (3.2.16) and Eq. (3.2.17) can be rewritten as

$$\mathcal{G}^{+}(t-t_0) = \mathcal{G}_0^{+}(t-t_0) + \int_{t_0}^{t} dt' \int_{t_0}^{t'} dt'' \mathcal{G}_0^{+}(t-t')\Sigma^{+}(t'-t'')\mathcal{G}^{+}(t''-t_0), \text{ for } t > t_0 \tag{3.2.18}$$

and

$$\mathcal{G}^{-}(t-t_0) = \mathcal{G}_0^{-}(t-t_0) + \int_{t}^{t_0} dt' \int_{t'}^{t_0} dt'' \mathcal{G}_0^{-}(t-t')\Sigma^{-}(t'-t'')\mathcal{G}^{-}(t''-t_0), \text{ for } t < t_0, \tag{3.2.19}$$

known as *Dyson's equation* for the retarded and advanced Green's functions, respectively. Within the mean-field approximation, the self-energy is simply

$$\Sigma^{\pm}(t'-t'') = \hat{V}\delta(t'-t''). \tag{3.2.20}$$

Up to this point, the Lippmann-Schwinger equation and Dyson's equation present no difference when solving the problem. However, when interactions among particles are present, the self-energy might be more complicated than the one of Eq. (3.2.20). In this case, the Dyson's equation presents a more compact way to represent these interactions.

3.2.1 Time-independent Lippmann-Schwinger equation

One can rewrite the Lippmann-Schwinger equations via Fourier transforming the time-dependent retarded and advanced Green's functions. Therefore,

$$\mathcal{G}^{+}(E) = \int_{-\infty}^{\infty} dt e^{iEt/\hbar} e^{-\delta t/\hbar} \mathcal{G}^{+}(t) = \int_{0}^{\infty} dt e^{iEt/\hbar} e^{-\delta t/\hbar} \mathcal{G}^{+}(t) \tag{3.2.21}$$

and

$$\mathcal{G}^{-}(E) = \int_{-\infty}^{0} dt e^{iEt/\hbar} e^{+\delta t/\hbar} \mathcal{G}^{-}(t) = \int_{0}^{\infty} dt e^{iEt/\hbar} e^{-\delta t/\hbar} \mathcal{G}^{-}(t) \tag{3.2.22}$$

for the full Hamiltonian and

$$\mathcal{G}_0^{+}(E) = \int_{0}^{\infty} dt e^{iEt/\hbar} e^{-\delta t/\hbar} \mathcal{G}_0^{+}(t) \tag{3.2.23}$$

and

$$\mathcal{G}_0^{-}(E) = \int_{0}^{\infty} dt e^{iEt/\hbar} e^{-\delta t/\hbar} \mathcal{G}_0^{-}(t) \tag{3.2.24}$$

for the unperturbed Hamiltonian. The infinitesimal quantity $\delta > 0$ in the exponential term guarantees that the integral converges. If we insert the results of Eq. (3.2.7) into Eq. (3.2.21) and Eq. (3.2.22) we have

$$\mathcal{G}^{+}(E) = \frac{\mathbb{1}}{E + i\delta - \hat{H}}, \tag{3.2.25}$$

for the retarded Green's function and

$$\mathcal{G}^{-}(E) = \frac{\mathbb{1}}{E - i\delta - \hat{H}} \tag{3.2.26}$$

for the advanced Green's function. Similarly, if we insert the results of Eq. (3.2.11) into Eq. (3.2.23) and Eq. (3.2.24), we have

$$\mathcal{G}_0^{+}(E) = \frac{\mathbb{1}}{E + i\delta - \hat{H}_0}, \tag{3.2.27}$$

for the free retarded Green's function and

$$\mathcal{G}_0^{-}(E) = \frac{\mathbb{1}}{E - i\delta - \hat{H}_0} \tag{3.2.28}$$

for the free advanced Green's function.

All the Green's functions have poles that corresponds to the eigenvalues of the respective Hamiltonian. Moreover, by simple inspection, they are related via

$$\left[\mathcal{G}^{+}(E)\right]^{\dagger} = \mathcal{G}^{-}(E), \tag{3.2.29}$$

and the same relation holds for the free Green's functions. After Fourier transforming the self-energies, we can rewrite the Dyson's equation as a function of energy

$$\mathcal{G}^{\pm}(E) = \mathcal{G}_0^{\pm}(E) + \mathcal{G}_0^{\pm}(E)\Sigma^{\pm}(E)\mathcal{G}^{\pm}(E), \tag{3.2.30}$$

which can be presented also as

$$\mathcal{G}^{\pm}(E) = \frac{\mathbb{1}}{E \pm i\delta - \hat{H}_0 - \Sigma^{\pm}(E)}. \tag{3.2.31}$$

3.2.2 Spectral representation of the Green's function

Let us assume the single-particle Hamiltonian of Eq. (3.2.1) and rewrite the Schrödinger equation as

$$H\,|\psi_n\rangle = E_n S\,|\psi_n\rangle\,, \tag{3.2.32}$$

where the N_u-dimensional vectors $|\psi_n\rangle$ are the single-particle wave functions with eigenvalues E_n, and S is the overlap matrix that accounts for the non-orthogonal basis set. One can always normalize the state vectors so that the orthogonality relation becomes $\langle\psi_n|\,S\,|\psi_m\rangle = \delta_{mn}$. The corresponding completeness relation for the set of eigenvectors is $\sum_n |\psi_n\rangle\,\langle\psi_n|\,S = \mathbb{1}_{N_u}$, where $\mathbb{1}_{N_u}$ is the $N_u \times N_u$ identity matrix. The Hamiltonian in its spectral representation is given by

$$\hat{H} = \sum_{n=1}^{N_u} E_n S\,|\psi_n\rangle\,\langle\psi_n|\,, \tag{3.2.33}$$

so that the retarded Green's function of Eq. (3.2.25) can be written as

$$\mathcal{G}^{+}(E) = \sum_{n=1}^{N_u} \frac{\mathbb{1}}{E + i\delta - E_n}\,|\psi_n\rangle\,\langle\psi_n|\,. \tag{3.2.34}$$

The spectral function is defined as

$$A(E) = i\left[\mathcal{G}^{+}(E) - \mathcal{G}^{-}(E)\right], \tag{3.2.35}$$

and it can be seen as a *generalized density of states*. From the spectral representation of $\mathcal{G}^{+}$ we can write

$$\begin{aligned} A(E) &= i\sum_{n=1}^{N_u} \frac{\mathbb{1}}{E + i\delta - E_n}\,|\psi_n\rangle\,\langle\psi_n| - \frac{\mathbb{1}}{E - i\delta - E_n}\,|\psi_n\rangle\,\langle\psi_n| \\ &= 2\sum_{n=1}^{N_u} \frac{\delta}{(E - E_n)^2 + \delta^2}\,|\psi_n\rangle\,\langle\psi_n|\,, \end{aligned} \tag{3.2.36}$$

and if we take the limit $\delta \to 0^{+}$ we have

$$A(E) = 2\pi\sum_{n=1}^{N_u} \delta(E - E_n)\,|\psi_n\rangle\,\langle\psi_n|\,. \tag{3.2.37}$$

Therefore, the density of states (DOS) is written as

$$\nu(E) = \frac{1}{2\pi}\mathrm{Tr}\left[A(E)S\right]. \tag{3.2.38}$$

In many situations, it is useful to count the contributions due to a single orbital, so that one defines the projected density of states (PDOS) as

$$\nu(E) = \frac{1}{2\pi}\sum_{l}^{N_u} A_{lp}(E)S_{lp}, \tag{3.2.39}$$

where the indeces l and p are single-particle basis set orbitals. Eq. (3.2.37) and Eq. (3.2.38) show that the spectral function, and therefore the Green's function, contains all the information about the states of the system. Moreover, the density matrix

$$\rho = \sum_{n=1}^{N_u} p_n \left|\psi_n\right\rangle \left\langle\psi_n\right|, \tag{3.2.40}$$

can be equally expressed as a function of the spectral function. If it is assumed that the system is in thermal equilibrium with the environment, for a system of Fermions the weight function, p_n, becomes the Fermi-Dirac distribution function, $f(E)$, as given by Eq. (3.1.3). From Eq. (3.2.37), the density matrix can be written as

$$\rho = \frac{1}{2\pi}\int dE f(E)A(E), \tag{3.2.41}$$

where the energy integral is over the entire real energy axis (from $-\infty$ to ∞). At equilibrium the knowledge of the spectral function therefore uniquely determines the density matrix and consequently all the ground state properties of the system. We note that due to the assumption of thermal equilibrium with a reference system, ρ is implicitly a time averaged quantity. For a system out of equilibrium the same argument can be applied, the only difference being that the state vectors, $|\psi_n\rangle$, are split up into separate sets, in local equilibrium with only one of the reservoirs, with different local chemical potential.

3.3 Non-equilibrium Green's function formalism

3.3.1 Green's function for the scattering region

In this Chapter we present the so-called *non-equilibrium Green's function formalism* (NEGF) also known as the *Keldysh formalism* [63]. This is done by solving the equations of motion for specific time-dependent single-particle Green's functions, from which we can compute physical properties, such as charge density and electrical currents. This formalism is exact only when dealing with a closed quantum system, but not necessarily

isolated. External perturbations may drive the system away from its thermodynamic equilibrium. The NEGF formalism allows us to describe the out of equilibrium state of a quantum system, which consists of a scattering region (SR) attached to semi-infinite electron reservoirs or electrodes.

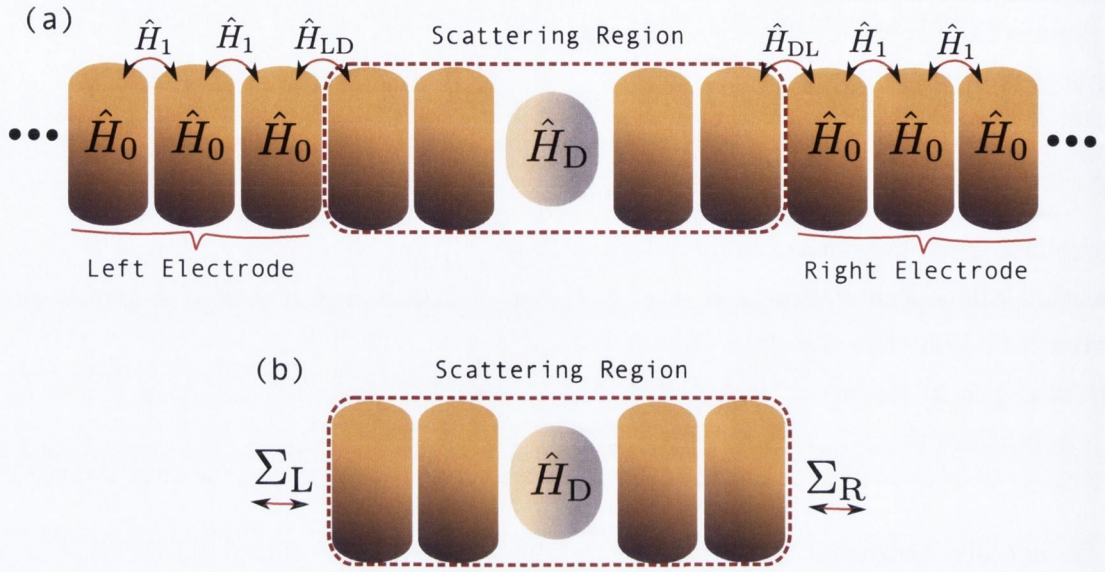

Figure 3.1: Schematic representation of the general transport setup using NEGF. (a) The different parts of the system are identified by their Hamiltonian. The scattering region or the device is highlighted in the dashed square. (b) the electrodes are replaced by their self-energies.

In the present work we are interested in studying the electronic transport properties of nanoscale devices, which consist of a nanoscale object connected to two electrodes, as schematically shown in Fig. 1.1. In such systems, the SR is a nanoscale structure and the full system is a quantum system with open boundary conditions, *i.e.* it is an infinite non-periodic system, as schematically shown in Fig. 3.1(a).

The quantum transport problem can be discussed from three distinct view points, namely, thermodynamics, electrostatic and quantum mechanics. From the thermodynamic point of view, as discussed in Sec. 3.1.1, the electrodes are considered as electrons reservoirs in their thermodynamic equilibrium and therefore characterized by their chemical potentials. When the system is in equilibrium, *i.e.* no external bias is applied, electrons will flow between the parts of the system until a common chemical potential is reached. However, if a bias is applied to the system, *e.g.* a battery keep a chemical difference between electrodes, according to Eq. (3.1.10) and Eq. (3.1.11), an electrical current can be established. The current is the result of the attempt to restore the equilibrium condition. Thus, by keeping the external bias, the system can reach a stationary state current.

When the system is under an external bias, a redistribution of charge will occur. Since the electrodes are assumed to be good conductors, they screen any perturbation caused by the presence of the SR. Then, from a electrostatic point of view, the potential drop

due to the applied bias is assumed to occur only in the SR.

From the quantum mechanics point of view, the system can be divided into three regions: the left and right electrodes and the SR, as shown in Fig. 3.1(a). We define the SR as a quantum structure that breaks the translation symmetry of the electrodes, *e.g.* a molecule, a defect and so on. The electrodes are semi-infinite in size and they hold periodicity along the transport direction. Each electrode unit cell can be described by a Hamiltonian $\hat{H}_{0(\mathrm{L,R})}$. This operator can be represented by a matrix with dimensions depending on the basis set used to describe the atoms of each unit cell. In terms of localized basis set, one can define the size of the unit cell to assure that each unit cell interacts only with its first-nearest-neighbor cells. Then, the dimensions of the matrix that represents the operator $\hat{H}_{0(\mathrm{L,R})}$ will be $N \times N$, where $N = \sum_i^{N_{species}} N_{atoms} \times N_{orbitals}$ is the total number of degrees of freedom in each electrode unit cell. Moreover, the operator $\hat{H}_1$ describes the coupling between each unit cell and its neighbors and $\hat{H}_{\mathrm{D}}$ is the Hamiltonian of the SR where "D" stands for "device". Finally, the coupling between the device region and the left (right) electrode is given by $\hat{H}_{\mathrm{LD}}$ ($\hat{H}_{\mathrm{DR}}$).

The Hamiltonian of the entire system can be written in matrix form as

$$\mathcal{H} = \begin{pmatrix} . & . & . & . & . & . & . & . & . & . \\ . & 0 & H_{-1} & H_0 & H_1 & 0 & . & . & . & . \\ . & . & 0 & H_{-1} & H_0 & H_{\mathrm{LD}} & 0 & . & . & . \\ . & . & . & 0 & H_{\mathrm{LD}} & H_{\mathrm{D}} & H_{\mathrm{DR}} & 0 & . & . \\ . & . & . & . & 0 & H_{\mathrm{DR}} & H_0 & H_1 & . & . \\ . & . & . & . & . & 0 & H_{-1} & H_0 & H_1 & . \\ . & . & . & . & . & . & . & . & . & . \end{pmatrix} \tag{3.3.1}$$

where $H_{-1} = H_1^{\dagger}$, $H_{\mathrm{DL}} = H_{\mathrm{LD}}^{\dagger}$ and $H_{\mathrm{DR}} = H_{\mathrm{RD}}^{\dagger}$. In principle, one solve the problem by diagonalizing this matrix, however, it is infinite.

The NEGF offers another way to treat the problem. In this framework, we start by rewriting the Schrödinger equation in terms of Green's functions as:

$$[\epsilon^{\pm} S - \mathcal{H}]\mathcal{G}(E) = \mathcal{I} \tag{3.3.2}$$

where $\epsilon^{\pm} = \lim_{\delta \to 0^{\pm}} (E \pm i\delta)$ is the energy and S is the overlap matrix that appears when one is dealing with non-orthogonal basis set. In terms of matrices, Eq. (3.3.2) is given by

$$\begin{pmatrix} \epsilon^{\pm} S_{\mathrm{L}} - \mathcal{H}_{\mathrm{L}} & \epsilon^{\pm} S_{\mathrm{LD}} - \mathcal{H}_{\mathrm{LD}} & 0 \\ \epsilon^{\pm} S_{\mathrm{DL}} - \mathcal{H}_{\mathrm{DL}} & \epsilon^{\pm} S_{\mathrm{D}} - H_{\mathrm{D}} & \epsilon^{\pm} S_{\mathrm{RD}} - \mathcal{H}_{\mathrm{RD}} \\ 0 & \epsilon^{\pm} S_{\mathrm{RD}} - \mathcal{H}_{\mathrm{RD}} & \epsilon^{\pm} S_{\mathrm{R}} - \mathcal{H}_{\mathrm{R}} \end{pmatrix} \begin{pmatrix} \mathcal{G}_{\mathrm{L}} & \mathcal{G}_{\mathrm{LD}} & \mathcal{G}_{\mathrm{LR}} \\ \mathcal{G}_{\mathrm{DL}} & \mathcal{G}_{\mathrm{D}} & \mathcal{G}_{\mathrm{DR}} \\ \mathcal{G}_{\mathrm{RL}} & \mathcal{G}_{\mathrm{RD}} & \mathcal{G}_{\mathrm{R}} \end{pmatrix} = \begin{pmatrix} \mathcal{I} & 0 & 0 \\ 0 & \mathcal{I} & 0 \\ 0 & 0 & \mathcal{I} \end{pmatrix} \tag{3.3.3}$$

where all the elements of the Green's function matrix are energy dependent (we omit the explicit energy dependence to simplify the notation). Moreover, the matrices $\mathcal{H}_{\mathrm{L}}$, $\mathcal{H}_{\mathrm{R}}$,

$\mathcal{H}_{\mathrm{LD}}$ and $\mathcal{H}_{\mathrm{DR}}$ are semi-infinite and are written as

$$\mathcal{H}_{\mathrm{L}} = \begin{pmatrix} \ddots & \ddots & \ddots & \ddots & \vdots \\ 0 & H_{-1} & H_0 & H_1 & 0 \\ \cdots & 0 & H_{-1} & H_0 & H_1 \\ \cdots & \cdots & 0 & H_{-1} & H_0 \end{pmatrix}, \tag{3.3.4}$$

$$\mathcal{H}_{\mathrm{R}} = \begin{pmatrix} H_0 & H_1 & 0 & \cdots & \cdots \\ H_{-1} & H_0 & H_1 & 0 & \cdots \\ 0 & H_{-1} & H_0 & H_1 & 0 \\ \vdots & \ddots & \ddots & \ddots & \ddots \end{pmatrix}, \tag{3.3.5}$$

$$\mathcal{H}_{\mathrm{LD}} = \begin{pmatrix} \vdots \\ 0 \\ H_{\mathrm{LD}} \end{pmatrix} \tag{3.3.6}$$

and

$$\mathcal{H}_{\mathrm{DR}} = \begin{pmatrix} H_{\mathrm{RD}} & 0 & \cdots \end{pmatrix}. \tag{3.3.7}$$

Eq. 3.3.3 can be solved by conventional matrices multiplication, which leads to nine equations. However, by considering metallic electrodes, the coupling between the device and the electrodes will not affect their electronic structure. This allows us to focus on the device region and solve explicitly only three equations. Therefore, from Eq. 3.3.2, the Green's function of the device region is given by solving the following equations

$$(\epsilon^{\pm} S_{\mathrm{L}} - \mathcal{H}_{\mathrm{L}})\mathcal{G}_{\mathrm{LD}}(E) + (\epsilon^{\pm} S_{\mathrm{LD}} - \mathcal{H}_{\mathrm{LD}})\mathcal{G}_{\mathrm{D}}(E) = 0, \tag{3.3.8}$$

$$(\epsilon^{\pm} S_{\mathrm{DL}} - \mathcal{H}_{\mathrm{DL}})\mathcal{G}_{\mathrm{LD}}(E) + (\epsilon^{\pm} S_{\mathrm{D}} - H_{\mathrm{D}})\mathcal{G}_{\mathrm{D}}(E) + (\epsilon^{\pm} S_{\mathrm{DR}} - \mathcal{H}_{\mathrm{DR}})\mathcal{G}_{\mathrm{RD}}(E) = \mathcal{I}, \tag{3.3.9}$$

and

$$(\epsilon^{\pm} S_{\mathrm{RD}} - \mathcal{H}_{\mathrm{RD}})\mathcal{G}_{\mathrm{LD}}(E) + (\epsilon^{\pm} S_{\mathrm{R}} - \mathcal{H}_{\mathrm{R}})\mathcal{G}_{\mathrm{RD}}(E) = 0. \tag{3.3.10}$$

The third line of the first matrix was multiplied by the second column of the second matrix. Solving Eq. (3.3.8) and Eq. (3.3.10) for $\mathcal{G}_{\mathrm{LD}}(E)$ and $\mathcal{G}_{\mathrm{RD}}(E)$, respectively, we obtain

$$\mathcal{G}_{\mathrm{LD}}(E) = (\epsilon^{\pm} S_{\mathrm{L}} - \mathcal{H}_{\mathrm{L}})^{-1}(\mathcal{H}_{\mathrm{LD}} - \epsilon^{\pm} S_{\mathrm{LD}})\mathcal{G}_{\mathrm{D}}(E), \tag{3.3.11}$$

$$\mathcal{G}_{\mathrm{RD}}(E) = (\epsilon^{\pm} S_{\mathrm{R}} - \mathcal{H}_{\mathrm{R}})^{-1}(\mathcal{H}_{\mathrm{RD}} - \epsilon^{\pm} S_{\mathrm{RD}})\mathcal{G}_{\mathrm{D}}(E). \tag{3.3.12}$$

By defining the Green's functions for the isolated electrodes as

$$g_{\mathrm{L}}(E) = (\epsilon^{\pm} S_{\mathrm{L}} - \mathcal{H}_{\mathrm{L}})^{-1}, \tag{3.3.13}$$

$$g_{\mathrm{R}}(E) = (\epsilon^{\pm} S_{\mathrm{R}} - \mathcal{H}_{\mathrm{R}})^{-1}, \tag{3.3.14}$$

we can write Eq. (3.3.11) and Eq. (3.3.12) as

$$\mathcal{G}_{\mathrm{LD}}(E) = g_{\mathrm{L}}(E)\left[\mathcal{H}_{\mathrm{LD}} - \epsilon^{\pm} S_{\mathrm{LD}}\right]\mathcal{G}_{\mathrm{D}}(E), \tag{3.3.15}$$

$$\mathcal{G}_{\mathrm{RD}}(E) = g_{\mathrm{R}}(E)\left[\mathcal{H}_{\mathrm{RD}} - \epsilon^{\pm} S_{\mathrm{RD}}\right]\mathcal{G}_{\mathrm{D}}(E). \tag{3.3.16}$$

By inserting Eq. (3.3.15) and Eq. (3.3.16) into Eq. (3.3.9) and solving it for $\mathcal{G}_{\mathrm{D}}(E)$, we have:

$$\mathcal{G}_{\mathrm{D}}(E) = \left[(\epsilon^{\pm} S_{\mathrm{D}} - H_{\mathrm{D}}) - \Sigma_{\mathrm{L}}(E) - \Sigma_{\mathrm{R}}(E)\right]^{-1}, \tag{3.3.17}$$

which corresponds to the retarded and advanced Green's functions for the SR in the presence of the electrodes. Moreover, $\Sigma_{\mathrm{L}}(E)$ and $\Sigma_{\mathrm{R}}(E)$ are given by,

$$\Sigma_{\mathrm{L}}(E) = (\mathcal{H}_{\mathrm{LD}} - \epsilon^{\pm} S_{\mathrm{LD}}) g_{\mathrm{L}}(E) (\mathcal{H}_{\mathrm{DL}} - \epsilon^{\pm} S_{\mathrm{DL}}), \tag{3.3.18}$$

$$\Sigma_{\mathrm{R}}(E) = (\mathcal{H}_{\mathrm{RD}} - \epsilon^{\pm} S_{\mathrm{RD}}) g_{\mathrm{R}}(E) (\mathcal{H}_{\mathrm{DR}} - \epsilon^{\pm} S_{\mathrm{DR}}). \tag{3.3.19}$$

These are the electrodes self-energies. Unlike the self-energy shown in Eq. (3.2.20), the self-energies $\Sigma_{\mathrm{L}}(E)$ and $\Sigma_{\mathrm{R}}(E)$ are non-Hermitian, *i.e.* $\Sigma^{\dagger}_{\mathrm{L,R}}(E) \neq \Sigma_{\mathrm{L,R}}(E)$. In fact, from the general property of the Green's functions presented in Eq. (3.2.29) we obtain from Eq. (3.3.18) and Eq. (3.3.19) that

$$\left[\Sigma^{+}_{\mathrm{L,R}}(E)\right]^{\dagger} = \Sigma^{-}_{\mathrm{L,R}}(E), \tag{3.3.20}$$

i.e. the advanced self-energy is the Hermitian conjugate of the retarded self-energy and vice-versa. This is a consequence of partitioning the system into electrodes and SR so that the interface potentials act on the states of the central region, as if the central region Hamiltonian is perturbed by the presence of the electrodes through their self-energies, as schematically shown in Fig. 3.1(b).

3.3.2 Energy renormalization and lifetime

From Eq. (3.3.17), one can see that in absence of the self-energies ($\Sigma = 0$), the Green's functions have poles in correspondence to the eigenvalues of $\mathcal{H}_{\mathrm{D}}$. Therefore, the self-energies make the Green's functions analytic by renormalizing the eigenenergies of the device Hamiltonian. If we write the self-energies as

$$\Sigma_{\mathrm{LR}}(E) = \mathrm{Re}\{\Sigma_{\mathrm{LR}}(E)\} + \mathrm{Im}\{\Sigma_{\mathrm{LR}}(E)\}, \tag{3.3.21}$$

i.e. in terms of their real and imaginary parts, we can rewrite Eq. (3.3.17) as

$$\mathcal{G}_{\mathrm{D}}(E) = \frac{\mathbb{1}}{(\epsilon^{\pm} S_{\mathrm{D}} - H_{\mathrm{D}}) - \mathrm{Re}\{\Sigma_{\mathrm{L}}(E) + \Sigma_{\mathrm{R}}(E)\} - \mathrm{Im}\{\Sigma_{\mathrm{L}}(E) + \Sigma_{\mathrm{R}}(E)\}}. \tag{3.3.22}$$

Thus the real part of the self-energies shift the energies of the Hamiltonian of the device. By using explicitly the retarded and advanced Green's functions of Eq. (3.3.22), we define

$$\begin{aligned}\left[\mathcal{G}^{+}(E)\right]^{-1} - \left[\mathcal{G}^{-}(E)\right]^{-1} &= \left(\Sigma_{\mathrm{L}}^{+}(E) - \Sigma_{\mathrm{L}}^{-}(E)\right) + \left(\Sigma_{\mathrm{R}}^{+}(E) - \Sigma_{\mathrm{R}}^{-}(E)\right) \\ &\equiv i\Big[\Gamma_{\mathrm{L}}(E) + \Gamma_{\mathrm{R}}(E)\Big] \equiv i\Gamma(E) \end{aligned} \tag{3.3.23}$$

where one can define the electronic coupling between the scattering region and the electrodes by

$$\Gamma_{\mathrm{L,R}}(E) = i\Big[\Sigma_{\mathrm{L,R}}^{+}(E) - \Sigma_{\mathrm{L,R}}^{-}(E)\Big] = -2\mathrm{Im}\{\Sigma_{\mathrm{L,R}}^{+}(E)\}. \tag{3.3.24}$$

Without the imaginary part of the self-energies, the eigenenergies associated with the solution of the Green's function would be shifted with respect to the eigenenergies of the free device Hamiltonian. The imaginary parts, however, move these solutions away from the real energy axis, inside the complex plane. This imaginary part is associated with the decay of the solutions, therefore, they can be interpreted as the rate at which the electrons are scattered out from the states of the isolated device Hamiltonian. Thus the states of the device region acquire a *broadening* due to the interaction with the electrodes.

3.3.3 Density matrix

As discussed at the end of Sec. 3.2.2, for a system out of equilibrium, we can split up the contributions to the density matrix attributed to states in local equilibrium with only one of the reservoirs, namely

$$\rho_{\mathrm{D}} = \rho_{\mathrm{DL}} + \rho_{\mathrm{DR}}. \tag{3.3.25}$$

The individual parts are

$$\rho_{\mathrm{DL}} = \int dE \sum_{n=1}^{N_{\mathrm{L}}} p_{\mathrm{L},n}(E)\ \nu_{\mathrm{L},n}(E)\ \left|\psi_{\mathrm{L,n}}^{\mathrm{D}}\right\rangle \left\langle\psi_{\mathrm{L,n}}^{\mathrm{D}}\right|, \tag{3.3.26}$$

$$\rho_{\mathrm{DR}} = \int dE \sum_{n=1}^{N_{\mathrm{R}}} p_{\mathrm{R},n}(E)\ \nu_{\mathrm{R},n}(E)\ \left|\psi_{\mathrm{R,n}}^{\mathrm{D}}\right\rangle \left\langle\psi_{\mathrm{R,n}}^{\mathrm{D}}\right|, \tag{3.3.27}$$

where $|\psi_{\{\mathrm{L/R}\},n}^{\mathrm{D}}\rangle$ is part of the state vector extending over the SR. The occupation number $p_{\{\mathrm{L/R}\},n}(E)$ lies between 0 and 1 and determines the occupation of each state. We now assume that the left and the right leads are in local thermal equilibrium, and therefore have a local Fermi energy, $E_{\mathrm{F},\{\mathrm{L/R}\}}$. Thus each of the states $|\psi_{\{\mathrm{L/R}\}}\rangle\,(E)$ has a probability of being occupied given by the Fermi distribution $f_{\{\mathrm{L/R}\}}(E)$ of the lead it originates from. The $\{|\psi_{\mathrm{L},n}\rangle\}$ describe states originating from the left lead, we have $p_{\mathrm{L},n}(E) = f_{\mathrm{L}}(E)$, and analogously we have $p_{\mathrm{R},n}(E) = f_{\mathrm{R}}(E)$. This is one of the central approximations in the

NEGF formalism. A bias voltage $V_{\rm sd}$, which is defined as the difference between the Fermi energies of the two leads divided by the electron charge, e, so that $eV_{\rm sd} = E_{\rm F,L} - E_{\rm F,R}$, can now be specified. Note that the energy eigenvalue spectrum of the entire system is only defined up to a constant, so that one can choose the reference of energy. A convenient way is to consider the Fermi level of the system at equilibrium, $E_{\rm F}$, as reference and setting $E_{\rm F,L} = E_{\rm F} + eV_{\rm sd}/2$ and $E_{\rm F,R} = E_{\rm F} - eV_{\rm sd}/2$. This is the convention used throughout this work. We can therefore write

$$\begin{aligned} \rho_{\rm DL} &= \int dE\ f_{\rm L}(E) \left(\sum_{n=1}^{N_{\rm L}} \nu_{{\rm L},n}(E)\ |\psi^{\rm D}_{{\rm L},n}\rangle \langle \psi^{\rm D}_{{\rm L},n}| \right) \\ &= \frac{1}{2\pi} \int dE\ f_{\rm L}(E)\ A_{\rm DL}, \end{aligned} \tag{3.3.28}$$

and in the same way

$$\rho_{\rm DR} = \frac{1}{2\pi} \int dE\ f_{\rm R}(E)\ A_{\rm DR}. \tag{3.3.29}$$

Note that we have introduced the spectral functions for the parts of the system, $A_{\rm DL}$ and $A_{\rm DR}$. We now define the lesser Green's function for the SR, $\mathcal{G}^<_{\rm D}$, as [105]

$$\mathcal{G}^<_{\rm D} = i\ \mathcal{G}_{\rm D} \left[f_{\rm L}(E)\Gamma_{\rm L} + f_{\rm R}(E)\Gamma_{\rm R} \right] \mathcal{G}^\dagger_{\rm D}, \tag{3.3.30}$$

where the couplings, $\Gamma_{\rm L,R}$, are given by Eq. (3.3.24). By using this definition, and Eq. (3.3.25), Eq. (3.3.28) and Eq. (3.3.29), the density matrix of the SR becomes

$$\rho_{\rm D} = \frac{1}{2\pi i} \int dE\ \mathcal{G}^<_{\rm D}(E). \tag{3.3.31}$$

This is the central equation of the NEGF formalism [63], and allows one to obtain the charge density of the SR attached to leads also out of equilibrium. If all the leads have the same Fermi energy, then we recover the equilibrium result of Eq. (3.2.41).

The same procedure can be repeated for an arbitrary number of electrodes, $N_{electrodes}$. In that case the total lesser Green's function becomes

$$\mathcal{G}^<_{\rm D} = i\ \mathcal{G}_{\rm D} \left(\sum_n^{N_{\rm electrodes}} f_n(E)\Gamma_n \right) \mathcal{G}^\dagger_{\rm D}. \tag{3.3.32}$$

3.4 Transmission and current

3.4.1 Wave function

The Schrödinger equation for the partitioned system can be written in a matrix form as

$$\begin{pmatrix} \mathcal{H}_{\mathrm{L}} & \mathcal{H}_{\mathrm{LD}} & 0 \\ \mathcal{H}_{\mathrm{DL}} & H_{\mathrm{D}} & \mathcal{H}_{\mathrm{DR}} \\ 0 & \mathcal{H}_{\mathrm{RD}} & \mathcal{H}_{\mathrm{R}} \end{pmatrix} \begin{pmatrix} |\psi^{\mathrm{L}}\rangle \\ |\psi^{\mathrm{D}}\rangle \\ |\psi^{\mathrm{R}}\rangle \end{pmatrix} = E \begin{pmatrix} S_{\mathrm{L}} & S_{\mathrm{LD}} & 0 \\ S_{\mathrm{DL}} & S_{\mathrm{D}} & S_{\mathrm{DR}} \\ 0 & S_{\mathrm{RD}} & S_{\mathrm{R}} \end{pmatrix} \begin{pmatrix} |\psi^{\mathrm{L}}\rangle \\ |\psi^{\mathrm{D}}\rangle \\ |\psi^{\mathrm{R}}\rangle \end{pmatrix}. \tag{3.4.1}$$

We have divided the state vector into its parts corresponding to the individual parts of the system as

$$|\psi\rangle = \begin{pmatrix} |\psi^{\mathrm{L}}\rangle \\ |\psi^{\mathrm{D}}\rangle \\ |\psi^{\mathrm{R}}\rangle \end{pmatrix}, \tag{3.4.2}$$

where $|\psi^{\mathrm{L}}\rangle$ ($|\psi^{\mathrm{R}}\rangle$) is the part of the wave function (WF) extending over the left (right) lead, and $|\psi^{\mathrm{D}}\rangle$ is the part extending over the SR. Moreover,

$$|\psi_{\mathrm{L}}\rangle = \begin{pmatrix} |\varphi_{\mathrm{L}}\rangle \\ 0 \\ 0 \end{pmatrix} + |\psi_{\mathrm{L}}^{\Delta}\rangle\,, \tag{3.4.3}$$

where $|\varphi_{\mathrm{L}}\rangle$ is the state vector for the isolated left electrode so that

$$H_{\mathrm{L}}\,|\varphi_{\mathrm{L}}\rangle = ES\,|\varphi_{\mathrm{L}}\rangle\,. \tag{3.4.4}$$

When the isolated electrodes join the SR, the state vectors will be different due to their interaction with the SR and indirectly with the other electrodes. Therefore, $|\psi_{\mathrm{L}}^{\Delta}\rangle$ has the dimension of the entire system, *i.e.* the SR plus the electrodes, and it corresponds to the change in WF due to the presence of the SR. In an analogous way $|\psi_{\mathrm{R}}\rangle$ is given by

$$|\psi_{\mathrm{R}}\rangle = \begin{pmatrix} 0 \\ 0 \\ |\varphi_{\mathrm{R}}\rangle \end{pmatrix} + |\psi_{\mathrm{R}}^{\Delta}\rangle\,. \tag{3.4.5}$$

The $|\psi_{\mathrm{L},n}^{\Delta}\rangle$ then satisfy the equation

$$(\mathcal{H} - ES)\,|\psi_{\mathrm{L},n}^{\Delta}\rangle = \begin{pmatrix} 0 \\ -K_{\mathrm{DL}}\,|\varphi_{\mathrm{L},n}\rangle \\ 0 \end{pmatrix}, \tag{3.4.6}$$

where we have defined

$$K = \mathcal{H} - (E \pm i\delta)S. \tag{3.4.7}$$

From this definition it follows that $K_{\mathrm{D}} = K_{\mathrm{D}}^{\dagger}$ and $K_{\mathrm{D\{L/R\}}} = K_{\mathrm{\{L/R\}D}}^{\dagger}$. Eq. (3.4.6) has two sets of solutions [105]. One is obtained by multiplying Eq. (3.4.6) with the retarded

Green's function from the left

$$|\psi^{\Delta+}_{\mathrm{L},n}\rangle = \mathcal{G}^{+}\begin{pmatrix} 0 \\ K_{\mathrm{DL}}\,|\varphi_{\mathrm{L},n}\rangle \\ 0 \end{pmatrix}, \tag{3.4.8}$$

and the other is obtained by multiplying it with the advanced Green's function

$$|\psi^{\Delta-}_{\mathrm{L},n}\rangle = \mathcal{G}^{-}\begin{pmatrix} 0 \\ K_{\mathrm{DL}}\,|\varphi_{\mathrm{L},n}\rangle \\ 0 \end{pmatrix}. \tag{3.4.9}$$

The first describes electrons flowing from the left electrode into the SR and the second describes electrons propagating from the SR into the left lead [105]. If there is no right electrode attached to the SR these solutions are identical. Our aim is to distinguish the solutions arising from a given electrode. Therefore, we focus on the first set of solutions, *i.e.* those described by the retarded Green's function. If we use the matrix form of the Green's function given in Eq. (3.3.3), the total wave function originated in the left electrode can be written as

$$|\psi_{\mathrm{L},n}\rangle = \begin{pmatrix} \mathbb{1}_{\mathrm{L}} + g_{\mathrm{L}}K_{\mathrm{LD}}\mathcal{G}_{\mathrm{D}}K_{\mathrm{DL}} \\ \mathcal{G}_{\mathrm{D}}K_{\mathrm{DL}} \\ g_{\mathrm{R}}K_{\mathrm{RD}}\mathcal{G}_{\mathrm{D}}K_{\mathrm{DL}} \end{pmatrix}|\varphi_{\mathrm{L},n}\rangle\,, \tag{3.4.10}$$

where $\mathbb{1}_{\mathrm{L}}$ is a unity matrix with the dimensions of the left electrode. For the wave functions originated in the right electrode we obtain,

$$|\psi_{\mathrm{R},n}\rangle = \begin{pmatrix} g_{\mathrm{L}}K_{\mathrm{LD}}\mathcal{G}_{\mathrm{D}}K_{\mathrm{DR}} \\ \mathcal{G}_{\mathrm{D}}K_{\mathrm{DR}} \\ \mathbb{1}_{\mathrm{R}} + g_{\mathrm{R}}K_{\mathrm{RD}}\mathcal{G}_{\mathrm{D}}K_{\mathrm{DR}} \end{pmatrix}|\varphi_{\mathrm{R},n}\rangle\,. \tag{3.4.11}$$

3.4.2 Current per channel

In this section the current associated to a single state vector is calculated. Since the state vectors, $|\psi_n\rangle$, are normalized in such a way that $\langle\psi_n|\,S\,|\psi_n\rangle$, the electron charge in the SR, q_{D}, is

$$q_{\mathrm{D}} = \langle\psi^{\mathrm{L}}|S_{\mathrm{LD}}\,|\psi^{\mathrm{D}}\rangle + \langle\psi^{\mathrm{D}}|S_{\mathrm{D}}\,|\psi^{\mathrm{D}}\rangle + \langle\psi^{\mathrm{R}}|S_{\mathrm{RD}}\,|\psi^{\mathrm{D}}\rangle\,. \tag{3.4.12}$$

If the overlap terms proportional to S_{LD} and S_{RD} are neglected this becomes

$$q_{\mathrm{D}} = \langle\psi^{\mathrm{D}}|S_{\mathrm{D}}\,|\psi^{\mathrm{D}}\rangle\,. \tag{3.4.13}$$

In order to obtain the current we need to define the time-dependent state vector given by the time-dependent Schrödinger-like equation

$$H\left|\psi\right\rangle_t = i\hbar S\frac{\partial\left|\psi\right\rangle_t}{\partial t}, \tag{3.4.14}$$

where the index t in $\left|\psi\right\rangle_t$ indicates that this is the explicit time-dependent state vector. The solution for the time-dependent state vector is $\left|\psi\right\rangle_t = e^{-iEt/\hbar}\left|\psi\right\rangle$. The time derivative of the occupation of the SR for such an eigenstate is given by

$$\frac{\partial q_{\mathrm{D}}}{\partial t} = \frac{\partial\langle\psi^{\mathrm{D}}|_t S_{\mathrm{D}}\left|\psi^{\mathrm{D}}\right\rangle_t}{\partial t} = 0. \tag{3.4.15}$$

This means that the change in charge is zero, because the inflowing current from one lead is equal to the outflowing current through the other lead. These two currents can be obtained by explicitly taking the time-derivative of q_{D}. The time derivative of $\left|\psi^{\mathrm{D}}\right\rangle_t$ is

$$e^{iEt/\hbar}\, S_{\mathrm{D}}\frac{\partial\left|\psi^{\mathrm{D}}\right\rangle_t}{\partial t} = -\frac{i}{\hbar}ES_{\mathrm{D}}\left|\psi^{\mathrm{D}}\right\rangle \tag{3.4.16}$$

$$= -\frac{i}{\hbar}\left(K_{\mathrm{DL}}\left|\psi^{\mathrm{L}}\right\rangle + H_{\mathrm{D}}\left|\psi^{\mathrm{D}}\right\rangle + K_{\mathrm{DR}}\left|\psi^{\mathrm{R}}\right\rangle\right). \tag{3.4.17}$$

The time derivative of the occupation of the SR then is

$$\begin{aligned}\frac{\partial q_{\mathrm{D}}}{\partial t} &= \frac{\partial\langle\psi^{\mathrm{D}}|_t}{\partial t}S_{\mathrm{D}}\left|\psi^{\mathrm{D}}\right\rangle_t + \langle\psi^{\mathrm{D}}|_t S_{\mathrm{D}}\frac{\partial\left|\psi^{\mathrm{D}}\right\rangle_t}{\partial t}\\ &= \frac{i}{\hbar}\left(\langle\psi^{\mathrm{L}}|K_{\mathrm{LD}}\left|\psi^{\mathrm{D}}\right\rangle - \langle\psi^{\mathrm{D}}|K_{\mathrm{DL}}\left|\psi^{\mathrm{L}}\right\rangle\right)\\ &\quad + \frac{i}{\hbar}\left(\langle\psi^{\mathrm{R}}|K_{\mathrm{RD}}\left|\psi^{\mathrm{D}}\right\rangle - \langle\psi^{\mathrm{D}}|K_{\mathrm{DR}}\left|\psi^{\mathrm{R}}\right\rangle\right).\end{aligned} \tag{3.4.18}$$

This shows that the change in charge is equal to the sum of the total current flowing in from the left lead, I^{L}, and the total current flowing in from the right lead, I^{R}, so that

$$\frac{\partial q_{\mathrm{D}}}{\partial t} = I^{\mathrm{L}} + I^{\mathrm{R}} = 0, \tag{3.4.19}$$

and $I^{\mathrm{L}} = -I^{\mathrm{R}}$. The two currents of the single state vectors are

$$I^{\mathrm{L}} = \frac{i}{\hbar}\left(\langle\psi^{\mathrm{L}}|K_{\mathrm{LD}}\left|\psi^{\mathrm{D}}\right\rangle - \langle\psi^{\mathrm{D}}|K_{\mathrm{DL}}\left|\psi^{\mathrm{L}}\right\rangle\right), \tag{3.4.20}$$

$$I^{\mathrm{R}} = \frac{i}{\hbar}\left(\langle\psi^{\mathrm{R}}|K_{\mathrm{RD}}\left|\psi^{\mathrm{D}}\right\rangle - \langle\psi^{\mathrm{D}}|K_{\mathrm{DR}}\left|\psi^{\mathrm{R}}\right\rangle\right). \tag{3.4.21}$$

3.4.3 Transmission coefficients and total current

The total current from the left lead into the SR, I^{L}, is equal to the sum of all the

contributions from the single state vectors

$$I^{\mathrm{L}} = \int dE \sum_{n=1}^{N_{\mathrm{L}}} f_{\mathrm{L}}(E)\, \nu_{\mathrm{L},n}(E)\, I^{\mathrm{L}}_{\mathrm{L},n} + \int dE \sum_{n=1}^{N_{\mathrm{R}}} f_{\mathrm{R}}(E)\, \nu_{\mathrm{R},n}(E)\, I^{\mathrm{L}}_{\mathrm{R},n}, \tag{3.4.22}$$

where, by using Eq. (3.4.20) the current $I^{\mathrm{L}}_{\mathrm{L},n}$ due to a single state vector coming from the left lead $|\psi_{\mathrm{L},n}\rangle$ is

$$I^{\mathrm{L}}_{\mathrm{L},n} = \frac{i}{\hbar}\left(\langle\psi^{\mathrm{L}}_{\mathrm{L},n}|\, K_{\mathrm{LD}}\, |\psi^{\mathrm{D}}_{\mathrm{L},n}\rangle - \langle\psi^{\mathrm{D}}_{\mathrm{L},n}|K_{\mathrm{DL}}\, |\psi^{\mathrm{L}}_{\mathrm{L},n}\rangle\right), \tag{3.4.23}$$

and the current $I^{\mathrm{L}}_{\mathrm{R},n}$ due to a wave function originating in the right lead $|\psi_{\mathrm{R},n}\rangle$ is

$$I^{\mathrm{L}}_{\mathrm{R},n} = \frac{i}{\hbar}\left(\langle\psi^{\mathrm{L}}_{\mathrm{R},n}|\, K_{\mathrm{LD}}\, |\psi^{\mathrm{D}}_{\mathrm{R},n}\rangle - \langle\psi^{\mathrm{D}}_{\mathrm{R},n}|K_{\mathrm{DL}}\, |\psi^{\mathrm{L}}_{\mathrm{R},n}\rangle\right). \tag{3.4.24}$$

By inserting the explicit expressions for $\psi_{\mathrm{L},n}$ and $\psi_{\mathrm{R},n}$ [see Eq. (3.4.10) and Eq. (3.4.11)], and after some algebraic manipulations, we obtain

$$I^{\mathrm{L}}_{\mathrm{L},n} = \frac{1}{\hbar}\langle\varphi_{\mathrm{L},n}|\, K_{\mathrm{LD}}\mathcal{G}^{-}_{\mathrm{D}}\Gamma_{\mathrm{R}}\mathcal{G}^{+}_{\mathrm{D}}K_{\mathrm{DL}}\, |\varphi_{\mathrm{L},n}\rangle, \tag{3.4.25}$$

$$I^{\mathrm{L}}_{\mathrm{R},n} = -\frac{1}{\hbar}\langle\varphi_{\mathrm{R},n}|\, K_{\mathrm{RD}}\mathcal{G}^{-}_{\mathrm{D}}\Gamma_{\mathrm{L}}\mathcal{G}^{+}_{\mathrm{D}}K_{\mathrm{DR}}\, |\varphi_{\mathrm{R},n}\rangle. \tag{3.4.26}$$

We have used the definitions of $\mathcal{G}^{+}_{\mathrm{D}}$ [Eq. (3.3.17)], $\Gamma_{\mathrm{L,R}}$ [Eq. (3.3.24)], and also the fact that $K_{\mathrm{M}} = K^{\dagger}_{\mathrm{M}}$ and $K_{\mathrm{M\{L/R\}}} = K^{\dagger}_{\mathrm{\{L/R\}M}}$. Since Γ_{R} is positive-semidefinite, and considering that for any semidefinite matrix M also the matrix $UMU^{\dagger}$ is semidefinite for an arbitrary matrix U, it can be seen that $I^{\mathrm{L}}_{\mathrm{L},n} \geq 0$. This is consistent with the fact that states $\{|\psi_{\mathrm{L},n}\rangle\}$ describe electrons flowing from the left electrode into the SR (and then into the right electrode). By choosing $\psi^{\Delta+}_{\mathrm{L},n}$ [Eq. (3.4.9)], obtained by using the advanced Green's function, then the electron flow would be from the SR into the left electrode, so that such states would not originate in the left electrode. Thus, $I^{\mathrm{L}}_{\mathrm{R},n} \leq 0$, so that the $\{|\psi_{\mathrm{R},n}\rangle\}$ describe electrons flowing from the SR into the left electrode.

The total currents due to the states originating in the left ($I^{\mathrm{L}}_{\mathrm{L}}$) and right ($I^{\mathrm{L}}_{\mathrm{R}}$) electrodes are

$$I^{\mathrm{L}}_{\mathrm{L}} = \int dE \sum_{n=1}^{N_{\mathrm{L}}} f_{\mathrm{L}}(E)\nu_{\mathrm{L},n}(E) I^{\mathrm{L}}_{\mathrm{L},n}, \tag{3.4.27}$$

$$I^{\mathrm{L}}_{\mathrm{R}} = \int dE \sum_{n=1}^{N_{\mathrm{R}}} f_{\mathrm{R}}(E)\nu_{\mathrm{R},n}(E) I^{\mathrm{L}}_{\mathrm{R},n}, \tag{3.4.28}$$

so that $I^{\mathrm{L}} = I^{\mathrm{L}}_{\mathrm{L}} + I^{\mathrm{L}}_{\mathrm{R}}$. By using the result of Eq. (3.4.25) we obtain for $I^{\mathrm{L}}_{\mathrm{L}}$

$$I^{\mathrm{L}}_{\mathrm{L}} = \frac{1}{\hbar}\int dE f_{\mathrm{L}}(E) \sum_{n=1}^{N_{\mathrm{L}}} \nu_{\mathrm{L},n}(E) \left(\langle \varphi_{\mathrm{L},n} | \, K_{\mathrm{LD}} \mathcal{G}^{-}_{\mathrm{D}} \Gamma_{\mathrm{R}} \mathcal{G}^{+}_{\mathrm{D}} K_{\mathrm{DL}} \, | \varphi_{\mathrm{L},n} \rangle \right).$$

The current for each wave function is larger than or at least equal to zero, therefore, $I^{\mathrm{L}}_{\mathrm{L}} \geq 0$. The quantity in brackets is a scalar, so that it can be rewritten as a trace. We then rearrange the matrices to

$$I^{\mathrm{L}}_{\mathrm{L}} = \frac{1}{\hbar}\int dE f_{\mathrm{L}}(E) \ \mathrm{Tr}\left[K_{\mathrm{DL}} \left(\sum_{n=1}^{N_{\mathrm{L}}} \nu_{\mathrm{L},n}(E) \, |\varphi_{\mathrm{L},n}\rangle \, \langle \varphi_{\mathrm{L},n}| \right) K_{\mathrm{LD}} \mathcal{G}^{-}_{\mathrm{D}} \Gamma_{\mathrm{R}} \mathcal{G}^{+}_{\mathrm{D}} \right]. \tag{3.4.29}$$

By using Eq. (3.2.35) with the definition of the spectral function and Eq. (3.3.13) for the isolated electrode Green's function, we can write the spectral function for the isolated left electrode as

$$A_{\mathrm{L}}(E) = 2\pi \sum_{n=1}^{N_{\mathrm{L}}} \nu_{\mathrm{L,n}}(E) \, |\varphi_{\mathrm{L},n}\rangle \, \langle \varphi_{\mathrm{L},n}| \, . \tag{3.4.30}$$

Finally, by using the definition of Γ_{L} given by Eq. (3.3.24) with Eq. (3.4.30) and inserting both into Eq. (3.4.29), we obtain

$$I^{\mathrm{L}}_{\mathrm{L}} = \frac{1}{h}\int dE \ f_{\mathrm{L}}(E) \mathrm{Tr}\left(\Gamma_{\mathrm{L}} \mathcal{G}^{-}_{\mathrm{D}} \Gamma_{\mathrm{R}} \mathcal{G}^{+}_{\mathrm{D}} \right).$$

Likewise, the total current from the left electrode into the SR, carried by the states originating from the right electrode, is given by

$$I^{\mathrm{L}}_{\mathrm{R}} = -\frac{1}{h}\int dE \ f_{\mathrm{R}}(E) \mathrm{Tr}\left(\Gamma_{\mathrm{L}} \mathcal{G}^{-}_{\mathrm{D}} \Gamma_{\mathrm{R}} \mathcal{G}^{+}_{\mathrm{D}} \right). \tag{3.4.31}$$

We can now define the transmission coefficient T [103, 63] as

$$T = \mathrm{Tr}\left(\Gamma_{\mathrm{L}} \mathcal{G}^{-}_{\mathrm{D}} \Gamma_{\mathrm{R}} \mathcal{G}^{+}_{\mathrm{D}} \right), \tag{3.4.32}$$

with $T \geq 0$. The total probability current then is

$$I^{\mathrm{L}} = \frac{1}{h}\int dE \ T(E) \left[f_{\mathrm{L}}(E) - f_{\mathrm{R}}(E) \right]. \tag{3.4.33}$$

We note that I^{L} depends only on the difference between the Fermi energies of the electrodes, which by definition is equal to the bias voltage eV_{sd}. Eq. (3.4.33) shows that only the states within the bias window, *i.e.* those lying in the energy range between $E_{\mathrm{F,L}}$ and $E_{\mathrm{F,R}}$, contribute to the current with an amplitude proportional to $T(E)$. We note that if the density of states in any of the electrodes vanishes at a given energy, the corresponding Γ-matrix will be zero, and therefore also the current will vanish. For a two-terminal device

$I^{\mathrm{L}} = -I^{\mathrm{R}}$, then we can define the two-terminal current through the SR I as being equal to I^{L}, so that

$$I = \frac{1}{h} \int dE\, T(E)\, [f_{\mathrm{L}}(E) - f_{\mathrm{R}}(E)]\,. \tag{3.4.34}$$

We point out that Eq. (3.4.34) describes the probability current. Therefore, in order to obtain the electrical current, I_{e}, one needs to multiply it with the electron charge, e, so that

$$I_{\mathrm{e}} = \frac{2e}{h} \int dE\, T(E)\, [f_{\mathrm{L}}(E) - f_{\mathrm{R}}(E)]\,, \tag{3.4.35}$$

where the factor of 2 is due to the spin degree of freedom. This is the well-known Landauer-Büttiker result for the current through a two-terminal device [103, 63]. In the spin-polarized case the transmission for majority spins $[T^{\uparrow}(E)]$ and the one for minority spins $[T^{\downarrow}(E)]$ are independent, and have to be evaluated separately for each spin. The total transmission then is $T(E) = T^{\uparrow}(E) + T^{\downarrow}(E)$. The total current is $I_e = I_e^{\uparrow} + I_e^{\downarrow}$, where $I_e^{\uparrow}$ is the current carried by the majority spins, and $I_e^{\downarrow}$ is the one carried by minority spins. The total current taking into account spin is given by

$$I_e = \frac{2e}{h} \int \sum_{\sigma=\uparrow,\downarrow} \mathrm{Tr}\left[\Gamma_{\mathrm{L}}^{\sigma} \mathcal{G}_{\mathrm{D}}^{-\sigma} \Gamma_{\mathrm{R}}^{\sigma} \mathcal{G}_{\mathrm{D}}^{+\sigma}\right] [f_{\mathrm{L}}(E) - f_{\mathrm{R}}(E)] dE, \tag{3.4.36}$$

where all quantities depend on the energy. From now on, we refer to the electrical current as just I by omitting the subscript "e".

This formula was already presented in Eq. (3.1.13) where it was derived for non-interacting electrons, *i.e.* where all the coherences between the states were neglected. In other words, the Landauer-Büttiker approach presented in Sec. 3.1 is a particular case of the NEGF. In the former, interactions in the SR are taken into account via a self-energy function, which, in principle, contains all possible scattering events that a single-particle experiences in the presence of all other particles, *i.e.* in a mean-field approximation.

3.5 DFT and NEGF

Throughout the present work, we use DFT as the electronic structure theory in conjunction with the NEGF. Although this combination works satisfactorily for many systems, it presents important limitations that lead to erroneous predictions. Thus, we conclude this Chapter by discussing some of these limitations.

In principle, one would like to establish how accurate is a ground-state DFT calculation of current with respect to the true many-body current evaluated for a well-defined nanojunction. In fact, this is a fundamental problem associated with DFT itself. Even if one could evaluate the current using ground-state DFT (even with the exact ground-state functional in hands) within the Landauer-Büttiker approach, we do not know how

it would differ from the current obtained with the true many-body system developing in time. The reason is not to be found in the lack of the exact ground-state functional but rather because we are employing a ground-state theory to treat a non-equilibrium problem. Therefore, the use of ground-state DFT in combination with the Landauer-Büttiker approach must be understood as a sort of mean-field approximation, even if we know the exact ground-state functional [63].

In addition, it is assumed that the single-particle KS-eigenvalues correspond to the energy levels for the real interacting-electron system (an assumption which is usually made also in ground-state DFT calculations). It is also assumed that the KS Hamiltonian is also valid out of equilibrium. Moreover, as we will see in the next chapters, the problem of the correct position of the KS-eigenenergies (see Sec. 2.5.1) can lead to major errors in the prediction of the transport properties of molecular systems, as we shall discuss in Chapter 6. This is closely related to the problems of DFT presented in Sec. 2.5.2 and Sec. 2.5.3, namely the lack of the derivative discontinuity and the self-interaction error, respectively.

Due to the fact that the NEGF uses a single-particle picture to describe the electrons, it can not correctly describe transport through very weakly coupled states. This is the situation of quantum dots in the Coulomb blockade regime. In this cases many-body effects, that are not included in the NEGF formalism described here, may play an important role. The transport properties of these systems are usually calculated using master equation approaches, as we will see in Chapter 7.

Chapter 4

Density Matrix Formalism

Open or dissipative quantum systems have been the subject of intensive research since many decades [106, 107]. Such systems are conventionally described in terms of the reduced density-matrix formalism, where the corresponding equation of motion, *i.e.* the *master equation*, can be obtained by a number of techniques [108]. Among them, the Nakajima-Zwanzig projection technique [109] and the real-time diagrammatic technique developed by König *et al.* [110, 111, 112].

The pioneering Redfield theory for dissipation [106, 107], commonly described in textbooks [113] has more recently been applied, by several groups, to study tunneling through molecules [114, 115, 116, 117, 118, 119, 120, 121]. The ME within this formalism, called the *Wangsness-Bloch-Redfield* master equation (WBR-ME), is based on the reduced density-matrix approach and implies the Born and Markov approximations in the relaxation description, this allows one to explicitly trace out the bath variables from the relaxation operator and to obtain a local-in-time equation of motion for the reduced density matrix.

The master equation approach is a computationally efficient way to describe quantum transport in molecular systems. Moreover, it is relatively simple to account for important effects, such as, Coulomb blockade (see Chapter 7), temperature and light-induced charge transport (see Chapter 8), where the parameters can be obtained by means of first-principles. In this chapter, we start by presenting a brief overview of quantum mechanics concepts needed for the discussion. Then, in Sec. 4.3, we present a full derivation of the WBR-ME used throughout the manuscript and all the approximations related to the practical applicability to quantum transport. Another important approach constructed on top of the WBR-ME, namely, the $\mathcal{T}$-matrix approach, is also presented in Sec. 4.5.

4.1 Time evolution

The dynamics of a quantum system can be discussed using three different representations or "pictures", namely, the Schrödinger picture, the Heisenberg picture and the interaction picture. In this section we will present the different representations and dis-

cuss how they are related. The interaction picture is of particular interest when dealing with time-dependent perturbation theory, which will be used to derive the equation of motion for the density matrix operator, the ME.

4.1.1 The Schrödinger picture

This representation is useful when dealing with time-independent Hamiltonians so that $\frac{\partial \hat{H}}{\partial t} = 0$. Any other operator, $\hat{A}$, may be time-dependent. The state vectors, $|\psi(t)\rangle$, do depend on time and their evolution is given by

$$|\psi(t)\rangle = \hat{\mathcal{U}}(t,0)\,|\psi(0)\rangle\,, \tag{4.1.1}$$

where $\hat{\mathcal{U}}(t,0)$ is the time evolution operator. The Schrödinger equation is written as

$$i\hbar\frac{\partial}{\partial t}\,|\psi(t)\rangle = \hat{H}(t)\,|\psi(t)\rangle\,, \tag{4.1.2}$$

which implies the equation for the evolution operator

$$i\hbar\frac{\partial}{\partial t}\hat{\mathcal{U}}(t,0) = \hat{H}(t)\hat{\mathcal{U}}(t,0). \tag{4.1.3}$$

If the Hamiltonian is time-independent, then we see that the evolution operator is simply given by

$$\hat{\mathcal{U}}(t,0) = e^{-\frac{i}{\hbar}\hat{H}t}. \tag{4.1.4}$$

In summary,

$$\text{The Schrödinger picture} \begin{cases} \text{states:} & |\psi(t)\rangle = e^{-\frac{i}{\hbar}\hat{H}t}\,|\psi(0)\rangle \\ \text{operators:} & \begin{cases} \hat{A}\text{, may or may not be time-dependent} \\ \hat{H} \text{ is time-independent.} \end{cases} \end{cases} \tag{4.1.5}$$

4.1.2 The Heisenberg picture

Sometimes, it is preferable to incorporate all the time dependencies in the operators, $\hat{A}(t)$, and work with time-independent state vectors, $|\psi\rangle$. The Hamiltonian of the system, $\hat{H}$, remains time-independent. Note that if the matrix elements of any operator between any two state vectors are identical in the Schrödinger and Heisenberg representations, then both representations are fully equivalent since

$$\langle\psi'(t)|\,\hat{A}\,|\psi(t)\rangle = \langle\psi'|\,e^{\frac{i}{\hbar}\hat{H}t}\hat{A}e^{-\frac{i}{\hbar}\hat{H}t}\,|\psi\rangle = \langle\psi'|\,\hat{A}(t)\,|\psi\rangle \tag{4.1.6}$$

where the unitary transformation of Eq. (4.1.4) was used. This representation can be summarized as

$$\text{The Heisenberg picture} \begin{cases} \text{states:} & |\psi(t)\rangle = e^{-\frac{i}{\hbar}\hat{H}t}\,|\psi(0)\rangle \\ \text{operators:} & \begin{cases} \hat{A}(t) \equiv e^{\frac{i}{\hbar}\hat{H}t}\hat{A}(0)e^{-\frac{i}{\hbar}\hat{H}t} \\ \hat{H} \text{ is time-independent.} \end{cases} \end{cases} \tag{4.1.7}$$

4.1.3 The interaction picture

The Schrödinger and Heisenberg pictures both require a time-independent Hamiltonian. However, very often, we have to deal with time-dependent Hamiltonians. This is more conveniently treated within the interaction picture. In this representation, the full Hamiltonian is written as $\hat{H} = \hat{H}_0 + \hat{V}(t)$. Here, $\hat{H}_0$ is the time-independent part of the Hamiltonian so that $\hat{H}_0\,|n_0\rangle = \epsilon_{n_0}\,|n_0\rangle$. The states $|n_0\rangle$ are perturbed by some, possibly time-dependent, interaction $\hat{V}(t)$. The task in the interaction picture is to separate the fast time evolution due to the unperturbed Hamiltonian from the more complicated interaction $\hat{V}(t)$. This can be achieved by replacing the full Hamiltonian, $\hat{H}$, in Eq. (4.1.4) by its unperturbed part, $\hat{H}_0$. As a result, both the state vectors and the operators will depend on time.

$$\text{The interaction picture} \begin{cases} \text{states:} & |\psi_I(t)\rangle = e^{\frac{i}{\hbar}\hat{H}_0 t}\,|\psi(t)\rangle \\ \text{operators:} & \begin{cases} \hat{A}_I(t) \equiv e^{\frac{i}{\hbar}\hat{H}_0 t}\hat{A}(t)e^{-\frac{i}{\hbar}\hat{H}_0 t} \\ \hat{H}_0 \text{ is time-independent} \end{cases} \end{cases} \tag{4.1.8}$$

The Schrödinger equation for a state $|\psi_I(t)\rangle$ given in Eq. (4.1.8) is

$$\begin{aligned} i\hbar\frac{\partial}{\partial t}\,|\psi_I(t)\rangle &= i\hbar\left(\frac{\partial e^{\frac{i}{\hbar}\hat{H}_0 t}}{\partial t}\right)|\psi(t)\rangle + e^{\frac{i}{\hbar}\hat{H}_0 t}\left(i\hbar\frac{\partial}{\partial t}\,|\psi(t)\rangle\right) \\ &= e^{\frac{i}{\hbar}\hat{H}_0 t}\left(-\hat{H}_0 + \hat{H}\right)|\psi(t)\rangle \\ &= e^{\frac{i}{\hbar}\hat{H}_0 t}\hat{V}(t)\,|\psi(t)\rangle \\ &= e^{\frac{i}{\hbar}\hat{H}_0 t}\hat{V}(t)e^{\frac{-i}{\hbar}\hat{H}_0 t}\,|\psi_I(t)\rangle \\ i\hbar\frac{\partial}{\partial t}\,|\psi_I(t)\rangle &= \hat{V}_I(t)\,|\psi_I(t)\rangle\,. \end{aligned} \tag{4.1.9}$$

The resulting Schrödinger equation is explicitly written in terms of only the interaction part of the full Hamiltonian. If $\hat{V}_I(t) = 0$ then $i\hbar\frac{\partial}{\partial t}\,|\psi_I(t)\rangle = 0$, that is, the time dependence of $|\psi_I(t)\rangle$ originates entirely from the perturbation term. If this term is small, $|\psi_I(t)\rangle$ will vary slowly with time and Eq. (4.1.9) can be solved within the time-dependent perturbation theory framework, a task easier than solving directly Eq. (4.1.2). The time

evolution of a state $|\psi_I(t)\rangle$ from a time t_0 to a time t is given by an unitary transformation

$$|\psi_I(t)\rangle = \hat{U}_I(t,t_0)\,|\psi_I(t_0)\rangle\,, \tag{4.1.10}$$

where

$$\hat{U}_I(t,t_0) = e^{\frac{i}{\hbar}\hat{H}_0 t}\hat{U}(t,t_0)e^{\frac{-i}{\hbar}\hat{H}_0 t_0} \tag{4.1.11}$$

depends only on $\hat{V}(t)$ and $\hat{U}(t,t_0)$ is given by Eq. (4.1.4) in the Schrödinger representation.

4.2 Perturbative expansion

In principle, all cases where the interaction picture is used, a perturbative expansion in the interaction, $\hat{V}_I$, is carried out and this is implicit in the evolution operator. The task now is to find a useful formula for the time evolution operator. By evaluating the time derivative of Eq. (4.1.11), we have

$$\begin{aligned}
i\hbar\frac{\partial\hat{U}_I(t,t_0)}{\partial t} &= i\hbar\frac{\partial}{\partial t}\left(e^{\frac{i}{\hbar}\hat{H}_0 t}\hat{U}(t,t_0)e^{\frac{-i}{\hbar}\hat{H}_0 t_0}\right)\\
&= i\hbar\frac{\partial}{\partial t}\left(e^{\frac{i}{\hbar}\hat{H}_0 t}\hat{U}(t,t_0)\right)e^{\frac{-i}{\hbar}\hat{H}_0 t_0} + i\hbar\left(e^{\frac{i}{\hbar}\hat{H}_0 t}\hat{U}(t,t_0)\right)\cancelto{0}{\frac{\partial}{\partial t}e^{\frac{-i}{\hbar}\hat{H}_0 t_0}}\\
&= \left[i\hbar\frac{\partial}{\partial t}\left(e^{\frac{i}{\hbar}\hat{H}_0 t}\right)\hat{U}(t,t_0) + i\hbar e^{\frac{i}{\hbar}\hat{H}_0 t}\frac{\partial}{\partial t}\hat{U}(t,t_0)\right]e^{\frac{-i}{\hbar}\hat{H}_0 t_0}\\
&= e^{\frac{i}{\hbar}\hat{H}_0 t}\left(-\hat{H}_0 + \hat{H}\right)\hat{U}(t,t_0)e^{\frac{-i}{\hbar}\hat{H}_0 t_0}\\
&= e^{\frac{i}{\hbar}\hat{H}_0 t}\hat{V}(t)e^{\frac{-i}{\hbar}\hat{H}_0 t}e^{\frac{i}{\hbar}\hat{H}_0 t}\hat{U}(t,t_0)e^{\frac{-i}{\hbar}\hat{H}_0 t_0}\\
i\hbar\frac{\partial\hat{U}_I(t,t_0)}{\partial t} &= \hat{V}_I(t)\hat{U}_I(t,t_0)
\end{aligned} \tag{4.2.1}$$

where we used the results of Eq. (4.1.3). By integration of this differential equation we obtain the integral equation

$$\hat{U}_I(t,t_0) = \mathbb{I} + \frac{1}{i\hbar}\int_{t_0}^{t} dt'\hat{V}_I(t')\hat{U}_I(t',t_0), \tag{4.2.2}$$

where the initial condition is $\hat{U}_I(t_0,t_0) = \mathbb{I}$, that is, when $\hat{V}_I = 0$. For $\hat{V}_I(t)$ sufficiently small, $\hat{U}_I(t,t_0)$ will only differ slightly from $\mathbb{I}$. The operator $\hat{U}_I(t_0,t_0)$ can then be replaced by the identity operator and we obtain the first-order term given by

$$\hat{U}_I^{(1)}(t,t_0) = \mathbb{I} + \frac{1}{i\hbar}\int_{t_0}^{t} dt'\hat{V}_I(t'). \tag{4.2.3}$$

If we iterate this equation we derive the following pertubative expansion

$$\hat{U}_I(t,t_0) = \mathbb{I} + \frac{1}{i\hbar}\int_{t_0}^{t} dt_1 \hat{V}_I(t_1) - \frac{1}{\hbar^2}\int_{t_0}^{t} dt_1 \hat{V}_I(t_1)\int_{t_0}^{t_1} dt_2 \hat{V}_I(t_2) + ... \tag{4.2.4}$$

This equation describes the time evolution from time t_0 to time t of the system due to consecutive scattering events caused by the perturbation $\hat{V}_I$ at times t_1, t_2, t_3 and so on. In other words, it gives additional phase factors to the state vectors due to the perturbation on top of the trivial phase factors arising from $\hat{H}_0$.

4.3 Master equation I: the Wangsness-Bloch-Redfield master equation

The ME approach involves two steps. Firstly, one derives the ME from the von Neumann equation for the full system. This shows how the reduced density operator changes based on its present and often its past values. Secondly, one solves the ME to determine the time evolution of the system or its stationary state solution. It is generally more complicated to find the time evolution when the ME contains memory, or history of the past times. Therefore, approximations are called to circumvent this, usually to obtain a ME that is local in time. In the present Chapter we follow closely the derivation presented in Ref. [64].

4.3.1 Liouville equation in the interaction picture

Let us now write the density operator, $\hat{\rho}$, in the interaction picture. By evaluating the time derivative of this operator, we derive the Liouville equation

$$\begin{aligned}
i\hbar\frac{\partial\hat{\rho}_I(t)}{\partial t} &= i\hbar\frac{\partial}{\partial t}\left(\hat{U}_I(t,t_0)\hat{\rho}(t)\hat{U}_I^\dagger(t,t_0)\right) \\
&= i\hbar\frac{\partial}{\partial t}\left(\hat{U}_I(t,t_0)\hat{\rho}(t)\right)\hat{U}_I^\dagger(t,t_0) + i\hbar\left(\hat{U}_I(t,t_0)\hat{\rho}(t)\right)\frac{\partial}{\partial t}\hat{U}_I^\dagger(t,t_0) \\
&= \hat{V}_I(t)\hat{U}_I(t,t_0)\hat{\rho}(t)\hat{U}_I^\dagger(t,t_0) - \hat{U}_I(t,t_0)\hat{\rho}(t)\hat{U}_I^\dagger(t,t_0)\hat{V}_I(t) \\
&= \hat{V}_I(t)\hat{\rho}_I(t) - \hat{\rho}_I(t)\hat{V}_I(t) \\
&= \left[\hat{V}_I(t), \hat{\rho}_I(t)\right].
\end{aligned} \tag{4.3.1}$$

This is a rather important result, since the density operator depends only on the interaction Hamiltonian. This equation can be written in an integral form:

$$\hat{\rho}_I(t) = \hat{\rho}_I(0) + \frac{1}{i\hbar}\int_{t_0}^{t} dt_1 \left[\hat{V}_I(t_1), \hat{\rho}_I(t_1)\right], \tag{4.3.2}$$

which can also be solved iteratively

$$\hat{\rho}_I^{(0)}(t) = \hat{\rho}_I(0) \tag{4.3.3}$$

$$\hat{\rho}_I^{(1)}(t) = \hat{\rho}_I^{(0)}(0) + \frac{1}{i\hbar}\int_{t_0}^{t} dt_1 \left[\hat{V}_I(t_1), \hat{\rho}_I(0)\right] \tag{4.3.4}$$

$$\hat{\rho}_I^{(2)}(t) = \hat{\rho}_I^{(1)}(0) - \frac{1}{\hbar^2}\int_{t_0}^{t} dt_1 \int_{t_0}^{t} dt_2 \left[\hat{V}_I(t_1), \left[\hat{V}_I(t_2), \hat{\rho}_I(0)\right]\right], \tag{4.3.5}$$

and so on. By using the iterative procedure we compute the small changes in the density operator caused by a perturbation in the state of the system due to consecutive scattering events.

We are interested in studying the transport properties of physical systems comprising of a small sub-system (for instance, a molecule) connected to two fermionic electrodes. The small sub-system is not in equilibrium because of its interaction with the environment (the reservoirs or electrodes). The Hamiltonian of the entire system can be written as

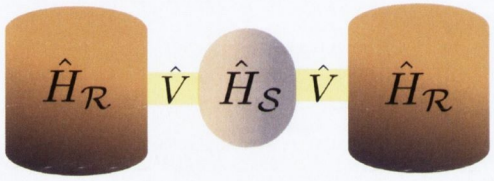

Figure 4.1: Schematic representation of an open quantum system. The sub-system $\mathcal{S}$, described by the Hamiltonian $\hat{H}_{\mathcal{S}}$, interacts via $\hat{V}$ with the environment $\mathcal{R}$, described by the Hamiltonian $\hat{H}_{\mathcal{R}}$.

$$\hat{H} = \hat{H}_{\mathcal{S}} + \hat{H}_{\mathcal{R}} + \hat{V}, \tag{4.3.6}$$

where $\mathcal{S}$ and $\mathcal{R}$ denote the small sub-system and the reservoirs, respectively, and $\hat{V}$ is the interaction between them. From this point on, we assume the interaction between the reservoirs and the small sub-system to be weak, so that we may treat $\hat{V}$ within perturbation theory. We use the interaction picture so that the time evolution of any operator, $\hat{A}_I$, is given by Eq. (4.1.8), where the unperturbed time-independent Hamiltonian is $\hat{H}_0 = \hat{H}_{\mathcal{S}} + \hat{H}_{\mathcal{R}}$. The Liouville equation for the density operator of the entire system, $\hat{\chi}_I$, can be written as

$$\dot{\hat{\chi}}_I(t) = -\frac{i}{\hbar}\left[\hat{V}_I(t), \hat{\chi}_I(0)\right] - \frac{1}{\hbar^2}\int_0^t dt' \left[\hat{V}_I(t'), \left[\hat{V}_I(t'), \hat{\chi}_I(t')\right]\right]. \tag{4.3.7}$$

4.3.2 Simplification: separability

If we assume the interaction between the systems $\mathcal{S}$ and $\mathcal{R}$ gets swiched on at $t_0 = 0$,[1] we separate the dynamics of $\mathcal{S}$ by tracing out the contribution of the reservoirs from the full density matrix in order to obtain the reduced density matrix [113], $\hat{\rho}_I = \mathrm{Tr}_{\mathcal{R}}(\hat{\chi}_I)$. By doing so, the initial full density matrix can be written as a product:

$$\hat{\chi}(0) = \hat{\chi}_I(0) = \hat{\chi}_{\mathcal{S}}(0) \otimes \hat{\chi}_{\mathcal{R}}(0), \tag{4.3.8}$$

where $\hat{\chi}_{\mathcal{S}}(0) = \hat{\rho}(0)$. In other words, the initial state between the systems $\mathcal{S}$ and $\mathcal{R}$ is uncorrelated for times prior to $t_0 = 0$, $t < t_0$.

4.3.3 Born approximation

One can always write the full density operator at any time as

$$\hat{\chi}_I(t) = \hat{\rho}_I(t) \otimes \hat{\chi}_{\mathcal{R}}(t) + \hat{\chi}_{\text{correlation}}(t), \tag{4.3.9}$$

where Eq. (4.3.9) provides the definition of $\hat{\chi}_{\text{correlation}}(t)$. If the interaction starts at $t_0 = 0$, for any time in the past, Eq. (4.3.8) holds. If we assume that the coupling between the two sub-systems is weak, Eq. (4.3.9) will approximate to

$$\hat{\chi}_I(t) \approx \hat{\rho}_I(t) \otimes \hat{\chi}_{\mathcal{R}}(t) \tag{4.3.10}$$

for timescales over which perturbation theory is valid. In addition, we assume that the correlation time of the reservoirs , $\tau_{\mathcal{R}}$, and consequently the relaxation time, is small so that

$$\hat{\chi}_{\mathcal{R}}(t) \approx \hat{\chi}_{\mathcal{R}}(0), \text{if } t \gg \tau_{\mathcal{R}} \tag{4.3.11}$$

and

$$\hat{\chi}_I(t) = \hat{\rho}_I(t)\hat{\chi}_{\mathcal{R}}(0). \tag{4.3.12}$$

In other words, the reservoirs are assumed to comprise so many degrees of freedom that they are not affected by the interaction with $\mathcal{S}$, independently on the amount of energy transferred to them from $\mathcal{S}$. Hence, they will remain at thermal equilibrium, *i.e.* the density matrix will be simply given by

$$\hat{\chi}_{\mathcal{R}}(0) = \frac{1}{Z} e^{-\beta \hat{H}_{\mathcal{R}}}, \tag{4.3.13}$$

where Z is the partition function, $Z = \mathrm{Tr}\left(e^{-\frac{1}{k_B \Theta} \hat{H}_{\mathcal{R}}}\right)$. This is the fundamental condition for *irreversibility*. We can then write the equation of motion for the reduced density

[1] Note that this can always be obtained by choosing $t_0 = 0$ appropriately.

operator as

$$\dot{\hat{\rho}}_I(t) = -\frac{i}{\hbar}\mathrm{Tr}_{\mathcal{R}}\left[\hat{V}_I(t), \hat{\rho}_I(0)\hat{\chi}_{\mathcal{R}}(0)\right] - \frac{1}{\hbar^2}\int_0^t dt' \mathrm{Tr}_{\mathcal{R}}\left[\hat{V}_I(t'), \left[\hat{V}_I(t'), \hat{\rho}_I(t')\hat{\chi}_{\mathcal{R}}(0)\right]\right]. \tag{4.3.14}$$

According to this equation, the behavior of $\mathcal{S}$ depends on the past events in the time interval $[0, t]$ because the integrals contain $\hat{\rho}_I(t')$, *i.e.* this ME is non-local in time.

4.3.4 Markov approximation

If we assume that the time scale for the reservoirs to keep their correlation is much faster than that in which the small sub-system $\mathcal{S}$ is modified, then the system loses its memory and the influence of past times do not affect the evolution of the system. This is also a consequence of the weak-coupling limit between the quantum sub-system and the reservoirs.[2] This is equivalent to say that $\hat{\rho}_I(t') \approx \hat{\rho}_I(t)$. This approximation is called the *Markov-approximation*. Then, Eq. (4.3.14) can be rewritten as

$$\dot{\hat{\rho}}_I(t) = -\frac{i}{\hbar}\mathrm{Tr}_{\mathcal{R}}\left[\hat{V}_I(t), \hat{\rho}_I(0)\hat{\chi}_{\mathcal{R}}(0)\right] - \frac{1}{\hbar^2}\int_0^t dt' \mathrm{Tr}_{\mathcal{R}}\left[\hat{V}_I(t'), \left[\hat{V}_I(t'), \hat{\rho}_I(t)\hat{\chi}_{\mathcal{R}}(0)\right]\right], \tag{4.3.15}$$

i.e. it becomes local in time. In Eq. (4.3.15), the rate of change of $\hat{\rho}_I$ at time t is determined by $\hat{\rho}_I$ at the same time t only. In order to solve this equation, we need to specify a form for the interaction $\hat{V}_I$. A generic form for the interaction operator is a product between the small sub-system operators, $\hat{s}_i$, and the reservoirs operators, $\hat{r}_i$. In the interaction picture, we have

$$\hat{V}_I(t) = \sum_i \hat{s}_i(t)\hat{r}_i(t), \tag{4.3.16}$$

where

$$\hat{s}_i(t) = e^{\frac{i}{\hbar}\hat{H}_{\mathcal{S}}t} s_i e^{\frac{-i}{\hbar}\hat{H}_{\mathcal{S}}t} \tag{4.3.17}$$

and

$$\hat{r}_i(t) = e^{\frac{i}{\hbar}\hat{H}_{\mathcal{R}}t} r_i e^{\frac{-i}{\hbar}\hat{H}_{\mathcal{R}}t}. \tag{4.3.18}$$

By inserting Eq. (4.3.16) into Eq. (4.3.15) we obtain

$$\begin{aligned}\dot{\hat{\rho}}_I(t) = &-\frac{i}{\hbar}\mathrm{Tr}_{\mathcal{R}}\sum_i \left[\hat{s}_i(t)\hat{r}_i(t), \hat{\rho}_I(0)\hat{\chi}_{\mathcal{R}}(0)\right] + \\ &-\frac{1}{\hbar^2}\int_0^t dt' \sum_{ij} \mathrm{Tr}_{\mathcal{R}}\left[\hat{s}_i(t)\hat{r}_i(t), \left[\hat{s}_j(t')\hat{r}_j(t'), \hat{\rho}_I(t)\hat{\chi}_{\mathcal{R}}(0)\right]\right].\end{aligned} \tag{4.3.19}$$

[2] A discussion on the validity of this approximation in terms of temperature can be found in reference [108].

The operators s_i act only on the subspace of the system $\mathcal{S}$ whereas the operators r_i act only on the subspace of the reservoirs $\mathcal{R}$. In other words they commute and therefore we can interchange their position. Also, by considering the cyclic property of the trace, $\mathrm{Tr}(\hat{A}\hat{B}\hat{C}\hat{D}) = \mathrm{Tr}(\hat{D}\hat{A}\hat{B}\hat{C}) = \mathrm{Tr}(\hat{C}\hat{D}\hat{A}\hat{B})$, the first term of Eq. (4.3.19) can be written as

$$
\begin{aligned}
&-\frac{i}{\hbar}\mathrm{Tr}_{\mathcal{R}}\sum_i[\hat{s}_i(t)\hat{r}_i(t),\hat{\rho}_I(0)\hat{\chi}_{\mathcal{R}}(0)] = \\
&= -\frac{i}{\hbar}\mathrm{Tr}_{\mathcal{R}}\sum_i\{\hat{s}_i(t)\hat{r}_i(t)\hat{\rho}_I(0)\hat{\chi}_{\mathcal{R}}(0) - \hat{\rho}_I(0)\hat{\chi}_{\mathcal{R}}(0)\hat{s}_i(t)\hat{r}_i(t)\} = \\
&= -\frac{i}{\hbar}\mathrm{Tr}_{\mathcal{R}}\sum_i\{\hat{s}_i(t)\hat{\rho}_I(0)\hat{r}_i(t)\hat{\chi}_{\mathcal{R}}(0) - \hat{r}_i(t)\hat{\chi}_{\mathcal{R}}(0)\hat{\rho}_I(0)\hat{s}_i(t)\} = \\
&= -\frac{i}{\hbar}\sum_i\{\hat{s}_i(t)\hat{\rho}_I(0) - \hat{\rho}_I(0)\hat{s}_i(t)\}\mathrm{Tr}_{\mathcal{R}}\left(\hat{r}_i(t)\hat{\chi}_{\mathcal{R}}(0)\right) = \\
&= -\frac{i}{\hbar}\sum_i\{\hat{s}_i(t)\hat{\rho}_I(0) - \hat{\rho}_I(0)\hat{s}_i(t)\}\langle\hat{r}_i(t)\rangle,
\end{aligned}
\tag{4.3.20}
$$

where the definition for the expectation value given by $\mathrm{Tr}_{\mathcal{R}}\left(\hat{r}_i(t)\hat{\chi}_{\mathcal{R}}(0)\right) = \langle\hat{r}_i(t)\rangle$ was used. If we use the same reasoning for the second term, we can rewrite Eq. (4.3.19) as

$$
\begin{aligned}
\dot{\hat{\rho}}_I(t) = &-\frac{i}{\hbar}\sum_i\Big\{\hat{s}_i(t)\hat{\rho}_I(0) - \hat{\rho}_I(0)\hat{s}_i(t)\Big\}\langle\hat{r}_i(t)\rangle + \\
&-\frac{1}{\hbar^2}\sum_{ij}\int_0^t dt'\Big\{\Big(\hat{s}_i(t)\hat{s}_j(t')\hat{\rho}_I(t) - \hat{s}_j(t')\hat{\rho}_I(t)\hat{s}_i(t)\Big)\langle\hat{r}_i(t)\hat{r}_j(t')\rangle + \\
&+\Big(\hat{\rho}_I(t)\hat{s}_j(t')\hat{s}_i(t) - \hat{s}_i(t)\hat{\rho}_I(t)\hat{s}_j(t')\Big)\langle\hat{r}_j(t')\hat{r}_i(t)\rangle\Big\}.
\end{aligned}
\tag{4.3.21}
$$

The task now is to calculate the expectation values and the correlation functions. If we assume that the reservoirs are in equilibrium and that the states $|\mathcal{R}\rangle$ are the eigenstates of $\hat{H}_{\mathcal{R}}$, the operator given in Eq. (4.3.13) is diagonal. Therefore, all the elements $\langle\mathcal{R}|\,\hat{r}_i(t)\,|\mathcal{R}\rangle$ must be non-diagonal. This means that there is no average energy shifts on the reservoirs, then $\langle\hat{r}_i(t)\rangle = 0$, and the first term of Eq. (4.3.21) vanishes. The time correlation functions, $\langle\hat{r}_i(t)\hat{r}_j(t')\rangle$, describe the average correlation between interactions that occur at times t and t'. The reservoirs dissipates quickly the effects of its interaction with the system $\mathcal{S}$ so that

$$
\langle\hat{r}_i(t)\hat{r}_j(t')\rangle \neq 0, \text{ if } t - t' \lesssim \tau_{\mathcal{R}}. \tag{4.3.22}
$$

On the contrary, for $t - t' \gg \tau_{\mathcal{R}}$, the interaction becomes less correlated and the correlation functions satisfy the condition

$$
\langle\hat{r}_i(t)\hat{r}_j(t')\rangle \approx 0. \tag{4.3.23}
$$

The integral in the second term of Eq. (4.3.21) is non-zero only for times in the time interval $[t - \tau_{\mathcal{R}}, t']$. Outside this interval, the values of $\hat{\rho}(t')$ have little influence on $\dot{\hat{\rho}}(t)$.

4.3.5 Relaxation time approximation

Because the correlation functions depend only on the time difference $t'' = t - t'$, it is more convenient to write them as

$$\langle \hat{r}_i(t)\hat{r}_j(t')\rangle = \langle \hat{r}_i(t-t')\hat{r}_j\rangle, \tag{4.3.24}$$

so that we can rewrite the equation of motion for the reduced density operator [Eq. (4.3.21)] as

$$\dot{\hat{\rho}}_I(t) = -\frac{1}{\hbar^2}\sum_{ij}\int_0^\infty dt''\Big\{\big[\hat{s}_i(t),\hat{s}_j(t-t'')\hat{\rho}_I(t)\big]\langle \hat{r}_i(t'')\hat{r}_j\rangle - \big[\hat{s}_i(t),\hat{\rho}_I(t)\hat{s}_j(t-t'')\big]\langle \hat{r}_j\hat{r}_i(t'')\rangle\Big\}, \tag{4.3.25}$$

where the limit of integration extended to infinity is justified by the discussions of Eq. (4.3.22) and Eq. (4.3.23), that is, for times t longer than $\tau_{\mathcal{R}}$.

4.3.6 Equation of motion

Let us consider the following set of state vectors $\{|\mathcal{S}\rangle\} = \{..., |m\rangle, ..., |n\rangle, ...\}$ to be the eigenstates of $\hat{H}_{\mathcal{S}}$. If we write the system Hamiltonian over the basis of its eigenstates, we can extract the time dependence from the system operators,

$$\begin{aligned}\langle m|\,\hat{s}_i(t)\,|n\rangle &= \langle m|\,e^{\frac{i}{\hbar}\hat{H}_{\mathcal{S}}t}\hat{s}_i e^{\frac{-i}{\hbar}\hat{H}_{\mathcal{S}}t}\,|n\rangle = \\ &= e^{\frac{i}{\hbar}\omega_{mn}t}\,\langle m|\,\hat{s}_i\,|n\rangle\,,\end{aligned} \tag{4.3.26}$$

where $\langle m|\,\hat{H}_{\mathcal{S}}\,|m\rangle - \langle n|\,\hat{H}_{\mathcal{S}}\,|n\rangle = \epsilon_m - \epsilon_n = \hbar\omega$. We can then write the matrix elements of the commutators of Eq. (4.3.25) as

$$\begin{aligned}&\langle m'|\big[\hat{s}_i(t),\hat{s}_j(t-t'')\hat{\rho}_I(t)\big]\,|m\rangle = \\ &\quad= \langle m'|\,\big\{\hat{s}_i(t)\hat{s}_j(t-t'')\hat{\rho}_I(t) - \hat{s}_j(t-t'')\hat{\rho}_I(t)\hat{s}_i(t)\big\}\,|m\rangle = \\ &\quad= \sum_{kk'}\Big(e^{i\omega_{m'k}t}e^{i\omega_{kk'}(t-t'')}\,\langle m'|\,\hat{s}_i\,|k\rangle\,\langle k|\,\hat{s}_j\,|k'\rangle\,\langle k'|\,\hat{\rho}_I(t)\,|m\rangle + \\ &\quad- e^{i\omega_{m'k'}(t-t'')}e^{i\omega_{km}t}\,\langle m'|\,\hat{s}_j\,|k'\rangle\,\langle k'|\,\hat{\rho}_I(t)\,|k\rangle\,\langle k|\,\hat{s}_i\,|m\rangle\Big)\end{aligned} \tag{4.3.27}$$

and

$$\begin{aligned}
&\langle m'| \left[\hat{s}_i(t), \hat{\rho}_I(t)\hat{s}_j(t-t'')\right] |m\rangle = \\
&= \langle m'| \left\{\hat{s}_i(t)\hat{\rho}_I(t)\hat{s}_j(t-t'') - \hat{\rho}_I(t)\hat{s}_j(t-t'')\hat{s}_i(t)\right\} |m\rangle = \\
&= \sum_{kk'} \Big(e^{i\omega_{m'k'}t} e^{i\omega_{km}(t-t'')} \langle m'| \hat{s}_i |k'\rangle \langle k'| \hat{\rho}_I(t) |k\rangle \langle k| \hat{s}_j |m\rangle + \\
&- e^{i\omega_{kk'}(t-t'')} e^{i\omega_{k'm}t} \langle m'| \hat{\rho}_I(t) |k\rangle \langle k| \hat{s}_j |k'\rangle \langle k'| \hat{s}_i |m\rangle \Big).
\end{aligned} \tag{4.3.28}$$

By inserting the results of Eq. (4.3.27) and Eq. (4.3.28) into Eq. (4.3.25), the matrix elements of the density operator write

$$\begin{aligned}
\langle m'| \dot{\hat{\rho}}_I(t) |m\rangle = &- \frac{1}{\hbar^2} \sum_{ijkk'} \langle k'| \hat{\rho}_I(t) |k\rangle \int_0^\infty dt'' \Big\{ \\
&e^{i(\omega_{m'k'}+\omega_{km})t} \delta_{mk} \sum_\alpha \langle m'| \hat{s}_i |\alpha\rangle \langle \alpha| \hat{s}_j |k'\rangle \int_0^\infty dt'' e^{-i\omega_{\alpha k'}t''} \langle \hat{r}_i(t'')\hat{r}_j\rangle + \\
&- e^{i(\omega_{m'k'}+\omega_{km})t} \langle m'| \hat{s}_j |k'\rangle \langle k| \hat{s}_i |m\rangle \int_0^\infty dt'' e^{-i\omega_{m'k'}t''} \langle \hat{r}_i(t'')\hat{r}_j\rangle + \\
&- e^{i(\omega_{m'k'}+\omega_{km})t} \langle m'| \hat{s}_i |k'\rangle \langle k| \hat{s}_j |m\rangle \int_0^\infty dt'' e^{-i\omega_{km}t''} \langle \hat{r}_j\hat{r}_i(t'')\rangle + \\
&+ e^{i(\omega_{m'k'}+\omega_{km})t} \delta_{m'k'} \sum_\alpha \langle k| \hat{s}_j |\alpha\rangle \langle \alpha| \hat{s}_i |m\rangle \int_0^\infty dt'' e^{-i\omega_{k\alpha}t''} \langle \hat{r}_j\hat{r}_i(t'')\rangle \Big\},
\end{aligned} \tag{4.3.29}$$

We have also multiplied the first and fourth terms by $e^{i\omega_{km}t}$ and $e^{i\omega_{m'k'}t}$, respectively, which is allowed because of the presence of the δ_{mk} and $\delta_{m'k'}$ functions.

By defining, for simplicity

$$\lambda^+_{mkln} = \frac{1}{\hbar^2} \sum_{ij} \langle m| \hat{s}_i |k\rangle \langle l| \hat{s}_j |n\rangle \int_0^\infty dt'' e^{-i\omega_{ln}t''} \langle \hat{r}_i(t'')\hat{r}_j\rangle, \tag{4.3.30}$$

and

$$\lambda^-_{mkln} = \frac{1}{\hbar^2} \sum_{ij} \langle m| \hat{s}_j |k\rangle \langle l| \hat{s}_i |n\rangle \int_0^\infty dt'' e^{-i\omega_{mk}t''} \langle \hat{r}_j\hat{r}_i(t'')\rangle, \tag{4.3.31}$$

we obtain the so-called *Redfield relaxation coefficients* given by

$$R_{m'mk'k} = -\delta_{mk} \sum_\alpha \lambda^+_{m'\alpha\alpha k'} + \lambda^+_{kmm'k'} + \lambda^-_{kmm'k'} - \delta_{m'k'} \sum_\alpha \lambda^-_{k\alpha\alpha m}. \tag{4.3.32}$$

The coefficients given in Eq. (4.3.30) and Eq. (4.3.31) obey the following conditions:

$$\lambda^{-*}_{mnkl} = \lambda^{+}_{lknm} \tag{4.3.33}$$

$$\lambda^{-}_{mmln} = \lambda^{-}_{lnmm} = 0, \tag{4.3.34}$$

where the condition of Eq. (4.3.34) is related to the fact that $\langle m|\,\hat{s}_j\,|m\rangle = \langle m|\,\hat{s}_i\,|m\rangle = 0$, that is, no energy shift is allowed in the system due to the interaction term $\hat{V}_I(t)$. We can now rewrite Eq. (4.3.29) in the form

$$\langle m'|\,\dot{\hat{\rho}}_I(t)\,|m\rangle = \sum_{kk'} \langle k'|\,\hat{\rho}_I(t)\,|k\rangle\, R_{m'mk'k} e^{i(\omega_{m'k'}+\omega_{km})t}. \tag{4.3.35}$$

In order to simplify further Eq. (4.3.35), we assume that the typical time-scale to observe any change in the system, ω^{-1}_{mn}, is much shorter than the time for the integration step. Note that the integration time must be also long enough to satisfy the conditions discussed in Eq. (4.3.22) and Eq. (4.3.23), that is, the Markov approximation. If this is the case, only the terms that satisfy the condition

$$\omega_{m'k'} + \omega_{km} = \epsilon_{m'} - \epsilon_{k'} + \epsilon_k - \epsilon_m = 0 \tag{4.3.36}$$

are kept. The other terms contribute to only fast oscillations and they can be neglected. If we assume that the states of the system $\mathcal{S}$ are non-degenerate with a non-regular energy separation between them, we can write three different conditions that satisfy Eq. (4.3.36)

- The first condition is

$$m' = k',\ m = k,\ m' \neq m. \tag{4.3.37}$$

  This applied to Eq. (4.3.35) gives

$$\langle m'|\,\dot{\hat{\rho}}_I(t)\,|m\rangle = (1 - \delta_{mm'})\,\langle m'|\,\hat{\rho}_I(t)\,|m\rangle\, R_{m'mm'm}, \tag{4.3.38}$$

  which will contribute to off-diagonal elements of the reduced density matrix operator.

- The second condition is

$$m' = m,\ k' = k,\ m' \neq k', \tag{4.3.39}$$

  where we have

$$\langle m'|\,\dot{\hat{\rho}}_I(t)\,|m\rangle = \delta_{mm'} \sum_{k\neq m} \langle k|\,\hat{\rho}_I(t)\,|k\rangle\, R_{mmkk}, \tag{4.3.40}$$

  and the delta function assures that this term is diagonal.

- The third condition is

$$m' = m = k' = k, \tag{4.3.41}$$

yielding

$$\langle m'|\,\dot{\hat{\rho}}_I(t)\,|m\rangle = \delta_{mm'}\,\langle m'|\,\hat{\rho}_I(t)\,|m'\rangle\,R_{m'm'm'm'}. \tag{4.3.42}$$

By adding up these three contributions we finally can rewrite a time-independent version of Eq. (4.3.35) as

$$\begin{aligned}\langle m'|\,\dot{\hat{\rho}}_I(t)\,|m\rangle = (1-\delta_{mm'})\,\langle m'|\,\hat{\rho}_I(t)\,|m\rangle\,R_{m'mm'm} + \delta_{mm'}\sum_{k\neq m}\langle k|\,\hat{\rho}_I(t)\,|k\rangle\,R_{mmkk} \\ + \delta_{mm'}\,\langle m'|\,\hat{\rho}_I(t)\,|m'\rangle\,R_{m'm'm'm'}.\end{aligned} \tag{4.3.43}$$

If we remove the constraint $m \neq m'$ from the first condition, the Redfield coefficients of the first condition can be grouped with the one from the the third condition since $R_{m'mm'm} = R_{m'm'm'm'}$. Furthermore, we can use the condition given in Eq. (4.3.34) to write

$$R_{m'mm'm} = -\sum_{\alpha\neq m'}\lambda^{+}_{m'\alpha\alpha m'} - \sum_{\alpha\neq m}\lambda^{-}_{m\alpha\alpha m} \equiv -\Lambda_{m'm} \tag{4.3.44}$$

and

$$R_{mmkk} = \lambda^{+}_{kmmk} + \lambda^{-}_{kmmk} = 2\mathrm{Re}\lambda^{+}_{kmmk} \equiv \Gamma^{km}. \tag{4.3.45}$$

This allows us to rewrite Eq. (4.3.43) as

$$\langle m'|\,\dot{\hat{\rho}}_I(t)\,|m\rangle = \delta_{mm'}\sum_{k\neq m}\langle k|\,\hat{\rho}_I(t)\,|k\rangle\,\Gamma^{km} - \langle m'|\,\hat{\rho}_I(t)\,|m\rangle\,\Lambda_{m'm}. \tag{4.3.46}$$

When we consider the diagonal terms, *i.e.* $m = m'$, the second term of Eq. (4.3.46) becomes

$$\Lambda_{mm} = \sum_{\alpha\neq m}\left(\lambda^{+}_{m\alpha\alpha m} - \lambda^{-}_{m\alpha\alpha m}\right) = \sum_{\alpha\neq m}\Gamma^{m\alpha} \tag{4.3.47}$$

and we finally can write the so-called *rate equation* for the reduced density matrix operator

$$\langle m|\,\dot{\hat{\rho}}_I(t)\,|m\rangle = \sum_{k\neq m}\left(\,\langle k|\,\hat{\rho}_I(t)\,|k\rangle\,\Gamma^{km} - \langle m|\,\hat{\rho}_I(t)\,|m\rangle\,\Gamma^{mk}\right). \tag{4.3.48}$$

This equation will be extensively applied in the present work in Chapter 7 and Chapter 8. The first term describes the increase in the population of a given state $|m\rangle$, while the second term describes the de-population of that state. For this reason, Eq. (4.3.48) is often called *gain and loss equation*. The coefficients Γ^{km} can be interpreted as *transition rates* from the state $|k\rangle$ to the state $|m\rangle$.

The off-diagonal elements, *i.e.* $m \neq m'$, describe coherence between the states of the system. In this case, the first term of Eq. (4.3.46) vanishes and we have

$$\langle m'|\,\dot{\hat{\rho}}_I(t)\,|m\rangle = -\,\langle m'|\,\hat{\rho}_I(t)\,|m\rangle\,\Lambda_{m'm}. \tag{4.3.49}$$

The real part of the $\Lambda_{m'm}$ can be related to the transition rates, Γ^{km}. By applying the condition given by Eq. (4.3.33) to Eq. (4.3.44) and by using the result of Eq. (4.3.45) we see that

$$\begin{aligned}\mathrm{Re}\left(\Lambda_{m'm}\right) &= \mathrm{Re}\Big(\sum_{\alpha\neq m'}\lambda^{+}_{m'\alpha\alpha m'} + \sum_{\alpha\neq m}\lambda^{-}_{m\alpha\alpha m}\Big) = \\ &= \mathrm{Re}\Big(\sum_{\alpha\neq m'}\lambda^{+}_{m'\alpha\alpha m'} + \sum_{\alpha\neq m}\lambda^{+}_{m\alpha\alpha m}\Big) = \\ &= \frac{1}{2}\Big(\sum_{\alpha\neq m'}\Gamma^{m'\alpha} + \sum_{\alpha\neq m}\Gamma^{m\alpha}\Big). \end{aligned} \tag{4.3.50}$$

The imaginary part is responsible for a small shift in the energies and can be disregarded. Finally, the matrix elements for the reduced density matrix can be written (in the Schrödinger picture where $\hat{\rho}_I(t) = e^{\frac{i}{\hbar}\hat{H}_S}\hat{\rho}(t)e^{\frac{-i}{\hbar}\hat{H}_S}$) as

$$\begin{aligned}\langle m|\,\dot{\hat{\rho}}(t)\,|m\rangle &= \sum_{k\neq m}\Big(\langle k|\,\hat{\rho}(t)\,|k\rangle\,\Gamma^{km} - \langle m|\,\hat{\rho}(t)\,|m\rangle\,\Gamma^{mk}\Big) \text{ for } m = m' \\ \langle m'|\,\dot{\hat{\rho}}(t)\,|m\rangle &= -\frac{i}{\hbar}\langle m'|\left[\hat{H}_S,\hat{\rho}(t)\right]|m\rangle - \frac{1}{2}\Big(\sum_{\alpha\neq m'}\Gamma^{m'\alpha} + \sum_{\alpha\neq m}\Gamma^{m\alpha}\Big)\langle m'|\,\hat{\rho}(t)\,|m\rangle \text{ for } m\neq m'.\end{aligned} \tag{4.3.51}$$

4.3.7 Transition rates

The probability, $\mathcal{P}_f(t)$, to find a quantum system in a final state $|f\rangle$ at a time t, starting from the system in the initial state $|i\rangle$, is given by $|\langle f|i\rangle|^2$. The time derivative of the probability, $\partial_t\mathcal{P}(t)$, is therefore the change in probability per unit of time. This is what we define as transition rate, namely

$$\Gamma^{if} \equiv \partial_t\mathcal{P}(t) = \partial_t|\langle f|i\rangle|^2. \tag{4.3.52}$$

In this Section we derive explicitly the equations for the transition rates defined in Eq. (4.3.45). In order to do that, we need to solve the correlation functions inside the integrals in Eq. (4.3.30) and Eq. (4.3.31). By writing them explicitly, we have

$$\begin{aligned}\langle\hat{r_i}(t'')\hat{r_j}\rangle &= \sum_{\mathcal{R}\mathcal{R}'\mathcal{R}''}\langle\mathcal{R}|\,\hat{r_i}(t'')\,|\mathcal{R}'\rangle\,\langle\mathcal{R}'|\,\hat{r_j}\,|\mathcal{R}''\rangle\,\langle\mathcal{R}''|\,\hat{\chi}_{\mathcal{R}}(0)\,|\mathcal{R}''\rangle = \\ &= \sum_{\mathcal{R}\mathcal{R}'}e^{\frac{i}{\hbar}(E_{\mathcal{R}}-E_{\mathcal{R}'})t''}\,\langle\mathcal{R}|\,\hat{r_i}\,|\mathcal{R}'\rangle\,\langle\mathcal{R}'|\,\hat{r_j}\,|\mathcal{R}\rangle\,\langle\mathcal{R}|\,\hat{\chi}_{\mathcal{R}}(0)\,|\mathcal{R}\rangle\,,\end{aligned} \tag{4.3.53}$$

where we have considered the fact that the density matrix of the reservoir is diagonal, the definition given in Eq. (4.3.18) and $\langle\mathcal{R}|\,\hat{H}_{\mathcal{R}}\,|\mathcal{R}\rangle = E_{\mathcal{R}}$. Similarly, we can write

$$\begin{aligned}\langle\hat{r_j}\hat{r_i}(t'')\rangle &= \sum_{\mathcal{R}\mathcal{R}'\mathcal{R}''}\langle\mathcal{R}|\,\hat{r_j}\,|\mathcal{R}'\rangle\,\langle\mathcal{R}'|\,\hat{r_i}(t'')\,|\mathcal{R}''\rangle\,\langle\mathcal{R}''|\,\hat{\chi}_{\mathcal{R}}(0)\,|\mathcal{R}''\rangle = \\ &= \sum_{\mathcal{R}\mathcal{R}'} e^{\frac{i}{\hbar}(E_{\mathcal{R}'}-E_{\mathcal{R}})t''}\,\langle\mathcal{R}|\,\hat{r_j}\,|\mathcal{R}'\rangle\,\langle\mathcal{R}'|\,\hat{r_i}\,|\mathcal{R}\rangle\,\langle\mathcal{R}|\,\hat{\chi}_{\mathcal{R}}(0)\,|\mathcal{R}\rangle\,. \end{aligned} \tag{4.3.54}$$

We can now rewrite Eq. (4.3.45) as

$$\begin{aligned}\Gamma^{km} &= \lambda^{+}_{kmmk} + \lambda^{-}_{kmmk} = 2\mathrm{Re}\lambda^{+}_{kmmk} = \\ &= \frac{1}{\hbar^2}\sum_{\mathcal{R}\mathcal{R}'}\langle\mathcal{R}|\,\hat{\chi}_{\mathcal{R}}(0)\,|\mathcal{R}\rangle\,\Big(\,\langle k\mathcal{R}|\,\hat{s}\hat{r}\,|m\mathcal{R}'\rangle\,\langle m\mathcal{R}'|\,\hat{s}\hat{r}\,|k\mathcal{R}\rangle\,\Big)\int_{-\infty}^{\infty}dt''e^{\frac{i}{\hbar}(E_{\mathcal{R}'}-E_{\mathcal{R}}+\omega_{mk})t''}, \end{aligned} \tag{4.3.55}$$

where we have made the variable change $t'' \to -t''$ in the second term. We can now use the definition of Dirac delta function given by $\int_{-\infty}^{\infty} dk e^{\pm ik(x-a)} = 2\pi\delta(x-a)$ and finally we obtain

$$\Gamma^{km} = \frac{2\pi}{\hbar}\sum_{\mathcal{R}\mathcal{R}'}\langle\mathcal{R}|\,\hat{\chi}_{\mathcal{R}}(0)\,|\mathcal{R}\rangle\,\Big|\,\langle m\mathcal{R}'|\,\hat{V}\,|k\mathcal{R}\rangle\,\Big|^2\delta(E_f - E_i). \tag{4.3.56}$$

Note that we have defined $E_i \equiv E_{k\mathcal{R}} = E_{\mathcal{R}} + \epsilon_k$ and $E_f \equiv E_{m\mathcal{R}'} = E_{\mathcal{R}'} + \epsilon_m$. This is the well-know *Fermi's Golden* rule for the first order time dependent perturbation theory.

4.4 Master equation II

4.4.1 Equation of motion: AC potentials

We want to study the effect of an oscillating (AC) external potential applied to the system $\mathcal{S}$ through, for instance, a gate voltage. The energy levels of the system will oscillate as $\epsilon_i \to \tilde{\epsilon}_i \cos\,\omega t$. With the AC potential applied, the Hamiltonian given in Eq. (4.3.6) becomes

$$\hat{H}(t) = \hat{H}_{\mathcal{S}}(t) + \hat{H}_{\mathcal{R}} + \hat{V}, \tag{4.4.1}$$

where $\hat{H}_{\mathcal{S}}(t) = \hat{H}_{\mathcal{S}} + \hat{H}_{\mathrm{AC}}(t)$ describes the time dependence of the system $\mathcal{S}$. By applying the unitary transformation

$$\hat{U}(t) = e^{-\frac{1}{\hbar}\int dt'\hat{H}_{\mathrm{AC}}(t')} \tag{4.4.2}$$

to Eq. (4.4.1), the explicit time dependence of $\hat{H}_{\mathcal{S}}(t)$ can be removed

$$\begin{aligned}\hat{\tilde{H}}(t) &= \hat{U}^{\dagger}(t)\left(\hat{H}(t) - i\hbar\partial_t\right)\hat{U}(t) = \\ &= e^{\frac{1}{\hbar}\int dt'\hat{H}_{\mathrm{AC}}(t')}\left(\hat{H}_{\mathcal{S}} + \hat{H}_{\mathrm{AC}}(t) + \hat{H}_{\mathcal{R}} + \hat{V} - i\hbar\partial_t\right)e^{-\frac{1}{\hbar}\int dt'\hat{H}_{\mathrm{AC}}(t')} = \\ &= \hat{H}_{\mathcal{S}} + \hat{H}_{\mathcal{R}} + e^{\frac{1}{\hbar}\int dt'\hat{H}_{\mathrm{AC}}(t')}\hat{V}e^{-\frac{1}{\hbar}\int dt'\hat{H}_{\mathrm{AC}}(t')} = \\ &= \hat{H}_{\mathcal{S}} + \hat{H}_{\mathcal{R}} + \hat{\tilde{V}}(t),\end{aligned} \tag{4.4.3}$$

where we have used the fact that $[\hat{H}_{\mathcal{S}}, \hat{H}_{\mathrm{AC}}(t)] = [\hat{H}_{\mathcal{R}}, \hat{H}_{\mathrm{AC}}(t)] = [\hat{H}_{\mathrm{AC}}(t), \hat{H}_{\mathrm{AC}}(t)] = 0$. By employing the definition of Eq. (4.3.16), the interaction Hamiltonian can be written in the interaction picture as

$$\begin{aligned}\hat{\tilde{V}}_I(t) &= \sum_i \left(e^{\frac{1}{\hbar}\int dt\hat{H}_{\mathrm{AC}}(t)}e^{\frac{1}{\hbar}\hat{H}_{\mathcal{S}}t}\hat{s}_i e^{-\frac{1}{\hbar}\int dt\hat{H}_{\mathrm{AC}}(t)}e^{-\frac{1}{\hbar}\hat{H}_{\mathcal{S}}t}\right)\left(e^{\frac{1}{\hbar}\hat{H}_{\mathcal{R}}t}\hat{r}_i e^{-\frac{1}{\hbar}\hat{H}_{\mathcal{R}}t}\right) = \\ &= \sum_i \left(e^{\frac{1}{\hbar}\int dt\hat{H}_{\mathcal{S}}(t)}\hat{s}_i e^{-\frac{1}{\hbar}\int dt\hat{H}_{\mathcal{S}}(t)}\right)\left(e^{\frac{1}{\hbar}\hat{H}_{\mathcal{R}}t}\hat{r}_i e^{-\frac{1}{\hbar}\hat{H}_{\mathcal{R}}t}\right) = \\ &= \sum_i \hat{s}_i(t)\hat{r}_i(t).\end{aligned} \tag{4.4.4}$$

After considering the same approximations as in Sec. 4.3, namely, the separability, the Born and the Markov approximation, one can insert Eq. (4.4.4) into Eq. (4.3.15) and follow the same procedure. Again, the following set of state vectors $\{|\mathcal{S}\rangle\} = \{..., |m\rangle, ..., |n\rangle, ...\}$ are assumed to be the eigenstates of $\hat{H}_{\mathcal{S}}(t)$. However, the eigenvalues are now given as

$$\begin{aligned}\langle m|\,\hat{s}_i(t)\,|n\rangle &= \langle m|\,e^{\frac{1}{\hbar}\int dt\hat{H}_{\mathcal{S}}(t)}\hat{s}_i e^{-\frac{1}{\hbar}\int dt\hat{H}_{\mathcal{S}}(t)}\,|n\rangle = \\ &= e^{\frac{i}{\hbar}\int dt(\hbar\omega_{mn}+\zeta_{mn}\cos\,\omega t)}\,\langle m|\,\hat{s}_i\,|n\rangle\,,\end{aligned} \tag{4.4.5}$$

where $\langle m|\,\hat{H}_{\mathcal{S}}(t)\,|m\rangle = \epsilon_m + \tilde{\epsilon}_m\cos\,\omega t$, $\hbar\omega_{mn} = \epsilon_m - \epsilon_n$ and $\zeta_{mn} = \tilde{\epsilon}_m - \tilde{\epsilon}_n$. We can then rewrite the matrix elements of the commutators of Eq. (4.3.25) as

$$\begin{aligned}&\langle m'|\left[\hat{s}_i(t), \hat{s}_j(t-t'')\hat{\rho}_I(t)\right]|m\rangle = \langle m'|\left\{\hat{s}_i(t)\hat{s}_j(t-t'')\hat{\rho}_I(t) = -\hat{s}_j(t-t'')\hat{\rho}_I(t)\hat{s}_i(t)\right\}|m\rangle + \\ &= \sum_{kk'}\Big(e^{i(\omega_{m'k}t+\frac{\zeta_{m'k}}{\hbar\omega}\sin\,\omega t)}e^{i[\omega_{kk'}(t-t'')+\frac{\zeta_{kk'}}{\hbar\omega}\sin\,\omega(t-t'')]}\,\langle m'|\,\hat{s}_i\,|k\rangle\,\langle k|\,\hat{s}_j\,|k'\rangle\,\langle k'|\,\hat{\rho}_I(t)\,|m\rangle \\ &- e^{i[\omega_{m'k'}(t-t'')+\frac{\zeta_{m'k'}}{\hbar\omega}\sin\,\omega(t-t'')]}e^{i(\omega_{km}t+\frac{\zeta_{km}}{\hbar\omega}\sin\,\omega t)}\,\langle m'|\,\hat{s}_j\,|k'\rangle\,\langle k'|\,\hat{\rho}_I(t)\,|k\rangle\,\langle k|\,\hat{s}_i\,|m\rangle\Big)\end{aligned} \tag{4.4.6}$$

and

$$\langle m'|\left[\hat{s}_i(t),\hat{\rho}_I(t)\hat{s}_j(t-t'')\right]|m\rangle = \langle m'|\left\{\hat{s}_i(t)\hat{\rho}_I(t)\hat{s}_j(t-t'') = -\hat{\rho}_I(t)\hat{s}_j(t-t'')\hat{s}_i(t)\right\}|m\rangle +$$
$$= \sum_{kk'}\Big(e^{i(\omega_{m'k'}t+\frac{\zeta_{m'k'}}{\hbar\omega}\sin\,\omega t)}e^{i[\omega_{km}(t-t'')=+\frac{\zeta_{km}}{\hbar\omega}\sin\,\omega(t-t'')]}\langle m'|\,\hat{s}_i\,|k'\rangle\langle k'|\,\hat{\rho}_I(t)\,|k\rangle\langle k|\,\hat{s}_j\,|m\rangle +$$
$$- e^{i[\omega_{kk'}(t-t'')+\frac{\zeta_{kk'}}{\hbar\omega}\sin\,\omega(t-t'')]}e^{i(\omega_{k'm}t+\frac{\zeta_{k'm}}{\hbar\omega}\sin\,\omega t)}\langle m'|\,\hat{\rho}_I(t)\,|k\rangle\langle k|\,\hat{s}_j\,|k'\rangle\langle k'|\,\hat{s}_i\,|m\rangle\Big). \tag{4.4.7}$$

By using the identity

$$e^{i\alpha\sin(\omega t)} = \sum_{\nu} J_\nu(\alpha)e^{i\nu\omega t}, \tag{4.4.8}$$

where $J_\nu(\alpha)$ is the ν-th order Bessel function of the first kind and $\alpha = \zeta_{km}/\hbar\omega$, we can define the coefficients

$$\mathcal{A}_{km}(t) = e^{i(\omega_{km}+\alpha\sin\omega t)} = \sum_{\nu} J_\nu(\alpha)e^{i(\omega_{km}+\nu\omega t)}. \tag{4.4.9}$$

Then Eq. (4.4.6) and Eq. (4.4.7) can be rewritten in a more simplified way as

$$\langle m'|\left[\hat{s}_i(t),\hat{s}_j(t-t'')\hat{\rho}_I(t)\right]|m\rangle =$$
$$= \sum_{kk'}\Big(\mathcal{A}_{m'k}(t)\mathcal{A}_{kk'}(t-t'')\langle m'|\,\hat{s}_i\,|k\rangle\langle k|\,\hat{s}_j\,|k'\rangle\langle k'|\,\hat{\rho}_I(t)\,|m\rangle +$$
$$- \mathcal{A}_{m'k'}(t-t'')\mathcal{A}_{km}(t)\langle m'|\,\hat{s}_j\,|k'\rangle\langle k'|\,\hat{\rho}_I(t)\,|k\rangle\langle k|\,\hat{s}_i\,|m\rangle\Big) \tag{4.4.10}$$

and

$$\langle m'|\left[\hat{s}_i(t),\hat{\rho}_I(t)\hat{s}_j(t-t'')\right]|m\rangle =$$
$$= \sum_{kk'}\Big(\mathcal{A}_{m'k'}(t)\mathcal{A}_{km}(t-t'')\langle m'|\,\hat{s}_i\,|k'\rangle\langle k'|\,\hat{\rho}_I(t)\,|k\rangle\langle k|\,\hat{s}_j\,|m\rangle +$$
$$- \mathcal{A}_{kk'}(t-t'')\mathcal{A}_{k'm}(t)\langle m'|\,\hat{\rho}_I(t)\,|k\rangle\langle k|\,\hat{s}_j\,|k'\rangle\langle k'|\,\hat{s}_i\,|m\rangle\Big). \tag{4.4.11}$$

By inserting the results of Eq. (4.4.10) and Eq. (4.4.11) into Eq. (4.3.25), the matrix elements of the density operator are

$$\begin{aligned}
\langle m'|\,\dot{\hat{\rho}}_I(t)\,|m\rangle = -\frac{1}{\hbar^2}\sum_{ijkk'}\langle k'|\,\hat{\rho}_I(t)\,|k\rangle\int_0^\infty dt''\Bigg\{ & \\
\delta_{km}\sum_l\sum_\nu J_\nu\left(\frac{\zeta_{m'l}}{\hbar\omega}\right)\sum_{\nu'}J_{\nu'}\left(\frac{\zeta_{lk'}}{\hbar\omega}\right)\langle m'|\,\hat{s}_i\,|l\rangle\,\langle l|\,\hat{s}_j\,|k'\rangle\,\langle\hat{r}_i(t'')\hat{r}_j\rangle & \\
\times e^{i(\omega_{m'l}+\nu\omega t)}e^{i[\omega_{lk'}+\nu'\omega(t-t'')]} & \\
-\sum_\nu J_\nu\left(\frac{\zeta_{m'k'}}{\hbar\omega}\right)\sum_{\nu'}J_{\nu'}\left(\frac{\zeta_{km}}{\hbar\omega}\right)\langle m'|\,\hat{s}_j\,|k'\rangle\,\langle k|\,\hat{s}_i\,|m\rangle\,\langle\hat{r}_i(t'')\hat{r}_j\rangle & \\
\times e^{i[\omega_{m'k'}+\nu\omega(t-t'')]}e^{i(\omega_{km}+\nu'\omega t)} & \\
-\sum_\nu J_\nu\left(\frac{\zeta_{m'k'}}{\hbar\omega}\right)\sum_{\nu'}J_{\nu'}\left(\frac{\zeta_{km}}{\hbar\omega}\right)\langle m'|\,\hat{s}_i\,|k'\rangle\,\langle k|\,\hat{s}_j\,|m\rangle\,\langle\hat{r}_j\hat{r}_i(t'')\rangle & \\
\times e^{i(\omega_{m'k'}+\nu\omega t)}e^{i[\omega_{km}+\nu'\omega(t-t'')]} & \\
+\delta_{m'k'}\sum_l\sum_\nu J_\nu\left(\frac{\zeta_{kl}}{\hbar\omega}\right)\sum_{\nu'}J_{\nu'}\left(\frac{\zeta_{lm}}{\hbar\omega}\right)\langle k|\,\hat{s}_j\,|l\rangle\,\langle l|\,\hat{s}_i\,|m\rangle\,\langle\hat{r}_j\hat{r}_i(t'')\rangle & \\
\times e^{i[\omega_{kl}+\nu\omega(t-t'')]}e^{i(\omega_{lm}+\nu'\omega t)}\Bigg\}. & \qquad (4.4.12)
\end{aligned}$$

As we did for Eq. (4.3.30) and Eq. (4.3.31), we can define, for simplicity, that

$$\lambda^+_{mkln,\nu\nu'} = \frac{1}{\hbar^2}\sum_{ij}J_\nu\left(\frac{\zeta_{mk}}{\hbar\omega}\right)J_{\nu'}\left(\frac{\zeta_{ln}}{\hbar\omega}\right)\langle m|\,\hat{s}_i\,|k\rangle\,\langle l|\,\hat{s}_j\,|n\rangle\int_0^\infty dt''e^{-i(\omega_{ln}+\nu'\omega)t''}\langle\hat{r}_i(t'')\hat{r}_j\rangle \qquad (4.4.13)$$

and

$$\lambda^-_{mkln,\nu\nu'} = \frac{1}{\hbar^2}\sum_{ij}J_{\nu'}\left(\frac{\zeta_{mk}}{\hbar\omega}\right)J_\nu\left(\frac{\zeta_{ln}}{\hbar\omega}\right)\langle m|\,\hat{s}_j\,|k\rangle\,\langle l|\,\hat{s}_i\,|n\rangle\int_0^\infty dt''e^{-i(\omega_{mk}+\nu\omega)t''}\langle\hat{r}_j\hat{r}_i(t'')\rangle, \qquad (4.4.14)$$

and we can now write the Redfield relaxation coefficients with the presence of an AC potential as

$$R_{m'mk'k,\nu\nu'} = -\delta_{mk}\sum_l\lambda^+_{m'llk'} + \lambda^+_{m'k'km} + \lambda^-_{m'k'km} - \delta_{m'k'}\sum_l\lambda^-_{kllm}. \qquad (4.4.15)$$

The matrix elements of the reduced density operator are given by

$$\langle m'|\,\dot{\hat{\rho}}_I(t)\,|m\rangle = \sum_{kk'\nu\nu'}\langle k'|\,\hat{\rho}_I(t)\,|k\rangle\,R_{m'mk'k,\nu\nu'}e^{i[\omega_{m'k'}+\omega_{km}+(\nu+\nu')\omega]t}. \qquad (4.4.16)$$

When the frequency of the AC potential does not match the energy difference between every two states of the sub-system $\mathcal{S}$ participating in the transition, only the secular terms can be kept by considering $\nu' = -\nu$, *i.e.* the same reasoning applied from Eq. (4.3.36)

to Eq. (4.3.43). Similarly to Eq. (4.3.44) and Eq. (4.3.45), we can define the following quantities

$$\Lambda_{m'm} = -\sum_{\nu} R_{m'mm'm,\nu-\nu} \tag{4.4.17}$$

and

$$\Gamma^{km} = \sum_{\nu} R_{mmkk,\nu-\nu} = 2\mathrm{Re}\sum_{\nu} \lambda^{+}_{kmmk,\nu-\nu}. \tag{4.4.18}$$

Finally, after following the steps from Eq. (4.3.46) to Eq. (4.3.51), we obtain (after going back to the Schöedinger picture) an equation of motion formally identical to the case without AC potential [see Eq. (4.3.51)].

4.4.2 Transition rates: AC potentials

In order to derive the transition rates for the case with of an AC potential, we need first to calculate the correlation functions inside the integrals of the coefficients defined in Eq. (4.4.13) and Eq. (4.4.14). In fact, they were already calculated in Eq. (4.3.53) and Eq. (4.3.54). By inserting these results into Eq. (4.4.18), we have

$$\begin{aligned}\Gamma^{km} &= \sum_{\nu} \lambda^{+}_{kmmk,\nu-\nu} + \sum_{\nu} \lambda^{-}_{kmmk,\nu-\nu} = 2\mathrm{Re}\sum_{\nu} \lambda^{+}_{kmmk,\nu-\nu} = \\ &= \frac{1}{\hbar^2}\sum_{\nu\mathcal{R}\mathcal{R}'} \langle\mathcal{R}|\,\hat{\chi}_{\mathcal{R}}(0)\,|\mathcal{R}\rangle \left(\langle k\mathcal{R}|\,\hat{s}\hat{r}\,|m\mathcal{R}'\rangle\,\langle m\mathcal{R}'|\,\hat{s}\hat{r}\,|k\mathcal{R}\rangle\right) \int_{-\infty}^{\infty} dt'' e^{\frac{i}{\hbar}(E_{\mathcal{R}'}-E_{\mathcal{R}}+\hbar\omega_{mk}-\hbar\nu\omega)t''},\end{aligned} \tag{4.4.19}$$

where we have used the property of the Bessel functions $J_{-\nu}(\alpha) = (-1)^{\nu} J_{\nu}(\alpha)$ and made the variable change $t'' \to -t''$ in the integration limits of the second term. We can now use the definition of Dirac delta function and finally write

$$\Gamma^{km} = \frac{2\pi}{\hbar}\sum_{\nu\mathcal{R}\mathcal{R}'} J_{\nu}^{2}\left(\frac{\zeta_{mk}}{\hbar\omega}\right) \langle\mathcal{R}|\,\hat{\chi}_{\mathcal{R}}(0)\,|\mathcal{R}\rangle \left|\,\langle m\mathcal{R}'|\,\hat{V}\,|k\mathcal{R}\rangle\,\right|^{2} \delta(E_f - E_i), \tag{4.4.20}$$

where $E_i \equiv E_{k\mathcal{R}} = E_{\mathcal{R}} + \epsilon_k + \nu\hbar\omega$ and $E_f \equiv E_{m\mathcal{R}'} = E_{\mathcal{R}'} + \epsilon_m$. Moreover, ν is the number of photons. This is again the Fermi's Golden rule for the first order time dependent perturbation theory in the presence of an AC potential acting on the quantum sub-system $\mathcal{S}$.

4.5 $\mathcal{T}$-matrix expansion and the generalized Fermi's golden rule

The $\mathcal{T}$-matrix approach [122] and its leading-order approximation, namely, the Fermi's golden rule [108, 116, 115, 118, 123, 124] are used by several groups to describe tunneling

processes, since they provide a simpler way to treat the problem. Bruus and Flensberg employ this technique in relation to the tunneling problem. The derivation starts by writing the Hamiltonian of the system as

$$\hat{H} = \underbrace{\hat{H}_{\mathcal{S}} + \hat{H}_{\mathcal{R}}}_{\hat{H}_0} + \underbrace{\hat{V} e^{\eta t}}_{\hat{V}(t)}, \tag{4.5.1}$$

where η is small and positive, so that the interaction between the quantum system and the electrodes is switched on very slowly. The basic idea of the $\mathcal{T}$-matrix approach is to apply many-body scattering theory where one calculates the time evolution of the occupation probabilities of a state of the system from the transition amplitudes.

Considering an initial state $|i\rangle$, its time evolution is given by Eq. (4.1.5) or in the interaction picture by

$$|i(t)\rangle = e^{-\frac{i}{\hbar}\hat{H}_0 t} \hat{U}_I(t, t_0) e^{\frac{i}{\hbar}\hat{H}_0 t_0} |i\rangle\,, \tag{4.5.2}$$

where the time-evolution operator is given by Eq. (4.2.4). The transition amplitudes between the initial and a final state, $|f\rangle$, is given by

$$\begin{aligned}\langle f|i(t)\rangle &= \left\langle f \left| e^{-\frac{i}{\hbar}\hat{H}_0 t} \left(\mathbb{I} + \frac{1}{i\hbar}\int_{t_0}^{t} dt_1 \hat{V}_I(t_1) - \frac{1}{\hbar^2}\int_{t_0}^{t} dt_1 \hat{V}_I(t_1) \int_{t_0}^{t_1} dt_2 \hat{V}_I(t_2) + \ldots \right) e^{\frac{i}{\hbar}\hat{H}_0 t_0} \right| i \right\rangle = \\ &= \left\langle f \left| e^{-\frac{i}{\hbar}\hat{H}_0 t} \left(\frac{1}{i\hbar}\int_{t_0}^{t} dt_1 \hat{V}_I(t_1) - \frac{1}{\hbar^2}\int_{t_0}^{t} dt_1 \hat{V}_I(t_1) \int_{t_0}^{t_1} dt_2 \hat{V}_I(t_2) + \ldots \right) e^{\frac{i}{\hbar}\hat{H}_0 t_0} \right| i \right\rangle,\end{aligned} \tag{4.5.3}$$

where the zeroth-order term vanishes since the two states are orthogonal before the interaction starts. It is then assumed that at time t_0, when the interaction is switched on, the state of the total system can be written as a product of the sub-systems $|i(t_0)\rangle = |m\rangle\,|k\rangle$, *i.e.* as the product of the quantum system state $|m\rangle$ and the leads state $|k\rangle$. This means that, the system is in an eigenstate of $\hat{H}_0$ at time t_0 with initial total energy E_i. In order to make sure that the "turning on" time given by $1/\eta$ is well separated from the duration $t - t_0$ of the interaction, *i.e.* $t - t_0 \gg 1/\eta$, we take $t_0 \to -\infty$ (stationary state limit),

$$\langle f|i(t)\rangle = \left| \sum_{n=1}^{\infty} \frac{1}{i^n} \left\langle f \left| \int_{-\infty}^{t} dt_1 \int_{-\infty}^{t_1} dt_2 \ldots \int_{-\infty}^{t_{n-1}} dt_n \hat{V}_I(t_1)\hat{V}_I(t_2)\ldots\hat{V}_I(t_n) e^{\eta t_n} \right| i \right\rangle \right|. \tag{4.5.4}$$

By inserting $\hat{V}_{\mathrm{I}}(t) = e^{\frac{i}{\hbar}\hat{H}_0}\hat{V}(t)e^{-\frac{i}{\hbar}\hat{H}_0}$ into Eq. (4.5.4) we finally obtain, after performing the integrations,

$$\langle f|i(t)\rangle = \left| \sum_{n=1}^{\infty} \langle f|\mathcal{T}|i\rangle \frac{e^{\eta t}}{E_i - E_f + i\eta} \right|, \tag{4.5.5}$$

where E_i and E_f are the initial and final total energies and

$$\mathcal{T}(E) = \hat{V} + \hat{V}\frac{1}{E_i - \hat{H}_0 + i\eta}\hat{V} + \hat{V}\frac{1}{E_i - \hat{H}_0 + i\eta}\hat{V}\frac{1}{E_i - \hat{H}_0 + i\eta}\hat{V} + ... \tag{4.5.6}$$

is the definition of the so-called $\mathcal{T}$-matrix. By taking the time-derivative of $|\langle f|i(t)\rangle|^2$ as given in Eq. (4.3.52) one write

$$\Gamma_{if} = \frac{2\pi}{\hbar}|\langle f|\mathcal{T}|i\rangle|^2\delta(E_f - E_i), \tag{4.5.7}$$

which is the *generalized Fermi's golden rule.*

4.5.1 Connection between the WBR master equation and the $\mathcal{T}$-matrix

For many problems, it is assumed that the off-diagonal components of the reduced density matrix operator rapidly decay and, therefore, they can be neglected. Thus, only the diagonal terms of Eq. (4.3.51) are calculated. For example, if two states $|m\rangle$ and $|n\rangle$ differ in an observable that strongly couples to the environment, the superpositions between these states will rapidly decay due to the interaction. This is important because in the derivation of the $\mathcal{T}$-matrix, there is no information about coherences, whereas in the derivation of the WBR-ME, this is naturally included in Eq. (4.3.51). If we consider that the initial state $|i\rangle$ and final state $|f\rangle$ can be written as products of the many-body states of the molecule $|k\rangle$ and of the leads $|\mathcal{R}\rangle$, summing over the leads states leads to the transition rates with the exact form of Eq. (4.3.56)

$$\Gamma^{km} = \frac{2\pi}{\hbar}\sum_{\mathcal{R}\mathcal{R}'}\langle\mathcal{R}|\,\hat{\chi}_{\mathcal{R}}(0)\,|\mathcal{R}\rangle\,\Big|\,\langle m\mathcal{R}'|\,\mathcal{T}\,|k\mathcal{R}\rangle\,\Big|^2\delta(E_f - E_i), \tag{4.5.8}$$

where the perturbation $\hat{V}$ is replaced by the $\mathcal{T}$-matrix. In the same way as done in the derivation of the WBR-ME, it is considered here that the probability to find the leads in the initial state, $\langle\mathcal{R}|\,\hat{\chi}_{\mathcal{R}}(0)\,|\mathcal{R}\rangle$, at time $t_0 \to -\infty$ to be independent of state of $\mathcal{S}$.

Eq. (4.5.8) is the rate of change of the probability of the state $|m\rangle$ under the condition that $\mathcal{S}$ was in state $|k\rangle$ at time $t_0 \to -\infty$. In other words, within the $\mathcal{T}$-matrix approach we are considering the stationary state limit. However, within the density matrix approach, [derivation of Eq. (4.3.56)], one calculates the rate of change of the probability of the state $|m\rangle$ under the condition that $\mathcal{S}$ is in a state $|k\rangle$ at the same time t, immediately before a possible transition. This means that, the $\mathcal{T}$-matrix approach considers the stationary occupations of the states, whereas in the WBR-ME this is done at a particular time, but it is yet local in time. Moreover, the Markov approximation is also implicitly included in the $\mathcal{T}$-matrix approach because the occupations do not change between the times t_0 and

t.

To leading order terms, $\mathcal{T} \equiv \hat{V}$, the two transition rates given by Eq. (4.3.56) and Eq. (4.5.8) are identical, since the latter reduces to the Fermi's golden rule. However, to higher order processes the two equations describe different quantities [108, 123]. In particular, the $\mathcal{T}$-matrix approach misses higher order contributions when compared to the WBR-ME and these terms are responsible for canceling out the divergent terms in Eq. (4.5.8) [108, 123]. The divergent terms appear already when considering fourth-order in the tunneling Hamiltonian due to the second-order poles from the energy denominators. Therefore, Eq. (4.5.8) can not be directly evaluated. This is because within a purely perturbative approach, the energy of the virtual states are considered to be well defined, *i.e.* with infinite lifetime [121]. In order to circumvent this problem, a regularization scheme has been developed by Koch *et al.* [116, 115, 114, 120, 121], and in Appendix C.4 we show in detail how to obtain the regularized transition rates that we will use in Chapter 7 and Chapter 8 in order to describe cotunneling processes.

Chapter 5

Organic/Inorganic Interfaces

5.1 The energy level alignment problem

5.1.1 DFT-LDA and energy level alignment

In general, conventional electronic structure theory struggles when predicting the levels alignment at a metal/molecule interface, since only rarely non-local correlation effects are explicitly included. This is for instance the case of DFT , as discussed in Sec. 2.5.1, Sec. 2.5.2 and Sec. 2.5.3. Moreover, in static DFT the standard approximations to the exchange and correlation functional, including the LDA [72], hybrid functionals [74, 75] or explicitly SIC ones [85, 125], do not include or they do but just poorly, non-local correlation effects. This means that, although even when some of the functionals can predict with satisfactory accuracy the energy levels of the molecule in the gas phase, they all fail in describing properly the level renormalization as the molecule approaches the surface. For instance in the LDA there is no change in the HOMO-LUMO gap as a molecule gets closer to a metallic surface [126].

A conceptually straightforward way to include such non-local correlation effects in the description is that of using many-body perturbation theory, namely the GW approximation constructed on top of DFT [127, 128, 129]. This approach has been used in the last few years for predicting levels alignment [126, 130, 131, 132, 133, 134], in general with a good success. The drawback of the GW scheme stays with its computational overheads, which limit the system size that can be tackled. This is particularly critical for the problem at hand since the typical simulation cells for a molecule on a surface are in general rather large. Furthermore, as the image charge may spread well beyond the size of the molecule investigated, one may even require cells significantly larger than those needed to physically contain the molecule.

Alternatives to the GW approach, which to some degree also go beyond taking the simple DFT Kohn-Sham spectrum, include scissor operators (the DFT+Σ approach) [135, 136, 137, 138, 139, 140], where the HOMO and LUMO eigenvalues are shifted to match

values obtained either from experimental data or from separate total energy difference calculations (ΔSCF) plus classical image charge models, and modified ΔSCF schemes [141, 142].

5.1.2 Charge-transfer energies: CDFT method

Using the CDFT approach presented in Sec. 2.6 we can evaluate the charge transfer energy between the molecules and the metal surface, and hence the position of the frontier energy levels with respect to the E_F of the metal. For a given substrate size and perpendicular distance, d, between the molecule and the surface atoms, first a standard DFT calculation without constraints is performed. This determines the total ground state energy of the combined molecule+substrate system, $E(\text{mol/sub}; d)$, and the amount of charge present on each fragment, one fragment being the molecule and the other the substrate. The molecule is only weakly coupled to the substrate, so that the amount of charge on each fragment is a well defined quantity. Although CDFT is designed for arbitrary geometries and constraints, in the case of overlapping fragments the amount of charge localized on each fragment becomes ill defined and the results have to be taken with care [91]. The next step consists in performing a new DFT calculation, where the constraint is set in such a way that one electron is removed from the molecule and one electron is added to the substrate. The total energy of such charge transfer state is $E(\text{mol}^+/\text{sub}^-; d)$. Hence the charge transfer energy needed to transfer one electron from the molecule to the substrate, E^+_{CT}, is given by

$$E^+_{\text{CT}}(d) = E(\text{mol}^+/\text{sub}^-; d) - E(\text{mol/sub}; d)\,. \tag{5.1.1}$$

In an analogous way we obtain the charge transfer energy gained by moving one electron from the surface to the molecule, E^-_{CT}, as

$$E^-_{\text{CT}}(d) = E(\text{mol/sub}; d) - E(\text{mol}^-/\text{sub}^+; d)\,, \tag{5.1.2}$$

where $E(\text{mol}^-/\text{sub}^+; d)$ is the CDFT ground state energy of the configuration where one electron is moved from the metal surface to the molecule. Note that such procedure always deals with globally charge neutral simulation cells, so that no monopole energy corrections are necessary under periodic boundary conditions. Moreover, for practical calculations the charge-transfer approach can be expected to be more accurate than a calculation using non-neutral cells, where the metal is kept neutral but the molecule is charged. For such non-neutral calculations the image charge is formed on the metal surface in an analogous way to the charge-transfer setup. However, in order for the metal cluster to be charge neutral a charge with opposite sign will also form on the surface of the metallic cluster. Given the finite size of the cluster this will lead to additional inaccuracies due to

the interaction between the image charge and such spuriously-confined additional surface charge.

Within the charge transfer procedure we can directly determine the energy level alignment at the interface, since -E^{+}_{CT} (-E^{-}_{CT}) corresponds to the energy of the HOMO (LUMO) with respect to the substrate E_{F}. In a similar constrained-DFT approach [142] Sau and co-workers calculated the charging energy associated to transferring small amounts of charge from the substrate to a specific molecular orbital. The charge transfer energy was then obtained by extrapolation to integer charge. In order to avoid the use of such extrapolation here we always transfer an entire electron between the molecule and the substrate. Since a CDFT calculation has a computational cost only marginally more expensive than that of a standard DFT ground-state one (the CPU time increases by about a factor two over the entire self-consistent cycle), CDFT allows us the study of large organic molecules on surfaces. This is a prohibitive task for many-body-corrected quasi-particle schemes, such as the GW method.

5.1.3 Case of study: benzene/Li interface

We apply this approach to a benzene/Li interface, as shown in Fig. 5.1, for which we can compare with results from the literature. In our calculations we consider d ranging from 4 Å to 14 Å. We apply the CDFT method to compute the energy level alignment of a benzene molecule as a function of its distance, d, from a Li(100) surface. The calculations are performed using norm-conserving relativistic pseudopotentials [143], and the LDA [72] for the exchange-correlation potential. The real space grid is set by an equivalent mesh-cutoff of 300 Ry and the charge density and all the operators are expanded over a double-ζ polarized basis set with an energy-shift of 0.03 eV [96]. The Li metallic surface is modeled by a 6 atomic layer thick slab. The *bcc* primitive unit cell lattice constant is set to 3.51 Å. We consider two types of boundary conditions in the plane of the Li substrate surface, namely periodic boundary conditions (PBC) and non-periodic boundary conditions (non-PBC). Furthermore, in order to investigate the finite size effects originating from the size of the Li surface, we consider three different cell sizes (for both PBC and non-PBC), namely small (3×3 atoms per layer), intermediate (6×6) and large (12×12) (see Fig. 5.1). In the case of non-PBC the real-space box containing the Li slab supercell has dimensions 55×55×55 Å^3. This is chosen in such a way that even for the 12×12 slab there is at least 15 Å of vacuum between the Li slab and the boundaries of the simulation box. By using a cubic box one can apply Madelung corrections in SIESTA, *i.e.* by adding a compensating background charge in order to avoid the divergence of the electrostatic potential. These are necessary since the electrostatic potential is calculated by using periodic boundary conditions [144]. In the case of PBC the in-plane dimensions are set by the Li supercell size and thus are 10.56×10.56 Å^2, 21.09×21.09 Å^2 and 42.12×42.12 Å^2, respectively for

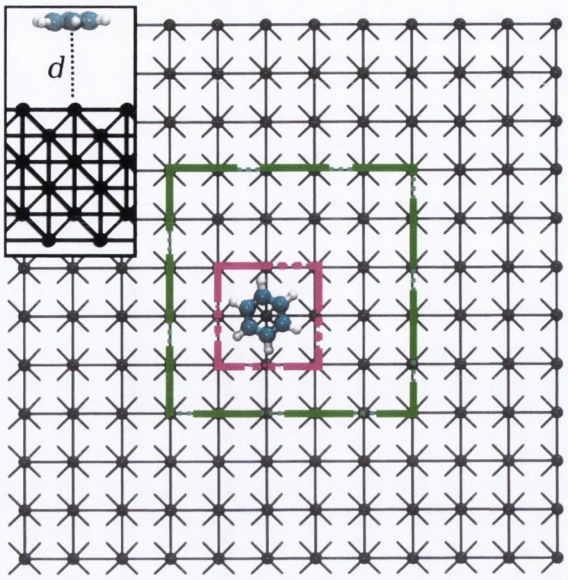

Figure 5.1: Top-view ball-stick representation of a benzene molecule at a Li(001) surface for a Li(001) 12×12 supercell. The dashed rectangles show the 3×3 (purple) and 6×6 (green) supercells. The inset in panel is the side view of the benzene lying flat at a distance d from the surface.

the 3×3, 6×6 and 12×12 cell. The cell dimension in the direction perpendicular to the surface plane is the same as for the case of non-PBC, namely 55 Å.

We use two different boundary conditions for the Li surface in order to investigate the effects arising from the spurious dipole-dipole interaction between image supercells. The size of this spurious interactions can be reduced by increasing the size of the unit cell. For the PBC setup the dimensions in the plane are set by the Li cluster size, while for non-PBC calculations we use a large simulation cell which minimizes the dipole-dipole interaction between periodic images. In this way we can disentangle the effects of changing the extension of the Li surface in plane from those associated with the size of the simulation box. Furthermore, in the case of non-PBC, edge effects may arise and our aim is to find the required cluster and cell size that gives quantitatively accurate charge transfer energies.

In order to determine the energy level alignment between the molecule and the surface, we first need to determine the Li workfunction (W_{F}). This is calculated by performing a simulation for the Li slab with PBC and no benzene adsorbed and by taking the difference between the vacuum potential and the slab E_{F}. The so obtained value for the Li(001) W_{F} is 2.91 eV. This is in fair agreement with previous calculations (3.03 eV) [145], which have also shown that the Li W_{F} can vary by about 0.5 eV depending on the crystallographic orientation of the surface. The experimental values reported for polycrystalline Li vary considerably (2.3-3.1 eV), as discussed in Ref. [146] and references therein.

In the case of non-PBC the Li substrate is essentially a giant molecule and we can calculate the I^{P} and the E^{A} by means of the ΔSCF method, where $I^{\mathrm{P}} = E^{(N-1)} - E^{(N)}$

Table 5.1: Ionization potential (I^{P}), electron affinity (E^{A}) and quasi particle gap ($E_{\mathrm{QP}}^{\mathrm{gap}}$), in eV, for the three Li substrates considered and for the benzene molecule in the gas phase compared with experimental data and GW calculations.

	Li substrates					
	3×3	6×6	12×12	benzene gas phase		
	ΔSCF			ΔSCF	*GW*	Exp.
I^{P}	3.46	3.44	3.55	9.56	9.23[a]/9.05[f]/7.9[e]	9.24[c]
E^{A}	1.57	2.18	2.63	-1.45	-0.80[a]/-1.51[f]/-2.7[e]	-1.14[d]
$E_{\mathrm{QP}}^{\mathrm{gap}}$	1.89	1.26	0.92	11.01	10.51[b]/10.55[f]/10.6[e]	10.38

[a]Ref. [150]; [b]Ref. [126]; [c]Ref. [147]; [d]Ref. [148]; [e]Ref. [131]; [f]Ref. [151]

and $E^{\mathrm{A}} = E^{(N)} - E^{(N+1)}$ (N is the number of electrons in the neutral system). The results are listed in Tab. 5.1 for the different Li cluster sizes. We note that there is a substantial difference between I^{P} and the E^{A}, resulting in a quasi-particle energy gap of the order of 1 eV for the Li clusters. Such a gap arises because of the charge confinement in the finite cluster. In this case electron-electron repulsion energy leads to a decrease of the E^{A} and an increase of the I^{P} as compared to the W_{F} calculated with PBC. If instead of adding a full electron we add/remove a small fractional charge (0.1 of an electron), electron-electron repulsion energy becomes negligible, the gap disappears, and we obtain I^{P}=3.1 eV and E^{A}=3.0 eV. Likewise, the gap is reduced for larger clusters, in which the electron density of the additional electron/hole can delocalize more. Before investigating the combined molecule/Li system we calculate also the I^{P} and the E^{A} for the isolated benzene molecule, and our results are shown in Tab. 5.1. We find the energy gap for the molecule in the gas phase, $E_{\mathrm{QP}}^{\mathrm{gap}} = I^{\mathrm{P}} - E^{\mathrm{A}}$, to be in good agreement with experiments [147, 148], with other works using the ΔSCF [149] approach and with GW calculations [126, 150].

The benzene/Li interface [see Fig. 5.1] consists of a benzene molecule, in its gas phase geometry, positioned parallel to the Li surface at a distance d. We now evaluate the dependence of the various charge transfer energies (positions of the HOMO and LUMO) on d for all the different Li supercells as well as for both non-PBC and PBC.

Supercell size dependence

We start by investigating how the charge transfer energies depend on the size of the supercell, therefore, for calculations performed with non-PBC. In Fig. 5.2(a) we plot $-E_{\mathrm{CT}}^{+}$ and $-E_{\mathrm{CT}}^{-}$ as a function of d for all the three Li clusters considered. As expected, due to the electron-hole attraction, the absolute value of the charge transfer energy decreases as d gets smaller. This in itself shows that CDFT can capture non-local Coulomb contributions to the energy. While for small d the energies of the three different clusters are approximately

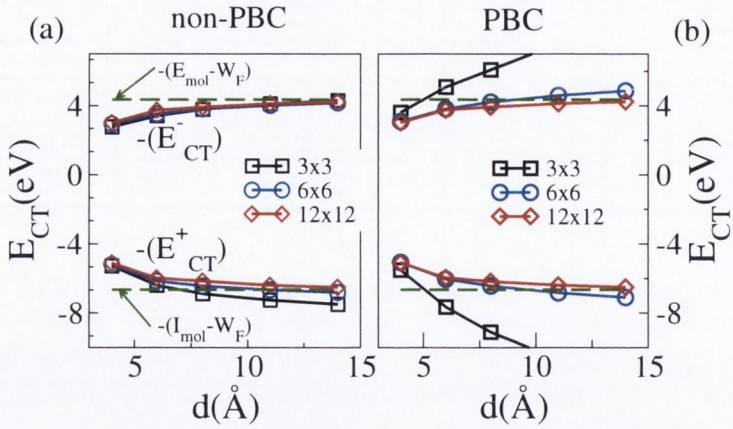

Figure 5.2: Negative of the charge transfer energy, E^{-}_{CT}, and removal energy, E^{+}_{CT}, as a function of the molecule-surface distance, d, for the three clusters considered. Panels (a) and (b) are for non-PBC and PBC calculations, respectively. The green dashed-lines represent the negative of the I^{P} and E^{A} of the isolated molecule (ΔSCF calculations) shifted by the calculated Li W_{F} of 2.91 eV.

equal to each other, for large distances they differ significantly. In order to determine the origin of such deviations we evaluate the same energies in the limit of very large distances ($d \to \infty$), where they become

$$E^{+}_{\mathrm{CT}}(\infty) = I^{\mathrm{P}}_{\mathrm{mol}} - E^{\mathrm{A}}_{\mathrm{Li}} \tag{5.1.3}$$

and

$$E^{-}_{\mathrm{CT}}(\infty) = E^{\mathrm{A}}_{\mathrm{mol}} - I^{\mathrm{P}}_{\mathrm{Li}}\,, \tag{5.1.4}$$

since the interaction energy between the charge on the Li slab and that on the molecule vanishes for $d \to \infty$. The charge transfer energy gap is then given by

$$\begin{aligned} E^{\mathrm{gap}}_{\mathrm{CT}}(\infty) &= E^{+}_{\mathrm{CT}}(\infty) - E^{-}_{\mathrm{CT}}(\infty) = \\ &= I^{\mathrm{P}}_{\mathrm{mol}} - E^{\mathrm{A}}_{\mathrm{mol}} + (I^{\mathrm{P}}_{\mathrm{Li}} - E^{\mathrm{A}}_{\mathrm{Li}})\,. \end{aligned} \tag{5.1.6}$$

While $I^{\mathrm{P}}_{\mathrm{mol}}$ and $E^{\mathrm{A}}_{\mathrm{mol}}$ are independent of the cluster size, this is not the case for $I^{\mathrm{P}}_{\mathrm{Li}}$ and $E^{\mathrm{A}}_{\mathrm{Li}}$ (see Table 5.1). This reflects in the fact that the charge transfer energies at large molecule-surface separation varies with the cluster size (see Table 5.2).

At large distances the variation of E^{+}_{CT} with the Li cluster sizes is mainly caused by significant changes in $E^{\mathrm{A}}_{\mathrm{Li}}$. Interestingly this is not the case for E^{-}_{CT}, since $I^{\mathrm{P}}_{\mathrm{Li}}$ is approximately the same for all the Li clusters considered. As d gets smaller the extension of the image charge on the Li slab is reduced, so that even small clusters are large enough to contain most of the image charge. Therefore the energy differences depend less on the cluster size. For d up to about 6 Å, Fig. 5.2(a) shows that E^{+}_{CT} and E^{-}_{CT} are converged even for the small 3×3 supercell. Since in organic-based devices the first molecular layer deposited on top of the metallic substrate is typically rather close to the surface, we

Table 5.2: Charge transfer energies (in eV) in the limit of large distances ($d \to \infty$) for the three molecule/Li cluster cells investigated. Values are obtained by evaluating Eqs. (5.1.3-5.1.6) with the I^{P}'s and the E^{A}'s taken from Tab. 5.1.

	Li substrates		
	3×3	6×6	12×12
$E^{+}_{\mathrm{CT}}(\infty)$	7.99	7.38	6.93
$E^{-}_{\mathrm{CT}}(\infty)$	4.91	4.89	5.0
$E^{\mathrm{gap}}_{\mathrm{CT}}(\infty)$	12.9	12.27	11.93

expect that in these situations a rather small cluster size will be already sufficient for our CDFT scheme to yield accurately converged levels alignment. This means that the CDFT approach is a valuable tool for an accurate evaluation of the electronic structure of molecules on surfaces in realistic conditions. Finally, when one looks at larger d, it is immediately clear that larger cluster sizes must be considered. The green dashed lines in Fig. 5.2 correspond to the infinite cluster size limit, for which we have $I^{\mathrm{P}}_{\mathrm{Li}} = E^{\mathrm{A}}_{\mathrm{Li}} = W_{\mathrm{F}} \approx 2.9$ eV. It can then be seen that even up to the largest considered d of 14 Å results obtained for the 12×12 cluster are within the infinite cluster limit (set in the figure by the two green dashed lines), so that they can be considered converged.

Substrate size dependence

We now move to the case of PBC, in which there are no edge effects due to the finite size of the cell. Results for the charge transfer energies are presented in Fig. 5.2(b). Although the general trends are analogous to the ones found for the case of non-PBC, we note that for the 3×3 supercell the changes in the charge transfer energy as a function of d are largely overestimated. This is due to the use of PBC, in which the lateral dimensions of the supercell box coincide to those of the Li slab (*i.e.*, there is no vacuum). Because of the PBC one effectively simulates a layer of charged molecules and not a single molecule on the surface. Thus, when the molecules are closely spaced, the charge transfer energy is that of two opposite charged surfaces facing each other (the molecular layer and the Li slab). This is significantly larger than that of a single molecule (note that we always compare the charge transfer energy per cell, *i.e.*, per molecule). When one increases the size of the supercell and arrives to 12×12, both PBC and non-PBC calculations produce the same results. This confirms the observation that the 12×12 supercell is large enough to contain a substantial part of the image charge as well as to minimize the Coulomb interaction between repeated supercell images up to $d = 14$ Å.

From the charge transfer energies we can now obtain an approximate value of the energies of the HOMO and LUMO orbitals, by offsetting them with the metal W_{F}, so that $E_{\mathrm{HOMO}} \simeq -(E^{+}_{\mathrm{CT}} + W_{\mathrm{F}})$ and $E_{\mathrm{LUMO}} \simeq -(E^{-}_{\mathrm{CT}} + W_{\mathrm{F}})$. Note that if the metal substrate is semi-infinite in size, then these relations become exact, since by definition the

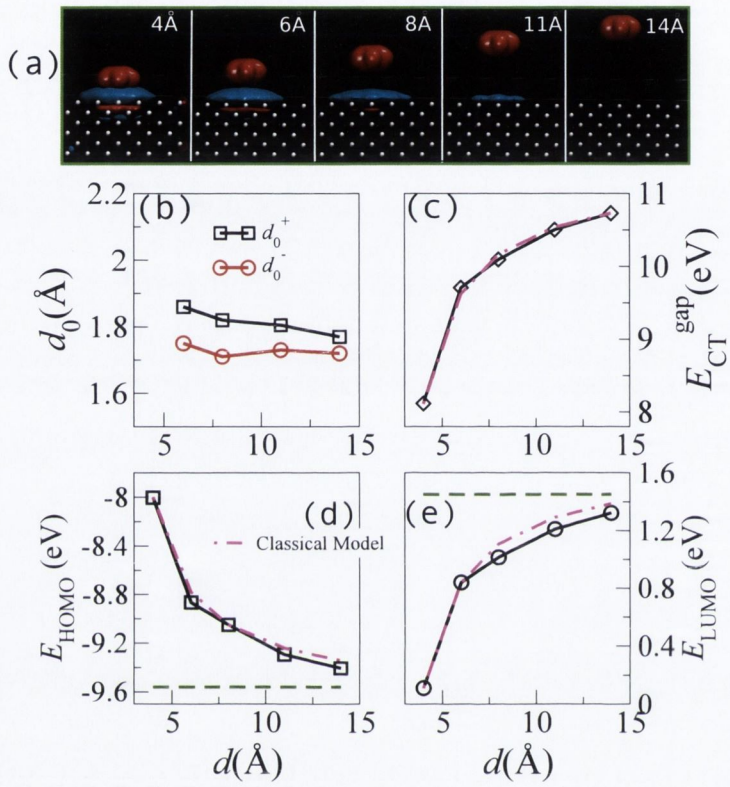

Figure 5.3: Image charge analysis. (a) Isosurface of the difference between the charge densities calculated with DFT (ground state) and CDFT (charge transfer state), $\Delta\rho(\mathbf{r})$. Note the formation and the spatial distribution of the image charge. Different panels correspond to different molecule/surface distances, d. The isosurfaces are taken at 10^{-4}e/Å^3. Red isosurfaces denote negative $\Delta\rho(\mathbf{r})$ (electrons depletion), while blue are for positive $\Delta\rho(\mathbf{r})$ (electrons excess). (b) position of the charge image plane taken from the surface atoms [see Eq. (5.1.9)] , respectively when one electron, d_0^+, or one hole, d_0^-, is transferred from the molecule to the Li substrate for the 12×12 PBC calculations as a function of d. (c), (d) and (e) are $E_{\mathrm{CT}}^{\mathrm{gap}}$, E_{HOMO} and E_{LUMO}, respectively, as a function of d and compared with the classical model of Eq. (5.1.7). The dashed-green lines are $-I_{\mathrm{mol}}^{\mathrm{P}}$ and $-E_{\mathrm{mol}}^{\mathrm{A}}$ calculated with ΔSCF.

energy required to remove an electron from the metal and that gained by adding it are equal to the workfunction. However, in a practical calculation a finite size slab is used, and therefore the relations are only approximately valid due to the inaccuracies in the calculated W_{F} for finite systems. As shown above, the W_{F} becomes more accurate as the cluster size is increased.

In Fig. 5.3(d) and Fig. 5.3(e) are shown the calculated values for the 12×12 supercell and PBC obtained by using the Li W_{F} of the infinite slab of 2.91 eV, and in Fig. 5.3(c) we present $E_{\mathrm{CT}}^{\mathrm{gap}}(d) = E_{\mathrm{CT}}^{+}(d) - E_{\mathrm{CT}}^{-}(d)$. In order to quantify how the image charge changes the charge transfer energies as a function of d, we can write $E_{\mathrm{CT}}^{\pm}(d) = E_{\mathrm{CT}}^{\pm}(\infty) + V(d)$, where the new quantity $V(d)$ corresponds to the energy lowering due to the distance dependent electron-hole attraction. It was demonstrated a long time ago [152], by using self-consistent DFT calculations, that for flat surfaces $V(d)$ can be accurately approximated by the classical image charge energy gain

$$V(d) = \frac{-q^2}{4(d - d_0)}\,, \tag{5.1.7}$$

for a single surface and for a point charge interacting with two infinite flat surfaces [138, 137] by

$$U(d) = -\frac{q^2}{2(d - d_0)}\ln 2. \tag{5.1.8}$$

The later will be useful in Chapter 6 when we discuss the transport through molecular junctions. On both equations, q is the charge on the molecule, and d_0 is the height of the image charge plane with respect to the topmost surface atomic layer

$$d_0(d) = \frac{\int_{d_A}^{d_B} z\ \Delta\rho_{xy}(z;d)\ \mathrm{d}z}{\int_{d_A}^{d_B} \Delta\rho_{xy}(z;d)\ \mathrm{d}z}\,. \tag{5.1.9}$$

In other words d_0 can be interpreted as the center of gravity of the screening charge density localized on the metal surface, and in general it depends on d. Here $\Delta\rho_{xy}(z;d) = \int \mathrm{d}x\mathrm{d}y\Delta\rho(\mathbf{r};d)$ and $\Delta\rho(\mathbf{r};d)$ is the difference between the charge densities of the DFT (ground state) and the CDFT (charge transfer state) solutions for a fixed d. Note that the charge transfer between the surface and the molecule leads to the formation of a spurious charge layer on the back side of the Li slab (*i.e.* opposite to the surface where the molecule is placed), which is due to the finite number of atomic layers used to simulate the metal surface. In order not to consider such spurious charge while evaluating the integral in Eq. (5.1.9), the two integration limits, d_A and d_B, are chosen in the following way: 1) d_A is taken after the first two $\Delta\rho(d)$ charge oscillations on the back of the cluster, and 2) d_B is the distance at which $\Delta\rho(d)$ changes sign between the top Li layer and the molecule (*i.e.* it is in the vacuum).

Fig. 5.3(a) provides a visual representation of the image charge formation as the

molecule approaches the surface and shows isosurface plots of $\Delta\rho(\mathbf{r};d)$ for different distances d. Here we present the case in which one electron is removed from the molecule and added to the Li surface. As one would expect, the further away the molecule is from the surface the more delocalized the image charge becomes [152]. Note that the isosurface value is kept constant for all d ($\Delta\rho(\mathbf{r};d) = 10^{-4}\text{e}/\text{Å}^3$), so that the apparent shrinking of the image charge for $d = 11$ Å simply reflects the fact that most of the image charge is now spread at an average density smaller than $10^{-4}\text{e}/\text{Å}^3$. Likewise, no isosurface contour appears on the Li slab for $d = 14$ Å, since now the image charge is rather uniformly spread at low density. In contrast at small d the oscillations of the charge density between the atomic layers of the metallic surface can also be seen. It can also be seen that at 4 Å the charges on the molecule and the image charge on the Li surface start to overlap. Note that for even shorter distances, when the overlap becomes very large, the CDFT approach presented here becomes ill defined, since the charge on each fragment is not well defined anymore.

By evaluating Eq. (5.1.9) we now determine $d_0(d)$ and the results obtained for the 12×12 PBC calculations are shown in Fig. 5.3(b) for both electron (d_0^+) and hole (d_0^-) transfer from the molecule to the surface. The average d_0 values are 1.81 Å and 1.72 Å for d_0^+ and d_0^-, respectively. Although the two values are similar, they are not identical. This is consistent with the small band-gap of the Li slab, which indicates that holes and electrons behave differently. The average values of d_0^+ and d_0^- can now be used to evaluate Eq. (5.1.7) for the classical model. The results are shown in Fig. 5.3(c) to Fig. 5.3(e) and demonstrate that the classical model works remarkably well for this system (the calculated slope of both $E_{\text{HOMO}}(d)$ and $E_{\text{HOMO}}(d)$ matches almost perfectly that obtained by CDFT). It also shows once again that the results for our 12×12 PBC cell are indeed well converged with respect to the slab and cell size.

Finally we make a comparison between our results and those available in the literature for many-body based calculations. We find an overall reduction of $E_{\text{CT}}^{\text{gap}}$ of 2.5 eV, when the benzene moves from infinity to $d = 4.5$ Å. García-Lastra *et al.* [131] studied the dependence of the frontier quasi-particle energy levels of a benzene molecule as a function of the distance to a Li substrate by means of GW calculations. They found an overall reduction in $E_{\text{QP}}^{\text{gap}}$ of ~3.2 eV as compared to the benzene HOMO-LUMO gap in the gas phase, as one can extract from Fig. 1(c) of Ref. [131]. The authors also fit their GW results to the classical model, finding the best match fitting for $d_0 = 1.72$ Å, in very good agreement with our calculated value. There is a small discrepancy in the results of Ref. [131], since if one uses the classical model of Eq. (5.1.7) with $d_0 = 1.72$ Å, then the HOMO-LUMO gap reduction should be smaller than 3.2 eV, namely 2.6 eV at $d = 4.5$ Å. Note that the GW results are obtained for cells much smaller than the converged 12×12 used here. If we now force the classical model to fit our results for the 3×3 and 6×6 supercells, we will obtain respectively $d_0 = 2.3$ Å and $d_0 = 2.1$ Å, for a corresponding

gap reduction of 3.27 eV and 3.0 eV. In these two cases however the fit is good at all d only for the 6×6 supercell, while it breakes down for the 3×3 one for d beyond 8 Å. This is somehow expected since for large molecular coverage (the 3×3 cell) the point-like classical approximation is no longer valid.

5.2 Conclusion

In summary, we have applied the CDFT discussed in Sec. 2.6 to determine the energy levels alignment of metal/organic interfaces in the weak electron coupling regime, *i.e.* for molecules physisorbed on surfaces [153]. In particular we have demonstrated how the frontier energy levels of a benzene molecule change, leading to a HOMO-LUMO gap reduction, when the molecule is brought close to a Li(100) surface. This effect is due to the screening charge formed on the metal surface. We have then shown that, in order to obtain quantitatively converged results, rather large metal cluster sizes are needed for large distances, whereas at small molecule-metal separations smaller clusters can also give quantitatively accurate results. Our calculated value for the image charge plane is 1.72 Å and 1.80 Å for E^{A} and I^{P}, respectively, in good agreement with the values fitted from GW calculations. Using these distances for the image charge plane height we have compared our *ab initio* results with a classical electrostatic model and found good agreement. The approach presented here offers several advantages over many-body quasi-particles schemes, namely: (i) rather large systems can be calculated, since the computational costs are similar to those of standard DFT calculations; (ii) surfaces with arbitrary shapes and reconstruction can be studied, including defective and contaminated surfaces; (iii) it gives a direct way of determining the position of the image charge for such interfaces. Overall CDFT applied to the levels alignment problem appears as a promising tool for characterizing theoretically organic/inorganic interfaces, so that it has a broad appeal in fields such as organic electronics, solar energy devices and spintronics.

Chapter 6

Ab initio Approach to Quantum Transport

6.1 Case of study: Au-benzenedithiol molecular junctions

As discussed in Chapter 1, the well-known prototype molecular junction that consists of a benzene-1,4-dithiol molecule between two gold electrodes is still not fully understood. This is partially due to the nature of the experiments, where several different geometrical contacts can be accessed during the stretching process of the junction. This leads to a statistical character of the experimental analysis. From the theoretical point of view, the quantitative description of such molecular junctions is challenging for two main reasons. Firstly, realistic electrode configurations and many arrangements should be considered in the calculations, which becomes prohibitive within a fully *ab initio* approach. More recently, we have [29, 30] applied a sophisticated method that combines Monte Carlo (MC) simulations and classical molecular dynamics (MD) to simulate the junction stretching process, allowing the sampling of hundreds of contact geometries between the molecule and the electrodes. In addition, it is generally assumed in the literature [154, 155, 156, 157, 29, 30, 158, 25, 26, 159, 28, 27, 160] that when the molecule attaches to the gold electrodes, the hydrogen atoms linked to the thiol groups are dissociated to form a thiolate-Au bond. However, recent DFT calculations exploring the details of the adsorption of the benzene-1,4-dithiol on gold have been reported [161, 162]. They find that the thiol-Au structure is energetically more stable than its thiolate-Au counterparts. This is true both when the molecule binds to a perfect flat surface [161] or to an adatom [162]. In fact, we demonstrate by means of stability and transport properties calculations that the thiol junctions can not be disregarded [31].

Usually transport calculations rely on the Kohn-Sham (KS) eigenvalues to evaluate G, even though these eigenvalues can not be rigorously interpreted as quasi-particle energy

levels. The only exception is for the HOMO energy, which is equal to the negative of the ionization potential [77, 79, 78], as discussed in Sec. 2.5.1. As discussed in Chapter 5, the quasi-particle energy gap, $E_{\mathrm{QP}}^{\mathrm{gap}}$, of a molecule shrinks with respect to that of the gas phase by adsorbing the molecule on a polarizable substrate. Nevertheless, electronic structure theories usually used for such calculations can only partly account for this renormalization of the molecular energy levels when the junction is formed. DFT, within the standard local and semi-local approximations to the exchange-correlation (XC) energy does not include non-local correlation effects, such as the dynamical response of the electron system to adding electrons or holes to the molecule. This limits its ability to predict the energy level alignment, when compared to experiments, which often leads to overestimated values for G [163]. Moreover, the lack of the derivative discontinuity and the self-interaction error in DFT-LDA, as discussed in Sec. 2.5.2 and Sec. 2.5.3, respectively, contributes to aggravate the problem. Therefore, different alternative approaches and corrections have been proposed to improve the description of the energy level alignment. These include, for instance, ASIC [27, 85], CDFT [153] and scissor operator (SCO) schemes [138, 159, 126, 163, 137].

In this Chapter we investigate, by means of total energy DFT and quantum transport calculations, the stability and conductivity of thiol and thiolate molecular junctions. We compare the results for the two systems and we relate them to experimental data. In Sec. 6.1.1 we present a systematic study of the adsorption process of two thiol-terminated molecules, namely, methanethiol and benzene-1,4-dithiol on Au(111) flat surface. For the latter, we also compare the stability of the thiol and thiolate systems when the junction is formed for several contact geometries [25, 26, 27, 29, 30]. In Sec. 6.1.2 we discuss the energy level alignment, and present three methods used to correct the DFT-LDA molecular energy levels, namely CDFT, ASIC and SCO. Based on these results in Sec. 6.1.4 we discuss the transport properties and present the dependence of G on the electrodes separation (L) for flat-flat contact geometries, for both the thiol and thiolate junctions. Finally, in Sec. 6.1.6 we present a combination of classical molecular dynamics and Monte Carlo to simulate more realistic configurations for the thiolate molecular junctions. Then, transport calculations are performed for representative molecular junctions and we compare with available experimental data.

6.1.1 Stability study of thiol-terminated molecules on a Au(111) flat surface and junctions

In this section we present a systematic study, by means of total energy DFT calculations, of the stability of thiol-terminated molecules on Au(111) flat surfaces, as well as when the molecule is attached to two Au electrodes forming a molecular junction. For the systems presented in this section, the gold surface is modeled by considering a 3×3

surface unit cell five-layer thick. This corresponds to a surface coverage of 1/3 [26, 161]. The three bottom layers of gold are kept fixed during the relaxation. For the junctions shown in Fig. 6.3 we use a slightly larger 4×4 surface unit cell, in order to be able to model the tip-tip-like contact as well.

We first discuss the adsorption process of benzene-1-4-dithiol ($C_6H_6S_2$) on the Au(111) flat surface, and compare it to adsorption properties of methanethiol (CH_3SH). These molecules represent two distinct classes, namely, aromatic and linear hydrocarbon compounds, respectively. From this point on, we refer to benzene-1-4-dithiol as BDT2H in order to distinguish it from the benzene-1-thiolate-4-thiol $C_6H_5S_2$ (BDT1H), and from benzene-1-4-dithiolate $C_6H_4S_2$ (BDT). The calculations are performed as follows: (i) a system with the molecule terminated by a thiol group (RSH/Au), where $R = CH_3$ for the methanethiol and $R = C_6H_5S$ for the BDT2H, is placed close to the Au(111) surface and the geometry is relaxed. (ii) Then a second system is built where the molecule is now terminated by a thiolate group and a H atom is attached to the surface (RS/Au + H), and again the geometry is relaxed. Fig. 6.1(a-c) shows the relaxed structures for the dissociative adsorption of the methanethiol molecule, and the analogous structures are shown for the BDT2H in Fig. 6.1(d-f). For the RSH/Au system, the molecule is tilted with respect to its vertical axis perpendicular to the surface, whereas for the RS/(Au + H) system the molecule is upright sitting on a hollow-site. Our relaxed geometries are in good agreement with literature [160, 161]. We have also calculated the binding energies, as given by

$$E_b = E_T(R\text{SH/Au}) - E_T(\text{Au}) - E_T(R\text{SH}), \tag{6.1.1}$$

for the methanethiol and methanethiolate molecules on the Au(111) surface, and we find 0.63 eV and 1.42 eV, respectively. For the BDT2H we find 0.12 eV whereas for the BDT1H, E_b is equal to 1.53 eV. Finally, we consider a third structure for which the H atom attached to the surface is released from the surface to form a H_2 molecule (RS + H_2)/Au. The formation energy of the thiolate structure with a H atom attached to the surface is given by

$$E_f = E_T(R\text{SH/Au}) - E_T(R\text{S/(Au + H)}). \tag{6.1.2}$$

Similarly, the formation energy for the dissociative adsorption followed by the formation of a H_2 molecule is calculated as

$$E_f = E_T(R\text{SH/Au}) + \frac{1}{2}E_T(\text{H}_2) - E_T((R\text{S} + \text{H}_2)/\text{Au}). \tag{6.1.3}$$

Fig. 6.1(g) and Fig. 6.1(h) schematically show the total energy differences between each step of the dissociative adsorption of the methanethiol and BDT2H molecules. For the methanethiol molecule, if the dissociative reaction is accompanied by the chemisorption of a H atom on the surface, as in Fig. 6.1(b), the thiolate structure is energetically

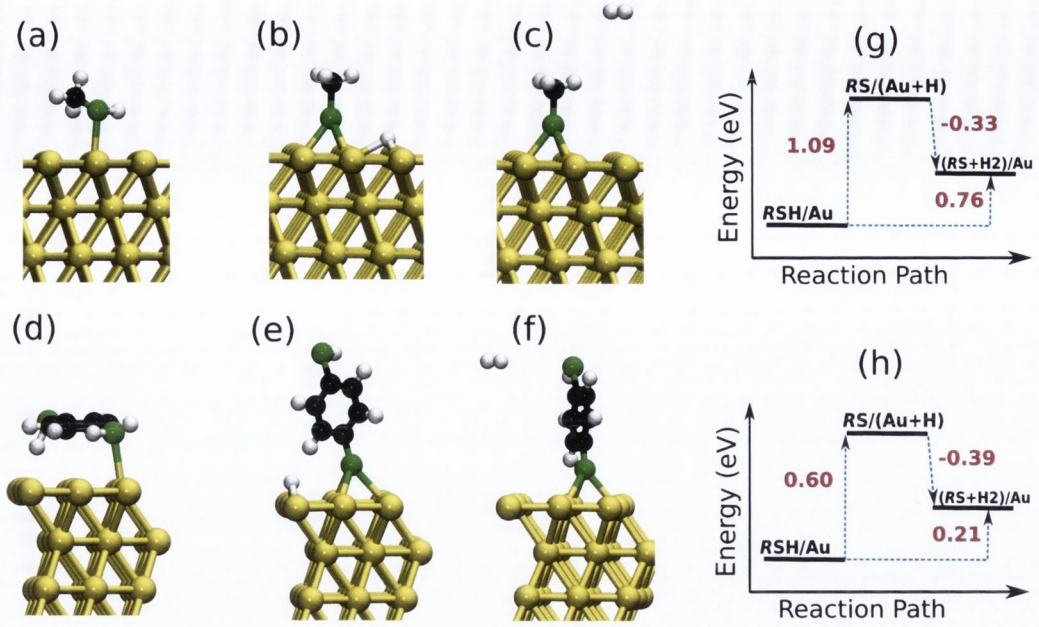

Figure 6.1: Ball-stick representation of the adsorption process of methanethiol (a-c) and BDT2H (d-f) on a flat Au(111) surface. (a) and (d) the thiol molecules (RSH/Au) are adsorbed on the surface; (b) and (e) the hydrogen atom is dissociated to form thiolates (RS/(Au+H)). Finally, in (c) and (f) the hydrogen atoms attached to the Au surface desorbs to form a H_2 molecule, (RS+H_2)/Au. (g) and (h) schematically show the total energy differences between each step of the reaction.

unfavorable by 1.09 eV, a result consistent with previous calculations by Zhou *et al.* [164] and temperature-programmed desorption (TPD) experiments [165, 166]. When the H atoms adsorbed on the surface are detached to form H_2 molecules as in Fig. 6.1(c), the thiolate system becomes more stable by 0.33 eV compared to the thiolate one with the H atom attached to the surface. Overall, the dissociative reaction followed by the formation of a H_2 molecule is unfavorable by 0.76 eV. For the BDT2H molecule, the thiolate with one H atom attached to the surface is unfavorable by 0.60 eV compared to the thiol structure, in good agreement with the value of 0.4 eV reported in recent studies by Ning *et al.* [162]. When the dissociative reaction is accompanied by the formation of a H_2 from the H atom attached to the surface, this reaction is exothermic by 0.39 eV. As a result, the dissociative absorption of BDT2H molecules on Au(111) surface followed by the desorption of H_2 is unfavorable by 0.21 eV. This partially contradicts the results obtained by Nara *et al.* [161], who found the dissociative reaction accompanied by the H atom on the surface to be indeed unfavorable by 0.22 eV. However, for the case where the reaction is followed by the formation of H_2, the system is further stabilized by 0.42 eV so that the thiolate system is more stable by ~0.20 eV. Overall our results show that for both classes of molecules the dissociative reaction is always unfavorable when considering either the formation of RS/(Au + H) or (RS + H_2)/Au structures. We point out that our calculations are based only on ground stated DFT total energy differences and that we

neglect zero-point energy and entropic contributions to the total energies. For an isolated gas-phase hydrogen molecule, we estimate the zero-point energy and entropy contributions (disregarding electronic contributions) to be equal to 0.27 eV and 1.3 meV/K, respectively. By considering these corrections the system (RS + H_2)/Au could also become energetically stable compared to the non-dissociated RSH/Au system, in agreement with the results of Strange *et al.* [159].

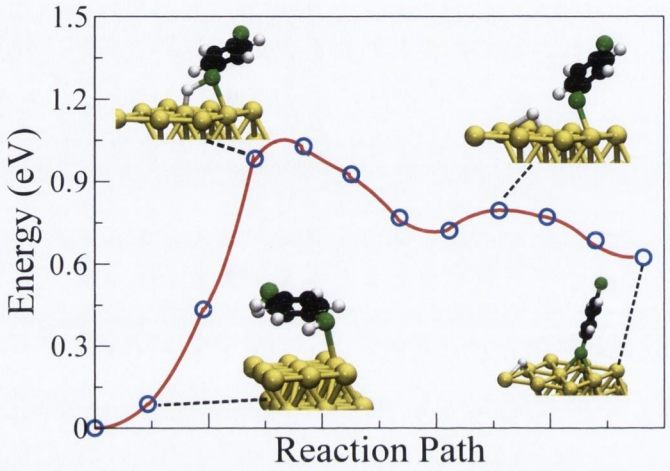

Figure 6.2: Activation barrier for the dissociative adsorption of BDT2H on a Au(111) surface as shown in Fig. 6.1(d)-(e).

In addition to the total energy differences between the dissociated and non-dissociated structures of BDT2H, we evaluate the barrier height between those states [Fig. 6.1(d) and Fig. 6.1(e)], by means of the Nudged Elastic Band (NEB) method [167, 168, 169], as shown in Fig. 6.2. This allows us to estimate the transition probability between the states. Our results show that the activation barrier is about 1 eV. The fact that the barrier is large provides evidence for possible existence of the thiol structures on the surface, since a high temperature is required to overcome such a barrier. We note that defects on the surface, such as adatom, or the presence of a solvent, can change the energy barrier and eventually dissociation might take place at lower energies.

For BDT2H we also compare the stability of the thiol and thiolate structures when the molecule is connected to two Au electrodes. We consider three types of junctions, as illustrated in Fig. 6.3. For the configuration shown in Fig. 6.3(a), ten gold atoms are added on each side of the junction forming a tip-like symmetric contact with the molecule. For the configuration shown in Fig. 6.3(b) an adatom is added symmetrically at each side of the junction, and for the one shown in Fig. 6.3(c) an adatom is added to one side of the junction and the molecule is connected to a flat surface at the other side. These junctions constitute typical models for transport calculations found in the literature [27, 28, 131]. In this case, the formation energy difference between the thiol and the thiolate structures

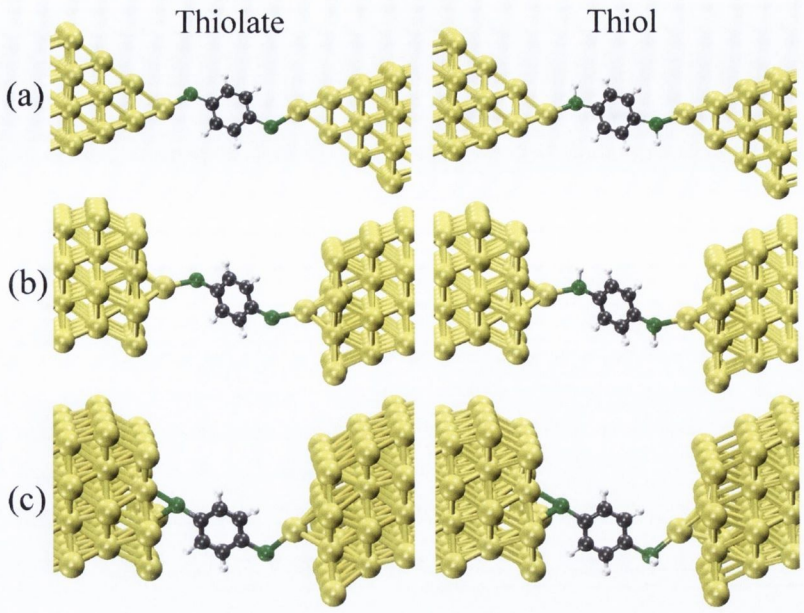

Figure 6.3: Ball-stick representation of three molecule-electrode contact geometries. (a), (b) and (c) shows the tip-tip, adatom-adatom and surface-adatom configurations, respectively. Left (right) panel shows the thiolate (thiol) junctions.

with respect to the formation of H_2 molecule is given by

$$E_f = E_T(\text{BDT2H/Au}) - E_T(\text{BDT/Au}) - E_T(H_2), \tag{6.1.4}$$

and the results are shown in Tab. 6.1. Note that for the adatom-flat configuration the binding energy is evaluated considering $\frac{1}{2}H_2$. For all the three junctions, the thiol configurations are energetically more stable than their thiolate counterparts.

Table 6.1: Formation energy difference between the thiol and the thiolate structures with respect to the formation of H_2 molecule, in eV, for the three molecular junctions shown in Fig. 6.3.

System	VASP	SIESTA
surface-adatom	-0.36	-0.42
adatom-adatom	-0.64	-0.40
tip-tip	-0.77	-0.88

One possibility that has been considered in order to determine whether there are thiols or thiolates in the junction is a simultaneous measurement of G and the force in a STM and atomic force microscopy (AFM) setup [170, 171, 172, 173]. Since the binding energy for thiol and thiolate can differ considerably, one might expect that the forces involved when stretching the junction should be different. Therefore, we investigate the energetics of Au(111)-BDT-Au(111) and Au(111)-BDT2H-Au(111) junctions as a function of L. For the Au(111)-BDT-Au(111) junctions, similar calculations have been reported in the

literature in an attempt to simulate a MCBJ experiment within DFT [26, 29, 30, 174, 175, 176, 177]. Details on how the stretching is performed can be found in Ref. [26]. Figs. 6.4(a)-(i) and Figs. 6.5(a)-(i) show the relaxed structures for the Au(111)-BDT-Au(111) and Au(111)-BDT2H-Au(111) junctions undergoing stretching.

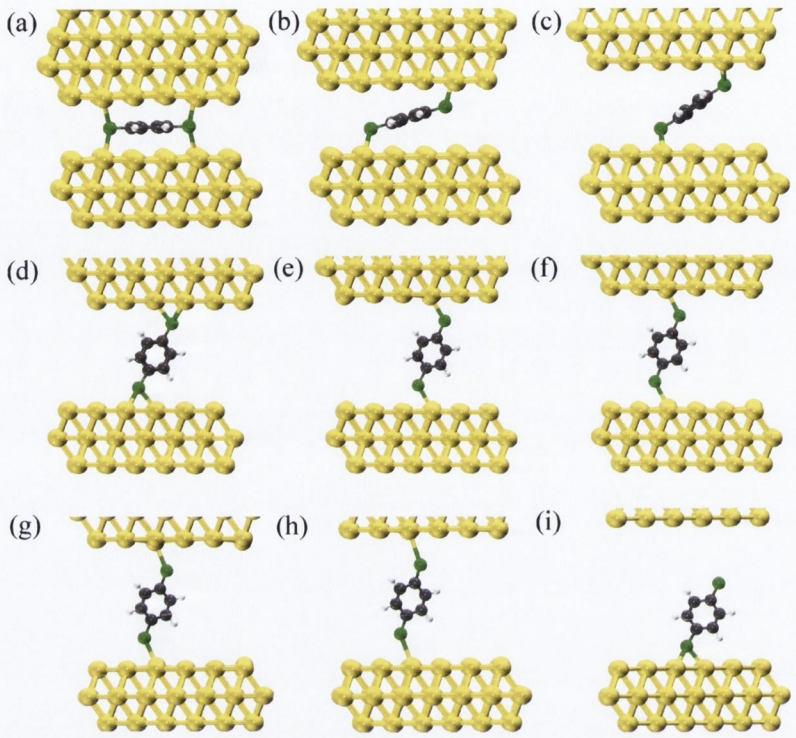

Figure 6.4: (a)-(i) Ball-stick representation of the stretching process of BDT between two flat Au(111) surfaces.

In Fig. 6.6 we show the energy and the forces as a function of L, for both Au(111)-BDT-Au(111) and Au(111)-BDT2H-Au(111) junctions. Our results show that the breaking force for the S-Au bond is about 1 nN, in good agreement with the independent DFT results by Romaner *et al.* [175] of 1.25 nN obtained using the same contact geometry. The authors also considered the scenario when the BDT molecule is attached to an adatom contact geometry, and they found that the breaking force can be as large as 1.9 nN [175]. In fact, it is possible that during the elongation process the molecule is bonded to a single Au atom rather than a flat surface [29]. For Au(111)-BDT2H-Au(111) our calculated breaking force is 0.3 nN, as shown in Fig. 6.6(b). Thus the breaking forces for the BDT2H junctions are smaller than those for BDT when the flat electrode geometry is considered. We note that this is much smaller than the calculated value of 1.1-1.6 nN for the BDT2H molecule attached to a tip-like contact geometry [162]. Our small breaking force value of 0.3 nN for the thiol junctions is consistent with the rather small calculated E_b of 0.12 eV, and indicates weak coupling between the molecule and the flat electrodes. A similar study for a octanedithiol-Au junction has also been reported [177], and for an

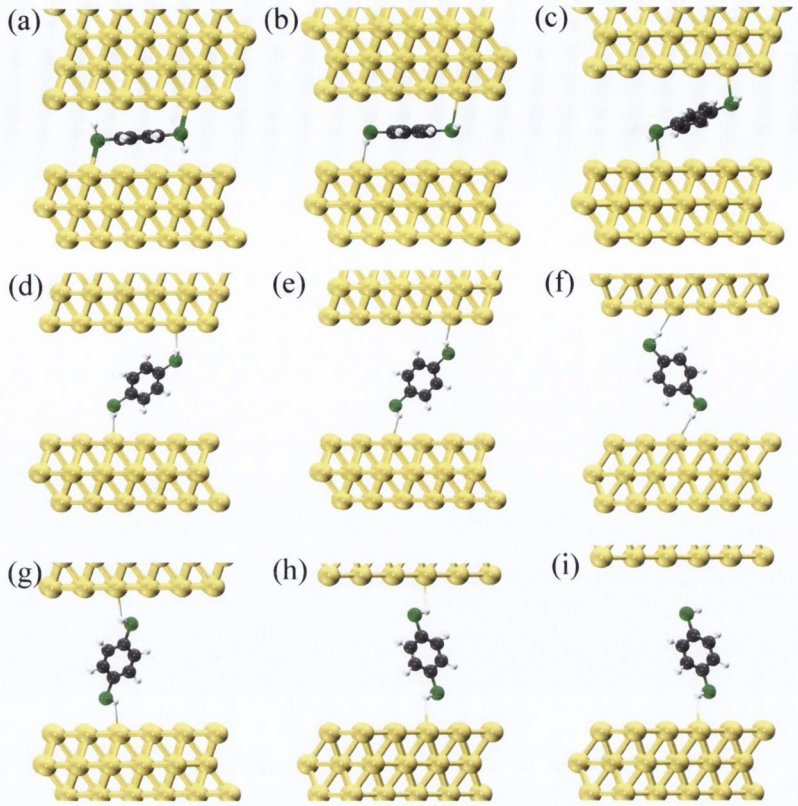

Figure 6.5: (a)-(i) Ball-stick representation of the stretching process of BDT2H between two flat Au(111) surfaces.

asymmetric junction it was found the breaking force of the Au-thiol bond to be 0.4-0.8 nN. Other experiments using the same molecule [172, 173] reported a breaking force of 1.5 nN, which is very similar to the breaking force of a Au-Au bond, therefore, leading to the conclusion that the junction might break at the Au-Au bond and also indicating the presence of Au-thiolate instead of Au-thiol junctions.

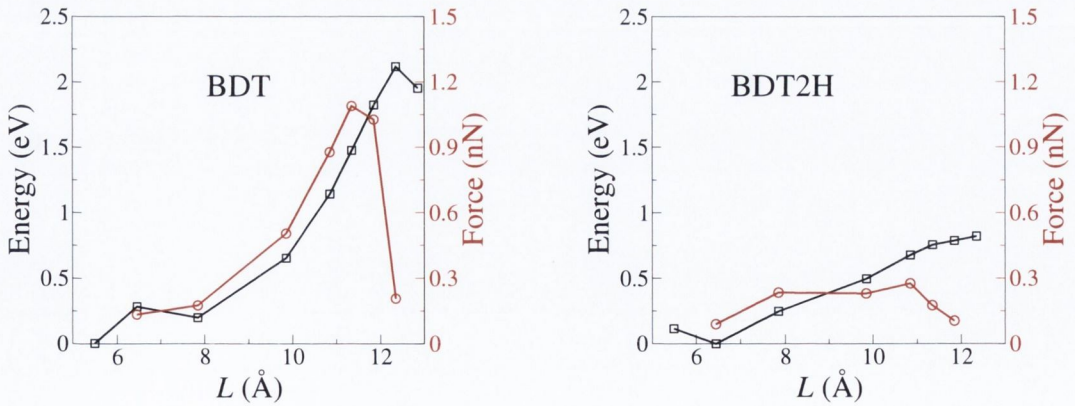

Figure 6.6: Total energy and pulling force as a function of L for the Au-BDT-Au and Au-BDT2H-Au molecular junctions shown in Fig. 6.4 and Fig. 6.5, respectively.

In summary, we find that the dissociative reaction of methanethiol and BDT2H on Au(111) is energetically unfavorable. Especially for BDT2H, the activation barrier of ~1

eV strongly suggests the presence of thiol structures when the molecules attach to the metallic surface. Moreover, for all the contact geometries of molecular junctions presented in Figs. 6.3-6.5, the thiol bonding is also energetically more stable. These results indicate that the non-dissociated structures are likely to exist in experiments, and therefore should be considered when modeling transport properties of such systems.

6.1.2 Energy level alignment of Au-BDT interface

One of the possible reasons for the discrepancies between theory and experiments regarding the conductance of molecular junctions is the difficulty, from a theoretical point of view, to obtain the correct energy level alignment of such systems. Tab. 6.2 shows the LDA eigenvalues for the frontier molecular states of BDT and BDT2H in the gas phase. $E_{\mathrm{LDA}}^{\mathrm{gap}}$ is largely underestimated when compared to $E_{\mathrm{QP}}^{\mathrm{gap}} = I^{\mathrm{P}} - E^{\mathrm{A}}$ calculated by the delta self-consistent field (ΔSCF) method. For the BDT molecule, our results show that the HOMO is higher in energy by 2.73 eV with respect to $-I^{\mathrm{P}}$ whereas the LUMO is lower in energy by 2.66 eV compared to $-E^{\mathrm{A}}$. For BDT2H, the HOMO is higher in energy by 2.49 eV with respect to $-I^{\mathrm{P}}$, and the LUMO is lower in energy by 2.51 eV when compared to $-E^{\mathrm{A}}$. The results clearly indicate that the GGA/LDA KS eigenvalues offer a poor description of the molecule quasi-particle levels even in the gas phase.

Fig. 6.7(a) shows schematically the energies of these states for the gas phase molecules. In the case of BDT2H molecule, the wavefunctions Ψ_0 (blue), Ψ_1 (red) and Ψ_2 (green) correspond to the HOMO-1, HOMO and LUMO of the isolated molecule, respectively. For the BDT the removal of 2 H atoms from BDT2H leads to a reduction of the number of electrons by 2 as well, so that to a first approximation the BDT2H HOMO becomes the LUMO for the BDT molecule [see Fig. 6.8(b) and Fig. 6.8(e)]. Therefore, for BDT, Ψ_0 corresponds to the HOMO, Ψ_1 to the LUMO, and Ψ_2 to the LUMO+1. Fig. 6.8 shows the real space representation of Ψ_0, Ψ_1 and Ψ_2 for BDT (left) and BDT2H (right) molecules in the gas phase.

Table 6.2: Calculated LDA eigenvalues (ϵ), $E_{\mathrm{LDA}}^{\mathrm{gap}}$, I^{P}, E^{A} and $E_{\mathrm{QP}}^{\mathrm{gap}}$ (calculated with ΔSCF) for the gas phase BDT and BDT2H molecules.

	LDA			ΔSCF		
System	ϵ_{HOMO}	ϵ_{LUMO}	$E_{\mathrm{LDA}}^{\mathrm{gap}}$	$-I^{\mathrm{P}}$	$-E^{\mathrm{A}}$	$E_{\mathrm{QP}}^{\mathrm{gap}}$
BDT	-5.74	-5.19	0.55	-8.47	-2.53	5.94
BDT2H	-5.09	-1.82	3.27	-7.58	0.69	8.27

CDFT method for Au-BDT interfaces

Fig. 6.7(b) shows the CDFT results for E_{HOMO} and E_{LUMO} as a function of d for BDT/Au(111) (see Chapter 5). In the CDFT calculations the metal is modeled by a 9×9 Au(111) surface five-atomic-layers thick and the molecule is placed upright at a distance, d, from the center of the molecule to the Au surface. We also introduce a 20 Å vacuum region in the direction perpendicular to the surface plane. We note that, although CDFT is in principle applicable at all d, when d becomes less than about 5.9 Å, for which the Au-S bond distance, $d_{\mathrm{Au-S}}$, is less than 2.5 Å, the amount of charge on each fragment becomes ill defined due to the hybridization between the molecular orbitals and the electrode continuous spectrum. Therefore, at those small distances, the CDFT charge-transfer energies are not well defined. At $d = 5.9$ Å, the CDFT calculations give an overall reduction of $E_{\mathrm{QP}}^{\mathrm{gap}}$ of 2.09 eV with respect to the value obtained for isolated BDT. Fig. 6.7(b) also shows the results of the classical model for the image charge

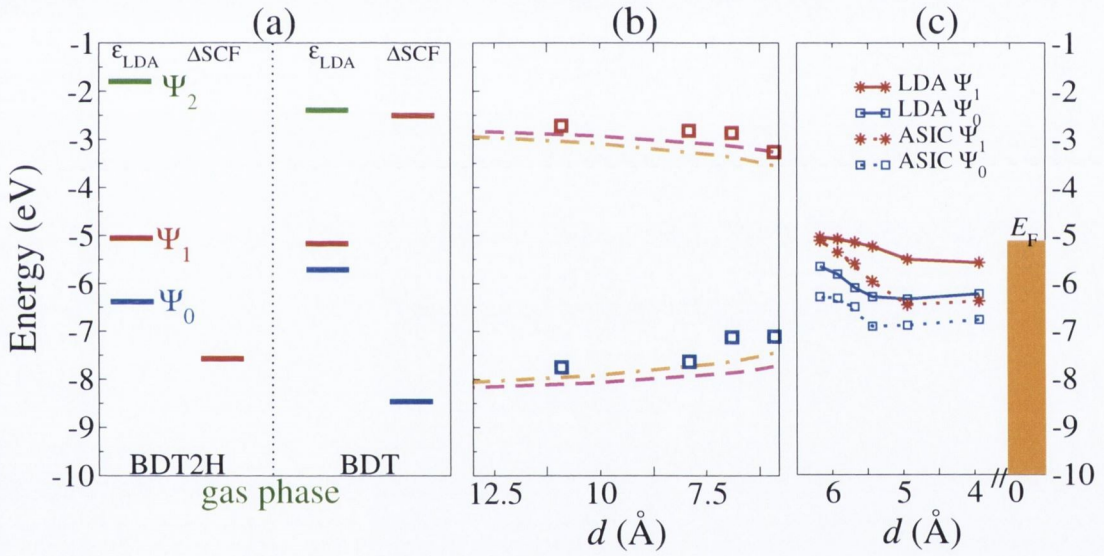

Figure 6.7: Energy level alignment of the frontier molecular orbitals for the BDT molecule from the gas phase to the formation of the Au-BDT-Au junction. (a) LDA eigenvalues (ϵ_{LDA}) and ΔSCF calculations in the gas phase BDT. For comparison, we also show results for the gas phase of BDT2H. All the values are given with respect to the vacuum level. (b) CDFT calculations for the charge-transfer energies between BDT molecule adsorbed and a single flat surface: $E_{\mathrm{CT}}^{+}(d)$ (blue squares) and $E_{\mathrm{CT}}^{-}(d)$ (red squares). The classical image charge contribution for two surfaces (dashed-line) and for a single surface (dashed-dotted line) are plotted for comparison where $E_{\mathrm{F}} = -5.1$ eV and $d_0 = 1$ Å. (c) LDA and ASIC energy levels for the HOMO (Ψ_0) and LUMO (Ψ_1) obtained from the PDOS peaks for the molecule at the junction as a function of $d = L/2$.

calculated for one [Eq. (5.1.7), dashed line] and for two [Eq. (5.1.8), dash-dotted line] surfaces. The CDFT d_0 ranges from 0.79 Å to 1.13 Å, depending on the distance, and we therefore take $d_0 = 1$ Å as average value. Coincidentally, this is the same value used in literature [137, 136, 37], although there it was not formally justified, but rather used as a

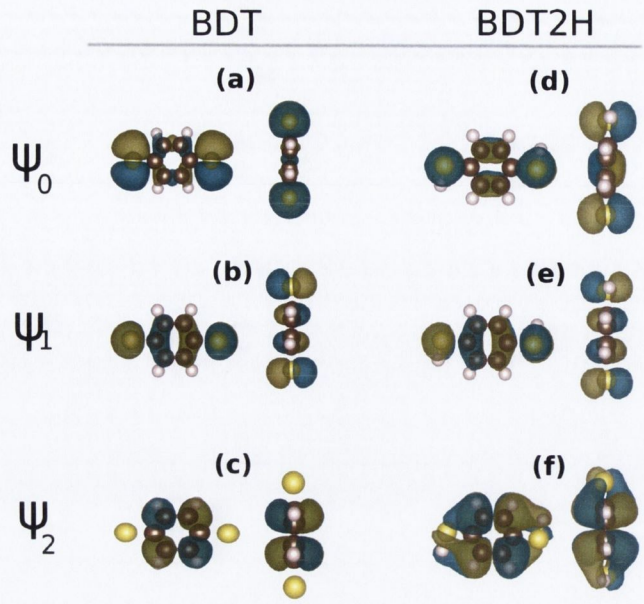

Figure 6.8: Plots of wavefunctions: (a), (b) and (c) show Ψ_0 (20th state), Ψ_1 (21st state) and Ψ_2 (22sd state), respectively, for the gas phase BDT molecule; (d), (e) and (f) show the same for the the BDT2H molecule. Isosurfaces are taken at a density of 0.06 $e/\text{Å}^3$.

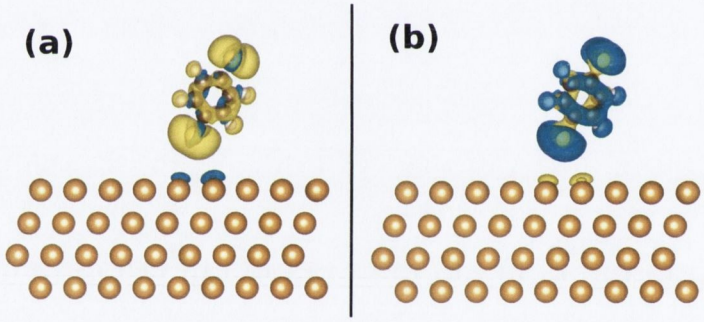

Figure 6.9: Charge density differences for (a) $E^{+}_{\text{CT}}(d)$ and (b) $E^{-}_{\text{CT}}(d)$ for $d = 6.9$ Å. Isosurfaces are taken at 10^{-4} e/Å^3.

free parameter. The corrections to I^{P} and E^{A} from the classical model when considering two surfaces are larger than the corrections for a single surface, since $U(d) > V(d)$ for all d, where $V(d)$ and $U(d)$ are given by Eq. (5.1.7) and Eq. (5.1.8), respectively. We evaluate the charge density differences between the constrained and the non-constrained calculations for $E^{+}_{\text{CT}}(d)$ and $E^{-}_{\text{CT}}(d)$ (Fig. 6.9). It can be seen that the hole (electron) left on the molecule has the same character as the corresponding Ψ_0 (Ψ_1) wavefunction [compare to Figs. 6.8(a)-(b)].

Fig. 6.7(c) shows the energies of the eigenvalues of the Ψ_0 and Ψ_1 states for the BDT molecule as a function of $d = L/2$, calculated with LDA (solid lines) and ASIC (dashed lines), for the stretching configurations shown in Fig. 6.4(c-h). The energies of these levels are set to be at the peaks of the corresponding PDOS. In the limit of weak coupling between the BDT molecule and the electrodes, which is the case for $L = 12.35$ Å, at which

$d_{\mathrm{Au-S}}$ is the largest before rupture of the junction, LDA gives the LUMO of the isolated BDT molecule (Ψ_1) slightly above E_{F}. However, as shown in Fig. 6.7(a) and Tab. 6.2, the corrected energy of Ψ_1 (which is given by $-E^{\mathrm{A}}$) is 2.66 eV above the LDA eigenvalue. Similarly, the LDA energy of Ψ_0 is too high by 2.73 eV when compared to $-I^{\mathrm{P}}$. The same analysis can be done for $L = 11.86$ Å and $L = 11.36$ Å, for which Ψ_1 is still above E_{F}. In other words, for $L \geq 11.36$Å, the molecule is weakly bonded to the electrodes, therefore, charge transfer from the electrodes to the molecule due to the hybridization of the molecular and electrodes states is small. These results show that for the Au-BDT-Au junctions in the weak coupling regime the LDA BDT HOMO (corresponding to Ψ_0) is in fact too high in energy whereas the LDA BDT LUMO (corresponding to Ψ_1) is too low.

6.1.3 Scissor operator method for energy level alignment

Since we obtain the energies of the HOMO and LUMO of the junction from the CDFT total energies, we can shift the DFT eigenvalues to lie at these energies by means of a SCO [135, 136, 137, 138, 139, 140]. This has been shown to improve G when compared to experimental data [138]. For the particular case of a single molecule attached to the electrodes, first a projection of the full KS-Hamiltonian matrix and of the overlap matrix is carried out onto the atomic orbitals associated with the molecule subspace, which we denote as H^0_{mol} and S^0_{mol} (the remaining part of $\hat{H}$ describes the electrodes). By solving the corresponding eigenvalue problem, $H^0_{\mathrm{mol}}\psi = \epsilon S^0_{\mathrm{mol}}\psi$, for this subblock we obtain the eigenvalues, $\{\epsilon_n\}_{n=1,\ldots,M}$, and eigenvectors, $\{\psi_n\}_{n=1,\ldots,M}$, where M is the number of atomic orbitals on the molecule. Subsequently, the corrections are applied to the eigenvalues, where all the occupied levels are shifted rigidly by the constant Σ_{o} ($\Sigma_{\mathrm{o}} < 0$) while the unoccupied levels are shifted rigidly by the constant Σ_{u} ($\Sigma_{\mathrm{u}} > 0$). We note that in principle each state can be shifted by a different amount. Using the shifted eigenvalues we can construct a transformed molecular Hamiltonian matrix, $H^{\mathrm{SCO}}_{\mathrm{mol}}$, given by

$$H^{\mathrm{SCO}}_{\mathrm{mol}} = H^0_{\mathrm{mol}} + \Sigma_{\mathrm{o}} \sum_{i_{\mathrm{o}}=1,n_{\mathrm{o}}} \psi_{i_{\mathrm{o}}}\psi^{\dagger}_{i_{\mathrm{o}}} + \Sigma_{\mathrm{u}} \sum_{i_{\mathrm{u}}=1,n_{\mathrm{u}}} \psi_{i_{\mathrm{u}}}\psi^{\dagger}_{i_{\mathrm{u}}}, \tag{6.1.5}$$

where the first sum runs over the n_{o} occupied orbitals, and the second one runs over the n_{u} empty states. In the full Hamiltonian matrix we then replace the subblock H^0_{mol} with $H^{\mathrm{SCO}}_{\mathrm{mol}}$ [136, 137, 138, 139, 140]. The SCO procedure can be applied self-consistently, although in this work we apply it non-selfconsistently to the converged DFT Hamiltonian.

The correction applied to the frontier energy levels of a molecule in a junction has two contributions. Firstly we need to correct for the fact that the gas-phase LDA HOMO-LUMO gap ($E^{\mathrm{gap}}_{\mathrm{LDA}}$) is too small when compared to the difference between I^{P} and E^{A}, where $I^{\mathrm{P}} = E^{(N-1)} - E^{(N)}$ and $E^{\mathrm{A}} = E^{(N)} - E^{(N+1)}$ ($E^{(N)}$ is the ground state total energy for a system with N electrons). Secondly, the renormalization of the energy levels, when

the molecule is brought close to metal surfaces needs to be added to the gas-phase HOMO and LUMO levels. Although CDFT in principle allows us to assess the renormalization of the energy levels in the junction, to reduce the computational costs we calculate the charge-transfer energies with one single surface. Since in transport calculations there are two surfaces, we then use the corresponding classical model [Eq. (5.1.8)], with d_0 obtained from CDFT for the single surface. Hence, for the molecule attached to two metallic surfaces forming a molecular junction, we approximate the overall corrections for the molecular levels below E_F by

$$\Sigma_o(d) = -[I^P + \epsilon_{HOMO}(d)] + U(d) \tag{6.1.6}$$

and similarly for the levels above E_F as

$$\Sigma_u(d) = -[E^A + \epsilon_{LUMO}(d)] - U(d); \tag{6.1.7}$$

where $\epsilon_{HOMO/LUMO}(d)$ is obtained from the position of the peaks of the PDOS and $U(d)$ is the classical potential given by Eq. (5.1.8). Here we assume that the character of the molecular states is preserved when the junction is formed, *i.e.* that the hybridization is not too strong.

Tab. 6.3 shows, for the Au-BDT2H-Au and Au-BDT-Au junctions, U [Eq. (5.1.8)], Σ_o [Eq. (6.1.6)] and Σ_u [Eq. (6.1.7)] as functions of L. As pointed out by Garcia-Suarez *et al.* [137], the shift of the energy level is unambiguous when there is no resonance at E_F [138, 136], so that the occupied levels are shifted downwards and the empty levels are shifted upwards in energy. This is the case for the BDT2H molecule, where the isolated molecule has 42 electrons, therefore the 21st molecular level is the HOMO of the isolated molecule (Ψ_1 in this case). Since it is already filled with two electrons, it lies below E_F when the molecule is in the junction, and the LUMO (Ψ_2) is always empty and well above E_F.

Table 6.3: Contribution due to the classical image charge for two surfaces model, U, and the final corrections Σ_o/Σ_u as a function of L for the BDT2H and BDT molecules in the junction. The first column correspond to the labels of a subset of the structures shown in Fig. 6.4 and Fig. 6.5. The Au-S bond distance, d_{Au-S}, is also shown for completeness.

				BDT2H		BDT	
	L (Å)	d_{Au-S} (Å)	U (eV)	Σ_o(eV)	Σ_u (eV)	Σ_o(eV)	Σ_u (eV)
(c)	7.86	2.11	1.70	0.18	1.63	-	-
(d)	9.89	2.08	1.26	-0.50	1.72	-	-
(e)	10.87	2.47	1.12	-0.80	1.78	-	-
(f)	11.36	2.67	1.06	-1.04	1.77	-1.13	1.45
(g)	11.84	2.90	1.01	-0.62	2.22	-1.63	1.53
(h)	12.35	3.18	0.96	-0.83	2.17	-1.84	1.55

For closer distances, due to the stronger coupling between the molecule and the electrodes, hybridization takes place leading to a fractional charge transfer from the electrodes to the molecule. For small d also for the BDT molecule the Ψ_1 state becomes partially occupied, and positioned slightly below E_F. This means that, for the structures considered in Fig. 6.4, the correction defined by Eq. (6.1.7) can not be applied for $L \leq 10.87$, since this is the distance where the level moves slightly below E_F. We note that when the level is pinned at E_F, many-body effects become important, and the GW method might be the most appropriate method [159] to resolve the energy level alignment. Once the coupling is strong enough and Ψ_1 is almost fully filled, it becomes effectively the HOMO of the BDT. In this case we expect its energy to be too high within LDA, and therefore application of ASIC is expected to improve its position with respect to E_F. In fact, ASIC corrects Ψ_1 by $\sim$1 eV as d decreases, as shown in Fig. 6.7(c).

For the weak coupling limit the calculated corrections show that Ψ_1 (the LUMO of the isolated BDT molecule) is empty and its LDA eigenvalue is too low in energy. In contrast, for the strong coupling limit the energy of Ψ_1 moves below E_F, so that the state becomes occupied, and its LDA eigenvalue is now too high in energy. In this regime we apply the ASIC method to give a better description of the energy level alignment.

6.1.4 Electronic transport properties: thiol versus thiolate junctions

We start the discussion of the electronic transport properties by presenting results for the molecular junctions at fixed distance and different molecule-surface bonding. Subsequently we discuss the conductivity of the thiol and thiolate bonding structure to flat Au electrodes under stretching.

Fig. 6.10 shows $T(E)$ for thiolate (left column) and thiol (right column) bonding, for the *tip-tip*, *adatom-adatom* and *surface-adatom* structures (see Fig. 6.3 for the structure geometries). Within the LDA, the transmission curves of all the thiolate junctions present a peak pinned at E_F. These results have been found in several works reported in the literature for Au-BDT-Au (thiolate) junctions [27, 26, 159, 17, 29, 30]. The resonant states at E_F yield high values of conductance with G of $1.35G_0$, $0.45G_0$ and $0.22G_0$ for *tip-tip*, *surface-adatom* and *adatom-adatom*, respectively. The observed peaks at E_F correspond to the hybridized Ψ_1 state of the BDT molecule. Note that the exact position of the peaks and so the exact G values depend on the atomistic details of the junctions, as well as on the DFT functional used. We point out that such high values of G have never been observed experimentally, indicating that LDA does not give the correct energy level alignment between the molecule and the electrodes, as already discussed in Sec. 6.1.2. In contrast, for the thiol junctions, no resonant states are found around E_F. The zero-bias conductance is in the range of 0.035-$0.004G_0$, which is in good agreement with experimental values of

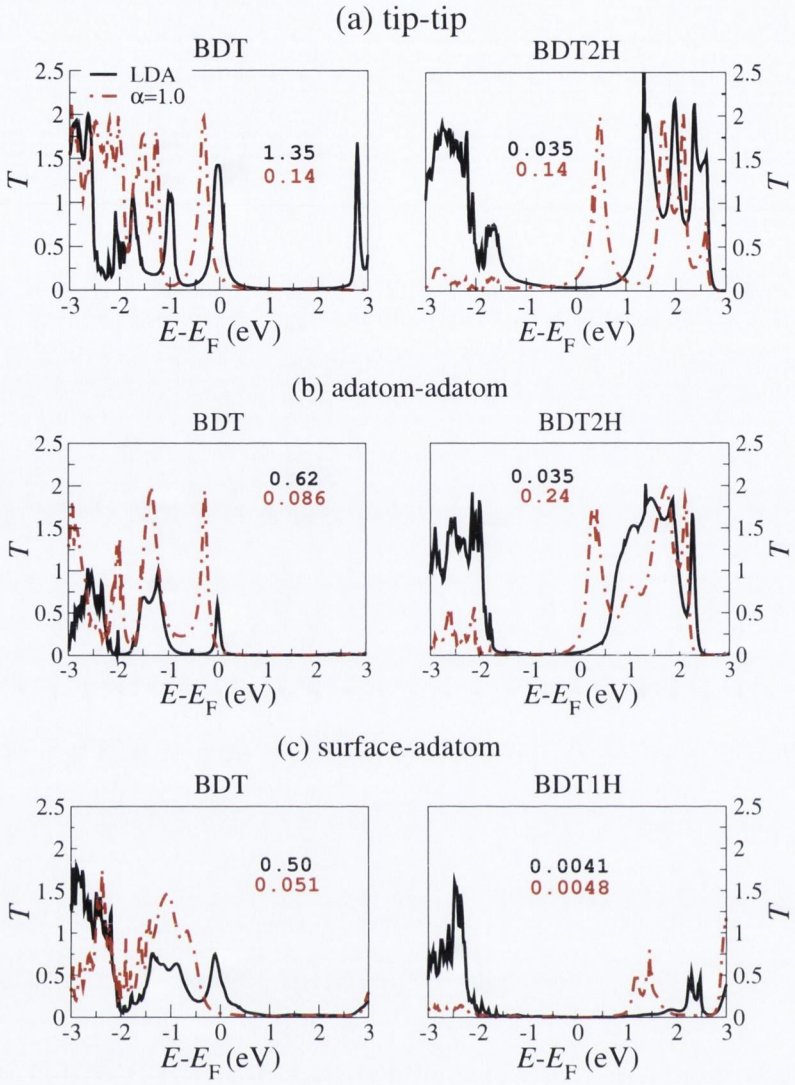

Figure 6.10: (a) Transmission coefficients as a function of energy for thiolate (left column) and thiol (right column) for the structures shown in Fig. 6.3. For each case we report, in the insets, the transmission at E_F for both LDA (black full-line) and ASIC (red dashed-line).

$0.011G_0$ [12, 4, 7, 23].

When ASIC is used, for the BDT structures the molecular energy level remains pinned at E_F, and it is just slightly shifted to lower energies. This slight shift is however enough to decrease G by one order of magnitude. For the hydrogenated junctions (BDT1H and BDT2H) there are no molecular states at E_F for the LDA electronic structure, and in this case ASIC shifts downwards the energy levels of the occupied states. We note that also the empty states are shifted down in energy, which is an artifact of the ASIC method presented in Sec. 2.5.3. The correction applied by ASIC depends on the atomic orbital occupation, not the molecular orbital occupation. Therefore, if different molecular orbitals are composed of a linear combination of a similar set of atomic orbitals, ASIC will shift their energy eigenvalues by a similar amount. For example, if empty states share the

same character as the occupied states, as it is usually the case for small molecules, the energy of these states will be spuriously shifted to lower energies. In order to apply ASIC, a scaling parameter, α, to the atomic-like occupations needs to be specified, where for $\alpha = 1$ the full correction is applied, while for $\alpha = 0$ no correction is applied. The value of α is related to the screening provided by the chemical environment [85]. For metals, where the SI is negligible, we therefore use $\alpha = 0$, whereas for molecules, where SI is more pronounced, we use $\alpha = 1$. This shows that, while the ASIC method improves the position of the levels below E_F, it can lead to down-shifts for the empty states, resulting in a spurious enhanced G due to the LUMO. Further corrections are therefore needed in order to give a quantitatively sound value of G in such systems.

6.1.5 Conductance change under stretching

Hereafter we present results for the transport properties as a function stretching of molecules attached to flat Au electrodes. Fig. 6.11 shows the transmission coefficients for the Au-BDT-Au junctions corresponding to Figs. 6.4(c)-(h), while Fig. 6.12 shows the same for the Au-BDT2H-Au junctions of Figs. 6.5(c)-(h). We start by discussing the results for the Au-BDT-Au junctions. In this case the HOMO moves from lower energies at small L towards E_F at larger L. This results in an increase of G under stretching [Fig. 6.13(a)], in agreement with previous theoretical works [26, 27, 175, 176] for BDT attached to flat Au electrodes.

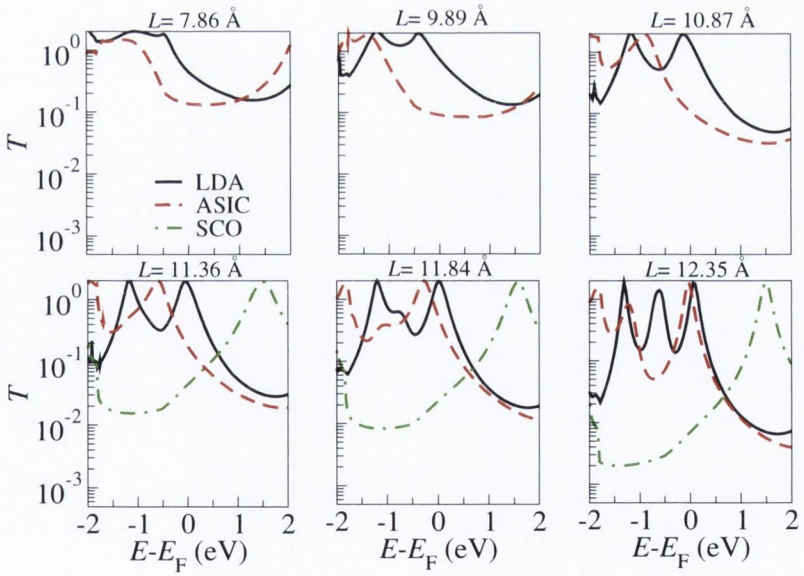

Figure 6.11: Transmission coefficients as a function of energy for different electrode separation for the Au-BDT-Au junctions. Comparison between LDA, ASIC and LDA+SCO.

By applying the ASIC the absolute value of G decreases by up to one order of magnitude when compared to the LDA value, since the HOMO level is shifted to lower energies (Fig. 6.11). For small L the ASIC $G(L)$ curve is approximately constant, while for large

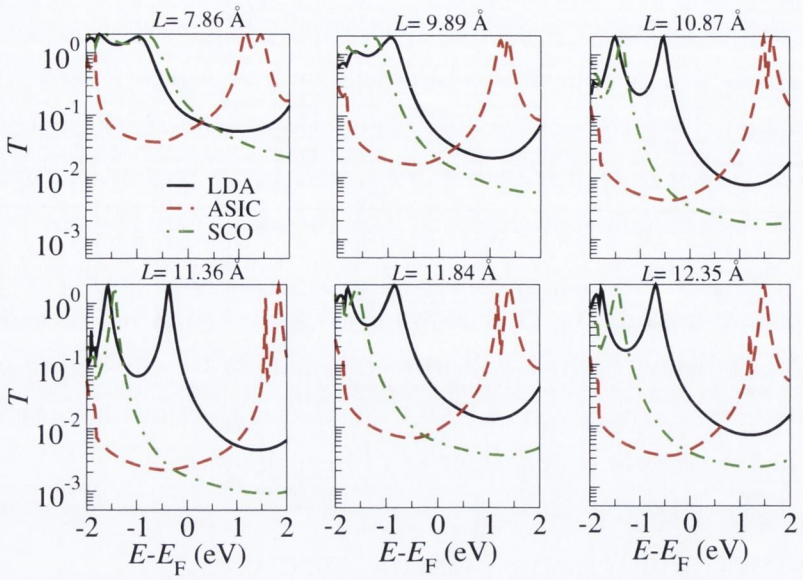

Figure 6.12: Transmission coefficients as a function of energy for different electrode separation for the Au-BDT2H-Au junctions. Comparison between LDA, ASIC and LDA+SCO.

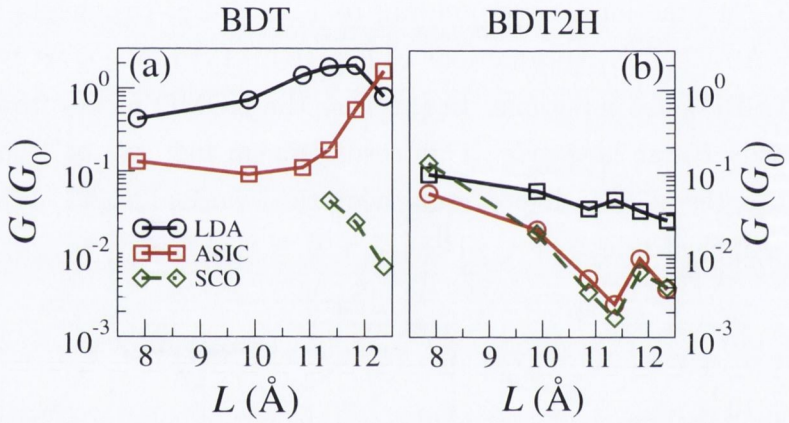

Figure 6.13: Conductance as a function of L for (a) Au-BDT-Au and (b) Au-BDT2H-Au molecular junctions. Comparison between LDA, ASIC and scissor operator (SCO) results.

L the value of G is found to increase for large L [Fig. 6.13(a)], which is also due to the fact that the HOMO level, Ψ_1, is approaching E_F as the junction is stretched. Our CDFT results presented in the previous section show that for $L \geq 11.36$ Å the Ψ_1 state is expected to be located at least $\sim$1.5 eV above E_F. Thus we apply the SCO to shift the eigenvalue of Ψ_1 to this energy and calculate the transmission (green-dashed lines) and G (for $L \geq 11.36$ Å) by using the calculated corrections presented in Tab. 6.3. The corrected G is smaller than the LDA results by up to two orders of magnitude and smaller than the ASIC by about a factor of 10.

In contrast, for the Au-BDT2H-Au structures, G decreases with increasing L for all used XC functionals (Fig. 6.12). For LDA G monotonically decreases from $0.1G_0$ to $0.026G_0$, while ASIC gives us values of G further reduced by up to one order of magnitude. By applying the SCO correction $E_{\mathrm{LDA}}^{\mathrm{gap}}$ increases, and consequently G decreases by more

than one order of magnitude when compared to the LDA results, except for the shortest distance considered. We note that although G is similar for ASIC and SCO, $T(E_F)$ is dominated by the LUMO tail for ASIC (see Fig. 6.12), while it is HOMO dominated for SCO. The agreement between ASIC and SCO is mainly due to the fact that both place E_F in the gap, and the change of G with stretching is mainly due to the change of the electronic coupling to the electrodes. Such decreasing trend of $G(L)$ was observed by Ning *et al.* [162] where considering Au-BDT2H-Au junctions and molecules symmetrically connected to an adatom structure. This is qualitatively in good agreement with the experiments of Kim *et al.* [17], where by means of low-temperature MCBJ, they reported values of G ranging from 6.6×10^{-4} to $0.5G_0$. Furthermore, high-conductance values were obtained when the molecular junction was compressed, *i.e.* for L decreasing. These are the key results of the present work since when combined with the results for the formation energy of the hydrogenated junctions, they indicate that the possibility of having thiol junctions can not be ruled out. In fact, the thiol structures might be the ones present in junctions where G decreases with elongation [172, 17].

An important difference between the Au-BDT-Au and the Au-BDT2H-Au junctions is the character of the charge carriers, *i.e.* whether the transport is hole-like or electron-like. For Au-BDT-Au, in the strong coupling limit where $L \leq 10.87$ Å, the charges tunnel through the tail of the HOMO-like level leading to a hole-like transport (see top panel of Fig. 6.11). In the weak coupling limit, after considering the SCO, the charge carriers tunnel through the tail of the LUMO-like level leading to an electron-like transport, as shown in the bottom panel of Fig. 6.11. For Au-BDT2H-Au junctions, the tunneling is always performed through the tail of the HOMO-like level (see Fig. 6.12) and therefore the charge carriers are holes. This is an important information since, experimentally, by means of thermoelectric transport measurements, it is possible to address which frontier molecular level is the conducting level. It has been shown [8] that for the systems discussed, this level is the HOMO, which agrees with our findings for the Au-BDT2H-Au junctions and also for the Au-BDT-Au junctions in the strong coupling limit.

6.1.6 Hybrid MD-MC for MCBJ simulations

As pointed out in Sec. 6.1, due to the nature of MCBJ experiments, several different geometrical contacts can be accessed during the stretching process of a junction. This leads to a statistical character of the experimental analysis. Moreover, temperature effects contribute to increase the number of possibilities to form the molecular junction. Therefore, it is important to incorporate these factors in the simulations in order to compare with experimental data. In this regard, balancing accuracy and computational efficiency can be challenging while attempting to simulate MCBJs. Simulations need to be accurate enough to capture the preferred bonding geometries and at the same time to incorporate

environmental factors. In the previous sections of the present Chapter, all the structures used for quantum transport were obtained using DFT, which is capable of describing accurately atomistic bonding, however, due to the high computational cost, the number of geometries one can deal with is limited. Moreover, DFT does not take into account temperature effects that may lead to structural changes.

Experimentally, the spontaneous formation of molecular junctions at fixed electrodes separation occurs of a time scale of ~0.1 s [178], which accounts for the time required for the bond formation and for the molecule to explore many different possible binding sites when forming the junction. In this section we present a hybrid classical molecular dynamics (MD) and Monte Carlo (MC) approach that allows us to mechanically and/or thermally evolve the Au-BDT-Au molecular junctions. We can then obtain more realistic molecular junction geometries that incorporate important aspects found in experiment, such as temperature effects, elongations rate effects, and non-ideal tip geometry. These geometries are then used as an input for the quantum transport calculations. This part of the work was done in collaboration with William French *et al.* (see Ref. [179]) who performed the MD-MC simulations.

The typical experimental time scales are inaccessible within MD simulations, since the time steps for integrating the equations of motions are on the order of femtoseconds (10^{-15} s). Usually, a MC approach, where configurational space is sampled randomly, can be used to overcome the slow kinetics of chemisorption. One of the limitations of these combined method is that classical MD can not describe the reactive nature of the SAM formation on top of the gold substrate. However, since the path to an equilibrium state has no meaning in MC, unphysical move types such as molecule identity swaps may be used to treat these reactions.

The MC sampling for the molecule to bind on the gold nanowire is performed within the semigrand canonical ensemble (SGCMC), *i.e.* constant-μVT, where μ is the chemical potential, V is the volume and T is the temperature and where the gold nanowire surface is in equilibrium with a bulk solution of the target molecules (see Sec. 3.2.2 of Ref. [179]). The SGCMC simulations begin with BDT molecules surrounding the gold nanowire and the probability of chemisorption increases as the molecules approach the nanowire. A cutoff distance for the S-Au bond is specified for the appropriate bonding site, *e.g.* on-top or on-bridge sites. Once the molecule has bonded, the hydrogen atoms attached to the sulfur atoms are dissociated and removed from the simulation box, so that the S atoms bind covalently to the gold site. Note that within MC, we do not obtain information about the dynamics of the bond formation. In fact, the MC method is used to produce thermodynamically favored equilibrium configurations. The moves within constant-μVT are performed until the density of BDT is relatively constant in the simulation box. Moreover, this is followed by MC moves within constant-NVT (N is the number of molecules), which allows the packing of BDT SAM to relax eventually leading to more

molecules attached to the surface.

During the MD simulations, the SGCMC sampling is applied to sample the preferred bonding geometries, where the results are passed back to the MD simulations. With this combined procedure, one can capture the dynamics of the packing and the bonding of the BDT SAM on the stretched nanowire. The SGCMC sampling is performed after some interval of MD stretching, *e.g.* between 0.1-1.0 Å, and the number of SGCMC sampling steps is determined by the MD interval. A large interval requires a larger number of SGCMC moves in order to fully sample the sites of the deformed nanowire. Fig. 6.14 shows representative molecular junctions for the MD-MC approach. Fig. 6.14(a) shows a gold nanowire coated with BDT SAM obtained with the MC SGCMC approach. Then MD simulations are performed where the nanowire is stretched in intervals Δx, Fig. 6.14(a)-(e), at finite temperature (77 K). When the molecule is trapped between the electrodes, Fig. 6.14(c), the SAM is removed from the simulation box in order to simulate the evaporation procedure carried out in experiments. The combined MD-MC moves are performed until the junction breaks down, as shown in Fig. 6.14(e). This procedure closely models the MCBJ's experiment and thus should produce representative experimental configurations. Moreover, it allows us to obtain a larger number of molecular junction geometries when compared to DFT, allowing for the assessment of better statistics, in the present case, ~100 different junctions.

Computational details

The gold nanowire for the MD-MC simulations consists of eight atoms in length and it is three-atom thick. It is connected between two rigid [100] leads four-atom long and six-atom thick. The BDT SAM consists of 30-36 molecules chemisorbed and it is placed onto the gold nanowire by performing SGCMC MC moves. The non-adsorbed molecules are then removed from the simulation box and 20 million constant-NVT are realized to equilibrate the monolayer. The stretching process of the full system (nanowire plus molecules) is carried out by displacing the right lead in steps of 0.1 Å in the [100] direction. The time interval for the MD simulations is 20 ps and we perform 100,000 MC moves at constant-NVT between MD intervals. The molecule may or may not connect between the two electrodes. In our simulations, a BDT molecule attaches between the two ruptured electrodes in ~30% of the runs (31 out of 104), which is in good agreement with experimental observation of 30-40% [180]. Moreover, in those in which it does form a molecular junction, the junction is stretched further allowing the molecule to sample different geometries. During the elongation, between intervals of 0.5-1.0 Å, geometries are extracted to be used in the quantum transport calculations in order to obtain the conductance.

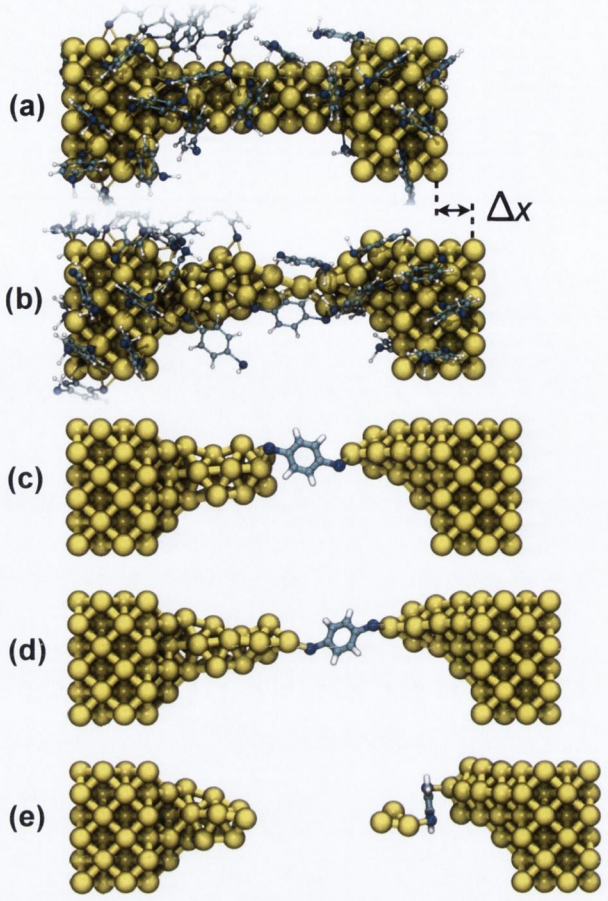

Figure 6.14: Representative snapshots of the elongation process from formation to rupture of a Au-BDT-Au molecular junction. From top to bottom, Δx =0.0, 4.0, 8.0, 12.0 and 16 Å. Once a molecule is trapped between the electrodes, the monolayer of molecules is removed in order to isolate electrode geometry effects.

Thermal evolution of Gold-BDT junctions

One can also investigate the thermal evolution of the Au-BDT-Au molecular junction. For representative electrodes separation during the stretching process, we fix the distance and we perform the MD-MC simulations where again geometries are extracted to be used as input for conductance calculations. 200 cycles of MD-MC are performed, where a cycle consists of 0.2 ns of MD with 200,000 MC moves. With this approach, one can study how the dynamics of the individual parts of the system affects the final geometries and therefore the calculated conductance. For instance, we can fix the electrodes and allow only the molecule to evolve during the MD-MC procedure or we can fix the molecule and allow just the electrodes to move. By doing so, we can identify the independent contributions of changes in the conductance due to the gold and BDT geometries fluctuations. Details of this study can be found in Ref. [29].

Conductance traces

Recently, using low-temperature MCBJs Bruot *et al.* [4] observed some conductance traces where G changed from $0.01G_0$ to $0.1G_0$ by increasing L. Although, the experiments are performed in low temperature (4 K) and room temperature, only in low temperature the conductance enhancement was observed. The authors attributed this to the HOMO level moving up in energy towards the E_F of the electrodes, which is in agreement with our findings for the strong coupling limit, as shown in Fig. 6.13(a). However, most experimental results [15, 16, 17, 18, 19, 20, 22, 23, 181, 3, 5, 6, 7, 8, 9, 10, 11, 12, 13] show conductance traces with either approximately constant G under stretching, or with decreasing G with increasing L [172, 17].

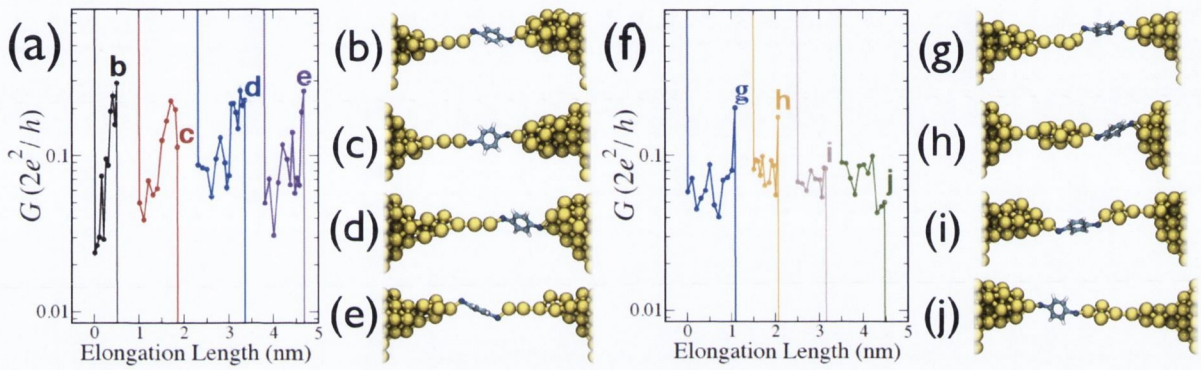

Figure 6.15: (a) Four gradually increasing conductance traces where the formation of MACs can be observed. The corresponding molecular junctions prior to rupture are shown in (b-e). The traces are offset along the x-axis for clarity. (f) Representative conductance traces without formation of MACs where the corresponding junctions prior to rupture are shown in (g-j).

In our MCBJs simulations [30], two types of conductance traces are found: (i) in Fig. 6.15(a), the conductance gradually increases with elongation. The increase of G is found only for junctions that form monoatomic chains (MACs) of gold atoms connected to the BDT molecules. (ii) Fig. 6.15(f) shows conductance traces where the curves are relatively flat with elongation. In Fig. 6.15(b-e) and Fig. 6.15(g-j) are shown the corresponding geometries prior to rupture. From the geometries that show conductance increase, the breaking geometries [Fig. 6.15(b-e)] show the formation of MACs of gold atoms connected to the BDT molecule. Approximately 13% of the formed molecular junctions show MACs formation during the elongation process. In order to further understand our findings, we build idealized molecular junctions where MAC are present and we perform the transport calculations. As shown in the inset of Fig. 6.16, a MAC is first inserted at the left tip, then at the left and right tips and the adatom-adatom geometry is shown for completeness. Indeed MACs formation leads to a broadly enhancement of the PDOS around E_F (not shown) due to contributions of gold s and p_z states, which

induce a stronger coupling between the molecular energy levels and the electrodes. This leads to higher transmission coefficients, Fig. 6.16, therefore higher conductance values. Such a trend adds to the increase of G due to the HOMO shifting closer to E_F under stretching. The magnitude and shape of the enhancement depends mainly on the length of the MAC, but also on the S-Au bonding and the remaining details of the junction structure. Note that adatoms or tip-like electrodes do not result in this enhancement, as discussed in Fig. 6.10.

Unlike MACs, other structures that present low-coordination electrodes such as Au-Au_2-Au units, as shown in Fig. 6.15(g-h), do not increase gradually the conductance. Although they present higher conductance, they have very short lifetimes, of the order of 1.0 ns, *i.e.* they are too short-living to be measured in experiment. On the contrary, MACs remain stable for the complete duration of a 1.0 μs simulation without stretching, which indicates that they show to be stable enough to be measured, a fact corroborated in experiments [182] and in simulations [183]. Thus, our results show how significant these MAC formation can have on the conductance.

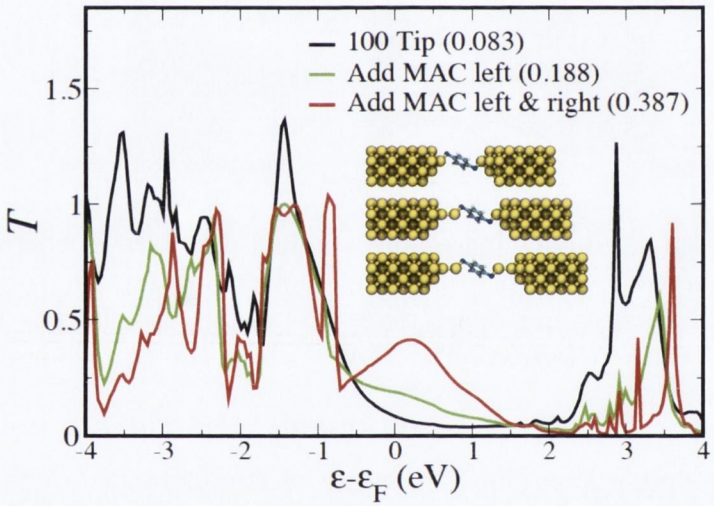

Figure 6.16: Transmission coefficients for three idealized Au-BDT-Au junctions where MACs are included. The PDOS at E_F is enhanced due to gold atoms and the conductance increases (values between brackets).

We further validate our findings by thermally evolving (at 77 K, without stretching) three structurally distinct Au-BDT-Au junctions. Fig. 6.17 shows the distribution of conductance for the three structures shown as insets. For the geometry that shows the MAC, the conductance distribution has almost no overlap with the histograms of the other deformed geometries studied. This indicates that the enhancement of conductance observed is related to their particular structure and not simply due to a short-lived configuration. Moreover, the conductance fluctuations (standard deviation) is approximately twice as large compared to the other distributions. When the simulations are repeated at room temperature (without stretching) for the junctions shown in Fig. 6.15(b-e), all of them

breakdown in less than 1.0 ns, indicating that MACs are not stable at high temperature. This explains why at room temperature Bruot *et al.* do not observe conductance enhancement with stretching.

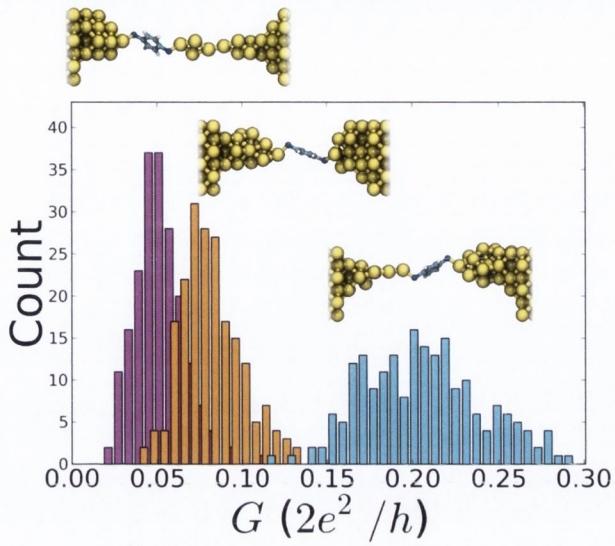

Figure 6.17: Conductance histograms of three thermally evolving Au-BDT-Au junctions. The structure containing MAC's show higher conductivity and negligible overlap with the other junctions that do not show MACs formation. The standard deviations of the histograms (from left to right) are $0.014G_0$, $0.018G_0$ and $0.034G_0$.

6.2 Conclusion

We have performed DFT calculations to study the adsorption process of methanethiol and BDT2H molecules on the Au(111) surface. For all the structures studied we find that thiols are energetically more stable than their thiolate counterparts. Moreover, we find a large activation barrier of about 1 eV for the the dissociation of the H atom from the thiol groups adsorbed on Au(111). These results indicate that the non-dissociated structures are likely to exist in experiments and therefore can not be ruled out.

The energy level alignment between molecule and electrodes is one of the main factors that determine the conductance. To overcome the limitations of using the LDA-DFT eigenvalues we apply a CDFT method, which is based on total energy differences in the same way as ΔSCF calculations, with the difference that it allows also the inclusion of the non-local Coulomb interaction that leads to the renormalization of the energy levels as the molecule is brought close to a metal surface. We find a reduction of the BDT $E_{\mathrm{QP}}^{\mathrm{gap}}$ of 2.09 eV with respect to its gas phase gap, when the molecule is brought closer to a single Au(111) surface. CDFT also allows us to obtain the height of the image charge plane on Au(111), which we find to be at about 1 Å above the gold surface. While for the BDT2H molecules the coupling to the surface remains small at all distances, for small

molecule-surface separation the electronic coupling between BDT and Au becomes very strong, and in this limit the use of the CDFT approach is not applicable. The strong coupling leads to a significant electron transfer from the surface to the molecule, so that the molecular LUMO of the isolated BDT becomes increasingly occupied as the molecule-surface distance decreases. For the Au(111)-BDT2H, the filling of the molecular orbitals does not depend on the distance to Au. When we correct for the self-interaction error in the LDA XC functional the electron transfer is enhanced and at the equilibrium bonding distance, the molecular LUMO of the isolated BDT becomes fully filled at the junction.

By means of NEGF+DFT we have then calculated the transport properties of the junctions with different contact geometries and compare the results obtained with LDA, ASIC and LDA+SCO functionals. For the thiol structures, the LDA values for G are about one order of magnitude smaller than their thiolate counterparts. ASIC leads to values of G in better agreement with experiments for the thiolate systems. However, ASIC also leads to a spurious increase of G for the thiol junctions due to the down-shift of the empty states towards E_{F}, an artifact avoided in the SCO approach. We find that Au-BDT-Au and Au-BDT2H-Au junctions show opposite trends concerning the dependence of G on the separation between flat Au electrodes; G decreases with L for the thiol junctions, whereas the thiolates show the opposite trend. Since for Au-BDT2H-Au there is no significant charge transfer between the electrodes and the molecule, we can apply the SCO approach to set the HOMO-LUMO gap to the one obtained from CDFT calculations. In this way G decreases by up to two orders of magnitude when compared to the LDA values, and this brings the results in good quantitative agreement with the experimental data.

We finally presented a hybrid classical molecular dynamics and Monte Carlo approach to mechanically and/or thermally evolve the Au-BDT-Au molecular junctions. This approach allowed us to obtain more realistic molecular junction geometries. Moreover, important aspects found in experiment, such as temperature effects, elongations rate effects were assessed. By performing transport calculations of representative geometries extracted from the MD-MC approach, we found that the conductance enhancement observed by Bruot *et al.* can well be explained by the formation of MACs during the elongation process. Our results therefore suggest that thiol junctions must be present in experiments where G decreases with L. In contrast, thiolates structures are likely to be present in experiments showing a increase of the conductance upon stretching.

Chapter 7

Electronic Transport and Level Alignment in the Coulomb Blockade

Perrin *et al.* [37] using a MCBJ were able to observe the energy level renormalization of a zinc-porphyrin molecule [Zn(5,15-di(p-thiolphenyl)-10,20-di(p-tolyl)porphyrin)], abbreviated ZnTPPdT, where the molecule is connected to two gold electrodes. In their experiment, besides the two electrodes connected to the molecule, a third electrode was used as gate electrode in order to uniformly shift the molecular energy levels. As the electrodes separation was reduced, *i.e.* the junction was compressed with respect to the initial equilibrium configuration, the authors could measure the dc current. By varying the gate voltage, they could observe that as the junction was compressed, the dc bias needed to reach the conducting energy level (onset of current) was reduced, indicating that this level was approaching E_{F}. Furthermore, this effect was reversible, which led to the conclusion that the molecular energy gap was renormalized by the image charge effect due to the change on the electrodes separation. One important aspect of these measurements is that the molecule was weakly coupled to the electrodes so that the transport is in the CB regime.

From a theoretical point of view, in order to simulate the experiment we need some ingredients. Firstly, we need to determine the atomic geometries of the junction as a function of the electrodes separation and this task is realized with ground state DFT [65, 66] calculations. Secondly, the energy level alignment as a function of the stretching [153, 31], which is achieved by evaluating the parameter-free classical image charge model, as we have discussed in Chapter 5 and in Chapter 6. Thirdly, we want to study the electronic transport properties of these molecular junctions and compare to the experimental data.

The study of the transport properties of molecular junctions have mostly employed the NEGF formalism [184, 185] and often combined with DFT as the chosen electronic structure theory. Despite of the great success of this combination, the method presents some important limitations, as discussed in Chapter 5 and Chapter 6. In fact, due to the lack of the derivative discontinuity of the XC potential in DFT-LDA (see Sec. 2.5.2),

CB type of transport can not be captured since the energy levels position depend linearly with their occupation. Thus, the transfer of integer number of electrons (fingerprint of CB processes) is not observed, although corrections for self-interaction have shown to recover part of this feature [186].

In the present chapter we present an inexpensive approach based on master equations (ME) [117, 118, 120, 121, 114] including cotunneling effects to molecular conduction in the CB regime. The parameters for the ME are obtained by performing DFT-NEGF. By employing this combined approach, we compare our results to experimental data.

7.1 Computational details

7.1.1 *Ab initio* approach: DFT+NEGF

All the *ab initio* calculations presented are based on DFT as implemented in the SIESTA package [96]. The XC energy is treated within the LDA approximation. We use norm-conserving pseudopotentials according to the Troullier-Martins procedure [143] and the basis set is double-ζ polarized for carbon, sulfur and hydrogen and single-ζ for gold atoms [29, 30]. The mesh cutoff is 300 Ry and four k-points are used for the Brillouin zone sampling in the perpendicular direction to the transport. For the *ab-initio* quantum transport calculations, we use the NEGF formalism as implemented in the SMEAGOL code [187, 188]. Within this approach, the retarded Green's function of the scattering region, $\mathcal{G}_{\mathrm{D}}$, is given by [see Eq. (3.3.17)]

$$\mathcal{G}_{\mathrm{D}}(E) = \lim_{\eta \to 0} \left[(ES_{\mathrm{D}} + i\eta) - H_{\mathrm{D}} - \Sigma_{\mathrm{L}}(E) - \Sigma_{\mathrm{R}}(E) \right]^{-1}, \tag{7.1.1}$$

where E is the energy, $\Sigma_{\mathrm{L,R}}(E)$ are the self-energies of the left and right electrodes, S_{D} is the overlap and H_{D} is the Hamiltonian matrix of the scattering region obtained from DFT calculation, see Chapter 3, Sec. 3.3. The coupling to the electrodes are given by $\Gamma^{\mathrm{NEGF}}_{\mathrm{L,R}}(E) = i\left(\Sigma_{\mathrm{L,R}} - \Sigma^{\dagger}_{\mathrm{L,R}}\right)$, *i.e.* the imaginary part of the self-energy defined as [see Eq. (3.3.18)]

$$\Sigma_{\mathrm{L}}(E) = (ES_{\mathrm{LD}} - V^{\dagger}_{\mathrm{LD}}) g_{\mathrm{L}}(E) (ES_{\mathrm{LD}} - V_{\mathrm{LD}}), \tag{7.1.2}$$

where $g_{\mathrm{L}}(E)$ is the surface Green's function of the isolated electrode L and V_{LD} is the interaction between the scattering region and the electrode. All these quantities are matrices. The same can be defined for the right electrode. Finally the density of states (DOS) of the isolated electrode L can be written in terms of its Green's function as $\nu^{\mathrm{NEGF}}_{\mathrm{L}}(E) = \frac{1}{2\pi}\mathrm{Tr}\left[g_{\mathrm{L}}(E) - g_{\mathrm{L}}(E)^{\dagger}\right] S_{\mathrm{LD}}$. From the Green's function and couplings, the non-equilibrium charge density can be computed and by following a self-consistent procedure, for a specific applied bias, the transmission coefficients are given by Eq. (3.4.32) and the electrical current given by Eq. (3.4.36).

7.1.2 Model Hamiltonian and master equation approach

We define the Hamiltonian of the system by

$$\hat{H} = \hat{H}_{\text{mol}} + \hat{H}_{\text{L}} + \hat{H}_{\text{R}} + \hat{H}_{\text{T}}, \tag{7.1.3}$$

where the molecular Hamiltonian is given by the Anderson-Holstein model as

$$\hat{H}_{\text{mol}} = \sum_{i}^{M} \epsilon_i \hat{n} + \sum_{i}^{M} \frac{\mathcal{U}}{2} \hat{n}\left(\hat{n}-1\right) + \hbar\omega_p \left(\hat{b}^\dagger \hat{b} + 1/2\right) + \sum_{i}^{M} \lambda\hbar\omega_p \left(\hat{b}^\dagger + \hat{b}\right) \hat{n} \tag{7.1.4}$$

with i single-particle states of energy ϵ_i and charging energy $\mathcal{U}$. Moreover, the operator $\hat{n} = \sum_\sigma \hat{c}^\dagger_{i\sigma}\hat{c}_{i\sigma}$ is the number operator and $\hat{c}^\dagger_{i\sigma}(\hat{c}_{i\sigma})$ creates (annihilates) an electron in the molecular state i with spin σ. The isolated Hamiltonian for the electrode α is given by

$$\hat{H}_\alpha = \sum_{\alpha\mathbf{k}\sigma} \epsilon_{\alpha\mathbf{k}\sigma} \hat{d}^\dagger_{\alpha\mathbf{k}\sigma} \hat{d}_{\alpha\mathbf{k}\sigma}, \tag{7.1.5}$$

where $\alpha = \text{L}, \text{R}$. The third and fourth terms of Eq. (7.1.4) describe the vibronic degrees of freedom for one vibron-mode of energy $\hbar\omega_p$, $\hbar$ is the Planck's constant, and λ is the electron-vibron coupling. $\hat{b}^\dagger(\hat{b})$ is the creation (annihilation) bosonic operator for the vibrons. The operator $\hat{d}^\dagger_{\alpha\mathbf{k}\sigma}(\hat{d}_{\alpha\mathbf{k}\sigma})$ creates (annihilates) an electron with momentum $\mathbf{k}$ in the electrode α with spin σ. Finally the interaction between the leads and the molecule is given by the so-called tunneling Hamiltonian

$$\hat{H}_{\text{T}} = \sum_{\alpha i\mathbf{k}} \left[\gamma_\alpha \hat{c}^\dagger_i \hat{d}_{\alpha\mathbf{k}} + \gamma^*_\alpha \hat{c}_i \hat{d}^\dagger_{\alpha\mathbf{k}}\right], \tag{7.1.6}$$

which is treated as a perturbation. The electron-vibron coupling term can be eliminated by a canonical transformation [189, 190, 116] (see Appendix C.2), leading to a renormalization of $\epsilon_i \to \tilde{\epsilon}_i = \epsilon_i - \lambda^2\hbar\omega_p$ and $\mathcal{U} \to \tilde{\mathcal{U}} = \mathcal{U} - 2\lambda^2\hbar\omega_p$ and it introduces a translation operator into the tunneling matrix elements $\gamma_\alpha \to \gamma_\alpha \text{exp}[-\lambda(\hat{b}^\dagger - \hat{b})]$ [116].

Within the $\mathscr{T}$-matrix [108, 119, 123, 114] approach presented in Sec. 4.5, we evaluate the diagonal terms of the reduced density matrix, which are given by [114, 115]

$$\dot{\rho}^q_m(t) = \sum_{\alpha; n\neq m, q'} \left(\Gamma^{nm;q'q}_\alpha \rho^{q'}_n - \Gamma^{mn;qq'}_\alpha \rho^q_m\right) + \sum_{\alpha\alpha'; n, q'} \left(\Gamma^{nm;q'q}_{\alpha\alpha'} \rho^{q'}_n - \Gamma^{mn;qq'}_{\alpha\alpha'} \rho^q_m\right) \tag{7.1.7}$$

$$+ \frac{1}{\tau}\left(\rho^q_m - \rho^q_{\text{eq}} \sum_{q'} \rho^{q'}_n\right), \tag{7.1.8}$$

where ρ^q_m is the occupation of the state $|m, q\rangle$; the first index m refers to electronic states whereas the index q runs over vibronic states. To lowest order in $\hat{H}_{\text{T}}$, one describes the *sequential-tunneling* processes where one electron is transferred from one electrode

to the molecule and vice-versa, as schematically shown in Fig. 7.1(a). The transition

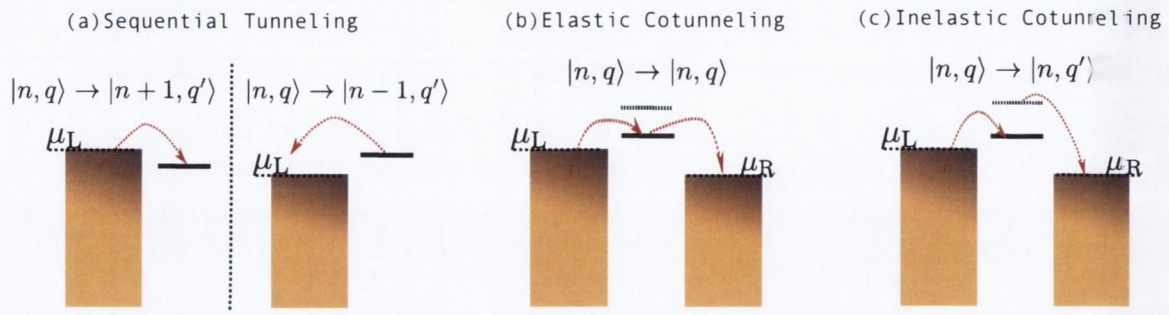

Figure 7.1: Schematic representation of different transport regimes. (a) Sequential tunneling from the electrode to the molecule (left) and from the molecule to the electrode (right). (b) Elastic cotunneling, where the molecule is left in the same charge state. (c) Inelastic cotunneling where the final charge state is different from the initial one. This can happen when vibrons and photon-assisted processes are considered.

rates, $\Gamma_\alpha^{mn,qq'}$, for electrons to tunnel between the molecule and the electrode α when the molecule makes a transition from the state $|m;q\rangle$ with total energy E_{mq} to the state $|n;q'\rangle$ of energy $E_{nq'}$ are given by [114, 117]

$$\Gamma_\alpha^{mn} = \frac{\Gamma_\alpha}{\hbar}\sum_{i\sigma}\left\{f(E_{mq}-E_{nq'}-\mu_\alpha)|A_{nm}^{i\sigma}|^2|F_{q'q}|^2 + \left[1-f(E_{nq'}-E_{mq}-\mu_\alpha)\right]|A_{mn}^{i\sigma}|^2|F_{qq'}|^2\right\}, \tag{7.1.9}$$

where $m \to n$ and $q \to q'$ represent changes on the number of electrons and excited vibrons, respectively. A complete derivation of this equation is given in Appendix C. $\Gamma_\alpha = 2\pi\gamma_\alpha^2\nu_\alpha$ are the bare electronic couplings to the electrodes, ν_α is the density of states and γ_α is the momentum independent hopping parameter. Moreover, $A_{n'n''}^{i\sigma} = \langle n'|\, c_{i\sigma}\,|n''\rangle = \delta_{n',n''+1}$ is the matrix element of the annihilation operator for the single-particle state i with spin σ and $F_{q'q} = \langle q'|\, e^{-\lambda(\hat{b}^\dagger-\hat{b})}\,|q\rangle$ are the Franck-Condon matrix elements [115, 116]. These processes are dominant as long as the conducting energy level is within the bias window. However, if the level is outside the bias window, the sequential tunneling decreases exponentially and higher order processes will dominate.

The next-to leading-order in the $\mathscr{T}$-matrix expansion is determined by *cotunneling* processes [second term of Eq. (7.1.8)] and the transition rates are given by (see Appendix C) [118, 119, 114, 120, 121]

$$\Gamma_{\alpha\alpha'}^{nn';qq'} = \frac{\Gamma_\alpha\Gamma_{\alpha'}}{2\pi\hbar}\sum_{i''\sigma''}\sum_{i'\sigma'}\int dE\left|\sum_{n'',q''}\left(\frac{A_{n'n''}^{i''\sigma''}A_{nn''}^{i'\sigma'*}F_{q'q''}F_{qq''}^*}{E+E_{nq}-E_{n''q''}+i\eta} + \frac{A_{n''n'}^{i''\sigma''*}A_{n''n}^{i'\sigma'}F_{q''q'}^*F_{q''q}}{-E+E_{n'q'}-E_{n''q''}+i\eta}\right)\right|^2$$
$$\times f(E-\mu_\alpha)\left[1-f(E+E_{nq}-E_{n'q'}-\mu_{\alpha'})\right]. \tag{7.1.10}$$

$\Gamma_{\alpha\alpha'}^{nn';qq'}$ describes the transition rates to transfer coherently (tunneling) one electron from the electrode α while the molecule is in the state $|n;q\rangle$ to the electrode α', leaving the molecule in the state $|n';q'\rangle$. The occupation of the molecule changes just virtually in the intermediate state, *i.e.* the number of electrons in the molecule is the same during cotunneling processes. Fig. 7.1(b-c) shows schematically the elastic and inelastic cotunneling processes. We disregard tunneling processes changing the number of electrons in the molecule by ± 2. This is achieved by constructing a general final state as $|j'\rangle\,|n'\rangle = \hat{d}_{\alpha'\mathbf{k}'}^{\dagger}\hat{d}_{\alpha\mathbf{k}}\,|j\rangle\,|n'\rangle$, with $\alpha \neq \alpha'$. Note that Eq. (7.1.10) diverges due to the second order poles. To circumvent this numerical problem, we apply a regularization [115] procedure that removes the singularities. The details are presented in Appendix C.

By solving Eq. (7.1.8) with the time derivatives set to zero and the normalization condition $\sum_i \rho_i = 1$ one obtains the steady-state current through the left electrode as [114, 115]

$$I^{\mathrm{L}} = -e \sum_{nm;qq'} (N_n - N_m)\,\Gamma_{\mathrm{L}}^{nm;q'q}\rho_{m;q} - e \sum_{nm;q'q} \left(\Gamma_{\mathrm{LR}}^{nm;q'q} - \Gamma_{\mathrm{RL}}^{nm;q'q}\right)\rho_{m;q}, \tag{7.1.11}$$

where N_n is the number of electrons in state $|n;q\rangle$. In our model, we map the problem onto an orthogonal basis set and we consider only the two single-particle states relevant to the problem, *i.e.* the frontier molecular orbital HOMO and LUMO. The states are considered spin-degenerated so that the contributions of each spin are cast out into a spin factor constant [115]. For simplicity, we do not allow a second electron in the molecule, *i.e.* $\mathcal{U} \to \infty$. Therefore, the states used to construct the basis set for the reduced density matrix are $|0;q\rangle$, $|1,0;q\rangle$ and $|0,1;q\rangle$, *i.e.* empty molecule, an electron in the HOMO and an electron in the LUMO, respectively, for q number of vibrons. The last term of Eq. (7.1.8) is added on a phenomenological basis and describes relaxation of the vibrations towards the equilibrium distribution $\rho_{\mathrm{eq}}^{q} = e^{-q\hbar\omega_p/k_{\mathrm{B}}\Theta}(1 - e^{-\hbar\omega_p/k_{\mathrm{B}}\Theta})$ on a time scale τ. For $\tau \to \infty$ the system is unrelaxed whereas $\tau \to 0$ the system is relaxed to the vibronic ground state.

7.2 Case of study: gold-ZnTPPdT molecular junctions

We start by discussing the results for the *ab-initio* transport calculations. For the MJs calculations, the electrode is modeled by considering a five-layer-thick 8×8 Au(111) supercell. The molecule is connected to the electrodes via a hollow site of the equilibrium distance [37] of $d \equiv d_{\mathrm{Au-Au}} = 23.2$ Å , as shown in Fig. 7.2(a). In order to model the effect of the image charge as a function of d, three new configurations are built (without structural relaxation) where the molecule is tilted forming an angle θ relative to the straight equilibrium configuration, as shown in Fig. 7.2(b-d).

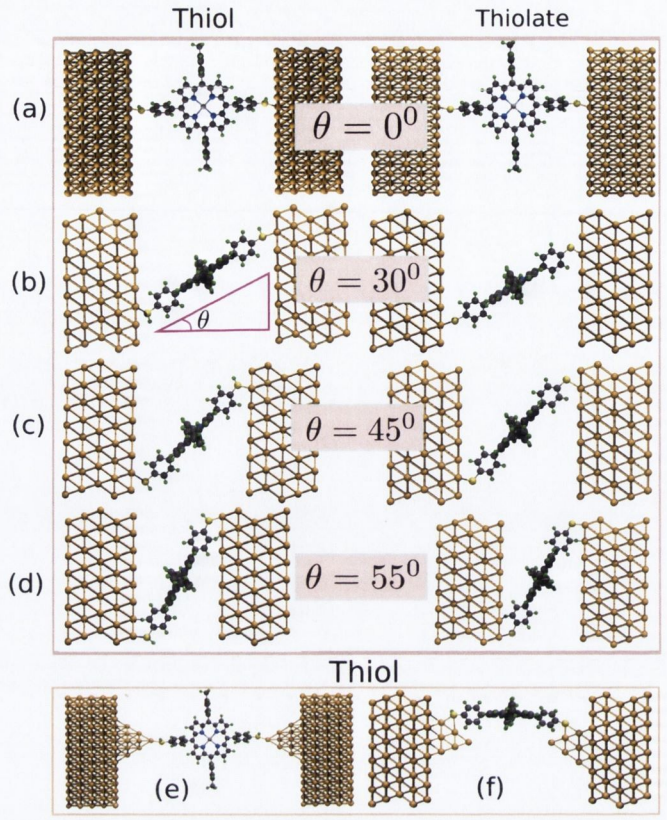

Figure 7.2: Ball-stick representation of Au-ZnTPPdT-Au molecular junctions when the junction is compressed to simulate a MCBJ experiment. (a)-(d) Two flat surfaces are considered and the molecule tilts making an angle θ between its plane and the transport direction. (e)-(f) Two tip electrodes are considered and the molecule slides on top of the two gold tips.

Fig. 7.3 shows the transmission coefficients (a-b) and the $I \times V$ characteristics (c-d) for different values of θ computed with DFT-NEGF for thiol and thiolate junctions, respectively. The thiolate junctions are obtained by removing the hydrogen atoms attached to the sulfur atoms in the SH group. In both cases, the transport is dominated by the HOMO level. The tunneling current for the thiolate junction is one order of magnitude larger than its thiol counterpart due to the stronger coupling to the electrodes, as shown in Tab. 7.1, and due to the fact that the HOMO enters the bias window for the range of applied bias. Moreover, the resonances position are essentially unchanged for different values of θ. This confirms the fact that LDA is not able to capture the renormalization of the energy levels due to the image charge effect.

In Chapter 6 we show that thiol and thiolate junctions may coexist in MCBJs experiments [31]. Since the thiolate junctions seems to lead to a systematic larger current than the thiol ones, we focus our attention on the thiol junctions. We first study the properties of the gas phase ZnTPPdT(thiol) molecule. $E_{\mathrm{LDA}}^{\mathrm{gap}}$ is largely underestimated when compared to $E_{\mathrm{QP}}^{\mathrm{gap}} = E^{\mathrm{A}} - I^{\mathrm{P}}$ calculated by using the ΔSCF method. Our results show that the HOMO is higher in energy by $\sim$1.4 eV when compared to $-I_{\mathrm{P}} = -6.39$ eV. On the

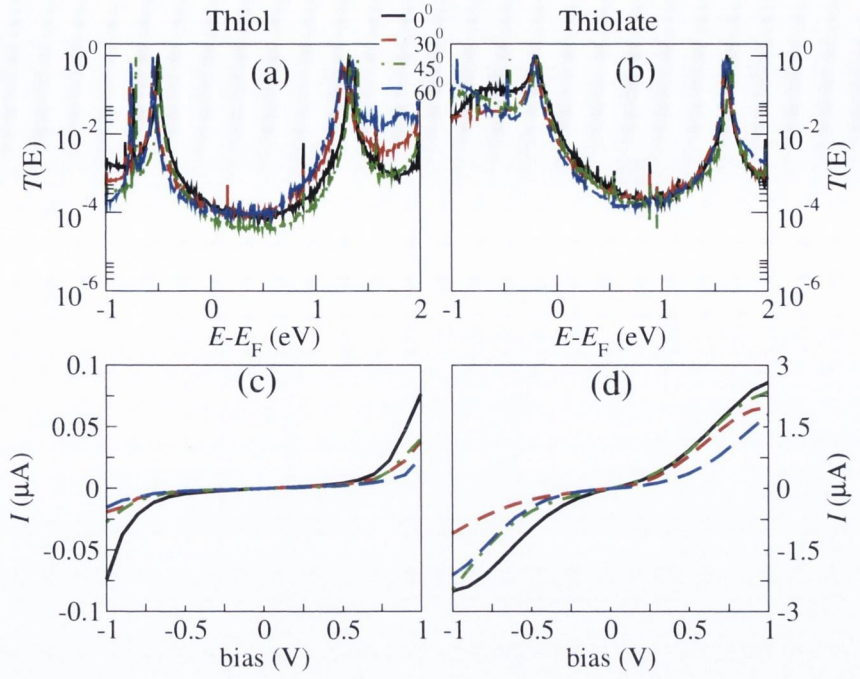

Figure 7.3: NEGF results: top panels show the transmission coefficients as a function of energy for different values of the stretching parameter θ for (a) thiol and (b) thiolate junctions. Bottom panels, the same for current as a function of bias voltage.

contrary, the LUMO is lower in energy by ~1.45 eV when compared to $-E^{\mathrm{A}} = -1.74$ eV. Similar differences are also found for the ZnTPPdT(thiolate) molecule. These results show that the KS eigenvalues offer a poor description of the molecular quasi-particle energy levels within LDA, in the gas phase, as also discussed in Chapter 5.

7.2.1 Energy level alignment

In order to account for the image charge effects (see Sec. 6.1.2) [31], when the molecule is in the junction, we calculate the corrections to the molecular energy levels as a function of d. Fig. 7.4 shows the corrected frontier energy levels as a function of d (the corresponding θ is also shown) for the ZnPPTdT(thiol) molecule in the junction. The energy levels are offset by the metal workfunction ($W_{\mathrm{F}} = 5.5$ eV). W_{F} is calculated by taking the difference between the vacuum potential and the slab Fermi energy (E_{F}) of the gold substrate. The green-dashed lines correspond to the gas-phase limit for the ZnPPTdT(thiol) molecule. Since the transport properties of MJs depends strongly on the energy level alignment between the molecular energy levels with respect to the electrodes chemical potentials, corrections to the frontier energy levels should be applied in order to compare our calculations with experimental data.

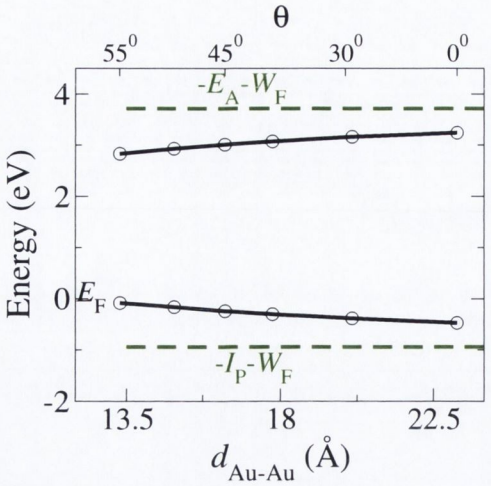

Figure 7.4: Corrected position for the frontier energy levels of the thiol junctions (with respect to $W_{\mathrm{F}} = 0$) as a function of the electrodes separation. Dashed-green lines are the $-E^{\mathrm{A}}$ and $-I^{\mathrm{P}}$ offset by W_{F} showing the gas-phase molecule limit. The calculations have been performed by means of Eq. (5.1.8) where the image charge plane height is obtained from CDFT.

7.2.2 Master equation approach: charge transport in Coulomb blockade regime

In order to describe the Coulomb blockade regime (weak coupling limit) observed in experiments, we apply the ME approach. Firstly, we validate the ME method by benchmarking it with the DFT-NEGF. Fig. 7.5(left) shows the LDA transmission coefficients as a function of energy for the thiol ($\theta = 0$) junction calculated with NEGF at equilibrium (0 V). Since LDA underestimates the position of the LUMO, we apply SCO [31] approach (Sec. 6.1.3) to correct its energy position to the one given in Fig. 7.4.

Extracting electronic couplings from DFT-NEGF calculations

We then perform the transport calculations within the NEGF framework and obtain the transmission coefficients for the corrected energy levels positions. The electronic couplings are extracted by fitting a Lorentzian curve to the transmission coefficients as

$$T(E) = \sum_i \frac{\Gamma_{\mathrm{L}i}\Gamma_{\mathrm{R}i}}{(E - E_i)^2 + \frac{1}{4}(\Gamma_i)^2}, \tag{7.2.1}$$

where $\Gamma_i = \Gamma_{\mathrm{L}i} + \Gamma_{\mathrm{R}i}$ for $i = \mathrm{HOMO}, \mathrm{LUMO}$ levels. The results for the electronic couplings are shown in Tab. 7.1.

Connection between the parameters obtained with NEGF and ME

In order to make the connection between the electronic couplings obtained with NEGF, $\Gamma^{\mathrm{NEGF}}_{\mathrm{L,R}}(E)$, and the ones defined within ME, Γ_α, we first assume that the scattering

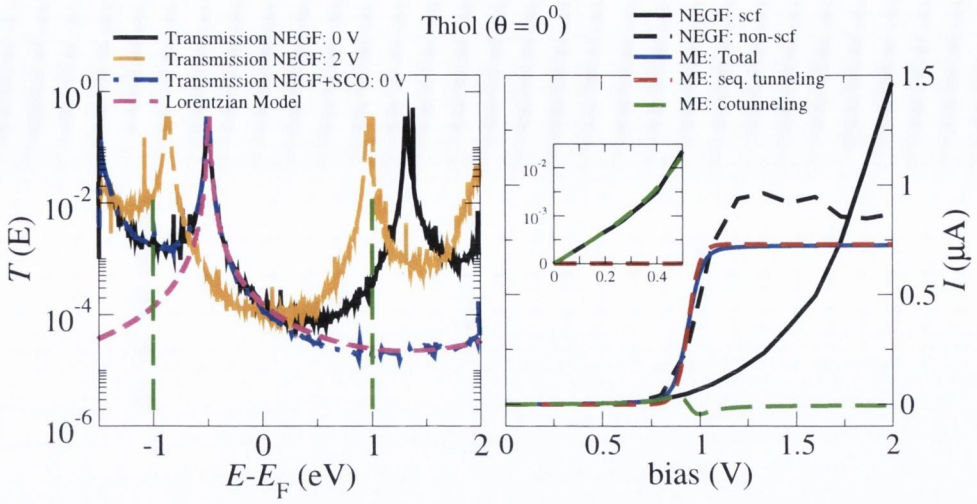

Figure 7.5: Thiol junction with $\theta = 0^0$. (left panel) Transmission coefficients as a function of energy obtained with NEGF at 0 V and 2 V. The transmission coefficient when the LUMO level is corrected to the E^{A} (NEGF+SCO) and best fit for the Lorentzian model (at equilibrium) to extract the couplings. (right panel) $I \times V$ comparison between the NEGF and ME. For the NEGF, the self-consistent (scf) current is compared to the non-self-consistent (non-scf). For the ME results, we also show for completeness the separated contributions for the sequential tunneling and cotunneling. Inset shows the low bias limit to which cotunneling dominates, therefore, the ME cotunneling current is very similar to the NEGF-scf. The bias window is highlighted with the vertical green-dotted lines shown on the left panel.

Table 7.1: Electronic couplings of the HOMO and LUMO to the left and right electrodes, obtained from DFT-NEGF, for the different values of θ for the thiol and thiolate junctions. All the values of Γ are in meV.

		Thiol				Thiolate			
		HOMO		LUMO		HOMO		LUMO	
Angle (^{0})	$d_{\mathrm{Au-Au}}$(Å)	Γ_L	Γ_R	Γ_L	Γ_R	Γ_L	Γ_R	Γ_L	Γ_R
0	23.2	6.0	5.5	6.5	6.5	19.0	16.0	8.0	8.0
30	19.9	5.7	5.0	8.0	5.0	25.0	8.0	9.0	8.0
45	16.40	6.5	3.5	6.0	3.5	15.0	10.0	7.0	6.0
60	12.9	5.0	3.6	7.0	5.0	12.0	10.0	7.0	7.0

region (within ME) is given just by the molecule and that its energy levels are non-degenerated and well separated in energy. Therefore, the interaction $V_{\mathrm{L,R}}$ between the scattering region and the electrode is given, for a single-particle level, by the momentum independent hopping parameter $\gamma_{\mathrm{L,R}}$. Then, the self-energy given in Eq. (7.1.2) becomes $\Sigma_{\mathrm{L,R}}(E) = \pi\gamma^2_{\mathrm{L,R}}\nu^{\mathrm{NEGF}}_{\mathrm{L,R}}(E)$. If we further assume the wide-band approximation, *i.e.* the density of states is energy independent, which is a good approximation for gold electrodes, we obtain

$$\Gamma^{\mathrm{NEGF}}_{\mathrm{L,R}} = 2\pi\gamma^2_{\mathrm{L,R}}\nu^{\mathrm{NEGF}}_{\mathrm{L,R}} \approx 2\pi\gamma^2_{\mathrm{L,R}}\nu_{\mathrm{L,R}} \equiv \Gamma_{\mathrm{L,R}}. \tag{7.2.2}$$

We note that, for a metallic surface, DFT-LDA generally yields satisfactory results for $\nu_{\mathrm{L,R}}$.

Fig. 7.5(right) shows the $I \times V$ curve calculated with the NEGF method compared to the total current (sequential tunneling plus cotunneling) obtained with the ME. When the energy level enters the bias window (± 0.9 V), the ME curve shows a step-like increase in the current. In contrast, when the calculation is self-consistent (NEGF:scf) the NEGF yields to a smoothed curve. The lack of a step-like increase in the NEGF:scf curve is directly related to the lack of the derivative discontinuity in continuous XC functionals, such as LDA [76, 191, 79], for which the position of the energy levels change linearly with the occupation. Therefore, during the self-consistency under bias, the energy levels shift to lower energies as the bias increases due to charging effect [186]. When the calculation is performed non-self-consistently, namely when the current is calculated by integrating the zero-bias transmission coefficient in the bias window, the results approximates the ME solution (ME:total). In this case, the step in the current for ME and NEGF-non-scf coincides because the transport is HOMO dominated. For $\theta = 0^0$, the LDA-HOMO is 0.5 eV below W_{F} [see Fig. 7.3)(a)] whereas the gas-phase $-I^{\mathrm{P}}$ is 1 eV bellow W_{F}. However, the correction due to image charge is 0.53 eV, which brings the $-I^{\mathrm{P}}$ in the junction to 0.47 eV. Therefore, due to error cancellation, LDA yields the corrected energy position for the HOMO. Nevertheless, this is not the case for smaller d for which $U(d)$ is larger. For a bias of 2 V, the self-consistent calculated current obtained with the NEGF approach is approximately twice the one obtained with ME. Due to charging effects, the levels shift considerably to lower energies and now the LUMO enters the bias window contributing to the current, as shown in the transmission of 2 V in Fig. 7.5(left). We also show for completeness the individual contributions of sequential tunneling and cotunneling. Note that for low bias, only cotunneling contributions are observed, as shown in the inset of Fig. 7.5(right). When the energy level enters the bias window, the cotunneling changes sign in order to reduce the sequential tunneling current [116]. For a single level, up to second order in $\hat{H}_{\mathrm{T}}$, it has been demonstrated [116] that current calculated with ME (with the regularized transition rates) yields identical results to the Lorentzian model.

The corrected energy level positions [Fig. 7.4] are used in the ME approach to calculate the $I \times V$ and the dI/dV curves. Fig. 7.6(a-b), show the results when the electronic couplings are the ones extracted from the NEGF calculations, as shown in Tab. 7.1. Since the HOMO level is responsible for the transport (the LUMO is too high in energy and does not contribute), its position with respect to the Fermi energy determines the gap of conductance whereas its couplings to the electrodes determine the current saturation. Furthermore, the renormalization of the HOMO level as a function of distance observed in the experiment agrees well with our simulations if we consider going from $\theta = 40^0$ to $\theta = 55^0$, which suggests that the molecule might be tilted from the start. Note that cotunneling contributions only broadens the current at the resonances and do not change

the current saturation for the set of parameters used.

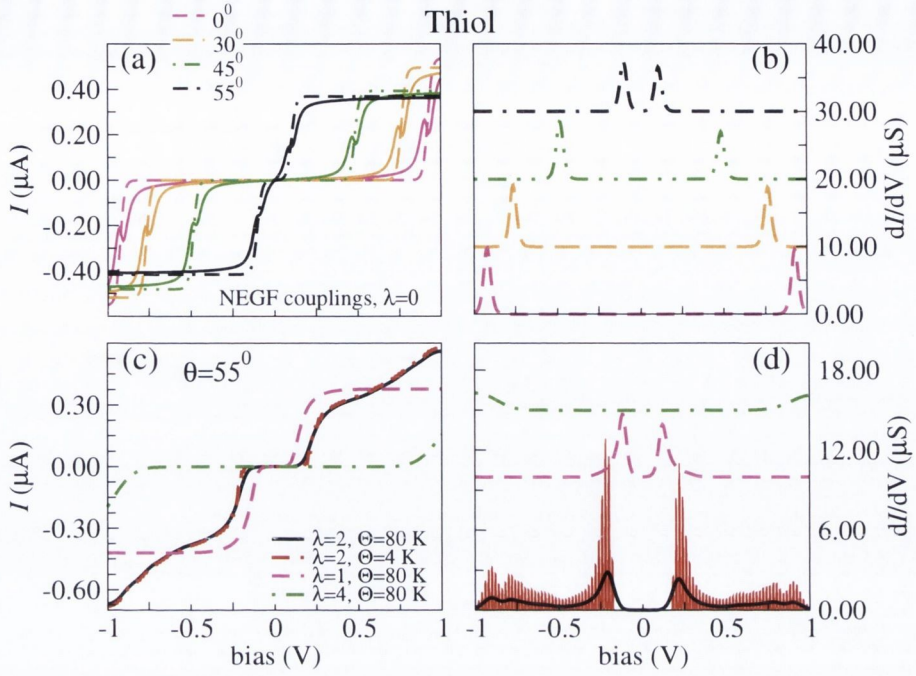

Figure 7.6: ME calculations for the thiol junctions. (a) Total current (solid lines) and sequential tunneling current (dashed-dotted lines) as a function of bias for different values of θ with $\Theta = 4$ K and $\lambda = 0$ (no vibrons). (b) dI/dV for sequential tunneling contributions. (c) $I \times V$ for $\theta = 55^0$ where vibrons are included and different values of λ and Θ are considered. The vibron energy is $\hbar\omega_p = 10$ meV, $q_{max} = 120$, $\tau = 1$ ps. (d) The corresponding dI/dV curves for (c). The energy level positions are the corrected ones, *i.e.* after taking into account image charge effect, as shown in Fig. 7.4, and Γ_L and Γ_R are from Tab. 7.1

7.2.3 Effects of vibrations in the charge transport

The experimental results show an approximately linear current increase with bias once the resonance is reached. It has been shown for molecular junctions that this is due to vibron excitations [57, 58]. By including vibronic degrees of freedom in our model, we can capture most of the linearity observed experimentally. Moreover, vibron relaxation is taken into account on a phenomenological ground by the parameter τ. Fig. 7.6(c) and Fig. 7.6(d) shows the $I \times V$ and dI/dV curves, respectively, for the thiol ($\theta = 55^0$) where vibrons are included in the simulation. We estimate the vibron energy of the isolated molecule by performing DFT calculations within a simple harmonic approximation. Several low-energy vibron modes are obtained in the range of 10-17 meV and they are related to the breathing modes of the porphyrin ring. Therefore, we consider an effective single vibron mode of energy $\hbar\omega_p = 10$ meV. Although we do not calculate the electron-vibron

coupling, λ, our calculations show that an intermediate value of $\lambda = 2$ leads to very good qualitative agreement with the experiment (solid line). Indeed, for weak electron-vibron coupling ($\lambda = 1$) vibration excitations that lead to the linear current increase do not occur (dashed line). On the contrary, strong electron-vibron coupling ($\lambda = 4$) leads the so-called Franck-Condon blockade (dashed-dotted line) [192, 116, 57], which is not observed by Perrin *et al.* [37]. We point out that the electron-vibron coupling might be dependent on the electrode separation, however, this is beyond the scope of the present work. In order to understand the effect of temperature, we perform the calculation with $\lambda = 2$ for $\Theta = 4$ K, which is the temperature used in the experiments. Our results for the dI/dV [Fig. 7.6(d)] at $\Theta = 4$ K show sharp peaks corresponding to vibration excitations. However, experimentally these peaks are broadened which suggests that local heating is taking place also in the electrodes.

Our results shown in Fig. 7.6 for the thiol junctions are by a factor four larger than the experimental data, see Fig. 1(c) of Ref. [37]. In order to understand the origin of this discrepancy, we have performed two other sets of calculations where the molecule is attached to a tip-like electrode, as shown in Fig. 7.2(c-d). In the first configuration, the molecule is between the two tips whereas in the second the molecule is positioned flat on top of the two tips in order to simulate a possible compressed geometry where the molecule slides on top of the electrodes. In both cases, a small reduction of the electronic coupling is observed, $\sim 20\%$, which would reduced the saturation current by the same amount, since the sequential tunneling transmission is proportional to the electronic couplings. Recently, it has been shown that effects of temperature [29, 30, 193] can reduce the couplings to the electrodes. Moreover, many-body calculations based on the GW approximation have also shown that LDA might overestimate the electronic couplings up to a factor of 3 [194], which would bring our results in quantitative agreement with experiment.

7.3 Conclusion

In summary, we have presented a combination of DFT-NEGF formalism and master equation approach to study the transport properties of molecular junctions, where all the parameters for the model can be obtained from first-principles calculation. We show that the inexpensive master equation approach can describe the transport properties of molecular junctions in the Coulomb blockade regime for which the NEGF within DFT-LDA fails due to the lack of the derivative discontinuity. We have applied this combined approach to reproduce experimental data for molecular junctions in the Coulomb blockade and demonstrate the importance of the energy level alignment as a function of electrodes separation, since this controls the conductance gap observed in the experiment. Moreover, the renormalization of the energy levels due to the image charge effect is well reproduced by a parameter-free classical image charge model. We demonstrate that vibration excitations

can be responsible for the linear-like current increase once the resonance is reached and we estimate an intermediate electron-vibron coupling of $\lambda = 2$.

Chapter 8

Light-induced Charge Transport

In the optical response of molecular junctions several physical processes and mechanisms can take place under suitable conditions. Many of these can be broadly categorized as adiabatic and non-adiabatic. In the former, the driving frequency is small relative to the characteristic level spacing of the system, so that light-induced mixing between energy levels can be disregarded. This is not the case for the metallic electrode where the characteristic level spacing can be of the same order of the driving frequency. However, for low frequencies the radiation field does not penetrate into the metal. Non-adiabatic processes are those processes dominated by electronic excitations of the molecular junction and those associated with electronic excitations of the electrodes.

From a theoretical point of view the description of the optical response of a molecular junction constitutes a complex problem. The molecular response to the local radiation field, while being a standard problem in spectroscopy, becomes much more complex when the molecule is in a junction. This is because now electrons can flow through the molecular system since it is in contact with electron reservoirs with possibly different chemical potentials. Therefore, the molecular subsystem is in a non-equilibrium state caused by the interplay between the electrons flux induced by an external bias and a photon flux associated with an incident radiation field. Thus, one can observe phenomena where the electronic current appears in response to the incidence of light or light-emission occurs due to electrical current passing through the system.

For adiabatic processes, *i.e.* when the light frequency is smaller than the energy levels spacing and interference between the charge states of the molecule can be disregarded, Cuevas *et al.* extended the well-known Landauer-Büttiker formalism based on Green's functions to incorporate a monochromatic electromagnetic radiation. They derived an expression for the linear-response conductance when the junction is illuminated [195]. For junctions where the E_{F} of the metal lies in the gap between the HOMO and the LUMO levels, depending on the radiation frequency, PAT can lead to an enhancement or a reduction of the dc conductance [196, 197]. Following the class of adiabatic approaches, in this chapter we apply a ME approach that takes into account light and vibrational

effects and we consider higher-order processes, such as cotunneling contributions, where the parameters can be obtained from first-principles calculations or experimental data. We end the chapter by showing how the linear conductance of a donor-acceptor structure depends on the charge state of the molecule, where the desired charge state is obtained via CDFT.

8.1 Master equation for light-induced charge transport

In this section, we apply the formalism presented in Chapter 4 to study electronic transport across a molecular system connected to two reservoirs when light-induced charge transport is considered. Our ME takes into account light-induced effects up to the fourth order in the tunneling Hamiltonian, *i.e.* cotunneling contributions. We argue that this approach is valid for junctions where the molecule is weakly coupled to the electrodes, the energy levels are well separated and the radiation frequency is smaller than $E_{\mathrm{QP}}^{\mathrm{gap}}$. This approach can be contrasted to the light-induced currents studied in Refs. [51, 52, 53] where internal transitions were taken into account.

8.1.1 Single quantum dot - sequential tunneling

We start by presenting some models of a single quantum dot (SQD), *e.g.* a molecule or any other nanostructure that show discrete energy levels. We follow the Tien-Gordon approach and we discuss the effect of an external oscillating potential to the transport across the SQD system. The Hamiltonian of a generic SQD can be written as

$$\hat{H} = \hat{H}_{\mathrm{mol}} + \hat{H}_{\mathrm{L}} + \hat{H}_{\mathrm{R}} + \hat{H}_{\mathrm{T}}, \tag{8.1.1}$$

where $\hat{H}_{\mathrm{L}}$ and $\hat{H}_{\mathrm{R}}$ are the Hamiltonians of the individual electrodes as in Eq. (7.1.5) for $\alpha = \mathrm{L}, \mathrm{R}$. The operator $\hat{d}^{\dagger}_{\alpha\mathbf{k}}(\hat{d}_{\alpha\mathbf{k}})$ creates (annihilates) an electron with momentum $\mathbf{k}$ in the electrode α, see Appendix A. The interaction between the leads and the molecule is given by the tunneling Hamiltonian , $\hat{H}_{\mathrm{T}}$, as in Eq. (7.1.6).

The molecular Hamiltonian is given by

$$\hat{H}_{\mathrm{mol}} = \sum_{i=1}^{M} \left(\sum_{\sigma=\uparrow\downarrow} \epsilon_i \hat{c}^{\dagger}_{i\sigma} \hat{c}_{i\sigma} + \mathcal{U}_i \hat{n}_{i\uparrow} \hat{n}_{i\downarrow} \right), \tag{8.1.2}$$

with M single-particle levels, σ is the spin and $\mathcal{U}_i$ is the single electron charging energy and it is treated as a free parameter. The operator $\hat{c}^{\dagger}_i(\hat{c}_i)$ creates (annihilates) an electron in the molecular state i and $\hat{n}_{i\uparrow} = \hat{c}^{\dagger}_{i\uparrow}\hat{c}_{i\uparrow}$ is the number operator for spin $\uparrow$ in the site i.

The simplest system one can think of is a SQD consisting of just one internal level coupled to two electrodes and we assume spinless electrons. In reality, quantum dots have many internal energy levels and the spacing between them is a important indicator of the energy scale of the problem. In contrast, in molecules, these energy levels are much more spaced thus that the single-energy level treatment is more suitable to model a molecular energy level instead. The energetics of the electrodes in this model are described by their thermodynamic properties such as chemical potentials and occupations given by the Fermi-distribution functions. The quantum aspect of the problem comes from the SQD Hamiltonian. In this section, we present the SQD for one and two internal energy levels and for the former for one and two electrons. In this simple case, there are no coherence

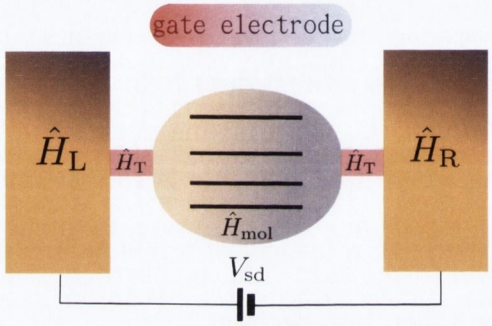

Figure 8.1: Schematic representation of a SQD connected to two electrodes. The gate electrode is used to shift the energy levels of the SQD. The contributions to the Hamiltonian are shown for clarity.

terms for the density matrix operator and the dynamics of the system can be described just by the diagonal contributions of Eq. (4.3.51), *i.e.*

$$\langle m|\,\dot{\hat{\rho}}(t)\,|m\rangle = \sum_{k\neq m}\Big(\langle k|\,\hat{\rho}(t)\,|k\rangle\,\Gamma^{km} - \langle m|\,\hat{\rho}(t)\,|m\rangle\,\Gamma^{mk}\Big).$$

As discussed in Sec. 4.4, the effect of a time-dependent potential, such as the interaction with a external source of light, is to create a time-dependence of the energy levels of the quantum dot. By applying a unitary transformation to the Hamiltonian of the entire system, this time-dependence can be transferred to the interacting Hamiltonians, and consequently, the transition rates between states of the electrodes and the states of the dot will carry the time-dependency [64]. For a external time-dependent potential applied through the gate voltage of a three-terminal device as shown in Fig. 8.1 , one can show that the transition rates are given by

$$\Gamma^{+}_{\alpha} = \frac{2\pi}{\hbar}\,|\gamma_\alpha|^2\,\rho_\alpha \sum_{\nu} J^2_{\nu}\left(\frac{\zeta_{n'n}}{\hbar\omega}\right)\left|\langle n'|\sum_i \hat{c}^{\dagger}_i\,|n\rangle\right|^2 f(E_{n'} - E_n - \nu\hbar\omega - \mu_\alpha) \tag{8.1.3}$$

and

$$\Gamma_{\alpha}^{-} = \frac{2\pi}{\hbar} |\gamma_{\alpha}|^2 \rho_{\alpha} \sum_{\nu} J_{\nu}^2 \left(\frac{\zeta_{n'n}}{\hbar\omega} \right) \left| \langle n' | \sum_{i} \hat{c}_i | n \rangle \right|^2 [1 - f(E_{n'} - E_n + \nu\hbar\omega - \mu_{\alpha})] . \quad (8.1.4)$$

The full derivation of Eq. (8.1.3) and Eq. (8.1.4) is given in Appendix B, Sec. B.2. Γ^{+} describes the transition rates for tunneling from the electrode α to the SQD, whereas Γ^{-} describes the transition rates for tunneling from the SQD to the electrode, while making a transition from the initial charge state $|n\rangle$ to the final charge state $|n'\rangle$. γ_{α} is the hopping parameter between the SQD and the electrode α, ρ_{α} is the density of states of the electrode α for which we assume the wide band limit, *i.e.* the density of states is energy independent. $f(E)$ is the Fermi-distribution function and μ_{α} is the chemical potential of the electrode α. $J_{\nu}(\xi)$ is the νth order Bessel function of the first kind and $\xi = \frac{\zeta_{n'n}}{\hbar\omega}$ is a dimensionless quantity that controls the ac-field intensity. Hereafter, we treat ξ as a free parameter. Again, by setting the time-derivative of the reduced density matrix to zero, *i.e.* $\langle m | \dot{\hat{\rho}}(t) | m \rangle = 0$, and using the normalization condition $\sum_i \rho_i = 1$ one obtains the steady-state current through the electrodes [114, 115]. The electrical current due to sequential tunneling through the contacts, for instance the left (L) contact, is then given by

$$I^{\mathrm{L}} = -e \sum_{nm} (n_n - n_m) \Gamma_{\mathrm{L}}^{nm} \rho_{mm}. \quad (8.1.5)$$

Γ_{L}^{nm} represents either Γ_{L}^{+} or Γ_{L}^{-} depending on whether the electron is tunneling to or from the molecule, respectively.

Sidebands

The square modules of the Bessel's functions has an important meaning. It gives the probability for the tunneling electrons to absorb ($\nu > 0$) or to emit ($\nu < 0$) ν photons of energy $\hbar\omega$. For $\nu = 0$ one recovers the case of no-PAT transport. This can be further understood by considering the spectral decomposition of the wave function for the different sidebands. By considering an electron confined in an infinite well interacting with a time-dependent external potential, $V\cos\,\omega t$, the Schrödinger equation can be written as

$$i\hbar \frac{\partial \psi}{\partial t} = \hat{H}(t)\psi(\mathbf{r}, t) = (\epsilon + V\cos\,\omega t)\psi(\mathbf{r}, t). \quad (8.1.6)$$

The solution of this equation is

$$\psi(\mathbf{r}, t) = \psi(\mathbf{r}, 0) e^{-i(\epsilon t + \frac{V}{\hbar\omega}\sin\,\omega t)/\hbar} = \psi(\mathbf{r}, 0) \sum_{\nu} J_{\nu} \left(\frac{V}{\hbar\omega} \right) e^{-i(\epsilon + \nu\omega)t/\hbar}, \quad (8.1.7)$$

which indicates that the electron has a probability proportional to $J_\nu^2\left(\frac{V}{\hbar\omega}\right)$ to have an energy equal to $\epsilon \pm \hbar\omega$ [44, 198, 199]. Sidebands can be detected by varying the gate voltage, which shifts up and down the energy levels of the quantum system. When the sideband enters the bias window, *i.e.* for $\mu_R > \epsilon \pm \nu\hbar\omega > \mu_L$, the current versus gate voltage ($I-V_g$) curve shows a resonant peak added to the undriven resonance. The height of this peak is proportional to $J_0^2\left(\frac{V}{\hbar\omega}\right)$. For other sidebands corresponding to the absorption or emition of ν photons, the current will have contributions with height proportional to $J_\nu^2\left(\frac{V}{\hbar\omega}\right)$.

Single energy level model

We first show how PAT changes the current through the tunneling barriers for the case of a single level, ϵ_1, in a SQD. Fig. 8.2 shows the current and the differential conductance as a function of gate voltage ($V_{sd} \to 0$) for different values of ξ. Without light irradiation

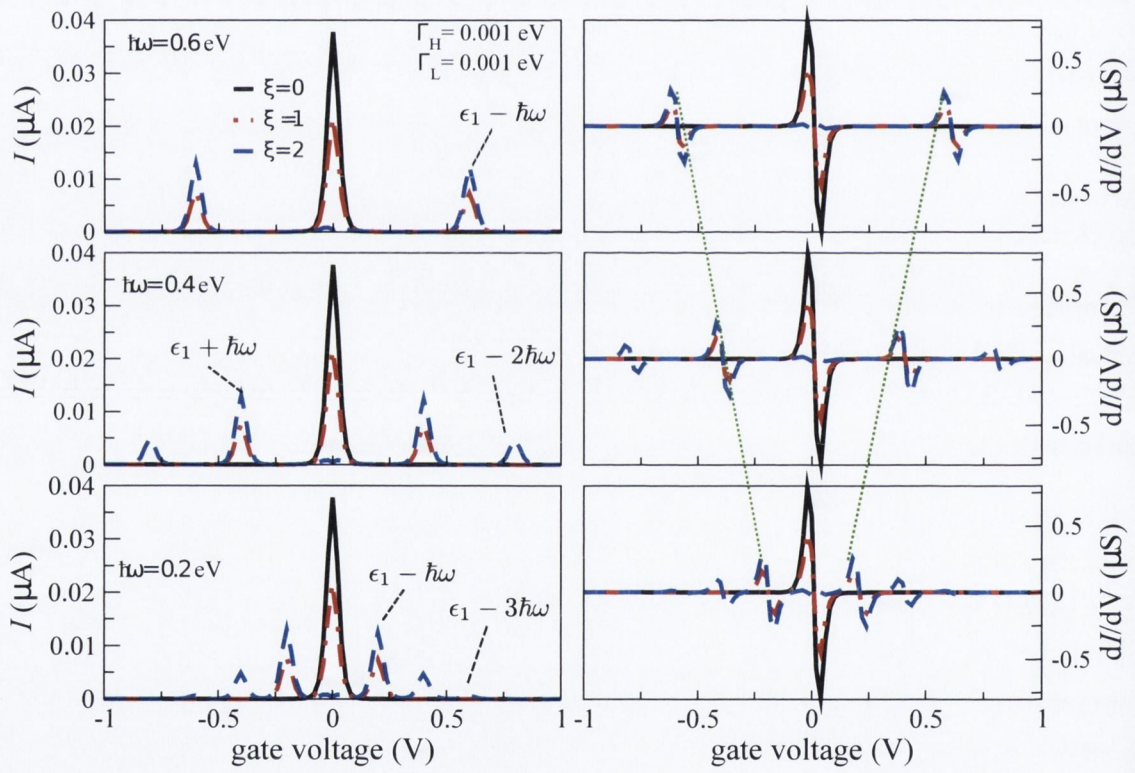

Figure 8.2: PAT for a single level model. Current (left) and differential conductance (right) as a function of gate voltage ($V_{sd} \to 0$) for different light intensities. Parameters used are $k_B\Theta = 15$ meV, $\Gamma_L = \Gamma_R = 1$ meV and $\epsilon_1 = 0$ eV. From top to bottom, decreasing the photon energy.

($\xi = 0$), the $I - V_g$ curve shows just one peak, which occurs when ϵ_1 is aligned with the chemical potentials of the electrodes [200]. However, when light is on, the electron that in absence of photons would be confined inside the SQD, can absorb energy from the photons to jump out of the SQD and be absorbed by the electrodes in such way that the

condition $\mu < \epsilon_1 + \nu\hbar\omega$ is satisfied. In other words, the effect of the interaction of a single energy level with a classical oscillating field is that the energy levels splits into several energy levels (sidebands) located at $\epsilon_1 \pm \nu\hbar\omega$, as shown in Fig. 8.3. Likewise, electrons on

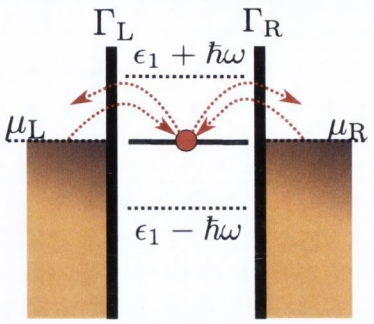

Figure 8.3: Energy diagram for a single level model where PAT is present.

the electrodes can absorb photons to jump into the SQD. With this process, occupation probabilities that were essentially forbidden can become available with PAT.

Two energy levels model

Single electron allowed

First we consider the case of two discrete single particle energy levels, ϵ_1 and ϵ_2, where just one electron is allowed in the SQD. In other words, $\mathcal{U} \to \infty$ so that only the charge states $|0\rangle$, $|1,0\rangle$ and $|0,1\rangle$ are considered. When PAT is taken into account, two transmission mechanisms can be observed. The first was already discussed in Fig. 8.2 where extra peaks arise at energies equal to $\epsilon_1 \pm \nu\hbar\omega$. The second mechanism gives rise to peaks where an excited state (in this case ϵ_2) is aligned with μ_α. For $\xi = 0$, the tunneling through ϵ_2 is forbidden due to Coulomb blockade, since ϵ_1 is already occupied. Thus, as shown in Fig. 8.4, we observe just one peak at $V_g = 0.1$ eV, which is the energy needed to align ϵ_1 with μ_α. However, for $\xi \neq 0$, an electron in ϵ_1 can absorb photons to jump out of the SQD, while another electron can then tunnel thought ϵ_2 following the sequence of transitions $|1,0\rangle \to |0\rangle \to |0,1\rangle$. The tunneling though ϵ_2 is now visible for $\xi = 1$ since ϵ_1 can be emptied due to photon absorption [201]. Other transitions can also be identified where both levels can absorb and emit photons.

Two electrons allowed

In the case of two electrons in the SQD, we need to take into account the charging energy $\mathcal{U}$ due to electron-electron interaction. As shown in Fig. 8.5, for $\xi = 0$, two main peaks are observed instead of just one and the spacing between these two peaks is given by $(\epsilon_1 - \epsilon_2) + \mathcal{U}$. The first peak at $V_g = 0.4$ V corresponds to one electron entering the

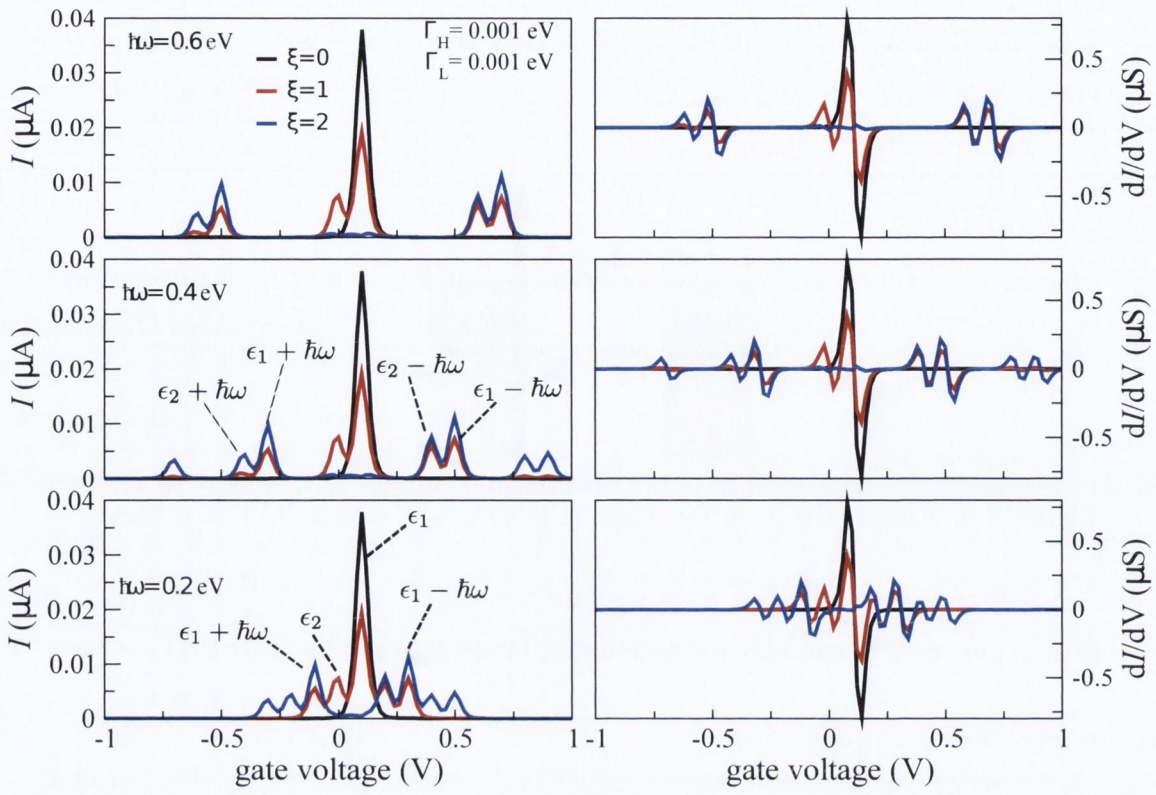

Figure 8.4: PAT for a two-level and one electron model in the SQD. Current (left) and differential conductance (right) as a function of gate voltage ($V_{\rm sd} \to 0$) for different light intensities. The parameters used are $k_{\rm B}\Theta = 15$ meV, $\Gamma_{\rm L} = \Gamma_{\rm R} = 1$ meV, $\epsilon_1 = -0.1$ eV and $\epsilon_2 = 0$ eV. From top to bottom, decreasing the energy of the photon.

SQD and tunneling through ϵ_1, *i.e.* the $|0\rangle \to |1,0\rangle$ transition. Once the ϵ_1 level is occupied, the next transition is $|1,0\rangle \to |1,1\rangle$, with final energy $\epsilon_2 + \mathcal{U}$. As a consequence, for $\xi = 0$, the two peaks corresponding to ϵ_2 and $\epsilon_1 + \mathcal{U}$ are hidden. However, they can be observed for $\xi = 1, 2$. As for the case of one electron in the SQD, the same analysis for the sidebands can be made and some of the peaks can be easily identified. As the number of internal states increases and the intensity of the light increases more transitions can occur and several peaks will be observed in the $I - V_{\rm g}$ plot, which can be seen as extra steps in the current versus bias voltage, $I - V_{\rm sd}$, plot. Similar results have been reported in the literature in good agreement with our simulations [202, 203].

8.1.2 Cotunneling with light effects

We then extend our model in order to include light effects in the cotunneling contributions to the current. To the best of our knowledge this has not been done yet with a

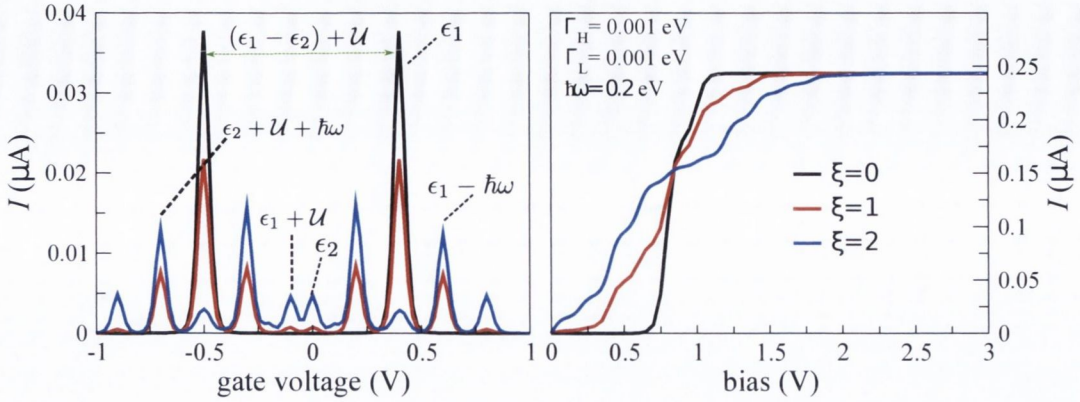

Figure 8.5: Current as a function of (a) gate voltage ($V_{\rm sd} \to 0$)[left] and as a function of bias voltage ($V_{\rm g} = 0$)[right]. The parameters used are $k_{\rm B}\Theta = 15$ meV, $\Gamma_{\rm L} = \Gamma_{\rm R} = 1$ meV, $\mathcal{U} = 0.5$ eV, $\hbar\omega = 0.2$ eV, $\epsilon_1 = -0.4$ eV and $\epsilon_2 = 0$ eV.

ME approach. The cotunneling rates take the form

$$\begin{aligned}\Gamma^{nn'}_{\alpha\alpha'} = {} & \frac{\Gamma_\alpha \Gamma_{\alpha'}}{2\pi\hbar} \sum_\nu J^2_\nu \left(\frac{\zeta_{n'n}}{\hbar\omega}\right) \sum_{i'''} \sum_{i''} \\ & \times \int d\epsilon \left| \sum_{n''} \left(\frac{A^{i'''}_{n'n''} A^{i''*}_{nn''}}{\epsilon + E_n - E_{n''} + \nu\hbar\omega + i\eta} + \frac{A^{i'''*}_{n''n'} A^{i''}_{n''n}}{-\epsilon + E_{n'} - E_{n''} + i\eta} \right) \right|^2 \\ & \times f(\epsilon - \mu_\alpha) \times \Big[1 - f(\epsilon + E_n - E_{n'} + \nu\hbar\omega - \mu_{\alpha'}) \Big], \end{aligned} \tag{8.1.8}$$

where the matrix elements of the annihilation operators are

$$\sum_{n''} \langle n' | \hat{c}_{i'''} | n'' \rangle \left(\langle n | \hat{c}_{i''} | n'' \rangle \right)^\dagger = \sum_{n''} A^{i'''}_{n'n''} A^{i''*}_{nn''} \tag{8.1.9}$$

and

$$\sum_{n''} \left(\langle n'' | \hat{c}_{i'''} | n' \rangle \right)^\dagger \langle n'' | \hat{c}_{i''} | n \rangle = \sum_{n''} A^{i'''*}_{n''n'} A^{i''}_{n''n}. \tag{8.1.10}$$

Again, $f(E)$ is the Fermi-distribution function and μ_α is the chemical potential of the electrode. $J_\nu(\xi)$ is the νth order Bessel function of the first kind, $\xi = \frac{\zeta_{n'n}}{\hbar\omega}$ is a dimensionless quantity that controls the ac-field intensity and E_n is the total energy of the charge state $|n\rangle$. Only elastic cotunneling contributions are considered since we do not include interference between molecular charge states, as schematically shown in Fig. 7.1(b). A full derivation of Eq. (8.1.8) is given in Sec. B.3.

Fig. 8.6 shows our results for a two-level model for spinless electrons, where the parameters could represent, for instance, the molecular junction discussed in Chapter 7, Sec. 7.2.2. As discussed in the previous sections, the photon creates side-bands and extra steps in the sequential tunneling current (left panels of Fig. 8.6). These extra steps occur

where the total energy difference between two charging states matches the applied bias. The low bias cotunneling contributions (right panels of Fig. 8.6), where the transition rates are calculated with Eq. (8.1.8) and the current by Eq. (7.1.11), are shown for different values of ξ and photon energies. The cotunneling contributions increase with the light intensity, since the transition rates are proportional to the module squared of the Bessel functions, which also increases with the intensity. It is interesting to note that for $\hbar\omega = 0.2$ eV, the cotunneling current is larger than, for instance, for $\hbar\omega = 0.8$ eV. This is due to the fact that for low photon energy, a higher number of sidebands, $\epsilon_{1,2} \pm \hbar\omega$, is available within the range of applied bias as compared to the case of high photon energy. In other words, there are more channels available for electrons to tunnel for smaller photon energies. The corresponding occupation probabilities for different light intensities and photon energies are shown in Fig. 8.7. Note that they correspond to the sequential tunneling contributions since elastic cotunneling does not modifies the occupations.

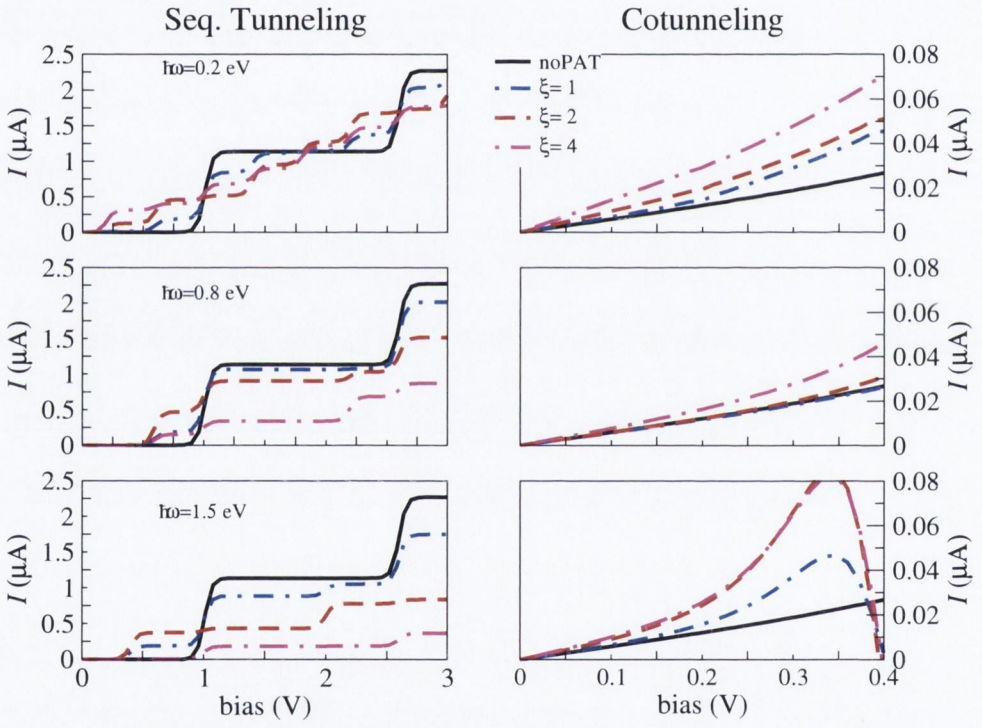

Figure 8.6: $I - V_{\rm sd}$ for sequential tunneling (left) and cotunneling (right) with PAT for different photon energy and light intensity. The parameters are: $\epsilon_{\rm LUMO} = 1.3$ eV, $\epsilon_{\rm HOMO} = -0.5$ eV, $\Gamma_{\rm L} = \Gamma_{\rm R} = 7$ meV, $k_{\rm B}\Theta = 15$ meV. The charge state energies are: $|0\rangle = 0$ eV, $|1,0\rangle = -0.5$ eV; $|0,1\rangle = 1.3$ eV and $|1,1\rangle = 0.8$ eV. We considered $\mathcal{U} = 0$ eV.

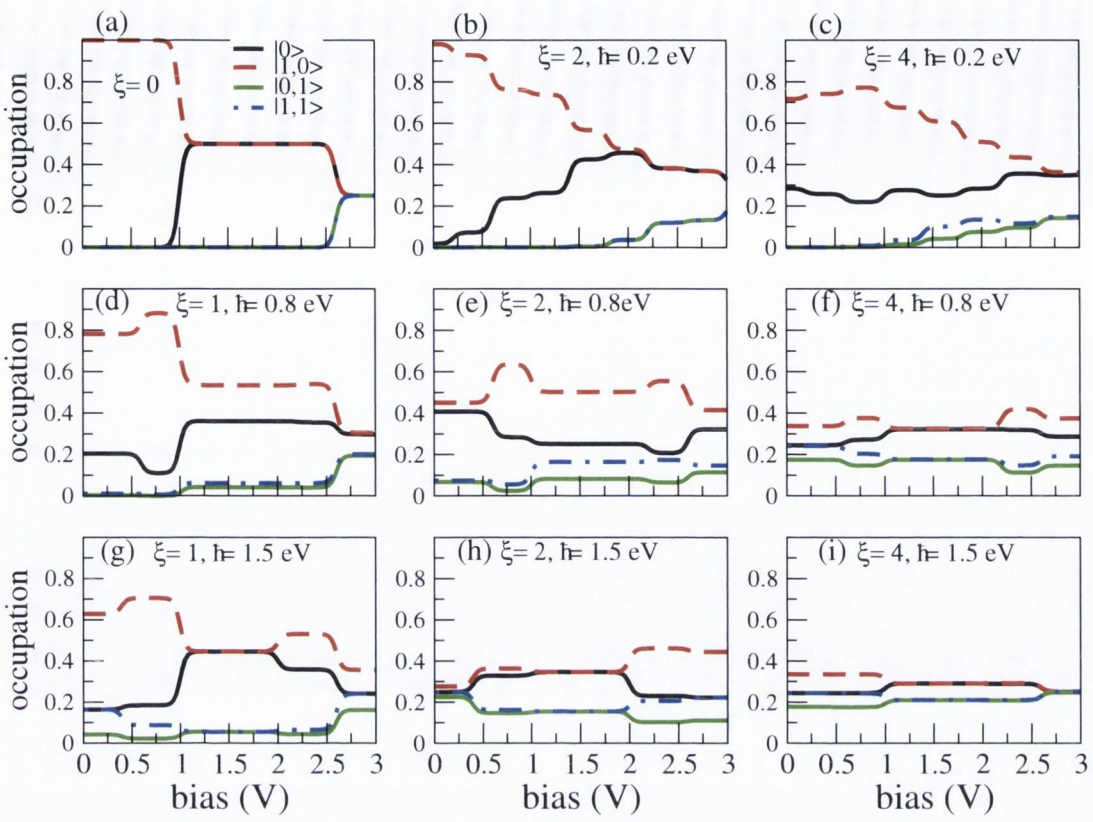

Figure 8.7: Occupation probabilities for different photon energy and light intensity (c-i) compared to no-PAT (a). The corresponding $I - V_{\mathrm{sd}}$ curves are those in Fig. 8.6.

8.2 Interplay of phonon and photon-induced charge transport

Franck-Condon blockade

The Franck-Condon blockade (FKB) is the suppression of the linear conductance of a nanostructure that shows strong electron-vibron coupling, λ. This dimensionless parameter measures the extent to which the geometrical structure of the molecule changes due to the change in its electronic structure, for instance, when an extra electron is added to it. When $\lambda \gg 1$, the displacements of the potential surfaces are large compared to the quantum fluctuations of the nuclear configuration in the vibronic ground state. This leads to a strong suppression of the overlap between the low-lying vibronic states. Therefore, the Franck-Condon matrix elements [see Eq. (C.2.20)] are strongly suppressed, leading to the suppression of the sequential tunneling current at low bias. This is schematically shown in Fig. 8.8(a) where only transitions that involve low-lying vibronic states, such as $|N, q\rangle$, to high-vibronic states, $|N+1, q'\rangle$, are allowed. $|N, q\rangle$ is the electronic ground state N electrons and q is the vibronic state of the molecule. This effect was first observed in quantum dots [204] and then in suspended carbon nanotubes [205]. Only recently Burzurí *et al.* could observe this effect in a very small single magnetic molecule [192]. A detailed

theoretical description of this effect has been already published some time ago by Koch *et al.* [116, 57].

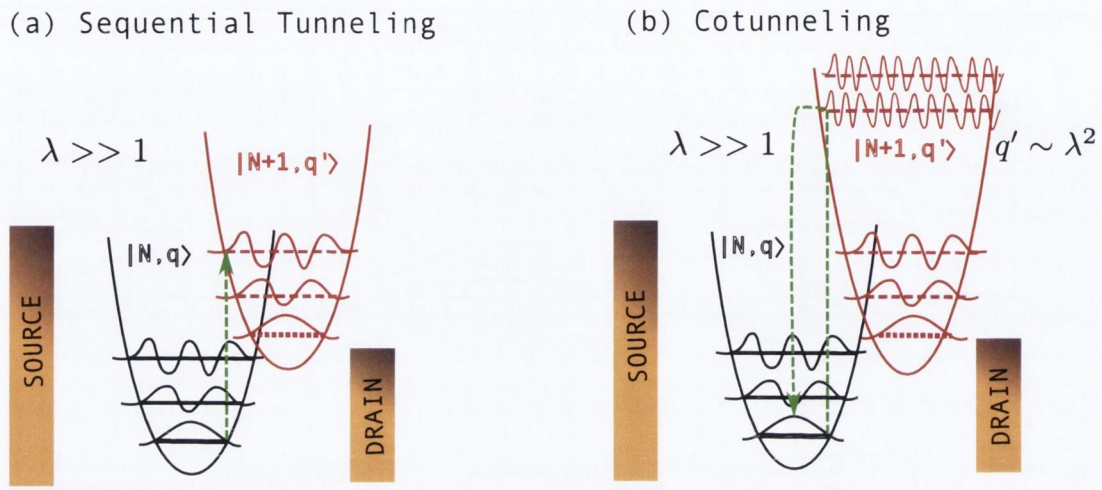

Figure 8.8: Schematic energy diagram for Franck-Condon blockade, $\lambda \gg 1$. (a) Sequential tunneling where only transitions from the charging state $|N, q\rangle$ to a high-vibron excited charging state $|N+1, q'\rangle$ is allowed. Ground-state transitions are suppressed. (b) The suppression of the conductance is partially lifted due to cotunneling involving contributions from highly excited virtual vibronic states. The curved arrow shows that, in cotunneling, the charge state of the molecule changes just virtually in the intermediate state.

An interesting fact about the FKB is that it can not be lifted by applying a gate voltage, as it can be done for the Coulomb blockade. Fig. 8.9 shows for a one-level model the stability diagrams as the electron-vibron coupling increases. As expected, the gate voltage does not lift the conductance gap, *i.e.* the system is in the FKB. Note that the center of the stability diagram is shifted to the right since the energy of the single particle level is renormalized, as shown in Sec. C.2.

The transition rates for sequential tunneling with vibrons are given by

$$\Gamma_{\alpha}^{+,qq'} = \frac{2\pi}{\hbar} |\gamma_\alpha|^2 \rho_\alpha \left| \langle n' | \sum_i \hat{c}_i^\dagger |n\rangle \langle q' | e^{-\lambda\left(\hat{b}^\dagger - \hat{b}\right)} |q\rangle \right|^2 f(E_{n'q'} - E_{nq} - \mu_\alpha), \tag{8.2.1}$$

for electrons entering the molecule through electrode α and changing the vibronic state of the molecule from q to q'. Likewise, for electrons leaving the molecule, the transition rate is

$$\Gamma_{\alpha}^{-,qq'} = \frac{2\pi}{\hbar} |\gamma_\alpha|^2 \rho_\alpha \left| \langle n' | \sum_i \hat{c}_i |n\rangle \langle q' | e^{-\lambda\left(\hat{b}^\dagger - \hat{b}\right)} |q\rangle \right|^2 [1 - f(E_{n'q'} - E_{nq} - \mu_\alpha)]. \tag{8.2.2}$$

A detailed derivation of these expressions is found in Sec. C.2. The transition rates for

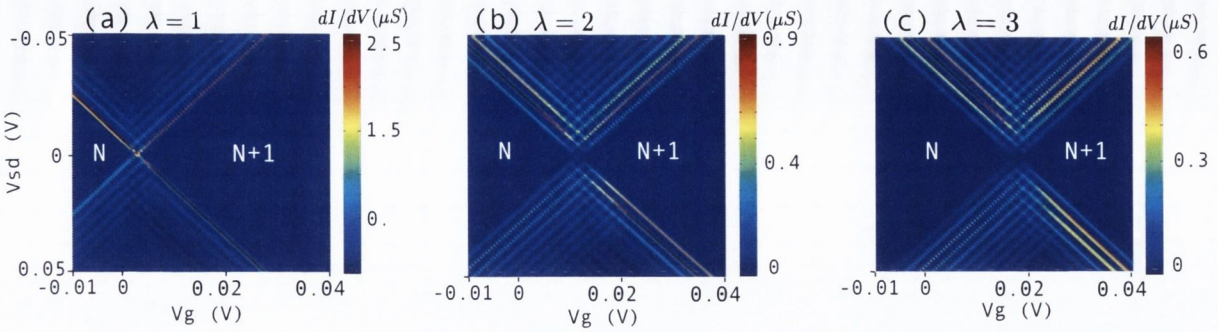

Figure 8.9: Stability diagram for sequential tunneling contributions for a one-level model for different electron-vibron coupling strength. Parameters: $\Gamma_{\mathrm{L}} = \Gamma_{\mathrm{R}} = 10$ meV, $k_{\mathrm{B}}\Theta = 1.7$ meV, $\epsilon = 0$ eV, $\hbar\omega_{\mathrm{q}} = 2.6$ meV and $q_{\max} = 15$.

cotunneling including vibrons are derived in Sec. C.3. Moreover, the electrical current is given by Eq. (7.1.11).

In the FKB regime, Koch *et al.* [116, 57] have shown, for the low temperature limit $\Gamma << k_{\mathrm{B}}\Theta << \hbar\omega_{\mathrm{q}}$, that the sequential tunneling contributions to the linear conductance is proportional to $e^{-\lambda^2}$, *i.e.* it is exponentially suppressed by the electron-vibron coupling. This is the case even for the conductance peak position. Fig. 8.10(a) shows the sequential tunneling current for different values of λ. For $\lambda = 3$ the current up to ~ 0.5 V is essentially quenched. The authors also have shown that the cotunneling transition rates are algebraically suppressed by the electron-vibron coupling, *i.e.* $\Gamma_{\alpha\alpha'}^{nn';qq'} \sim \lambda^{-4}$, and therefore cotunneling dominates the conductance for low-bias when the system is in the FKB, as shown in the inset of Fig. 8.8(b). This is related to the fact that for transitions originating in the vibronic ground state $q = 0$, the optimal overlap is obtained for virtual states q'' of the order of $q'' \approx \lambda^2$ (see Appendix C of Ref. [116]). Fig. 8.10(b) shows the individual contributions of the various processes to the total current.

Photon-induced removal of Franck-Condom blockade in molecular junctions

An interesting effect occurring when optical excitations are also considered in the model for a molecular junction with strong electron-vibron coupling [192] is the removal of the FKB. This represents an efficient way of switching optically the current through a single molecule. The sequential tunneling rates when both effects are included, namely, vibrons and photons, are given by (see Sec. C.2 for details)

$$\Gamma_{\alpha}^{+,qq'} = \frac{2\pi}{\hbar}\sum_{\nu} J_{\nu}^{2}\left(\frac{\zeta_{n'n}}{\hbar\omega}\right)|\gamma_{\alpha}|^{2}\rho_{\alpha}\left|\langle n'|\sum_{i}\hat{c}_{i}^{\dagger}|n\rangle\langle q'|e^{-\lambda\left(\hat{b}^{\dagger}-\hat{b}\right)}|q\rangle\right|^{2} \times f(E_{n'q'} - E_{nq} - \nu\hbar\omega - \mu_{\alpha}), \tag{8.2.3}$$

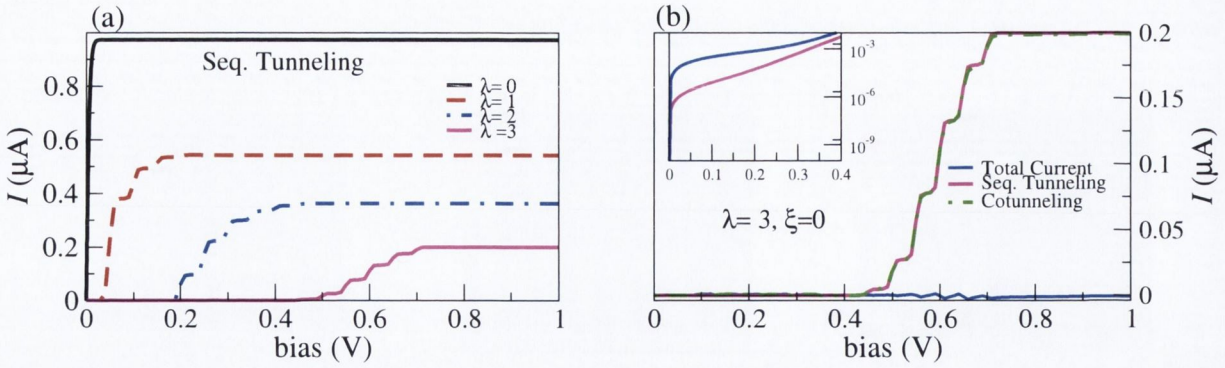

Figure 8.10: (a) Sequential tunneling current as a function of bias for different values of the electron-vibron coupling, λ. (b) For $\lambda = 3$, the current suppression up to 0.5 V is due to Franck-Condom blockade. The individual sequential tunneling and cotunneling contributions to the total current are shown for completeness in panel (b). The inset shows that the cotunneling contributions dominate at low bias. The parameters used are $k_B\Theta = 1.7$ meV, $\Gamma_L = \Gamma_R = 6$ meV, $\epsilon_1 = 0$ eV, $q_{max} = 5$ and $\hbar\omega_q = 25$ meV.

to transfer one electron from the electrode α to the molecule and

$$\Gamma_\alpha^{-,qq'} = \frac{2\pi}{\hbar}\sum_\nu J_\nu^2\left(\frac{\zeta_{n'n}}{\hbar\omega}\right)|\gamma_\alpha|^2\,\rho_\alpha\left|\langle n'|\sum_i \hat{c}_i\,|n\rangle\,\langle q'|\,e^{-\lambda\left(\hat{b}^\dagger-\hat{b}\right)}\,|q\rangle\right|^2 \times\left[1-f(E_{n'q'}-E_{nq}+\nu\hbar\omega-\mu_\alpha)\right] \tag{8.2.4}$$

to transfer an electron from the molecule to the electrode α.

Fig. 8.11(a) shows the sequential tunneling current in the FKB regime, for $\lambda = 3$, without light-assisted tunneling. Fig. 8.11(b) and Fig. 8.11(c) show the corresponding occupation probabilities for the neutral molecule ($|0;q\rangle$ state) and for the charged molecule ($|1;q\rangle$ state), respectively. For bias up to ~ 0.5 V, the system is in the $|1;0\rangle$ state, *i.e.* the molecule has one extra electron and it is in the vibronic ground state. When light is switched on, photons can assist electrons to excite vibronic states. As the light intensity increases, vibronic excited states of the charged molecule starts being populated. Furthermore, also excited vibronic states of the neutral molecule become accessible. Although the population of the neutral state is still one order of magnitude smaller than that of the charged molecule, an optical excitation creates a non-equilibrium thermal distribution. This provides the background for the removal of the FKB, as shown in Fig. 8.11(d-i). The action of the light is also shown in the stability diagrams of Fig. 8.11(j) when compared to Fig. 8.11(l). In the latter, one can also observe the many extra lines corresponding to side bands associated with the vibronic states.

Our results are in very good agreement with the results obtained by May *et al.* [206, 60, 62, 61], a generalized ME approach was used to study photo-induced charge transport in a two-level model molecular junction. In their model they included effects of intra-molecular photo-excitations (HOMO-LUMO transitions) and intra-molecular vibronic energy reor-

ganization. Although we do not include intra-molecular excitations, which would require to consider the off-diagonal elements of the reduced density matrix operator in our ME [see Eq. (4.3.51)], the agreement with the published results is not accidental, since the contribution from the intra-molecular excitations is at least an order of magnitude smaller than the main sequential tunneling contribution.

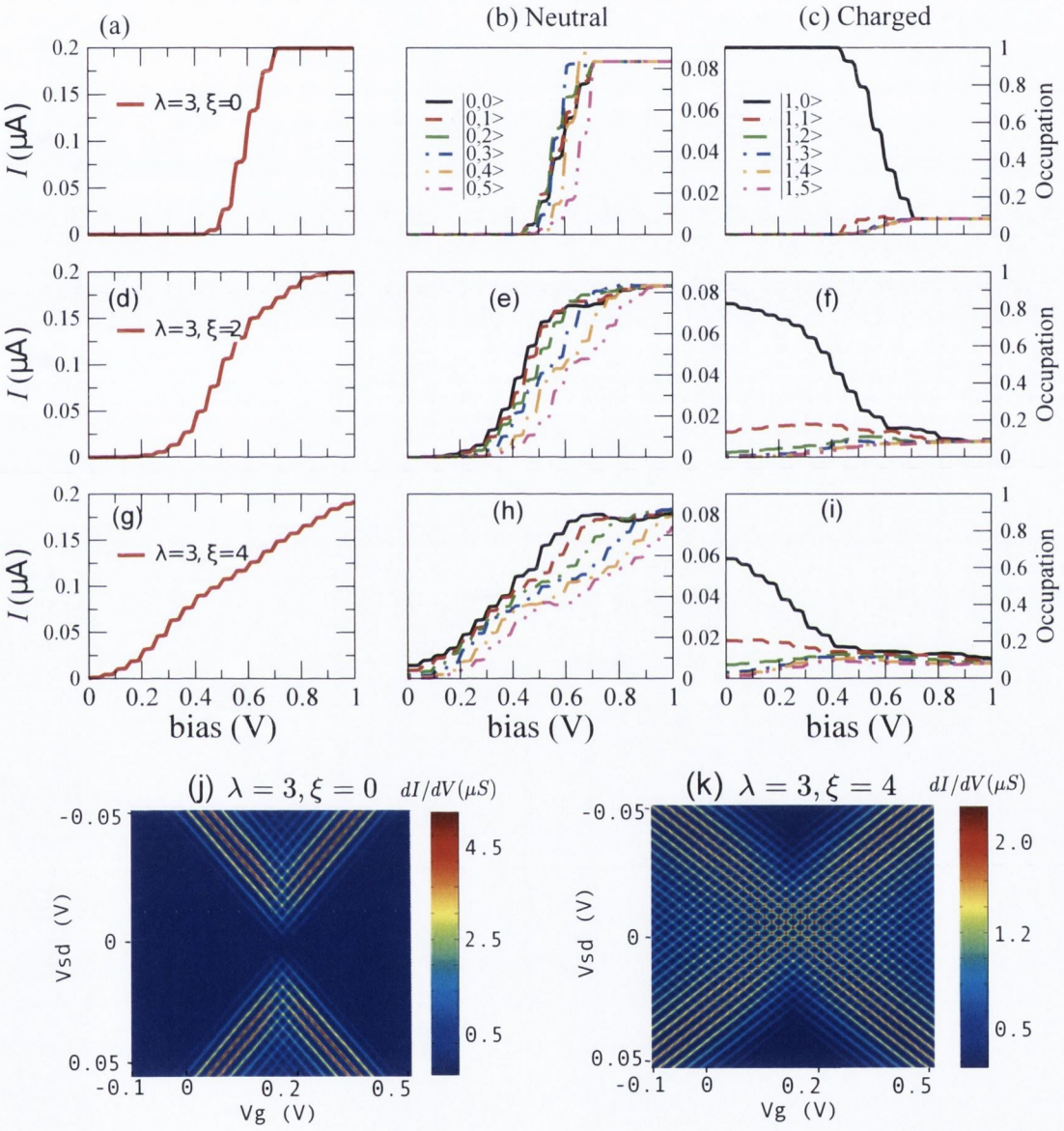

Figure 8.11: (a) Sequential tunneling current as a function of bias for $\lambda = 3$. The current suppression up to 0.5 V is due to Franck-Condon blockade. Panels (b) and (c) show the occupation of the vibronic states for charging state zero and one, respectively. Panels (d-f) and (g-i) are the same for $\xi = 2$ and $\xi = 4$, respectively. (j) The corresponding stability diagram for (a); (k) is the corresponding stability diagram for (g) where the light-induced FKB removal is demonstrated. The parameters used are $k_{\mathrm{B}}\Theta = 1.7$ meV, $\Gamma_{\mathrm{L}} = \Gamma_{\mathrm{R}} = 6$ meV, $\hbar\omega = 50$ meV, $\epsilon_1 = 0$ eV, $q_{\max} = 5$ and $\hbar\omega_{\mathrm{q}} = 25$ meV.

In order to verify the role of vibronic relaxation, we apply the ME presented in Eq. (7.1.8), *i.e.* taking into account the relaxation of vibrons with relaxation time τ, where for $\tau \to 0$, all the vibronic states collapse back to the ground state. Fig. 8.12(a) shows the same sequential tunneling current versus bias presented in Fig. 8.11(g) (unrelaxed) as well as when considering vibronic relaxations. As shown in Fig. 8.12(b) and Fig. 8.12(c), the occupation probabilities of the ground state vibronic states increase leading to a partial recover of the FKB, *i.e.* Fig. 8.12(b-c) should be compared with Fig. 8.11(h-i). This was also observed by May *et al.* [206, 60, 62, 61].

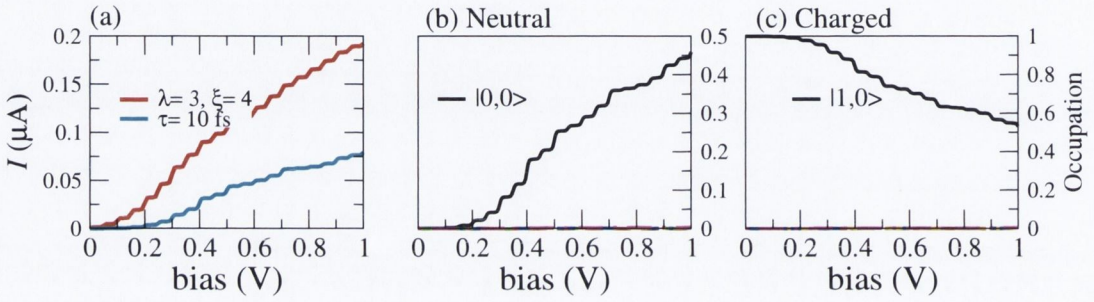

Figure 8.12: (a) Sequential tunneling current with PAT in the FKB regime without vibrational relaxation and including relaxation, with relaxation time $\tau = 10$ fs. (b) and (c) relaxed occupation probabilities for the neutral and charged molecule, respectively. The parameters used are the same as those used in Fig. 8.11.

8.3 Light-induced linear conductance enhancement in molecular junctions

Experimental observation of light-induced conductance enhancement in molecular junctions

S. Battacharyya *et al.* [38] have performed STM electronic transport measurements. In their experiments, a SAM of the target molecule, a fullerene-porphyrin structure, as shown in Fig. 8.13(a) is deposited on a indium-tin oxide (ITO) semiconducting surface and the gold STM tip closes the circuit. While measuring the tunneling current, simultaneously, a monochromatic laser pulse could pass through the transparent semiconductor and photo-excite the molecules trapped in the junction. The authors accomplished to measure the conductance of the molecule in two different electronic configurations, namely, the ground-state and the excited state. By breaking and forming the junction, a histogram of conductances can be plotted. Without light (dark), they observed a conductance average of ~2.5 nS [see Fig. 8.13(b)], whereas for the illuminated junction, a higher conductance peak is observed. They estimated that during the measurements, about 50% of the molecules are in a higher conducting state. Moreover, the enhancement of conductance

is not due to photocurrent since the maximum photocurrent that could be achieved with the intensity of the laser used is orders of magnitude smaller than the one measured.

The complex porphyrin-C60 molecule is a donor-acceptor structure giving rise to a charge-separated state when illuminated with visible light. However, the lifetime of the charge-separated state is of the order of nanoseconds in solution. This time scale is much shorter than the time scale to measured the conductance (~ms). Therefore, the fraction of molecules in the excited state at the time of a measurement should be vanishingly small. It has been shown that the conductance enhancement can be associated to the charging of the molecule [207], leading to an enhancement of the lifetime of the charge-separated state. The authors concluded that the light absorption creates an excitonic charge-separated state, in which an electron is transferred from the porphyrin to the fullerene moiety. The resulting charges migrate away from the site of initial electron transfer, via hopping to adjacent molecules and/or migration into the ITO substrate. This processes make the recombination of these separated charges slow, which allows the observation of the conductance enhancement.

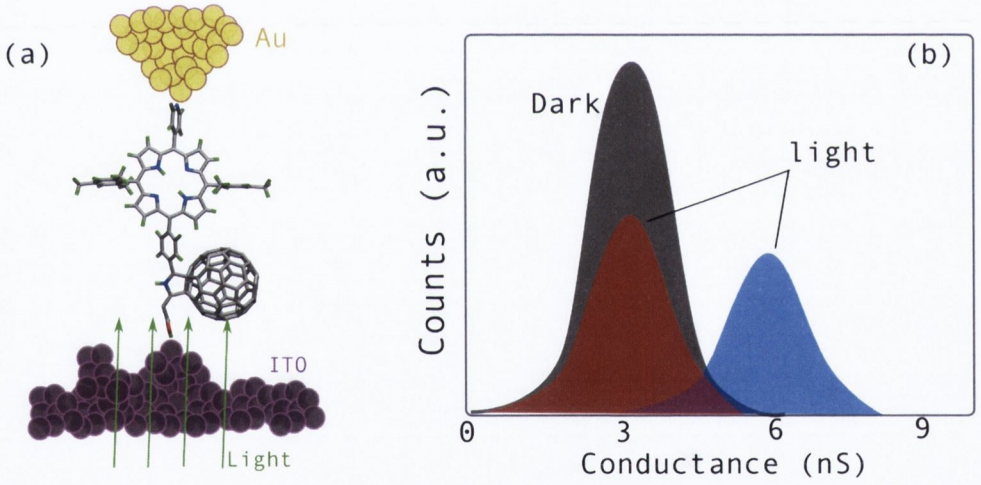

Figure 8.13: (a) Ball-and-stick representation of the expected bonding geometry of a porphyrin-C60 dyad molecule sandwiched in the gold-ITO junction. A carboxylate group interacts with the transparent semiconductor, while a pyridyl moiety binds to the gold probe. The light is represented by the vertical arrows. (b) Schematic representation of the experimental results of Ref. [38] where the average conductance is enhanced when the junction is under illumination.

8.3.1 *Ab initio* approach: constrained-DFT+NEGF for transport in charged molecular junctions

Computational details

In this section we want to investigate the transport properties of a donor-acceptor molecule when the molecule is charged. We combine CDFT described in Chapter 5 (details on the implementation of the method are described in Appendix E) with the NEGF formalism, as described in Chapter 3 and implemented in the SMEAGOL code [187, 188]. The XC energy is treated at the LDA level. We use norm-conserving pseudopotentials according to the Troullier-Martins procedure [143] and the basis set is double-ζ polarized for carbon, sulfur and hydrogen and single-ζ for gold [29, 30]. The mesh cutoff is 300 Ry and four k-points are used for sampling the Brillouin zone in the perpendicular direction to the transport.

Isolated molecule properties

The molecule used in the experiments of S. Battacharyya *et al.* [38] is shown in Fig. 8.13(a) and it consists of a porphyrin-fullerene complex terminated by carboxylate group that binds to the transparent semiconductor and a pyridyl moiety that binds to the gold probe. We abbreviate the molecule with PFC (porphyrin-fullerene-carboxylate). We modify this molecule in order to study the transport across a gold-molecule-gold junction. We replace the carboxylate group by a pyridyl moiety (abbreviated PFN), as shown in Fig. 8.14(c). Fig. 8.14(a) shows the PDOS for the molecule compared to the PDOS of the individual moieties, namely, the porphyrin and the fullerene. Our results show that the HOMO is localized on the porphyrin whereas the LUMO and LUMO+1 are localized on the fullerene, as shown in the plot of the electronic density of Fig. 8.14(c). This confirms the donor-acceptor structure. The I^{P} and E^{A} calculated, by means of the Δ-SCF approach, are equal to 6.23 eV and 3.10 eV, respectively. The LDA gap, $E^{\mathrm{gap}}_{\mathrm{LDA}}$, is underestimated by $\sim$2.5 eV, when compared to $E^{\mathrm{gap}}_{\mathrm{QP}}$. By performing the calculations with the ASIC method [see Fig. 8.14(b)], the $E^{\mathrm{gap}}_{\mathrm{LDA}}$ is modestly opened by 0.5 eV for $\alpha = 1$. We point out that the ordering of the levels are unchanged when ASIC is applied. When the molecule is incorporated in the junction, in order to have a quantitative description of the conductance, corrections to the energy levels should be applied, as we have shown in Chapter 6 and Chapter 7.

Case of study: gold-PFN-gold molecular junctions

Fig. 8.15(a-d) show four different geometrical couplings between the molecule and the electrodes and Fig. 8.15(e) their respective transmission coefficients. In (a) the PFN molecule is connected to a tip-like electrode at both sides; in (b) the NH_2-Au(tip) bond

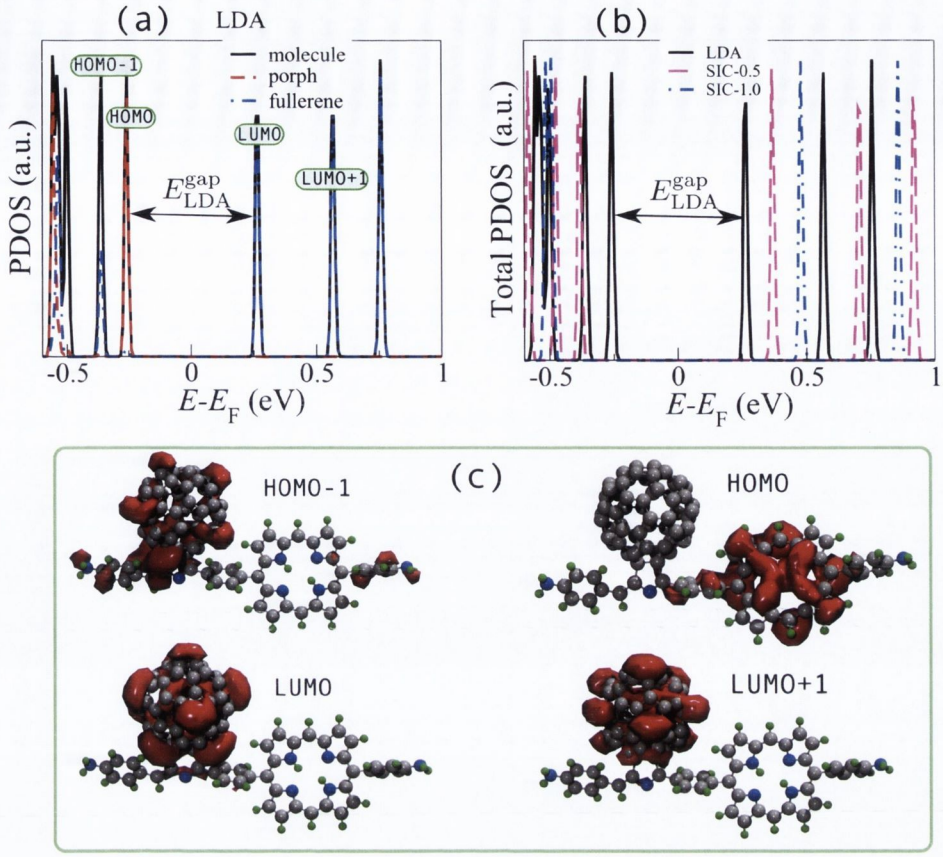

Figure 8.14: (a) and (b) PDOS for the individual units, namely, the fullerene and porphyrin, calculated with LDA and LDA+ASIC, respectively. (c) Isosurface plots of the electronic density of the frontier molecular orbitals.

to the right is replaced by a N-Au(tip) bond; in (c) the NH_2-Au(tip) bond is replaced by a N-Au(tip) bond at both sides. Lastly, for the geometry-4 shown in (d), a N-Au(flat) bond is considered at both sides of the junction. As seen in Fig. 8.15(e) the Landauer elastic transmission [given by Eq. (3.4.32)] at E_F increases by several orders of magnitude when going from the tip-like electrodes to the flat surface due to the stronger coupling to the electrodes. For geometry-4, the conductance is the same order of magnitude of the typical values found in the experiment of Ref. [38], thus we focus on this junction.

Molecular conductance enhancement

We are interested in calculating the conductance of the molecular junctions when the molecule is charged. This is one of the possible mechanism proposed to explain the enhancement of the conductance under illumination observed in experiments. Our approach consists of applying CDFT to constrain the molecule in different charge states, while performing the transport calculations. We perform two sets of calculations, namely, when the molecule is negatively charged and when it is positively charged. The former is achieved by removing one electron from the electrodes and adding it to the fullerene

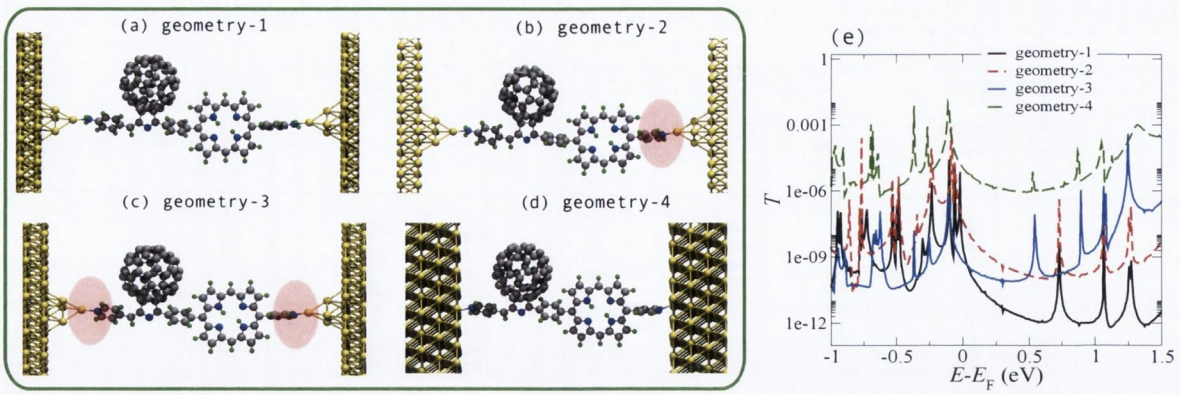

Figure 8.15: (a-d) Ball-and-stick representation of different contact geometries for the Au-PFN-Au molecular junction. (a) NH_2-Au(tip) bond on both sides; (b) NH_2-Au(tip) bond to the left and N-Au(tip) bond to the right; (c) N-Au(tip) bond on both sides and (d) N-Au(flat) bond on both sides of the junction. (e) Transmission coefficients as a function of energy for the different contact geometries obtained with DFT-LDA-NEGF.

moiety [see Fig. 8.16(a)] whereas for the later, an electron is removed from the porphyrin moiety and added to the electrodes, as shown in Fig. 8.16(b). Fig. 8.16(c) shows the

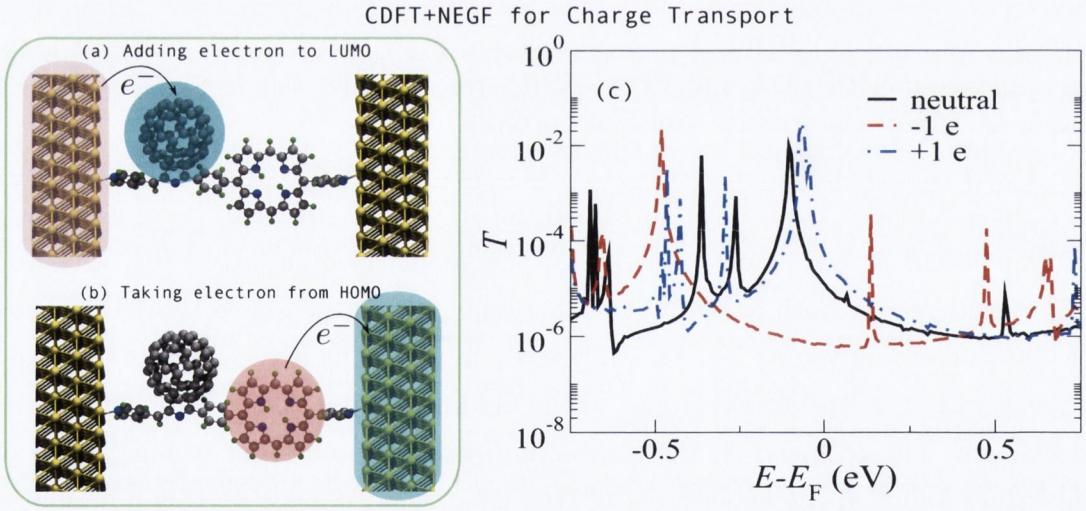

Figure 8.16: (a-b) Ball-and-stick representation of geometry-4 shown in Fig. 8.15 where we schematically show the charge transfer performed with CDFT. (c) Transmission coefficients for the non-constrained solution (neutral) compared to the results obtained by adding one electron to the fullerene ($+1e$) and removing one electron from the porphyrin moiety ($-1e$).

transmission coefficients of the two different charging states of the molecule compared to the calculation without any constraint (neutral molecule). As one would expect, the removal of one electron lowers the energy levels and the conductance at E_F is reduced. In contrast, when an electron is added to the molecule, due to the repulsion needed to

screen the extra charge, the energy levels are shifted upwards and the energy level close to E_F approaches even more E_F leading to an enhanced conductance. This shows that a negatively charged molecule is expected to provide an enhanced conductance. We point out that we assume that the time scale for electron tunneling is shorter than the lifetime of the charging state of the molecule. This is also consistent with the enhanced long-lived charge-transfer state observed experimentally. In order to verify if the molecule

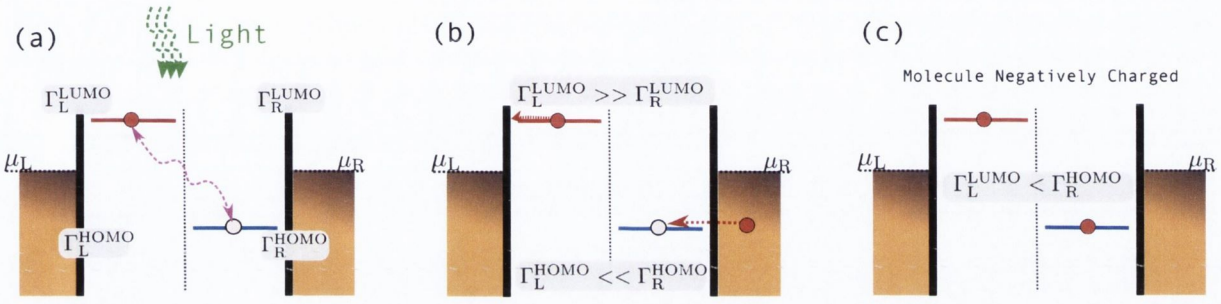

Figure 8.17: Energy level diagram for the model where the molecule becomes negatively charged. (a) The light hits the device and a charge-transfer state occurs with the formation of an exciton (curl arrow). (b) The HOMO state located in the porphyrin moiety is coupled to the right electrode stronger than to the left whereas, the LUMO located in the fullerene moiety is coupled to the left electrode than to the right. Therefore, the hole escapes to the right while the electron escapes to the left electrodes. (c) Moreover, since the coupling between the LUMO and the left electrode is smaller than the coupling between the HOMO and the right electrode, the molecule can become negatively charged. $\Gamma_R^{LUMO} = 3.0 \times 10^{-8}$ eV, $\Gamma_R^{HOMO} = 2.8 \times 10^{-3}$ eV, $\Gamma_L^{HOMO} = 2.3 \times 10^{-5}$ eV and $\Gamma_L^{LUMO} = 4.0 \times 10^{-4}$ eV.

can become negatively charged, we calculate the electronic couplings between the HOMO and LUMO to the left and right electrodes (see Chapter 7 for details on how to extract the electronic couplings). The calculated couplings show that Γ_L^{LUMO} is four orders of magnitude larger than Γ_R^{LUMO} and Γ_R^{HOMO} is two orders of magnitude larger than Γ_L^{HOMO}. This means that when the light excites the molecule, as schematically shown in Fig. 8.17(a) the electron excited to the LUMO level escapes faster to the left electrode than to the right electrode. Likewise, the hole left in the HOMO escapes faster to the right electrode than to the left electrode, as shown in Fig. 8.17(b). Moreover, since Γ_R^{HOMO} is larger than Γ_L^{LUMO} by one order of magnitude, the molecule can become negatively charged by the injection of the electron from the right electrode into the HOMO level [Fig. 8.17(c)].

8.4 Conclusion

In the present Chapter we have studied light-induced charge transfer in molecular junctions. We have presented a ME approach that takes into account both sequential tunneling and cotunneling contributions. This methodology can be applied in combination

with first-principles calculations in order to extract the parameters. We have shown that the cotunneling current increases (for a symmetric junction) with the light intensity, but the increase depends on the photon energy. For low photon energies, the number of sidebands or channels created for the given bias applied is larger than that for high photon energy. We have shown how light can be used to remove the FKB in molecular junctions that in presence of strong electron-vibron coupling. This demonstrates that light may be an efficient tool to optically switching the current through a single molecule. We have simplified the problem as we do not consider internal excitations, *i.e.* the HOMO-LUMO gap is larger than the photon energy, so that the off-diagonal elements of the reduced density matrix can be neglected. In Appendix D we give an example of a double quantum dot where coherent terms must be taken into account.

We have demonstrated by means of our combined approach of constrained-DFT and NEGF that the conductance enhancement observed in experiments can be achieved by negatively charging the molecule. An important assumption is that the time scale for tunneling is much shorter than the lifetime of the charging state. This is justified by the experimental evidence for a long-living charge separated state.

Chapter 9

Conclusion and Future Work

We have developed and applied computational tools to the study of electronic transport properties of molecular junctions. Chapter 2 was dedicated to presenting the electronic structure theory used throughout this thesis, namely, density functional theory. We have discussed the limitations of this approach, for instance, the lack of the derivative discontinuity in local and semi-local approximations of the XC potential and the self-interaction error. We have shown how corrected functionals, such as the LDA+ASIC method and the LDA+SCO method can be used to improve on the results. In Chapter 3, we have presented the general concepts of quantum transport at nanoscale and the non-equilibrium Green's function method, widely used to describe the electronic transport in nanojunctions. Moreover, in Chapter 4, we have also presented and applied a different framework to quantum transport, namely, the density matrix approach from which a set of master equations are solved. This is combined with model Hamiltonians so that it allows us to straightforwardly take into account important effects, such as, light and temperature.

Motivated by the limitations of DFT-LDA to account for non-local correlation effects, important for the energy level alignment of metal/organic interfaces, in Chapter 5, we have applied the CDFT discussed in Sec. 2.6 to determine the energy levels alignment of these interfaces in the weak electron coupling regime [153]. We have demonstrated how the frontier energy levels of a benzene molecule change due to the image charge effect, leading to a HOMO-LUMO gap reduction when the molecule is brought close to a Li(100) surface. We have then studied the size-dependence of the substrate as well as of the supercell used in the simulations in order to obtain quantitatively converged results. We have shown that a rather large metal cluster size is needed for long distances between the molecule and the surface, although at small molecule-metal separations smaller clusters can also give quantitatively accurate results. Our approach also allowed us to calculate the image charge plane, *i.e.* the center of gravity of the screening charge density and we have found 1.72 Å and 1.80 Å for adding and removing one electron, respectively. Moreover, when the calculated image charge plane is used in an effectively parameter-free electrostatic

classical model for the image charge, our CDFT results show very good agreement. This approach offers several advantages when calculating the energy level alignment: (i) rather large systems can be calculated, since the computational costs are similar to those of standard DFT; (ii) surfaces with arbitrary shapes and reconstruction can be studied, including defective and contaminated surfaces; (iii) it gives a direct way of determining the position of the image charge for such interfaces; (iv) there is a systematic way to establish convergence.

Chapter 6 has been dedicated to the study of the gold-BDT molecular junctions. A long-standing problem in the area of molecular electronics has been the difficult to establish a quantitative agreement between experiments and theory for this system. We have studied three main aspects of this system. Firstly, we performed DFT calculations to study the adsorption process of thiol terminated molecules on the gold surface in order to address the stability of the metal-molecule interface. For all the structures studied we have found that the thiol-terminated junctions are energetically more stable than their thiolate counterparts. Moreover, we have found a large activation barrier of about 1 eV for the dissociation of the H atom from the thiol groups adsorbed on gold. These results indicate that the non-dissociated structures are likely to exist in experiments, and therefore they can not be ruled out.

Secondly, from the electronic transport point of view we have shown that the energy level alignment between the molecule and the electrodes is one of the main factors that determine the linear conductance of the system. We have applied the CDFT method presented in Chapter 5 combined with an electrostatic classical image charge model to obtain an accurate description of the energy level alignment of these junctions. The image charge plane calculated with CDFT is 1 Å above the gold surface. While for the benzene-1,4-dithiol (BDT2H) molecules the coupling to the surface remains small at all distances, for small molecule-surface separation the electronic coupling between the benzene-1,4-dithiolate (BDT) and gold surface becomes very strong, and in this limit the use of the CDFT approach is not applicable. We have shown that in the limit of strong coupling, electron transfer from the surface to the molecule occur, so that the molecular LUMO of the isolated BDT becomes increasingly occupied as the molecule-surface distance decreases and the ASIC method is more appropriate to correct the molecular energy levels. Furthermore, by means of NEGF+DFT we have calculated the transport properties of the junctions with different contact geometries and compared the results obtained with LDA, ASIC and LDA+SCO functionals. We have found that Au-BDT-Au and Au-BDT2H-Au junctions show opposite trends concerning the dependence of the conductance on the separation between the flat gold electrodes, *i.e.* while the conductance decreases with the elongation for the thiol junctions, it shows the opposite trend for the thiolate junctions.

Thirdly, we have presented a hybrid classical molecular dynamics and Monte Carlo approach to mechanically and/or thermally evolve the Au-BDT-Au molecular junctions.

This have allowed us to incorporate important aspects found in experiments, such as temperature effects, elongations rate effects, and non-ideal tip contact geometries. By performing transport calculations of several geometries extracted from the MD-MC approach, we have found that conductance enhancement with the electrode separation can be explained by the formation of mono-atomic chains during the elongation process. Our results therefore suggest that thiol junctions must be present in experiments where the conductance decreases with the elongation of the junction. In contrast, the thiolates junctions are likely to be present in experiments showing an increase of the conductance upon stretching.

In Chapter 7 we have combined the DFT-NEGF formalism with the computationally efficient master equation approach to study the transport properties of molecular junctions, where all the parameters for the model Hamiltonian can be obtained from first-principles calculations. In particular, we have shown that the master equation approach can describe the transport properties of molecular junctions in the Coulomb blockade regime, in which the NEGF within DFT-LDA fails due to the lack of the derivative discontinuity in the LDA functional. We have applied this method to reproduce experimental data for a porphyrin-Zn-gold molecular junction in the weak coupling limit. The energy level renormalization due to the image charge is taken into account by means of a parameter-free classical image charge model. Moreover, within the model, we have included temperature effects by considering an effective single vibron-mode and have demonstrated that vibration excitations can be responsible for the linear-like current increase observed in the experiments and the current onset.

Chapter 8 was dedicated to the study of light-induced charge transfer in molecular junctions. All the calculations have been performed within the master equation approach where sequential tunneling and cotunneling contributions were taken into account. We have discussed the general aspects of light-assisted tunneling within the Tien-Gordon model and applied the method to simple models. We have then derived and implemented the transition rates for cotunneling contributions and we have shown that the cotunneling current increases (for a symmetric junction) with the light intensity, however, the increase depends also on the photon energy. Moreover, by considering vibrons and photons in our model, we have studied the interplay between these two excitations on the transport properties of the molecular junctions. We have shown how light can be used to remove the Franck-Condon blockade in molecular junctions that show strong electron-vibron coupling. Finally, motivated by experimental observations [38], we have studied by the combined approach of constrained-DFT and NEGF the conductance enhancement due to changes in the charge state of the molecule. We have shown that the conductance enhancement observed in the experiment can be achieved by negatively charging the molecule. An important assumption is that the time scale of tunneling electrons is much shorter than the time scale of the charging state. This is justified based on experimental evidences for

a long-lived charge separated state [38].

Concerning future work, it would be interesting to tackle the following. Firstly, by using the hybrid MD-MC/NEGF approach, one could perform similar calculations for the Au-BDT2H-Au junctions under stretching. This would allow one to compare one to one with our results for the Au-BDT-Au also when temperature effects and several contact geometries are considered. In terms of future development, the NEGF approach could be merged with a molecular dynamics package so that the transport properties would be calculated self-consistently with the molecular dynamics. This way, one could study the effect of electrical current onto the geometry of the system as well the effect of the change in the geometries on the electrical current.

Within the CDFT approach, one could extend the method to allow geometry relaxation under different constrained charge states. For instance, this could be used to calculate the electron-phonon coupling of isolated molecules as well as when they are in the junctions. This task would be accomplished by evaluating differences in the atomic structure of the system when, *e.g.* an electron is added to it or removed from it.

For the master equation approach, the off-diagonal elements of the reduced density matrix operator could be added, so that coherence between molecular charge states could be taken into account. This would allow us to calculate internal transitions between, for instance, HOMO and LUMO levels, and to calculate the photocurrent up to fourth order in the tunneling Hamiltonian. An interesting project would be to include in the SMEAGOL code electron-photon interaction by means of self-energies [208, 209, 210, 211]. This has been done within model Hamiltonians where just a few energy levels [51] were considered or coherence between internal energy levels were disregarded [195]. Therefore, a full first-principles transport calculation where light-induced tunneling is included, for the best of our knowledge, is still to be done.

Appendix A

Second Quantization Operators

A.1 Fermionic Operators

We first choose a complete set of single-particle states given by $\{|1\rangle, |2\rangle, ..., |M\rangle\}$, where the ordering is key when dealing with fermionic particles such as electrons. In terms of the occupation number representation (*second quantization*), we write a many-body state by simply listing the occupation numbers of each basis state,

$$N\text{-particle basis states} : \{|n_1\rangle, |n_2\rangle, ..., |n_M\rangle\}. \tag{A.1.1}$$

We can now define the molecular many-body charge-state in terms of the single-particle occupation numbers as

$$|\Psi_N\rangle = |n_1, n_2, n_3, ..., n_j, ..., n_M\rangle = |..., n_j, ...\rangle . \tag{A.1.2}$$

This can be written as

$$\begin{aligned} |n_1, n_2, n_3, ..., n_j, ..., n_M\rangle =& \hat{c}_1^\dagger |0, n_2, n_3, ..., n_j, ..., n_M\rangle = \\ & \hat{c}_1^\dagger \hat{c}_2^\dagger |0, 0, n_3, ..., n_j, ..., n_M\rangle = \\ & \hat{c}_1^\dagger \hat{c}_2^\dagger ... \hat{c}_M^\dagger |0, 0, ..., 0\rangle = \\ & \Pi_i \hat{c}_i^\dagger |0\rangle . \end{aligned} \tag{A.1.3}$$

The operator $\hat{c}_i^\dagger$ is called *creation operator* because it creates a fermionic particle in the single-particle state $|i\rangle$. The operator $\hat{c}_j$ is called *annihilation operator* since it destroys a fermionic particle in the single-particle state $|j\rangle$. For fermions, a single-particle state can be occupied by just one particle at a time, then

$$n_i = \begin{cases} 1, & \text{if } |i\rangle \text{ is occupied} \\ 0, & \text{if } |i\rangle \text{ is empty} \end{cases} \tag{A.1.4}$$

and consequently

$$\hat{c}_j^\dagger \left| n_1, n_2, ..., 1_j, ..., n_M \right\rangle = 0 \tag{A.1.5}$$

$$\hat{c}_j \left| n_1, n_2, ..., 0_j, ..., n_M \right\rangle = 0. \tag{A.1.6}$$

By ensuring the *Pauli's principle*, *i.e.* by enforcing the anti-symmetry, the wave functions need to be written as

$$\begin{aligned} \left| n_1, n_2, n_3, ..., n_j, ..., n_M \right\rangle = & \hat{c}_1^\dagger \hat{c}_2^\dagger ... \hat{c}_M^\dagger \left| 0, 0, ..., 0 \right\rangle = \\ & -\hat{c}_2^\dagger \hat{c}_1^\dagger ... \hat{c}_M^\dagger \left| 0, 0, ..., 0 \right\rangle = \\ & - \left| n_2, n_1, n_3, ..., n_j, ..., n_M \right\rangle . \end{aligned} \tag{A.1.7}$$

As a consequence of the anti-symmetric property of the wave function for fermions, the fermionic operators follow the anti-commutation written as

$$\{\hat{c}_i, \hat{c}_j^\dagger\} = \hat{c}_i \hat{c}_j^\dagger + \hat{c}_j^\dagger \hat{c}_i = \delta_{ij}, \tag{A.1.8}$$

$$\{\hat{c}_i, \hat{c}_j\} = \{\hat{c}_i^\dagger, \hat{c}_j^\dagger\} = 0. \tag{A.1.9}$$

We can now define how the fermionic operators act on the many-body states. Here 1_j means that one particle has beeen added to (removed from) single particle state j. The fermionic operators rules are the following:

$$\begin{aligned} \hat{c}_j^\dagger \left| \Psi_N \right\rangle &= \hat{c}_j^\dagger \left| n_1, n_2, n_3, ..., n_j, ..., n_M \right\rangle \\ &= \sqrt{n_j + 1} \left| n_1, n_2, n_3, ..., n_j + 1, ..., n_M \right\rangle = \sqrt{n_j + 1} \left| n + 1_j \right\rangle \\ \hat{c}_j \left| \Psi_N \right\rangle &= \hat{c}_j \left| n_1, n_2, n_3, ..., n_j, ..., n_M \right\rangle = \\ &\sqrt{n_j} \left| n_1, n_2, n_3, ..., n_j - 1, ..., n_M \right\rangle = \sqrt{n_j} \left| n - 1_j \right\rangle \\ \hat{c}_j \hat{c}_j^\dagger \left| \Psi_N \right\rangle &= \hat{c}_j \hat{c}_j^\dagger \left| n_1, n_2, n_3, ..., n_j, ..., n_M \right\rangle = (n_j + 1) \left| \Psi_N \right\rangle \end{aligned} \tag{A.1.10}$$

$$\hat{c}_j^\dagger \hat{c}_j \left| \Psi_N \right\rangle = \hat{c}_j^\dagger \hat{c}_j \left| n_1, n_2, n_3, ..., n_j, ..., n_M \right\rangle = n_j \left| \Psi_N \right\rangle \tag{A.1.11}$$

and

$$\hat{n}_j^{\text{mol}} \left| \Psi_N \right\rangle = \hat{c}_j^\dagger \hat{c}_j \left| \Psi_N \right\rangle = n_j \left| \Psi_N \right\rangle \tag{A.1.12}$$

$$\hat{n}^{\text{mol}} \left| \Psi_N \right\rangle = \sum_i^M \hat{n}_i \left| n \right\rangle = \sum_i n_i \left| \Psi_N \right\rangle \tag{A.1.13}$$

$$N = \sum_i n_i \rightarrow \text{number of electrons in the molecule} \tag{A.1.14}$$

where $\hat{n}_j^{\text{mol}}$ is the so-called *occupation number operator* and the superscript 'mol' stands for 'molecule'. The eigenstates of the number operator are $|n_j\rangle$ and the eigenvalues correspond

to the number of particles occupying the single-particle state $|j\rangle$.

In the same way, we can define a many-body wave function as a convolution of two Hilbert's space in order to describe, for example, the many body wave function of two fermionic electrodes. For example, the many-body state for the two electrodes in their equilibrium state can be written in the form

$$|j\rangle = |j_{\mathrm{L}}, j_{\mathrm{R}}\rangle \tag{A.1.15}$$

$$|j_\alpha\rangle = |j_{\alpha\mathbf{k}_1}, j_{\alpha\mathbf{k}_2}, ..., j_{\alpha\mathbf{k}'}, ..., j_{\alpha\mathbf{k}_{\max}}\rangle = |..., j_{\alpha\mathbf{k}'}, ...\rangle \tag{A.1.16}$$

where $\alpha = \mathrm{L}, \mathrm{R}$, and L and R correspond to the left and right electrodes, respectively. $\mathbf{k}$ is the momentum quantum number.

Likewise, for the operators that act on the electrodes states, we have the following definitions

$$\begin{aligned} \hat{d}^\dagger_{\alpha\mathbf{k}'} |j\rangle &= \hat{d}^\dagger_{\alpha\mathbf{k}'} |j_{\alpha\mathbf{1}}, j_{\alpha\mathbf{2}}, ..., j_{\alpha\mathbf{k}'}, ...\rangle \\ &= \sqrt{j_{\alpha\mathbf{k}'} + 1}\, |j_{\alpha\mathbf{1}}, j_{\alpha\mathbf{2}}, ..., j_{\alpha\mathbf{k}'+1}, ...\rangle = \sqrt{j_{\alpha\mathbf{k}'} + 1}\, |j + 1_{\mathbf{k}'}\rangle \end{aligned} \tag{A.1.17}$$

$$\begin{aligned} \hat{d}_{\alpha\mathbf{k}'} |j\rangle &= \hat{d}^\dagger_{\alpha\mathbf{k}'} |j_{\alpha\mathbf{1}}, j_{\alpha\mathbf{2}}, ..., j_{\alpha\mathbf{k}'}, ...\rangle \\ &= \sqrt{j_{\alpha\mathbf{k}'}}\, |j_{\alpha\mathbf{1}}, j_{\alpha\mathbf{2}}, ..., j_{\alpha\mathbf{k}'}, ...\rangle = \sqrt{j_{\alpha\mathbf{k}'}}\, |j - 1_{\mathbf{k}'}\rangle \end{aligned} \tag{A.1.18}$$

$$\hat{d}_{\alpha\mathbf{k}'}\hat{d}^\dagger_{\alpha\mathbf{k}'} |j\rangle = \hat{d}_{\alpha\mathbf{k}'}\hat{d}^\dagger_{\alpha\mathbf{k}'} |j_{\alpha\mathbf{1}}, j_{\alpha\mathbf{2}}, ..., j_{\alpha\mathbf{k}'}, ...\rangle = (j_{\alpha\mathbf{k}'} + 1)\, |j\rangle \tag{A.1.19}$$

$$\hat{d}^\dagger_{\alpha\mathbf{k}'}\hat{d}_{\alpha\mathbf{k}'} |j\rangle = \hat{d}^\dagger_{\alpha\mathbf{k}'}\hat{d}_{\alpha\mathbf{k}'} |j_{\alpha\mathbf{1}}, j_{\alpha\mathbf{2}}, ..., j_{\alpha\mathbf{k}'}, ...\rangle = j_{\alpha\mathbf{k}'}\, |j\rangle \tag{A.1.20}$$

and

$$\{\hat{d}_{\alpha\mathbf{k}}, \hat{d}^\dagger_{\alpha'\mathbf{k}'}\} = \hat{d}_{\alpha\mathbf{k}}\hat{d}^\dagger_{\alpha'\mathbf{k}'} + \hat{d}^\dagger_{\alpha'\mathbf{k}'}\hat{d}_{\alpha\mathbf{k}} = \delta_{\alpha'\mathbf{k}'\alpha\mathbf{k}} \tag{A.1.21}$$

$$\{\hat{d}^\dagger_{\alpha\mathbf{k}}, \hat{d}^\dagger_{\alpha'\mathbf{k}'}\} = \{\hat{d}_{\alpha\mathbf{k}}, \hat{d}_{\alpha'\mathbf{k}'}\} = 0 \tag{A.1.22}$$

$$\hat{d}_{\alpha\mathbf{k}'} |j_{\alpha\mathbf{1}}, j_{\alpha\mathbf{2}}, ..., 0_{\alpha\mathbf{k}'}, ...\rangle = 0 \tag{A.1.23}$$

$$\hat{d}^\dagger_{\alpha\mathbf{k}'} |j_{\alpha\mathbf{1}}, j_{\alpha\mathbf{2}}, ..., 1_{\alpha\mathbf{k}'}, ...\rangle = 0. \tag{A.1.24}$$

Similarly,

$$\hat{n}^{\mathrm{elec}}_{\alpha\mathbf{k}'} |j\rangle = \hat{d}^\dagger_{\alpha\mathbf{k}'}\hat{d}_{\alpha\mathbf{k}'} |j\rangle = j_{\alpha\mathbf{k}'}\, |j\rangle \tag{A.1.25}$$

$$\hat{n}^{\mathrm{elec}} |j\rangle = \sum_{\alpha\mathbf{k}} \hat{n}^{\mathrm{elec}}_{\alpha\mathbf{k}} |j\rangle = \sum_{\alpha\mathbf{k}} j_{\alpha\mathbf{k}}\, |j\rangle \tag{A.1.26}$$

$$N = \sum_{\alpha\mathbf{k}} j_{\alpha\mathbf{k}} \rightarrow \text{number of electrons on both electrodes} \tag{A.1.27}$$

where $\hat{n}^{\mathrm{elec}}_{\alpha\mathbf{k}}$ is the occupation number operator for the electrodes.

Appendix B

Transition Rates for External Oscillating Potential

B.1 Model Hamiltonian

In this Appendix we explicitly derive the equations for the transition rates used in the master equation to calculate the electrical current across a molecular junction. The system of interest consists of a molecule connected to two metallic electrodes so that the Hamiltonian is given by

$$\hat{H} = \hat{H}_{\text{mol}} + \hat{H}_{\text{L}} + \hat{H}_{\text{R}} + \hat{H}_{\text{T}}, \tag{B.1.1}$$

where the molecular Hamiltonian with M single-particle levels is

$$\hat{H}_{\text{mol}} = \sum_{i=1}^{M} \epsilon_i \hat{c}_i^{\dagger} \hat{c}_i. \tag{B.1.2}$$

Note that this Hamiltonian will change its form depending on the physics we want to describe. For the moment we use this simple model in order to simplify the derivation of the transition rates. The individual electrodes Hamiltonian is given by

$$\hat{H}_{\alpha} = \sum_{\mathbf{k}} \epsilon_{\alpha\mathbf{k}} \hat{d}_{\alpha\mathbf{k}}^{\dagger} \hat{d}_{\alpha\mathbf{k}}. \tag{B.1.3}$$

For this example we disregard the spin degrees of freedom and we assume that the single-particle energies ϵ_i already contain all the many-body effects, such as, charging energy, image charge effect etc. Moreover, the operators $\hat{c}_i^{\dagger}, \hat{c}_i, \hat{d}_{\alpha\mathbf{k}}^{\dagger}$ and $\hat{d}_{\alpha\mathbf{k}}$ are defined in Appendix A and they commute.

The interaction between the leads and the molecule is given by the so-called tunneling

Hamiltonian , $\hat{H}_{\mathrm{T}}$, where

$$\hat{H}_{\mathrm{T}} = \sum_{\alpha i \mathbf{k}} \left[\gamma_{\alpha} \hat{c}_i^{\dagger} \hat{d}_{\alpha \mathbf{k}} + \gamma_{\alpha}^{*} \hat{c}_i \hat{d}_{\alpha \mathbf{k}}^{\dagger} \right]. \tag{B.1.4}$$

Here γ_{α} is the hopping parameter. We are interested in calculating the electrical current across the system, where one electron is transferred from one electrode to the other by crossing the molecule attached to them. For this task, we use the density matrix formalism. The master equation for the diagonal terms of the reduced density matrix is given by

$$\dot{\rho}(t)_{mm} = \sum_{\alpha; n \neq m} \left(\Gamma_{\alpha}^{mn} \rho_{nn} - \Gamma_{\alpha}^{nm} \rho_{mm} \right) + \sum_{\alpha \alpha'; n, m} \left(\Gamma_{\alpha \alpha'}^{mn} \rho_{nn} - \Gamma_{\alpha \alpha'}^{nm} \rho_{mm} \right) \tag{B.1.5}$$

where ρ_{mm} is the occupation of the molecular charge state $|m\rangle$ and Γ^{mn} is the transition rates for electrons tunneling between the molecule and the electrodes when the molecule makes a transition from the charging state $|n\rangle$ to the charging state $|m\rangle$. The first term of Eq. (B.1.5) corresponds to the *sequential-tunneling* and the second term corresponds to *cotunneling*. For the later, if $m = n$, we have *elastic-cotunneling* whereas $m \neq n$ gives the *inelastic-cotunneling*. The current through the left electrode is given by

$$I^{\mathrm{L}} = \underbrace{-e \sum_{nm} \left(n_n - n_m \right) \Gamma_{\mathrm{L}}^{nm} \rho_{mm}}_{\textit{Seq. tunneling}} \underbrace{-e \sum_{nm} \left(\Gamma_{\mathrm{LR}}^{nm} - \Gamma_{\mathrm{RL}}^{nm} \right) \rho_{mm}}_{\textit{Cotunneling}} \tag{B.1.6}$$

The main task now is to calculate the transition rates

$$\Gamma_{\alpha}^{nn'} = \frac{2\pi}{\hbar} \sum_{\nu j j'} J_{\nu}^{2} \left(\frac{\zeta_{n'n}}{\hbar \omega} \right) \langle j | \hat{\chi}_{\alpha}(0) | j \rangle \left| \langle n' j' | \hat{V} | n j \rangle \right|^{2} \delta(E_{j'n'} - E_{jn} - \nu \hbar \omega) \tag{B.1.7}$$

derived in Sec. 4.4.2 of Chapter 4. Here, ν is the number of photons, $\hbar\omega$ is the energy of the incident photon, $\zeta_{n'n} = \tilde{\epsilon_{n'}} - \tilde{\epsilon_{n}}$, as defined in Eq. (4.4.5) of Sec. 4.4 in Chapter 4, and $\hat{V}$ is a generic perturbation. E_{nj} and $E_{n'j'}$ are the initial and final total energies of the system, respectively. χ_{α} is given by Eq. (4.3.13) and $\chi_{\alpha} = \langle j | \hat{\chi}_{\alpha}(0) | j \rangle$ is the probability of finding the electrode α on state $|j\rangle$ for which the condition $\sum_j \chi_{\alpha} = 1$ holds. If $\nu = 0$, we recover the non-driven equation derived in Sec. 4.3.7.

If we consider that the interaction between the molecule and electrodes is weak, the tunneling Hamiltonian [Eq. (B.1.4)] can be treated as a perturbation. Then, an expansion of the *$\mathscr{T}$-matrix* is carried out

$$\mathscr{T} = \hat{H}_{\mathrm{T}} + \hat{H}_{\mathrm{T}} \frac{1}{(E_i + i\eta) - \hat{H}_0} \hat{H}_{\mathrm{T}} + \ldots \tag{B.1.8}$$

where $\hat{H}_0 = \hat{H}_{\mathrm{mol}} + \hat{H}_{\mathrm{L}} + \hat{H}_{\mathrm{R}}$, and i is the index of the initial state. E_i is the energy of the

initial state, which is an eigenstate of $\hat{H}_0$. From now on η is always assumed to be a small positive number, $\eta \to 0^+$. By replacing the perturbation operator $\hat{V}$ by the appropriate terms of Eq. (B.1.8), we can describe different electronic transport regimes.

B.2 Sequential tunneling

To the lowest order in $\hat{H}_{\mathrm{T}}$, one describes the *sequential-tunneling* processes where a single electron is transferred from one electrode to the molecule and vice versa. Eq. (B.1.7) becomes,

$$\Gamma_{\alpha}^{nn'} = \frac{2\pi}{\hbar} \sum_{\nu} \sum_{jj'} J_{\nu}^2 \left(\frac{\zeta_{n'n}}{\hbar\omega} \right) \chi_{\alpha} \left| \langle n'j' | \hat{H}_{\mathrm{T}} | nj \rangle \right|^2 \delta(E_{j'n'} - E_{jn} - \nu\hbar\omega). \tag{B.2.1}$$

Inserting $\hat{H}_{\mathrm{T}}$ given in Eq. (B.1.4) into Eq. (B.2.1) we have

$$\Gamma_{\alpha}^{nn'} = \frac{2\pi}{\hbar} \sum_{\nu} \sum_{jj'} J_{\nu}^2 \left(\frac{\zeta_{n'n}}{\hbar\omega} \right) \sum_{\alpha i \mathbf{k}} \chi_{\alpha} \left| \langle n'j' | \left(\gamma_{\alpha} \hat{c}_i^{\dagger} \hat{d}_{\alpha\mathbf{k}} + \gamma_{\alpha}^{*} \hat{c}_i \hat{d}_{\alpha\mathbf{k}}^{\dagger} \right) | nj \rangle \right|^2 \delta(E_{j'n'} - E_{jn} - \nu\hbar\omega). \tag{B.2.2}$$

We want to describe processes that transfer one electron from the electrode α to the molecule. If we assume that a generic *initial* many-body state for the entire system can be defined as

$$|..., n_j, ...\rangle \, |..., j_{\mathrm{L}\mathbf{k}}, ...\rangle \, |..., j_{\mathrm{R}\mathbf{k}}, ...\rangle = |..., n_j, ...\rangle \, |..., j_{\alpha\mathbf{k}}, ...\rangle = |n\rangle \, |j\rangle = |nj\rangle \, , \tag{B.2.3}$$

we then define a generic *final* state as

$$\begin{aligned} |j'\rangle \, |n'\rangle &= \hat{c}_i^{\dagger} \hat{d}_{\alpha\mathbf{k}} \, |..., n_i, ...\rangle \, |..., j_{\alpha\mathbf{k}}, ...\rangle \\ &= \sqrt{n_i + 1} \, |..., n_i + 1, ...\rangle \, \hat{d}_{\alpha\mathbf{k}} \, |j\rangle \\ &= \hat{d}_{\alpha\mathbf{k}} \, |n'\rangle \, |j\rangle \end{aligned} \tag{B.2.4}$$

consequently,

$$\begin{aligned} (|j'\rangle \, |n'\rangle)^{\dagger} &= \left(\hat{d}_{\alpha\mathbf{k}} \, |n'\rangle \, |j\rangle \right)^{\dagger} \\ &= \langle n'| \, \langle j| \, \hat{d}_{\alpha\mathbf{k}}^{\dagger} \\ &= \langle n'j| \, \hat{d}_{\alpha\mathbf{k}}^{\dagger}. \end{aligned} \tag{B.2.5}$$

Transition rates from electrodes to the molecule

Once we have defined the initial [Eq. (B.2.3)] and final [Eq. (B.2.5)] many-body states, we can define how the unperturbed Hamiltonian acts on these states. First, for the initial

state we have

$$\begin{aligned}\hat{H}_0 |nj\rangle = \left(\hat{H}_{\text{mol}} + \hat{H}_{\text{L}} + \hat{H}_{\text{R}}\right) |nj\rangle &= \left(\sum_{i=1}^{\text{occup.}} \epsilon_i + \sum_{\mathbf{k};\alpha=\text{L,R}}^{\text{occup.}} \epsilon_{\alpha\mathbf{k}}\right) |nj\rangle \\ &= (E_n + E_{j\alpha}) |nj\rangle \\ &= E_{nj} |nj\rangle \,. \end{aligned} \tag{B.2.6}$$

For the final state,

$$\begin{aligned}\hat{H}_0 |j'n'\rangle &= \left(\hat{H}_{\text{mol}} + \hat{H}_{\text{L}} + \hat{H}_{\text{R}}\right) \hat{c}_i^\dagger \hat{d}_{\alpha\mathbf{k}} |..., n_i, ...\rangle |..., j_{\alpha\mathbf{k}}, ...\rangle \\ &= \left(\underbrace{E_n + \epsilon_i}_{} + \underbrace{E_{j\alpha} - \epsilon_{\alpha\mathbf{k}}}_{}\right) |j'n'\rangle \\ &= (E_{n'} + E_{j'\alpha}) |j'n'\rangle \\ &= (E_{n'} + E_{j'}) |j'n'\rangle \\ &= E_{j'n'} |j'n'\rangle \,, \end{aligned} \tag{B.2.7}$$

where we have assumed for the sake of this example that $n_i = j_{\alpha\mathbf{k}} = 1$. Now we can rewrite Eq. (B.2.2) as

$$\begin{aligned}\Gamma_\alpha^+ =& \frac{2\pi}{\hbar} \sum_\nu \sum_j J_\nu^2 \left(\frac{\zeta_{n'n}}{\hbar\omega}\right) \chi_\alpha |\gamma_\alpha|^2 \sum_{\alpha i\mathbf{k}} \Big| \Big\{ \langle n'j| \hat{d}_{\alpha\mathbf{k}}^\dagger \hat{c}_i^\dagger \hat{d}_{\alpha\mathbf{k}} |nj\rangle \\ &+ \underbrace{\langle n'j| \hat{d}_{\alpha\mathbf{k}}^\dagger \hat{c}_i \hat{d}_{\alpha\mathbf{k}}^\dagger |nj\rangle}_{=0, |nj\rangle \to |n-2\rangle|j+2\rangle} \Big\} \Big|^2 \delta(E_n + \epsilon_i + E_{j\alpha} - \epsilon_{\alpha\mathbf{k}} - E_n - E_{j\alpha} - \nu\hbar\omega), \end{aligned} \tag{B.2.8}$$

where the second term inside the curl braket is zero since we do not consider the hopping of two electrons at the same time, where $|nj\rangle \to |n-2\rangle\,|j+2\rangle$ means that two electrons are removed from the molecule and added to the electrode. Note that we have changed the notation $\Gamma^{nn'} \to \Gamma^+$ in order to make clear that the number of particles in the molecule is increasing. Eq. (B.2.8) is finally written as

$$\Gamma_\alpha^+ = \frac{2\pi}{\hbar} |\gamma_\alpha|^2 \sum_\nu J_\nu^2 \left(\frac{\zeta_{n'n}}{\hbar\omega}\right) \sum_{\alpha i\mathbf{k}} \sum_j \chi_\alpha \left| \langle j| \hat{d}_{\alpha\mathbf{k}}^\dagger \hat{d}_{\alpha\mathbf{k}} |j\rangle \langle n'| \hat{c}_i^\dagger |n\rangle \right|^2 \delta(E_{n'} - E_n - \epsilon_{\alpha\mathbf{k}} - \nu\hbar\omega). \tag{B.2.9}$$

The term $\langle j| \hat{d}_{\alpha\mathbf{k}}^\dagger \hat{d}_{\alpha\mathbf{k}} |j\rangle$ gives the occupation of the state $|j\rangle$ and is therefore either one or zero, then the modulus square can be omitted. We can then define the Fermi distribution function of the electrode α by

$$f(\epsilon_{\alpha\mathbf{k}} - \mu_\alpha) = \sum_j \chi_\alpha \langle j| \hat{d}_{\alpha\mathbf{k}}^\dagger \hat{d}_{\alpha\mathbf{k}} |j\rangle = \frac{1}{e^{(\epsilon_{\alpha\mathbf{k}} - \mu_\alpha)/k_{\text{B}}T} + 1}. \tag{B.2.10}$$

and write

$$\Gamma_{\alpha}^{+} = \frac{2\pi}{\hbar} |\gamma_{\alpha}|^2 \sum_{\nu} J_{\nu}^2 \left(\frac{\zeta_{n'n}}{\hbar\omega} \right) \sum_{\alpha\mathbf{k}} \left| \langle n' | \sum_{i} \hat{c}_i^{\dagger} | n \rangle \right|^2 f(\epsilon_{\alpha\mathbf{k}} - \mu_{\alpha}) \delta(E_{n'} - E_n - \epsilon_{\alpha\mathbf{k}} - \nu\hbar\omega). \tag{B.2.11}$$

By assuming that we have a continuous number of states in the electrodes, we can replace the sum by an integral and introduce the density of states of the electrode α, ρ_{α},

$$\Gamma_{\alpha}^{+} = \frac{2\pi}{\hbar} |\gamma_{\alpha}|^2 \rho_{\alpha} \sum_{\nu} J_{\nu}^2 \left(\frac{\zeta_{n'n}}{\hbar\omega} \right) \int d\epsilon_{\alpha\mathbf{k}} \left| \langle n' | \sum_{i} \hat{c}_i^{\dagger} | n \rangle \right|^2 f(\epsilon_{\alpha\mathbf{k}} - \mu_{\alpha}) \delta(E_{n'} - E_n - \epsilon_{\alpha\mathbf{k}} - \nu\hbar\omega). \tag{B.2.12}$$

We considered that the density of states is energy independent (*wide band approximation*), which is a good approximation for metallic electrodes. We solve the integral of Eq. (B.2.12) by using the property of the delta function

$$\int_{-\infty}^{+\infty} d\epsilon f(\epsilon) \delta(\epsilon - T) = f(T), \tag{B.2.13}$$

to we finally obtain

$$\Gamma_{\alpha}^{+} = \frac{2\pi}{\hbar} |\gamma_{\alpha}|^2 \rho_{\alpha} \sum_{\nu} J_{\nu}^2 \left(\frac{\zeta_{n'n}}{\hbar\omega} \right) \left| \langle n' | \sum_{i} \hat{c}_i^{\dagger} | n \rangle \right|^2 f(E_{n'} - E_n - \nu\hbar\omega - \mu_{\alpha}). \tag{B.2.14}$$

Transition rates from the molecule to the electrodes

For electrons hopping from the molecule to the electrodes, we just need to redefine the final state given in Eq. (B.2.5) accordingly

$$\begin{aligned} |j'\rangle |n'\rangle &= \hat{c}_i \hat{d}_{\alpha\mathbf{k}}^{\dagger} |..., n_i, ...\rangle |..., j_{\alpha\mathbf{k}}, ...\rangle \\ &= \sqrt{n_i - 1} |..., n_i - 1, ...\rangle \hat{d}_{\alpha\mathbf{k}}^{\dagger} |j\rangle \\ &= \hat{d}_{\alpha\mathbf{k}}^{\dagger} |n'\rangle |j\rangle \end{aligned} \tag{B.2.15}$$

consequently,

$$\begin{aligned} (|j'\rangle |n'\rangle)^{\dagger} &= \left(\hat{d}_{\alpha\mathbf{k}}^{\dagger} |n'\rangle |j\rangle \right)^{\dagger} \\ &= \langle n' | \langle j | \hat{d}_{\alpha\mathbf{k}} \\ &= \langle n'j | \hat{d}_{\alpha\mathbf{k}}. \end{aligned} \tag{B.2.16}$$

Therefore, after inserting this definition into Eq. (B.2.2), we have

$$\Gamma_{\alpha}^{-} = \frac{2\pi}{\hbar} \sum_{\nu} \sum_{j} J_{\nu}^{2} \left(\frac{\zeta_{n'n}}{\hbar\omega} \right) \chi_{\alpha} \left| \gamma_{\alpha} \right|^{2} \sum_{\alpha i \mathbf{k}} \Big| \Big\{ \underbrace{\langle n'j | \, \hat{d}_{\alpha\mathbf{k}} \hat{c}_{i}^{\dagger} \hat{d}_{\alpha\mathbf{k}} \, | nj \rangle}_{=0, |nj\rangle \to |n+2\rangle |j-2\rangle} + \langle n'j | \, \hat{d}_{\alpha\mathbf{k}} \hat{c}_{i} \hat{d}_{\alpha\mathbf{k}}^{\dagger} \, | nj \rangle \Big\} \Big|^{2} \delta(E_n - \epsilon_i + E_{j\alpha} + \epsilon_{\alpha\mathbf{k}} - E_n - E_{j\alpha} - \nu\hbar\omega), \tag{B.2.17}$$

where we disregard the first term inside the curl bracket since, by construction, the transfer of two electrons at the same time is forbidden, *i.e.* $|nj\rangle \to |n+2\rangle \, |j-2\rangle$ means that two electrons are added to the molecule and removed from the electrode. Then we obtain

$$\Gamma^{-} = \frac{2\pi}{\hbar} \left| \gamma_{\alpha} \right|^{2} \sum_{\nu} J_{\nu}^{2} \left(\frac{\zeta_{n'n}}{\hbar\omega} \right) \sum_{\alpha i \mathbf{k}} \sum_{j} \chi_{\alpha} \left| \langle j | \left(1 - \hat{d}_{\alpha\mathbf{k}}^{\dagger} \hat{d}_{\alpha\mathbf{k}} \right) | j \rangle \, \langle n' | \, \hat{c}_{i} \, | n \rangle \right|^{2} \times \delta(E_n - E_{n'} + \epsilon_{\alpha\mathbf{k}} - \nu\hbar\omega), \tag{B.2.18}$$

where we have used Eq. (A.1.21). The term $\langle j | \, \hat{d}_{\alpha\mathbf{k}}^{\dagger} \hat{d}_{\alpha\mathbf{k}} \, | j \rangle$ again gives the occupation of the state $|j\rangle$ and is therefore either one or zero, then the square modulus can be omitted. After using Eq. (B.2.10) and Eq. (B.2.13), we write

$$\Gamma_{\alpha}^{-} = \frac{2\pi}{\hbar} \left| \gamma_{\alpha} \right|^{2} \rho_{\alpha} \sum_{\nu} J_{\nu}^{2} \left(\frac{\zeta_{n'n}}{\hbar\omega} \right) \left| \langle n' | \sum_{i} \hat{c}_{i} \, | n \rangle \right|^{2} \left[1 - f(E_{n'} - E_n + \nu\hbar\omega - \mu_{\alpha}) \right]. \tag{B.2.19}$$

B.3 Cotunneling

By considering the next-order term, we describe *cotunneling* processes. The transition rates become

$$\Gamma_{\alpha\alpha'}^{nn'} = \frac{2\pi}{\hbar} \sum_{\nu} \sum_{j} J_{\nu}^{2} \left(\frac{\zeta_{n'n}}{\hbar\omega} \right) \hat{\chi}_{\alpha} \left| \langle j' | \, \langle n' | \, \hat{H}_{\mathrm{T}} \frac{1}{E_{jn} + \nu\hbar\omega - \hat{H}_0 + i\eta} \hat{H}_{\mathrm{T}} \, | n \rangle \, | j \rangle \right|^{2} \times \delta(E_{n'j'} - E_{nj} - \nu\hbar\omega). \tag{B.3.1}$$

We are interested in cotunneling processes that effectively transfer one electron from one electrode to the other. Therefore, following the definition for a generic initial state, as stated in Eq. (B.2.3), one can define a generic *final* many-body state as

$$\begin{aligned} |j'\rangle \, |n'\rangle &= \hat{d}_{\alpha'\mathbf{k}'}^{\dagger} \hat{d}_{\alpha\mathbf{k}} \hat{c}_{p}^{\dagger} \hat{c}_{i} \, |..., n_p, ..., n_i, ...\rangle \, |..., j_{\alpha\mathbf{k}}, ..., j_{\alpha'\mathbf{k}'}, ...\rangle \\ &= \left(\sqrt{n_i} \sqrt{n_p + 1} \right) \hat{d}_{\alpha'\mathbf{k}'}^{\dagger} \hat{d}_{\alpha\mathbf{k}} \, |..., n_p + 1, ..., n_i - 1\rangle \, |..., j_{\alpha\mathbf{k}}, ..., j_{\alpha'\mathbf{k}'}, ...\rangle \\ &= \left(\sqrt{n_i} \sqrt{n_p + 1} \right) \hat{d}_{\alpha'\mathbf{k}'}^{\dagger} \hat{d}_{\alpha\mathbf{k}} \, |j\rangle \, |n'\rangle \end{aligned} \tag{B.3.2}$$

consequently,

$$\left(|j'\rangle \, |n'\rangle \right)^{\dagger} = \left(\hat{d}_{\alpha'\mathbf{k}'}^{\dagger} \hat{d}_{\alpha\mathbf{k}} \, |j\rangle \, |n'\rangle \right)^{\dagger} = \langle j | \, \langle n' | \, \hat{d}_{\alpha'\mathbf{k}'} \hat{d}_{\alpha\mathbf{k}}^{\dagger}. \tag{B.3.3}$$

We note that a generic molecular many-body state $|n\rangle$ has the same number of particles as a final state $|n'\rangle$. The difference between them is the way the particles are distributed among the single-particle states $\{|1\rangle, |2\rangle, ..., |M\rangle\}$. Likewise, for the electrodes, the number of particles (for the two electrodes) is the same for the initial $|j\rangle$ and final $|j'\rangle$ states. The difference is that, since one electron is transferred from one electrode to the other, one electrode will have one less electron and the other one additional electron. For example, a final state $|j'\rangle$ could be

$$|j'\rangle = |..., j_{\mathrm{L}\mathbf{k}} - 1, ..., j_{\mathrm{R}\mathbf{k}'} + 1, ...\rangle . \tag{B.3.4}$$

This state represents a many-body state for the two electrodes where one electron from the left electrode with momentum $\mathbf{k}$ is annihilated and a electron with momentum $\mathbf{k}'$ is created on the right electrode.

Once we have defined the initial [Eq. (B.2.3)] and final [Eq. (B.3.3)] many-body states, we can define how the unperturbed Hamiltonian acts on these states. First, for the initial state we have

$$\begin{aligned}
\hat{H}_0 |nj\rangle = \left(\hat{H}_{\mathrm{mol}} + \hat{H}_{\mathrm{L}} + \hat{H}_{\mathrm{R}}\right) |nj\rangle &= \left(\sum_{i=1}^{\text{occup.}} \epsilon_i + \sum_{\mathbf{k};\alpha=\mathrm{L,R}}^{\text{occup.}} \epsilon_{\alpha\mathbf{k}}\right) |nj\rangle \\
&= (E_n + E_{j\alpha}) |nj\rangle \\
&= E_{nj} |nj\rangle .
\end{aligned} \tag{B.3.5}$$

For the final state we write

$$\begin{aligned}
\hat{H}_0 |j'n'\rangle &= \left(\hat{H}_{\mathrm{mol}} + \hat{H}_{\mathrm{L}} + \hat{H}_{\mathrm{R}}\right) \hat{d}^\dagger_{\alpha'\mathbf{k}'} \hat{d}_{\alpha\mathbf{k}} \hat{c}^\dagger_p \hat{c}_i \, |..., n_p, ..., n_i, ...\rangle \, |..., j_{\alpha\mathbf{k}}, ..., j_{\alpha'\mathbf{k}'}, ...\rangle \\
&= \left(\underbrace{E_n - \epsilon_i + \epsilon_p}_{} + \underbrace{E_{j\alpha} - \epsilon_{\alpha\mathbf{k}}}_{} + \underbrace{E_{j\alpha'} + \epsilon_{\alpha'\mathbf{k}'}}_{}\right) |j'n'\rangle \\
&= \left(E_{n'} + \underbrace{E_{j'\alpha} + E_{j'\alpha'}}_{}\right) |j'n'\rangle \\
&= (E_{n'} + E_{j'}) |j'n'\rangle \\
&= E_{j'n'} |j'n'\rangle ,
\end{aligned} \tag{B.3.6}$$

where we have assumed for the sake of this example that $n_i = j_{\alpha\mathbf{k}} = 1$ and $n_p = j_{\alpha'\mathbf{k}'} = 0$.

We now insert Eq. (B.1.4) and Eq. (B.3.3) into Eq. (B.3.1) and multiply all terms by

the identity operator $\sum_{n''} |n''\rangle \langle n''|$,

$$\begin{aligned}
\Gamma^{nn'}_{\alpha\alpha'} = \frac{2\pi}{\hbar} \sum_{\nu} \sum_{j} J^2_{\nu} \left(\frac{\zeta_{n'n}}{\hbar\omega} \right) \sum_{\alpha\alpha'\mathbf{k}\mathbf{k}'} \hat{\chi}_{\alpha} \sum_{\alpha'''\mathbf{k}'''i'''} \sum_{\alpha''\mathbf{k}''i''} |\gamma_{\alpha'''}|^2 |\gamma_{\alpha''}|^2 \\
\times \Bigg| \sum_{n''} \Bigg(\langle j| \langle n'| \hat{d}_{\alpha'\mathbf{k}'} \hat{d}^{\dagger}_{\alpha\mathbf{k}} \hat{d}^{\dagger}_{\alpha'''\mathbf{k}'''} \hat{c}_{i'''} \frac{1}{E_{jn} + \nu\hbar\omega - \hat{H}_0 + i\eta} \hat{d}^{\dagger}_{\alpha''\mathbf{k}''} |n''\rangle \langle n''| \hat{c}_{i''} |n\rangle |j\rangle \\
+ \langle j| \langle n'| \hat{d}_{\alpha'\mathbf{k}'} \hat{d}^{\dagger}_{\alpha\mathbf{k}} \hat{d}^{\dagger}_{\alpha'''\mathbf{k}'''} \hat{c}_{i'''} \frac{1}{E_{jn} + \nu\hbar\omega - \hat{H}_0 + i\eta} \hat{d}_{\alpha''\mathbf{k}''\sigma''} |n''\rangle \langle n''| \hat{c}^{\dagger}_{i''} |n\rangle |j\rangle \\
+ \langle j| \langle n'| \hat{d}_{\alpha'\mathbf{k}'} \hat{d}^{\dagger}_{\alpha\mathbf{k}} \hat{c}^{\dagger}_{i'''} \hat{d}_{\alpha'''\mathbf{k}'''} \frac{1}{E_{jn} + \nu\hbar\omega - \hat{H}_0 + i\eta} \hat{d}^{\dagger}_{\alpha''\mathbf{k}''} |n''\rangle \langle n''| \hat{c}_{i''} |n\rangle |j\rangle \\
+ \langle j| \langle n'| \hat{d}_{\alpha'\mathbf{k}'} \hat{d}^{\dagger}_{\alpha\mathbf{k}} c^{\dagger}_{i'''} \hat{d}_{\alpha'''\mathbf{k}'''} \frac{1}{E_{jn} + \nu\hbar\omega - \hat{H}_0 + i\eta} \hat{d}_{\alpha''\mathbf{k}''} |n''\rangle \langle n''| \hat{c}^{\dagger}_{i''} |n\rangle |j\rangle \Bigg) \Bigg|^2 \\
\times \delta \Bigg(\underbrace{E_n - \epsilon_i + \epsilon_{i'}}_{E_{n'}} + \underbrace{E_{j\alpha} - \epsilon_{\alpha\mathbf{k}}}_{E_{j'\alpha}} + \underbrace{E_{j\alpha'} + \epsilon_{\alpha'\mathbf{k}'}}_{E_{j'\alpha'}} - \underbrace{E_n - E_{j\alpha} - E_{j\alpha'}}_{E_{nj}} - \nu\hbar\omega \Bigg) .
\end{aligned} \tag{B.3.8}$$

We then apply the operator $\hat{H}_0$ in the denominator by using the results of Eq. (B.3.5). Formally, we first carry out a Taylor expansion $1/(\mathcal{E}_{jn} - \hat{H}_0) = (1/\mathcal{E}_{jn}) \sum_{l=0}^{\infty} (\hat{H}_0/\mathcal{E}_{jn})^l$ so that,

$$\begin{aligned}
\hat{H}_0 \hat{d}^{\dagger}_{\alpha''\mathbf{k}''} |n''\rangle |j\rangle = \\
\hat{H}_0 \hat{d}^{\dagger}_{\alpha''\mathbf{k}''} |n''\rangle |..., j_{\alpha''\mathbf{k}''}, ...\rangle = \\
\hat{H}_0 \sqrt{j_{\alpha''\mathbf{k}''} + 1} |n''\rangle |..., j_{\alpha''\mathbf{k}''} + 1, ...\rangle = \\
\left[\left(\sum_{i=1}^{\text{occup.}} \epsilon_i + \sum_{\mathbf{k};\alpha=\text{L,R}}^{\text{occup.}} \epsilon_{\alpha\mathbf{k}} \right) + \epsilon_{\alpha''\mathbf{k}''} \right] \sqrt{j_{\alpha''\mathbf{k}''} + 1} |n''\rangle |..., j_{\alpha''\mathbf{k}''} + 1, ...\rangle = \\
\left(E_{n''} + E_j + \epsilon_{\alpha''\mathbf{k}''} \right) \sqrt{j_{\alpha''\mathbf{k}''} + 1} |n''\rangle |..., j_{\alpha''\mathbf{k}''} + 1, ...\rangle = \\
\left(E_{n''} + E_j + \epsilon_{\alpha''\mathbf{k}''} \right) \hat{d}^{\dagger}_{\alpha''\mathbf{k}''} |n''\rangle |j\rangle .
\end{aligned} \tag{B.3.9}$$

Eq. (B.3.8) is then given by

$$\Gamma^{nn'}_{\alpha\alpha'} = \frac{2\pi}{\hbar}\sum_{\nu}\sum_{j} J^2_{\nu}\left(\frac{\zeta_{n'n}}{\hbar\omega}\right)\sum_{\alpha\alpha'\mathbf{k}\mathbf{k}'}\hat{\chi}_{\alpha}\sum_{\alpha'''\mathbf{k}'''i'''}\sum_{\alpha''\mathbf{k}''i''}|\gamma_{\alpha'''}|^2|\gamma_{\alpha''}|^2\Bigg|\sum_{n''}$$

$$\times\Bigg(\underbrace{\langle j|\langle n'|\hat{d}_{\alpha'\mathbf{k}'}\hat{d}^{\dagger}_{\alpha\mathbf{k}}\hat{d}^{\dagger}_{\alpha'''\mathbf{k}'''}\hat{c}_{i'''}\frac{1}{E_{jn}+\nu\hbar\omega-(E_{n''}+E_j+\epsilon_{\alpha''\mathbf{k}''})+i\eta}\hat{d}^{\dagger}_{\alpha''\mathbf{k}''}|n''\rangle\langle n''|\hat{c}_{i''}|n\rangle}_{=0,\ |n\rangle|j\rangle\to|n-2\rangle|j+2\rangle}$$

$$+\langle j|\langle n'|\hat{d}_{\alpha'\mathbf{k}'}\hat{d}^{\dagger}_{\alpha\mathbf{k}}\hat{d}^{\dagger}_{\alpha'''\mathbf{k}'''}\hat{c}_{i'''}\frac{1}{E_{jn}+\nu\hbar\omega-(E_{n''}+E_j-\epsilon_{\alpha''\mathbf{k}''})+i\eta}\hat{d}_{\alpha''\mathbf{k}''\sigma''}|n''\rangle\langle n''|\hat{c}^{\dagger}_{i''}|n\rangle$$

$$+\langle j|\langle n'|\hat{d}_{\alpha'\mathbf{k}'}\hat{d}^{\dagger}_{\alpha\mathbf{k}}\hat{c}^{\dagger}_{i'''}\hat{d}_{\alpha'''\mathbf{k}'''}\frac{1}{E_{jn}+\nu\hbar\omega-(E_{n''}+E_j+\epsilon_{\alpha''\mathbf{k}''})+i\eta}\hat{d}^{\dagger}_{\alpha''\mathbf{k}''}|n''\rangle\langle n''|\hat{c}_{i''}|n\rangle|j$$

$$+\underbrace{\langle j|\langle n'|\hat{d}_{\alpha'\mathbf{k}'}\hat{d}^{\dagger}_{\alpha\mathbf{k}}c^{\dagger}_{i'''}\hat{d}_{\alpha'''\mathbf{k}'''}\frac{1}{E_{jn}+\nu\hbar\omega-(E_{n''}+E_j-\epsilon_{\alpha''\mathbf{k}''})+i\eta}\hat{d}_{\alpha''\mathbf{k}''}|n''\rangle\langle n''|\hat{c}^{\dagger}_{i''}|n\rangle|j}_{=0,\ |n\rangle|j\rangle\to|n-2\rangle|j+2\rangle}$$

$$\times\delta\Bigg(\underbrace{E_n-\epsilon_i+\epsilon_{i'}}_{E_{n'}}+\underbrace{E_{j\alpha}-\epsilon_{\alpha\mathbf{k}}}_{E_{j'\alpha}}+\underbrace{E_{j\alpha'}+\epsilon_{\alpha'\mathbf{k}'}}_{E_{j'\alpha'}}-\underbrace{E_n-E_{j\alpha}-E_{j\alpha'}}_{E_{nj}}-\nu\hbar\omega\Bigg)\,, \tag{B.3.10}$$

$$\Gamma^{nn'}_{\alpha\alpha'} = \frac{2\pi}{\hbar}\sum_{\nu}\sum_{j} J^2_{\nu}\left(\frac{\zeta_{n'n}}{\hbar\omega}\right)\sum_{\alpha\alpha'\mathbf{k}\mathbf{k}'}\hat{\chi}_{\alpha}\sum_{\alpha'''\mathbf{k}'''i'''}\sum_{\alpha''\mathbf{k}''i''}|\gamma_{\alpha'''}|^2|\gamma_{\alpha''}|^2\Bigg|\sum_{n''}$$

$$\times\Bigg(\langle j|\hat{d}_{\alpha'\mathbf{k}'}\hat{d}^{\dagger}_{\alpha\mathbf{k}}\hat{d}^{\dagger}_{\alpha'''\mathbf{k}'''}\hat{d}_{\alpha''\mathbf{k}''\sigma''}|j\rangle\frac{1}{E_{jn}+\nu\hbar\omega-(E_{n''}+E_j-\epsilon_{\alpha''\mathbf{k}''})+i\eta}\langle n'|\hat{c}_{i'''}|n''\rangle\langle n''|\hat{c}^{\dagger}_{i}$$

$$+\langle j|\hat{d}_{\alpha'\mathbf{k}'}\hat{d}^{\dagger}_{\alpha\mathbf{k}}\hat{d}_{\alpha'''\mathbf{k}'''}\hat{d}^{\dagger}_{\alpha''\mathbf{k}''}|j\rangle\frac{1}{E_{jn}+\nu\hbar\omega-(E_{n''}+E_j+\epsilon_{\alpha''\mathbf{k}''})+i\eta}\langle n'|\hat{c}^{\dagger}_{i'''}|n''\rangle\langle n''|\hat{c}_{i''}|n\rangle$$

$$\times\delta\left(E_{n'}-E_n-\epsilon_{\alpha\mathbf{k}}+\epsilon_{\alpha'\mathbf{k}'}-\nu\hbar\omega\right)., \tag{B.3.11}$$

Here, we do not consider tunneling events that transfer two particles at a time, therefore, the first and fourth terms of Eq. (B.3.10) are set to zero. We can now define the matrix elements of the annihilation operators as

$$\sum_{n''}\langle n'|\hat{c}_{i'''}|n''\rangle\langle n''|\hat{c}^{\dagger}_{i''}|n\rangle=\sum_{n''}\langle n'|\hat{c}_{i'''}|n''\rangle\langle n|\hat{c}_{i''}|n''\rangle^{\dagger}=\sum_{n''}A^{i'''}_{n'n''}A^{i''*}_{nn''} \tag{B.3.12}$$

and

$$\sum_{n''}\langle n'|\hat{c}^{\dagger}_{i'''}|n''\rangle\langle n''|\hat{c}_{i''}|n\rangle=\sum_{n''}\langle n''|\hat{c}_{i'''}|n'\rangle^{\dagger}\langle n''|\hat{c}_{i''}|n\rangle=\sum_{n''}A^{i'''*}_{n''n'}A^{i''}_{n''n} \tag{B.3.13}$$

and Eq. (B.3.11) becomes

$$\Gamma^{nn'}_{\alpha\alpha'} = \frac{2\pi}{\hbar}\sum_{\nu}\sum_{j} J^2_{\nu}\left(\frac{\zeta_{n'n}}{\hbar\omega}\right)\sum_{\alpha\alpha'\mathbf{k}\mathbf{k}'}\chi_{\alpha}\sum_{\alpha'''\mathbf{k}'''i'''}\sum_{\alpha''\mathbf{k}''i''}|\gamma_{\alpha'''}|^2|\gamma_{\alpha''}|^2$$
$$\times\left|\sum_{n''}\left(\langle j|\,\hat{d}_{\alpha'\mathbf{k}'}\hat{d}^{\dagger}_{\alpha\mathbf{k}}\hat{d}^{\dagger}_{\alpha'''\mathbf{k}'''}\hat{d}_{\alpha''\mathbf{k}''\sigma''}\,|j\rangle\,\frac{A^{i'''}_{n'n''}A^{i''*}_{nn''}}{E_n+\nu\hbar\omega-E_{n''}+\epsilon_{\alpha''\mathbf{k}''}+i\eta}\right.\right.$$
$$\left.\left.+\,\langle j|\,\hat{d}_{\alpha'\mathbf{k}'}\hat{d}^{\dagger}_{\alpha\mathbf{k}}\hat{d}_{\alpha'''\mathbf{k}'''}\hat{d}^{\dagger}_{\alpha''\mathbf{k}''}\,|j\rangle\,\frac{A^{i'''*}_{n''n'}A^{i''}_{n''n}}{E_n+\nu\hbar\omega-E_{n''}-\epsilon_{\alpha''\mathbf{k}''}+i\eta}\right)\right|^2$$
$$\times\,\delta\left(E_{n'}-E_n-\epsilon_{\alpha\mathbf{k}}+\epsilon_{\alpha'\mathbf{k}'}-\nu\hbar\omega\right)..\tag{B.3.14}$$

By looking at the operators in the first term and recalling that $\sum_j \chi_\alpha = \sum_j \langle j|\,\hat{\chi}_\alpha(0)\,|j\rangle$, we have

$$\sum_{\alpha\alpha'}\sum_{\alpha''\alpha'''}\sum_{j}\chi_{\alpha}\langle j|\hat{d}_{\alpha'\mathbf{k}'}\hat{d}^{\dagger}_{\alpha\mathbf{k}}\hat{d}^{\dagger}_{\alpha'''\mathbf{k}'''}\hat{d}_{\alpha''\mathbf{k}''}\,|j\rangle$$
$$=\sum_{\alpha\alpha'}\sum_{\alpha''\alpha'''}\sum_{j}\chi_{\alpha}\langle j|\,\hat{d}_{\alpha'\mathbf{k}'}\hat{d}^{\dagger}_{\alpha'''\mathbf{k}'''}\hat{d}^{\dagger}_{\alpha\mathbf{k}}\hat{d}_{\alpha''\mathbf{k}''}\,|j\rangle$$
$$=\sum_{\alpha\alpha'}\sum_{\alpha''\alpha'''}\sum_{j}\chi_{\alpha}\langle j|\left(\delta_{\alpha'\alpha'''}\delta_{\mathbf{k}'\mathbf{k}'''}-d^{\dagger}_{\alpha'''\mathbf{k}'''}d_{\alpha'\mathbf{k}'}\right)\hat{d}^{\dagger}_{\alpha\mathbf{k}}\hat{d}_{\alpha''\mathbf{k}''}\,|j\rangle$$
$$=\sum_{\alpha\alpha'}\sum_{\alpha''\alpha'''}[1-f(\epsilon_{\alpha'\mathbf{k}'}-\mu_{\alpha'})]\delta_{\alpha'\alpha'''}\delta_{\mathbf{k}'\mathbf{k}'''}\times f(\epsilon_{\alpha\mathbf{k}}-\mu_{\alpha})\delta_{\alpha\alpha''}\delta_{\mathbf{k}\mathbf{k}''},\tag{B.3.15}$$

where we have used Eq. (A.1.21) and Eq. (B.2.10). Note that by construction we want to transfer one electron from one electrode to the other, therefore, the conditions $\alpha' \neq \alpha$ and $\alpha''' \neq \alpha''$ holds. Moreover, $[\hat{d}^{\dagger}_{\alpha\mathbf{k}}, \hat{d}^{\dagger}_{\alpha'''\mathbf{k}'''}] = 0$, since by construction, they belong to different sub-spaces, so that we can swap their position. In other words, this term is non-zero only if $\alpha \neq \alpha'''$. Similarly, for the second term, the condition that $\alpha' \neq \alpha$ and $\alpha''' \neq \alpha''$ is enforced. This means that the operators with these indices act on different sub-spaces and we can swap their position without changing the results. Then, the only non-zero contribution is obtained when $\alpha = \alpha'''$ and we can group the operator $\hat{d}_{\alpha'''\mathbf{k}'''}$

with $\hat{d}^{\dagger}_{\alpha''\mathbf{k}''}$ without changing the results. Therefore,

$$\begin{aligned}
&\sum_{\alpha\alpha'}\sum_{\alpha''\alpha'''}\sum_{j}\chi_{\alpha}\left\langle j\right|\hat{d}_{\alpha'\mathbf{k}'}\hat{d}^{\dagger}_{\alpha\mathbf{k}}\hat{d}_{\alpha'''\mathbf{k}'''}\hat{d}^{\dagger}_{\alpha''\mathbf{k}''}\left|j\right\rangle \\
&\qquad=\sum_{\alpha\alpha'}\sum_{\alpha''\alpha'''}\sum_{j}\chi_{\alpha}\left\langle j\right|\hat{d}^{\dagger}_{\alpha\mathbf{k}}\hat{d}_{\alpha'''\mathbf{k}'''}\hat{d}_{\alpha'\mathbf{k}'}\hat{d}^{\dagger}_{\alpha''\mathbf{k}''}\left|j\right\rangle \\
&\qquad=\sum_{\alpha\alpha'}\sum_{\alpha''\alpha'''}\sum_{j}\chi_{\alpha}\left\langle j\right|\left(\delta_{\alpha'\alpha''}\delta_{\mathbf{k}'\mathbf{k}''}-d^{\dagger}_{\alpha''\mathbf{k}''}d_{\alpha'\mathbf{k}'}\right)\hat{d}^{\dagger}_{\alpha\mathbf{k}}\hat{d}_{\alpha'''\mathbf{k}'''}\left|j\right\rangle \\
&\qquad=\sum_{\alpha\alpha'}\sum_{\alpha''\alpha'''}\Big[1-f\left(\epsilon_{\alpha'\mathbf{k}'}-\mu_{\alpha'}\right)\Big]\delta_{\alpha'\alpha''}\delta_{\mathbf{k}'\mathbf{k}''}\times f(\epsilon_{\alpha\mathbf{k}}-\mu_{\alpha})\delta_{\alpha\alpha'''}\delta_{\mathbf{k}\mathbf{k}'''}. \qquad \text{(B.3.16)}
\end{aligned}$$

Now, Eq. (B.3.14) can be rewritten as

$$\begin{aligned}
\Gamma^{nn'}_{\alpha\alpha'}=&\frac{2\pi}{\hbar}\sum_{\nu}J^{2}_{\nu}\left(\frac{\zeta_{n'n}}{\hbar\omega}\right)\sum_{\alpha\alpha'\mathbf{k}\mathbf{k}'}\sum_{i'''}\sum_{i''}|\gamma_{\alpha'}|^{2}|\gamma_{\alpha}|^{2}\\
&\times\left|\sum_{n''}\left(\frac{A^{i'''}_{n'n''}A^{i''*}_{nn''}}{E_{n}+\nu\hbar\omega-E_{n''}+\epsilon_{\alpha\mathbf{k}}+i\eta}+\frac{A^{i'''*}_{n''n'}A^{i''}_{n''n}}{E_{n}+\nu\hbar\omega-E_{n''}-\epsilon_{\alpha'\mathbf{k}'}+i\eta}\right)\right|^{2}\\
&\times\Big[1-f\left(\epsilon_{\alpha'\mathbf{k}'}-\mu_{\alpha'}\right)\Big]\times f\left(\epsilon_{\alpha\mathbf{k}}-\mu_{\alpha}\right)\times\delta\left(E_{n'}-E_{n}-\epsilon_{\alpha\mathbf{k}}+\epsilon_{\alpha'\mathbf{k}'}-\nu\hbar\omega\right).
\end{aligned}\qquad \text{(B.3.17)}$$

Note that the indices of the eigenvalues changed $\epsilon_{\alpha''\mathbf{k}''}\rightarrow\epsilon_{\alpha\mathbf{k}}$ and $\epsilon_{\alpha''\mathbf{k}''}\rightarrow\epsilon_{\alpha'\mathbf{k}'}$ when we apply the delta functions to remove the sums. If we consider a continuous of energy levels in the electrodes, the sums that run over the electrodes energy will become integrals and by inserting the density of states, $\sum_{\mathbf{k}\mathbf{k}'}\rightarrow\rho_{\alpha}\rho_{\alpha'}\int d\epsilon_{\alpha}\int d\epsilon_{\alpha'}$, we write

$$\begin{aligned}
\Gamma^{nn'}_{\alpha\alpha'}=&\frac{2\pi}{\hbar}|\gamma_{\alpha'}|^{2}|\gamma_{\alpha}|^{2}\rho_{\alpha}\rho_{\alpha'}\sum_{\nu}J^{2}_{\nu}\left(\frac{\zeta_{n'n}}{\hbar\omega}\right)\sum_{i'''}\sum_{i''}\int d\epsilon_{\alpha}\int d\epsilon_{\alpha'}\\
&\times\left|\sum_{n''}\left(\frac{A^{i'''}_{n'n''}A^{i''*}_{nn''}}{E_{n}+\nu\hbar\omega-E_{n''}+\epsilon_{\alpha}+i\eta}+\frac{A^{i'''*}_{n''n'}A^{i''}_{n''n}}{E_{n}+\nu\hbar\omega-E_{n''}-\epsilon_{\alpha'}+i\eta}\right)\right|^{2}\\
&\times\Big[1-f\left(\epsilon_{\alpha'}-\mu_{\alpha'}\right)\Big]\times f\left(\epsilon_{\alpha}-\mu_{\alpha}\right)\times\delta\left(E_{n'}-E_{n}-\epsilon_{\alpha}+\epsilon_{\alpha'}-\nu\hbar\omega\right).
\end{aligned}\qquad \text{(B.3.18)}$$

Then the cotunneling rates become

$$\Gamma^{nn'}_{\alpha\alpha'} = \frac{2\pi}{\hbar}\sum_{\nu} J^2_{\nu}\left(\frac{\zeta_{n'n}}{\hbar\omega}\right)\sum_{i'''}\sum_{i''}|\gamma^*_{\alpha'}|^2|\gamma_{\alpha}|^2\rho_{\alpha}\rho_{\alpha'}\int d\epsilon_{\alpha}\int d\epsilon_{\alpha'}$$
$$\times\left|\sum_{n''}\left(\frac{A^{i'''}_{n'n''}A^{i''*}_{nn''}}{E_n+\nu\hbar\omega-E_{n''}+\epsilon_{\alpha}+i\eta}+\frac{A^{i'''*}_{n''n'}A^{i''}_{n''n}}{E_n+\nu\hbar\omega-E_{n''}-\epsilon_{\alpha'}+i\eta}\right)\right|^2$$
$$\times\Big[1-f\left(\epsilon_{\alpha'}-\mu_{\alpha'}\right)\Big]\times f\left(\epsilon_{\alpha}-\mu_{\alpha}\right)\times\delta\left(\underbrace{\epsilon_{\alpha'}}_{\epsilon}-\left[\underbrace{\epsilon_{\alpha}+E_n-E_{n'}+\nu\hbar\omega}_{T}\right]\right), \tag{B.3.19}$$

where we define the electronic couplings as $\Gamma_{\alpha}=2\pi|\gamma_{\alpha}|^2\rho_{\alpha}$. We solve one of the integrals of Eq. (B.3.19) by using the property of the delta function $\int_{-\infty}^{+\infty} d\epsilon f(\epsilon)\delta(\epsilon-T)=f(T)$ and after making the variable change $\epsilon_{\alpha}\to\epsilon$ we finally have

$$\Gamma^{nn'}_{\alpha\alpha'} = \frac{\Gamma_{\alpha}\Gamma_{\alpha'}}{2\pi\hbar}\sum_{\nu} J^2_{\nu}\left(\frac{\zeta_{n'n}}{\hbar\omega}\right)\sum_{i'''}\sum_{i''}\int d\epsilon$$
$$\times\left|\sum_{n''}\left(\frac{A^{i'''}_{n'n''}A^{i''*}_{nn''}}{\epsilon+E_n-E_{n''}+\nu\hbar\omega+i\eta}+\frac{A^{i'''*}_{n''n'}A^{i''}_{n''n}}{-\epsilon+E_{n'}-E_{n''}+i\eta}\right)\right|^2$$
$$\times f\left(\epsilon-\mu_{\alpha}\right)\times\Big[1-f\left(\epsilon+E_n-E_{n'}+\nu\hbar\omega-\mu_{\alpha'}\right)\Big]. \tag{B.3.20}$$

Again, we can recover the non-driven case by considering $\nu=0$.

B.4 Exact solvable model

In this section we show, for a non-interacting single-level model, that the two contributions of sequential tunneling and cotunneling can be obtained exactly. Within scattering theory formalism, the electrical current for this model can be written as

$$I=\frac{e}{h}\int dE\frac{\Gamma_{\mathrm{L}}(E)\Gamma_{\mathrm{R}}(E)}{\Gamma_{\mathrm{L}}(E)+\Gamma_{\mathrm{R}}(E)}\mathcal{A}(E)\Big[f_{\mathrm{L}}(E)-f_{\mathrm{R}}(E)\Big], \tag{B.4.1}$$

where $\mathcal{A}(E)$ is the spectral function of the molecule, given by

$$\mathcal{A}(E)=-2\ \mathrm{Im}\ \mathcal{G}^{+}_{i}(E)=\frac{\Gamma(E)}{\left[E-\epsilon_i\right]^2+\left[\Gamma(E)/2\right]^2}, \tag{B.4.2}$$

with the broadening of the energy level given by $\Gamma(E)=\Gamma_{\mathrm{L}}(E)+\Gamma_{\mathrm{R}}(E)$ and $\Gamma_{\mathrm{L/R}}(E)=2\pi\rho_{\mathrm{L/R}}(E)\gamma^2_{\mathrm{L/R}}$. In the wide band approximation, *i.e.* the electrode density of states $\rho_{\mathrm{L/R}}$ is considered energy independent so that $\Gamma_{\mathrm{L/R}}(E)\to\Gamma_{\mathrm{L/R}}$, we have for a symmetric bias

voltage drop, by performing the integration we have the following solution [116],

$$\begin{aligned} I_{\mathrm{L}} &= \frac{e}{h}\frac{\Gamma_{\mathrm{L}}\Gamma_{\mathrm{R}}}{\Gamma_{\mathrm{L}}+\Gamma_{\mathrm{R}}}\int dE \frac{\Gamma}{[E-\epsilon_i]^2\,[\Gamma/2]^2}\Big[f_{\mathrm{L}}(E)-f_{\mathrm{R}}(E)\Big] \\ &= \frac{e}{h}\frac{\Gamma_{\mathrm{L}}\Gamma_{\mathrm{R}}}{\Gamma_{\mathrm{L}}+\Gamma_{\mathrm{R}}}\frac{1}{\pi}\mathrm{Im}\left\{\psi\left(\frac{1}{2}+\frac{\Gamma\beta}{4\pi}+i\frac{\beta}{2\pi}\left[\epsilon_i+\mu_{\mathrm{L}}\right]\right)-\psi\left(\frac{1}{2}+\frac{\Gamma\beta}{4\pi}+i\frac{\beta}{2\pi}\left[\epsilon_i-\mu_{\mathrm{R}}\right]\right)\right\} \end{aligned} \tag{B.4.3}$$

where ψ is the digamma function defined as the first logarithmic derivative of the gamma function ($\mathcal{J}$)

$$\psi^n(z) \equiv \frac{d^{n+1}}{dz^{n+1}}\ln\mathcal{J}(z) = \frac{d^n}{dz^n}\frac{\mathcal{J}(z)'}{\mathcal{J}(z)}, \tag{B.4.4}$$

and $\beta = 1/k_{\mathrm{B}}\Theta$. Eq. (B.4.3) can be expanded in powers of Γ to obtain [116]

$$\begin{aligned} I &= \frac{e}{h}\frac{\Gamma_{\mathrm{L}}\Gamma_{\mathrm{R}}}{\Gamma_{\mathrm{L}}+\Gamma_{\mathrm{R}}}\Big[f_{\mathrm{L}}(E)-f_{\mathrm{R}}(E)\Big] \\ &= \frac{e}{h}\frac{\beta}{2\pi}\Gamma_{\mathrm{L}}\Gamma_{\mathrm{R}}\mathrm{Im}\left\{\psi'\left(\frac{1}{2}+i\frac{\beta}{2\pi}\left[\epsilon_i+\mu_{\mathrm{L}}\right]\right)-\psi'\left(\frac{1}{2}+i\frac{\beta}{2\pi}\left[\epsilon_i-\mu_{\mathrm{R}}\right]\right)\right\}+\mathcal{O}(\Gamma^3). \end{aligned} \tag{B.4.5}$$

If we consider the weak-coupling limit, the ME approach can be used and in the case of stationary current ($I_{\mathrm{L}} = -I_{\mathrm{R}}$), we can write

$$I_{\mathrm{L}} = e[\Gamma^+_{\mathrm{L}}\rho_0 - \Gamma^-_{\mathrm{L}}\rho_1] + e[\left(\Gamma^{00}_{\mathrm{LR}}-\Gamma^{00}_{\mathrm{RL}}\right)\rho_0 + \left(\Gamma^{11}_{\mathrm{LR}}-\Gamma^{11}_{\mathrm{RL}}\right)\rho_1], \tag{B.4.6}$$

where Γ^+, Γ^- are given by Eq. (B.2.14) and Eq. (B.2.19), *i.e.* they are the sequential tunneling rates to increase and decrease the number of electrons in the molecule, respectively. Γ^{nn} is given by Eq. (B.3.20) and represents the cotunneling rates for an electron to tunnel coherently through the molecule. Note that for a single level model, only elastic cotunneling is possible. Therefore, the initial and the final state are the same and the occupations are not affected. The stationary occupations are obtained by considering the stationary limit

$$0 = \frac{d\rho}{dt} = \Gamma^-\rho_1 - \Gamma^+\rho_0 \tag{B.4.7}$$

and the normalization condition $\rho_0 + \rho_1 = 1$. When no light is considered ($\nu = 0$), Eq. (B.2.14) and Eq. (B.2.19) are just given by

$$\Gamma^+_a = \frac{\Gamma_a}{\hbar}f_a(\epsilon_i),\ \Gamma^-_a = \frac{\Gamma_a}{\hbar}[1-f_a(\epsilon_i)]. \tag{B.4.8}$$

By inserting this into Eq. (B.4.7) we have

$$\rho_0 = \frac{\sum_a \Gamma_a[1 - f_a(\epsilon_i)]}{\Gamma_\mathrm{L} + \Gamma_\mathrm{R}}, \ \rho_1 = \frac{\sum_a \Gamma_a f_a(\epsilon_i)}{\Gamma_\mathrm{L} + \Gamma_\mathrm{R}} \tag{B.4.9}$$

and after substituting into Eq. (B.4.6), we have the sequential tunneling contribution

$$I^\mathrm{seq} = \frac{e}{h}\frac{\Gamma_\mathrm{L}\Gamma_\mathrm{R}}{\Gamma_\mathrm{L} + \Gamma_\mathrm{R}}\Big[f_\mathrm{L}(E) - f_\mathrm{R}(E)\Big], \tag{B.4.10}$$

which coincides with the leading-order term of Eq. (B.4.5).

For the cotunneling contributions we use Eq. (B.3.20) in order to calculate the transition rate. For the single level model and for $\nu = 0$, we have

$$\Gamma^{nn}_\mathrm{LR} = \frac{\Gamma_\mathrm{L}\Gamma_\mathrm{R}}{2\pi\hbar}\int dE \Big|\frac{1}{E - \epsilon_i}\Big|^2 f_\mathrm{L}(\epsilon_i)\left[1 - f_\mathrm{R}(\epsilon_i)\right]. \tag{B.4.11}$$

After following the regularization procedure that will be presented in Sec. C.4, we obtain

$$\Gamma^{nn}_\mathrm{LR} = \frac{\beta}{2\pi\hbar}\frac{\Gamma_\mathrm{L}\Gamma_\mathrm{R}}{2\pi} n_\mathrm{B}\left(\mu_\mathrm{R} - \mu_\mathrm{L}\right) \mathrm{Im}\left\{\psi'\left(\frac{1}{2} + i\frac{\beta}{2\pi}\left[\mu_\mathrm{R} - \epsilon_i\right]\right) - \psi'\left(\frac{1}{2} + i\frac{\beta}{2\pi}\left[\mu_\mathrm{L} - \epsilon_i\right]\right)\right\}. \tag{B.4.12}$$

By inserting this result along with Eq. (B.4.9) into the second term of Eq. (B.4.6), we finally get

$$I^\mathrm{cot} = \frac{e}{h}\frac{\beta}{2\pi}\Gamma_\mathrm{L}\Gamma_\mathrm{R}\mathrm{Im}\Big\{\psi'\left(\frac{1}{2} + i\frac{\beta}{2\pi}\left[\epsilon_i + \mu_\mathrm{L}\right]\right) - \psi'\left(\frac{1}{2} + i\frac{\beta}{2\pi}\left[\epsilon_i - \mu_\mathrm{R}\right]\right)\Big\}, \tag{B.4.13}$$

which again is identical to the next-to-leading order term obtained in Eq. (B.4.5).

Appendix C

Transition Rates Including vibrations

C.1 Model Hamiltonian: Anderson-Holstein model

In this Appendix we explicitly derive the equations for the transition rates including electron-vibron coupling. Again the system is the same represented by the Hamiltonian given by Eq. (8.1.1). However, the molecular Hamiltonian with M single-particle levels is given by the *Anderson-Holstein* model

$$\hat{H}_{\text{mol}} = \sum_{i}^{M} \epsilon_i \hat{n} + \sum_{i}^{M} \frac{\mathcal{U}}{2} \hat{n}\left(\hat{n}-1\right) + \hbar\omega_p \left(\hat{b}^{\dagger}\hat{b} + 1/2\right) + \sum_{i}^{M} \lambda\hbar\omega_p \left(\hat{b}^{\dagger} + \hat{b}\right)\hat{n}, \qquad \text{(C.1.1)}$$

with $\hat{n} = \sum_{\sigma} \hat{c}^{\dagger}_{i\sigma}\hat{c}_{i\sigma}$ The first two terms correspond to the on-site and interaction energies for the electronic degrees of freedom. The third terms describes the vibron energy and the last term describes the electron-vibron interaction where the electron-vibron coupling is given by the parameter λ. The operators $\hat{b}$ and $\hat{b}^{\dagger}$ are the bosonic operators that destroys and creates, respectively, a vibron with energy $\hbar\omega_p$. The operators $\hat{c}^{\dagger}_{i\sigma}, \hat{c}_{i\sigma}, \hat{d}^{\dagger}_{\alpha\mathbf{k}\sigma}$ and $\hat{d}_{\alpha\mathbf{k}\sigma}$, now including the spin σ, are defined in Appendix A. The individual electrodes Hamiltonian is given by Eq. (7.1.5) and the interaction Hamiltonian is given by Eq. (7.1.6). Within this model we assume that the transport occurs by tunneling through one spin-degenerate orbital of the molecule and that only one mode of molecular vibrations is taken into account within the harmonic approximation.

C.2 Lang-Firsov canonical transformation

Electron-vibron coupling can be treated exactly by means of the Lang-Firsov canonical transformation [189]. This is a unitary transformation that preserves the Hermiticity of the Hamiltonian operator. It implies that the transformation's generator $\hat{S}$ must be anti-

Hermitian, *i.e.* $\hat{S}^\dagger = -\hat{S}$, so that $\tilde{H} = e^{\hat{S}}\hat{H}e^{-\hat{S}}$ where $\tilde{H}$ is the transformed Hamiltonian. The appropriate choice for $\hat{S}$ to eliminate explicitly the electron-vibron coupling term is

$$\hat{S} = \lambda\left(\hat{b}^\dagger - \hat{b}\right)\hat{c}^\dagger_{i\sigma}\hat{c}_{i\sigma}. \tag{C.2.1}$$

By using the following relation

$$e^A B e^{-A} = \sum_{m=0}^{\infty}\frac{1}{m!}[A,B]_m = B + [A,B] + \frac{1}{2}[A,[A,B]] + \frac{1}{6}[A,[A,[A,B]]] + ..., \tag{C.2.2}$$

the operators used in the Hamiltonian can be transformed as

$$\tilde{d}_{\alpha\mathbf{k}\sigma} = e^{\hat{S}}\hat{d}_{\alpha\mathbf{k}\sigma}e^{-\hat{S}} = \sum_m^{\infty}\frac{\lambda^m\left(\hat{b}^\dagger - \hat{b}\right)}{n!}\left[\hat{c}^\dagger_{i\sigma}\hat{c}_{i\sigma}, \hat{d}_{\alpha\mathbf{k}\sigma}\right]_m = \hat{d}_{\alpha\mathbf{k}\sigma}e^{\lambda\left(\hat{b}-\hat{b}^\dagger\right)}, \tag{C.2.3}$$

$$\tilde{d}^\dagger_{\alpha\mathbf{k}\sigma} = \hat{d}^\dagger_{\alpha\mathbf{k}\sigma}e^{-\lambda\left(\hat{b}-\hat{b}^\dagger\right)}, \tag{C.2.4}$$

$$\tilde{b} = e^{\hat{S}}\hat{b}e^{-\hat{S}} = \sum_m^{\infty}\frac{\lambda^m\hat{c}^\dagger_{i\sigma}\hat{c}_{i\sigma}}{n!}\left[\hat{b}^\dagger - \hat{b}, \hat{b}\right]_m = \hat{b} - \lambda\hat{c}^\dagger_{i\sigma}\hat{c}_{i\sigma}, \tag{C.2.5}$$

$$\tilde{b}^\dagger = \hat{b}^\dagger - \lambda\hat{c}^\dagger_{i\sigma}\hat{c}_{i\sigma}, \tag{C.2.6}$$

$$\tilde{c}_{i\sigma} = \hat{c}_{i\sigma}, \tag{C.2.7}$$

$$\tilde{c}^\dagger_{i\sigma} = \hat{c}^\dagger_{i\sigma}. \tag{C.2.8}$$

Here we have used $\left[\hat{c}^\dagger_{i\sigma}\hat{c}_{i\sigma}, \hat{d}_{\alpha\mathbf{k}\sigma}\right] = (-1)^n\hat{d}_{\alpha\mathbf{k}\sigma}$ and $\left[\hat{b}^\dagger - \hat{b}, \hat{b}\right] = -1$. Based on these relations, the transformed molecular Hamiltonian takes the form

$$\hat{H}_{\text{mol}} = \sum_i^M \tilde{\epsilon}_i\hat{n} + \sum_i^M\frac{\tilde{\mathcal{U}}}{2}\hat{n}\left(\hat{n}-1\right) + \hbar\omega_p\left(\hat{b}^\dagger\hat{b} + 1/2\right), \tag{C.2.9}$$

where $\tilde{\epsilon}_i = \epsilon_i - \lambda^2\hbar\omega_p$ and $\tilde{\mathcal{U}} = \mathcal{U} - 2\lambda^2\hbar\omega_p$. The transformed interaction Hamiltonian takes the form

$$\hat{H}_{\text{T}} = \sum_{\alpha i\mathbf{k}\sigma}\left[\gamma_\alpha e^{-\lambda\left(\hat{b}^\dagger-\hat{b}\right)}\hat{c}^\dagger_{i\sigma}\hat{d}_{\alpha\mathbf{k}\sigma} + \gamma^*_\alpha e^{\lambda\left(\hat{b}^\dagger-\hat{b}\right)}\hat{c}_{i\sigma}\hat{d}^\dagger_{\alpha\mathbf{k}\sigma}\right]. \tag{C.2.10}$$

The electrodes Hamiltonian are not transformed since we do not consider any coupling term between the electrodes and the vibrons degrees of freedom located in the molecule.

Transition rates from the electrodes to the molecule

We assume that a generic *initial* many-body state for the entire system can be defined as

$$|..., n_j, ...; \sigma; q\rangle\,|..., j_{\alpha\mathbf{k}}, ...\rangle = |n\sigma, q\rangle\,|j\rangle = |n\sigma qj\rangle\,, \tag{C.2.11}$$

where the spin component $\sigma = \uparrow, \downarrow$ is only relevant for the singly-occupied molecule. q is the vibron quantum number. Since we consider spin-degenerate single-particle states, we can simplify the notation by introducing spin factors into the transition rates, as we will show bellow. For the moment, we drop the spin variable. A generic *final* state can be defined as

$$\begin{aligned} |j'\rangle |n'q'\rangle &= \hat{c}_i^\dagger \hat{d}_{\alpha\mathbf{k}} |..., n_i, ...; q\rangle |..., j_{\alpha\mathbf{k}}, ...\rangle \\ &= \sqrt{n_i + 1} |..., n_i + 1, ...\rangle \hat{d}_{\alpha\mathbf{k}} |j\rangle \\ &= \hat{d}_{\alpha\mathbf{k}} |n'q'\rangle |j\rangle , \end{aligned} \tag{C.2.12}$$

consequently,

$$\begin{aligned} (|j'\rangle |n'q'\rangle)^\dagger &= \left(\hat{d}_{\alpha\mathbf{k}} |n'q'\rangle |j\rangle\right)^\dagger \\ &= \langle n'q'| \langle j| \hat{d}_{\alpha\mathbf{k}}^\dagger \\ &= \langle n'q'j| \hat{d}_{\alpha\mathbf{k}}^\dagger . \end{aligned} \tag{C.2.13}$$

Here we assumed that the a vibron excitation can occur and therefore the vibron index, q', in the final state is different from that of the initial state, q. Then

$$\Gamma_\alpha^{nn';qq'} = \frac{2\pi}{\hbar} \sum_{jj'} \sum_{\alpha i\mathbf{k}} \hat{\chi}_\alpha \left| \langle n'q'j'| \left(\gamma_\alpha e^{-\lambda\left(\hat{b}^\dagger - \hat{b}\right)} \hat{c}_i^\dagger \hat{d}_{\alpha\mathbf{k}} + \gamma_\alpha^* e^{\lambda\left(\hat{b}^\dagger - \hat{b}\right)} \hat{c}_i \hat{d}_{\alpha\mathbf{k}}^\dagger \right) |nqj\rangle \right|^2 \delta(E_{j'n'q'} - E_{jnq}). \tag{C.2.14}$$

We can now calculate the total energies of the initial and final many-body states. Firstly, for the initial state we have

$$\hat{H}_0 |nj\rangle = \left(\hat{H}_{\text{mol}} + \hat{H}_{\text{L}} + \hat{H}_{\text{R}}\right) |nqj\rangle , \tag{C.2.15}$$

$$\begin{aligned} &= \left[\sum_i^{\text{occup.}} \left(\tilde{\epsilon}_i + \frac{\tilde{\mathcal{U}}_i}{2} N(N-1) \right) + \hbar\omega_p \left(q + 1/2\right) + \sum_{\mathbf{k};\alpha=\text{L,R}}^{\text{occup.}} \epsilon_{\alpha\mathbf{k}} \right] |nqj\rangle , \\ &= \left(E_{nq} + E_{j\alpha}\right) |nqj\rangle , \\ &= E_{nqj} |nqj\rangle . \end{aligned} \tag{C.2.16}$$

For the final state,

$$\begin{aligned}\hat{H}_0 \left|j'n'q'\right\rangle &= \left(\hat{H}_{\text{mol}} + \hat{H}_{\text{L}} + \hat{H}_{\text{R}}\right) \hat{c}_i^\dagger \hat{d}_{\alpha\mathbf{k}} \left|..., n_i, ...; q'\right\rangle \left|..., j_{\alpha\mathbf{k}}, ...\right\rangle \\ &= \left(\underbrace{E_{nq'} + \epsilon_i}_{} + \underbrace{E_{j\alpha} - \epsilon_{\alpha\mathbf{k}}}_{}\right) \left|j'n'q'\right\rangle \\ &= \left(E_{n'q'} + E_{j'\alpha}\right) \left|j'n'q'\right\rangle \\ &= \left(E_{n'q'} + E_{j'}\right) \left|j'n'q'\right\rangle \\ &= E_{j'n'q'} \left|j'n'q'\right\rangle, \end{aligned} \tag{C.2.17}$$

where we have assumed for the sake of this example that $n_i = j_{\alpha\mathbf{k}} = 1$. Following the same reasoning applied in Appendix B, Sec. B.2, to derive Eq. (B.2.14) and Eq. (B.2.19), we obtain

$$\Gamma_\alpha^{+,qq'} = \frac{2\pi}{\hbar} \left|\gamma_\alpha\right|^2 \rho_\alpha \left| \left\langle n' \right| \sum_i \hat{c}_i^\dagger \left|n\right\rangle \left\langle q' \right| e^{-\lambda\left(\hat{b}^\dagger - \hat{b}\right)} \left|q\right\rangle \right|^2 f(E_{n'q'} - E_{nq} - \mu_\alpha), \tag{C.2.18}$$

for electrons entering the molecule through electrode α and changing the vibronic state of the molecule from $q \to q'$. Likewise, for electrons leaving the molecule, the transition rate is

$$\Gamma_\alpha^{-,qq'} = \frac{2\pi}{\hbar} \left|\gamma_\alpha\right|^2 \rho_\alpha \left| \left\langle n' \right| \sum_i \hat{c}_i \left|n\right\rangle \left\langle q' \right| e^{-\lambda\left(\hat{b}^\dagger - \hat{b}\right)} \left|q\right\rangle \right|^2 \left[1 - f(E_{n'q'} - E_{nq} - \mu_\alpha)\right]. \tag{C.2.19}$$

The coefficients $\left\langle q' \right| e^{-\lambda\left(\hat{b}^\dagger - \hat{b}\right)} \left|q\right\rangle \equiv F_{q'q}$ are given by [115]

$$F_{q'q} = \left(\frac{q_1!}{q_2!}\right)^{1/2} \lambda^{q_2 - q_1} e^{-\lambda^2/2} L_{q1}^{q_2 - q_1}(\lambda^2) \times \begin{cases} (-1)^{q'-q} & \text{for } \; q' \geq q \\ 1 & \text{for } \; q' < q, \end{cases} \tag{C.2.20}$$

where $q_1 = \min\{q, q'\}$ and $q_2 = \max\{q, q'\}$ and L_i^j are the generalized Laguerre's polynomial. In order to include light effects we consider the substitution $\epsilon_i \to \tilde{\epsilon}_i \cos\,\omega t$ in Eq. (C.1.1) and we have

$$\Gamma_\alpha^{+,qq'} = \frac{2\pi}{\hbar} \sum_\nu J_\nu^2 \left(\frac{\zeta_{n'n}}{\hbar\omega}\right) \left|\gamma_\alpha\right|^2 \rho_\alpha \left| \left\langle n' \right| \sum_i \hat{c}_i^\dagger \left|n\right\rangle \left\langle q' \right| e^{-\lambda\left(\hat{b}^\dagger - \hat{b}\right)} \left|q\right\rangle \right|^2 f(E_{n'q'} - E_{nq} - \nu\hbar\omega - \mu_\alpha) \tag{C.2.21}$$

and

$$\Gamma_{\alpha}^{-,qq'} = \frac{2\pi}{\hbar}\sum_{\nu} J_{\nu}^{2}\left(\frac{\zeta_{n'n}}{\hbar\omega}\right)|\gamma_{\alpha}|^{2}\rho_{\alpha}\left|\langle n'|\sum_{i}\hat{c}_{i}|n\rangle\langle q'|e^{-\lambda\left(\hat{b}^{\dagger}-\hat{b}\right)}|q\rangle\right|^{2}[1-f(E_{n'q'}-E_{nq}+\nu\hbar\omega- \tag{C.2.22}$$

C.3 Cotunneling

In order to include vibrons in the cotunneling transition rates, we follow the same reasoning used to derived Eq. (B.3.20) with the following definition of a final state

$$|j'\rangle|n';q'\rangle = \hat{d}_{\alpha'\mathbf{k}'}^{\dagger}\hat{d}_{\alpha\mathbf{k}}\hat{c}_{p}^{\dagger}\hat{c}_{i}|...,n_{p},...,n_{i},...;q\rangle|...,j_{\alpha\mathbf{k}},...,j_{\alpha'\mathbf{k}'},...\rangle\,, \tag{C.3.1}$$

consequently,

$$(|j'\rangle|n',q'\rangle)^{\dagger} = \left(\hat{d}_{\alpha'\mathbf{k}'}^{\dagger}\hat{d}_{\alpha\mathbf{k}}|j\rangle|n',q'\rangle\right)^{\dagger} = \langle j|\langle n',q'|\hat{d}_{\alpha'\mathbf{k}'}\hat{d}_{\alpha\mathbf{k}}^{\dagger}, \tag{C.3.2}$$

where we assume that the number of vibrons, q, can change during the electronic tunneling. This leads to the following expression for the transition rates for cotunnling including a single-vibron mode

$$\begin{aligned}\Gamma_{\alpha\alpha'}^{nn';qq'} = {} & \frac{\Gamma_{\alpha}\Gamma_{\alpha'}}{2\pi\hbar}\sum_{i'''}\sum_{i''}\int d\epsilon \\ & \times\left|\sum_{n'',q''}\left(\frac{A_{n'n''}^{i'''}A_{nn''}^{i''*}F_{q'q''}F_{qq''}^{*}}{\epsilon+E_{nq}-E_{n''q''}+i\eta}+\frac{A_{n''n'}^{i'''*}A_{n''n}^{i''}F_{q''q'}^{*}F_{q''q}}{-\epsilon+E_{n'q'}-E_{n''q''}+i\eta}\right)\right|^{2} \\ & \times f\left(\epsilon-\mu_{\alpha}\right)\times\left[1-f\left(\epsilon+E_{nq}-E_{n'q'}-\mu_{\alpha'}\right)\right].\end{aligned} \tag{C.3.3}$$

In order to include light effects we consider the substitution $\epsilon_{i}\rightarrow\tilde{\epsilon}_{i}\cos\omega t$ in Eq. (C.1.1) and we have

$$\begin{aligned}\Gamma_{\alpha\alpha'}^{nn';qq'} = {} & \frac{\Gamma_{\alpha}\Gamma_{\alpha'}}{2\pi\hbar}\sum_{\nu}J_{\nu}^{2}\left(\frac{\zeta_{n'n}}{\hbar\omega}\right)\sum_{i'''}\sum_{i''}\int d\epsilon \\ & \times\left|\sum_{n'',q''}\left(\frac{A_{n'n''}^{i'''}A_{nn''}^{i''*}F_{q'q''}F_{qq''}^{*}}{\epsilon+E_{nq}-E_{n''q''}+\nu\hbar\omega+i\eta}+\frac{A_{n''n'}^{i'''*}A_{n''n}^{i''}F_{q''q'}^{*}F_{q''q}}{-\epsilon+E_{n'q'}-E_{n''q''}+i\eta}\right)\right|^{2} \\ & \times f\left(\epsilon-\mu_{\alpha}\right)\times\left[1-f\left(\epsilon+E_{nq}-E_{n'q'}+\nu\hbar\omega-\mu_{\alpha'}\right)\right].\end{aligned} \tag{C.3.4}$$

This can be written in a generic form as,

$$\Gamma_{\alpha\alpha'}^{nn',qq'} = \frac{\Gamma_\alpha \Gamma_{\alpha'}}{2\pi\hbar} \sum_\nu J_\nu^2 \left(\frac{\zeta_{n'n}}{\hbar\omega}\right) \sum_{i'''} \sum_{i''} \int d\epsilon$$
$$\times \left| \sum_k \left(\frac{A_k}{\epsilon - E_{Ak} + i\Gamma} + \frac{B_k}{-\epsilon - E_{Bk} + i\Gamma} \right) \right|^2 f\left(\epsilon - E_1\right) \times \left[1 - f\left(\epsilon - E_2\right)\right] \tag{C.3.5}$$

$$= \frac{\Gamma_\alpha \Gamma_{\alpha'}}{2\pi\hbar} \sum_\nu J_\nu^2 \left(\frac{\zeta_{n'n}}{\hbar\omega}\right) \sum_{i'''} \sum_{i''} \int d\epsilon f\left(\epsilon - E_1\right) \times \left[1 - f\left(\epsilon - E_2\right)\right]$$
$$\times \Bigg\{ \sum_k \left| \frac{A_k}{\epsilon - E_{Ak} + i\Gamma} \right|^2 \rightarrow \text{Integral type J}$$
$$+ \sum_k \left| \frac{B_k}{-\epsilon - E_{Bk} + i\Gamma} \right|^2 \rightarrow \text{Integral type J}$$
$$+ 2Re \sum_q \sum_{k<q} \frac{A_k}{\epsilon - E_{Ak} + i\Gamma} \frac{A_q}{\epsilon - E_{Aq} - i\Gamma} \rightarrow \text{Integral type I}$$
$$+ 2Re \sum_q \sum_{k<q} \frac{B_k}{-\epsilon - E_{Bk} + i\Gamma} \frac{B_q}{-\epsilon - E_{Bq} - i\Gamma} \rightarrow \text{Integral type I}$$
$$+ 2Re \sum_q \sum_k \frac{A_k}{\epsilon - E_{Ak} + i\Gamma} \frac{B_q}{-\epsilon - E_{Bq} - i\Gamma} \Bigg\} \rightarrow \text{Integral type I} \tag{C.3.6}$$

where we have redefined the variables as following:

$$\begin{aligned} A_k &= A_{n'k}^{i'''} A_{nk}^{i''*} F_{q'k} F_{qk}^* \\ B_k &= A_{kn'}^{i'''*} A_{kn}^{i''} F_{kq'}^* F_{kq} \\ E_{Ak} &= E_k - E_{nq} - \nu\hbar\omega \\ E_{Bk} &= E_k - E_{n'q'} \\ E_1 &= \mu_\alpha \\ E_2 &= \mu_{\alpha'} + E_{n'q'} - E_{nq} - \nu\hbar\omega. \end{aligned} \tag{C.3.7}$$

C.4 Regularization scheme for the cotunneling transition rates

Eq. (C.3.6) can not be directly evaluated because it diverges due to the second-order poles from the energy denominators. This is because within a purely perturbative approach, the energy of the virtual states are considered to be well defined, *i.e.* with infinite lifetime [121]. In order to remove the singularities, we apply a regularization scheme [116, 115, 114, 120, 121], which is motivated by two observations. (i) Second-order

perturbation theory misses the fact that the virtual states obtains a finite width $\sim \Gamma$ due to the tunneling events. (ii) For a specific cotunneling transition at finite temperature, the final state can also be reached from the same initial state by two sequential processes. The regularization is as follows. In the weak tunneling regime, this width is of second order in the tunneling amplitudes γ so that it is introduced in the denominator by replacing η in order to shift the poles away from the real axis. The integrals are then expanded in powers of Γ. The leading order term is proportional to $1/\Gamma$, which turns out to be of the same order of sequential tunneling contributions and this term has to be subtracted based on point (ii) in order to avoid double counting in the sequential tunneling processes. The next term of the expansion in powers of Γ is proportional to the zeroth-order, therefore, it gives the regularized expression for cotunneling rates [116]. By solving the integrals of type J after subtracting the sequential tunneling contributions $[\mathcal{O}(1/\Gamma)]$, we have

$$J(E_1,E_2,\epsilon_1) = \lim_{\Gamma\to 0}\left[\int d\epsilon f(\epsilon-E_1)[1-f(\epsilon-E_2)]\frac{1}{(\epsilon-\epsilon_1)^2+\Gamma^2} - \mathcal{O}\left(1/\Gamma\right)\right] \tag{C.4.1}$$
$$= \frac{\beta}{2\pi} n_B(E_2-E_1) Im\left[\psi'\left(\frac{1}{2}+\frac{i\beta}{2\pi}[E_2-\epsilon_1]\right) - \psi'\left(\frac{1}{2}+\frac{i\beta}{2\pi}[E_1-\epsilon_1]\right)\right]$$

and of type I

$$I(E_1,E_2,\epsilon_1,\epsilon_2) = \lim_{\Gamma\to 0} Re\int d\epsilon f(\epsilon-E_1)[1-f(\epsilon-E_2)]\frac{1}{(\epsilon-\epsilon_1-i\Gamma)}\frac{1}{(\epsilon-\epsilon_2+i\Gamma)} \tag{C.4.2}$$
$$= \frac{n_B(E_2-E_1)}{\epsilon_1-\epsilon_2} Re\left[\psi\left(\frac{1}{2}+\frac{i\beta}{2\pi}[E_2-\epsilon_1]\right) - \psi\left(\frac{1}{2}-\frac{i\beta}{2\pi}[E_2-\epsilon_2]\right)\right.$$
$$\left. - \psi\left(\frac{1}{2}+\frac{i\beta}{2\pi}[E_1-\epsilon_1]\right) + \psi\left(\frac{1}{2}-\frac{i\beta}{2\pi}[E_1-\epsilon_2]\right)\right].$$

The functions ψ and ψ' are the digamma and trigamma functions, respectively. $n_B(E-\mu) = \frac{1}{e^{(E-\mu)/k_BT}-1}$ is the Bose-Einstein distribution function where μ is the chemical potential, k_B is the Boltzmann constant, T is the temperature and $\beta = 1/k_BT$. Finally, the regularized transition rates can be written as

$$\Gamma_{\alpha\alpha'}^{nn';qq'} = \frac{\Gamma_\alpha\Gamma_{\alpha'}}{2\pi\hbar}\sum_\nu J_\nu^2\left(\frac{\zeta_{n'n}}{\hbar\omega}\right)\sum_{i'''}\sum_{i''}\times\left\{\sum_k\left[A_k^2 J(E_1,E_2,E_{Ak}) + B_k^2 J(E_1,E_2,E_{Bk})\right]\right.$$
$$+ 2\sum_q\sum_{k<q}\left[A_kA_q I(E_1,E_2,E_{Ak},E_{Aq}) + B_kB_q I(E_1,E_2,E_{Bk},E_{Bq})\right]$$
$$\left. + 2\sum_q\sum_k A_kB_q I(E_1,E_2,E_{Ak},E_{Bq})\right\}. \tag{C.4.3}$$

Appendix D

Including off-diagonal Terms of the Master Equation

D.1 Example of a double quantum dot

In this Appendix we present PAT for a double quantum dot system (DQD) [212]. The system consists of two quantum dots weakly connected in series with each other (for any coupling strength see Ref. [213]) and with two reservoirs by tunnel barriers, as shown in Fig. D.1. For weak inter-dot coupling, the electron is localized on the individual dots

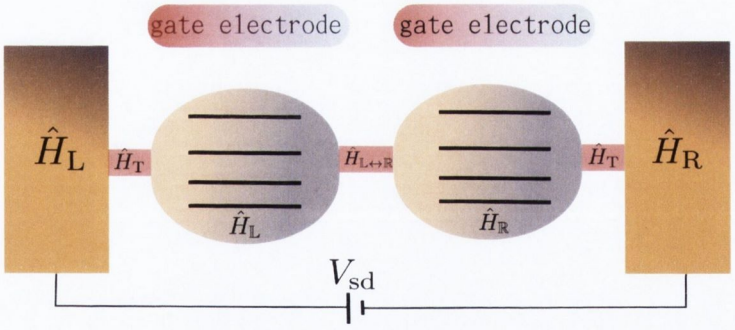

Figure D.1: Schematic representation of a DQD device connected in series with each other and to the two electrodes. Two independent gate electrodes are used to shift the energy levels of the individual quantum dots. Each term of the full Hamiltonian is shown for clarity.

and mixing of states can be disregarded. This way, the master equation can be written in terms of the isolated quantum dot charging states. We reduce the problem by considering only one single particle state on each quantum dot. Moreover, each level can accommodate up to one electron at a time due to Coulomb blockade. We further simplify the problem by considering spinless electrons. For spin-dependent calculations, see Ref. [64, 214]. The

Hamiltonian of the whole system is given by

$$\hat{H} = \hat{H}_{\mathbb{L}} + \hat{H}_{\mathbb{R}} + \hat{H}_{\mathbb{L}\leftrightarrow\mathbb{R}} + \hat{H}_{\alpha} + \hat{H}_{T}, \tag{D.1.1}$$

where

$$\hat{H}_{\{\mathbb{L},\mathbb{R}\}} = \sum_{i} \left(\sum_{\sigma} \epsilon_i \hat{c}^{\dagger}_{i\sigma} \hat{c}_{i\sigma} + \mathcal{U}_i \hat{n}_{i\uparrow} \hat{n}_{i\downarrow} \right) + \mathcal{U}_{\mathbb{LR}} \hat{n}_{\mathbb{L}} \hat{n}_{\mathbb{R}} \tag{D.1.2}$$

represents the left ($\mathbb{L}$) and the right ($\mathbb{R}$) isolated quantum dots with intra and inter-dot Coulomb interaction $\mathcal{U}_i$ and $\mathcal{U}_{\mathbb{LR}}$, respectively. The term $\hat{H}_{\mathbb{L}\leftrightarrow\mathbb{R}} = \sum_{\sigma}(t_{\mathbb{LR}} \hat{c}^{\dagger}_{\mathbb{L}\sigma} \hat{c}_{\mathbb{R}\sigma} + \text{H.c.})$ describes the coupling between the two dots. The isolated electrodes are given by $\hat{H}_{\alpha} = \sum_{\alpha\mathbf{k}\sigma} \epsilon_{\alpha\mathbf{k}\sigma} \hat{d}^{\dagger}_{\alpha\mathbf{k}\sigma} \hat{d}_{\alpha\mathbf{k}\sigma}$ and finally the coupling between the electrodes and the quantum dots is given by $\hat{H}_{\mathrm{T}} = \sum_{\alpha\mathbf{k}\sigma} \gamma_{\alpha} \hat{c}^{\dagger}_{\alpha\sigma} \hat{d}_{\alpha\mathbf{k}\sigma}$. When an AC potential is applied to the system by means of the gate electrodes, the term

$$\hat{H}_{\mathrm{AC}}(t) = \frac{V_{\mathrm{AC}}}{2\hbar\omega} \cos\,\omega t \sum_{\sigma} \left(\hat{c}^{\dagger}_{\mathbb{L}\sigma} \hat{c}_{\mathbb{L}\sigma} - \hat{c}^{\dagger}_{\mathbb{R}\sigma} \hat{c}_{\mathbb{R}\sigma} \right) \tag{D.1.3}$$

has to be added to the Hamiltonian so that Eq. D.1.1 becomes explicitly time-dependent

$$\hat{H}(t) = \hat{H}_{\mathbb{L}}(t) + \hat{H}_{\mathbb{R}}(t) + \hat{H}_{\mathbb{L}\leftrightarrow\mathbb{R}}(t) + \hat{H}_{\alpha} + \hat{H}_{\mathrm{T}}(t). \tag{D.1.4}$$

A difference of phase of π between the oscillations of the two gate voltages on each dot is required in order to observe internal changes in the dynamics of the DQD. By applying an unitary transformation

$$\hat{U}(t) = e^{i \int_{t_0}^{t} dt' \hat{H}_{\mathrm{AC}}(t')/\hbar} = e^{\frac{iV_{\mathrm{AC}}}{2\hbar\omega} \sin\,\omega t (\hat{n}_{\mathbb{L}} - \hat{n}_{\mathbb{R}})}, \tag{D.1.5}$$

the explicit time-dependence is transferred to the coupling terms since $\hat{H}_{\mathbb{L},\mathbb{R}}$ and $\hat{H}_{\alpha}$ both commute with $\hat{U}(t)$. Therefore, the total Hamiltonian can be written as

$$\hat{H}(t) = \hat{H}_{\mathbb{L}} + \hat{H}_{\mathbb{R}} + \hat{H'}_{\mathbb{L}\leftrightarrow\mathbb{R}}(t) + \hat{H}_{\alpha} + \hat{H'}_{\mathrm{T}}(t) \tag{D.1.6}$$

where

$$\hat{H'}_{\mathbb{L}\leftrightarrow\mathbb{R}} = \sum_{\nu=-\infty}^{\infty} (-1)^{\nu} J_{\nu} \left(\frac{V_{\mathrm{AC}}}{\hbar\omega} \right) \sum_{\sigma} \left(t_{\mathbb{LR}} e^{i\nu\omega t} \hat{c}^{\dagger}_{\mathbb{L}\sigma} \hat{c}_{\mathbb{R}\sigma} + \text{H.c.} \right) \tag{D.1.7}$$

and

$$\hat{H'}_{\mathrm{T}} = \sum_{\nu=-\infty}^{\infty} (-1)^{\nu} J_{\nu} \left(\frac{V_{\mathrm{AC}}}{2\hbar\omega} \right) \sum_{\alpha k\sigma} \left(\gamma_{\alpha} e^{i\nu\omega t} \hat{c}^{\dagger}_{\alpha\sigma} \hat{d}_{\alpha k\sigma} + \text{H.c.} \right), \tag{D.1.8}$$

where we used the following rules:

$$[\hat{c}^{\dagger}_{\mathbb{R}\sigma}\hat{c}_{\mathbb{L}\sigma}, \hat{n}_{\mathbb{L}}] = \hat{c}^{\dagger}_{\mathbb{R}\sigma}\hat{c}_{\mathbb{L}\sigma}, \tag{D.1.9}$$

$$[\hat{c}^{\dagger}_{\mathbb{R}\sigma}\hat{c}_{\mathbb{L}\sigma}, \hat{n}_{\mathbb{R}}] = -\hat{c}^{\dagger}_{\mathbb{R}\sigma}\hat{c}_{\mathbb{L}\sigma}, \tag{D.1.10}$$

$$[\hat{d}^{\dagger}_{\alpha k\sigma}\hat{c}_{\alpha\sigma}, \hat{n}_{\alpha'}] = \hat{d}^{\dagger}_{\alpha k\sigma}\hat{c}_{\alpha\sigma}\delta_{\alpha\alpha'}. \tag{D.1.11}$$

The effect of the AC potential is to produce coherent delocalization between the two quantum dots by means of the interaction with ν photons, if the condition $\epsilon_{\mathbb{L}} - \epsilon_{\mathbb{R}} \sim \nu\hbar\omega$ is satisfied. Eq. (D.1.7) can be simplified by applying the rotating wave approximation (RWA) [215, 216], *i.e.* by keeping just the terms that contributes to the coherence,

$$\hat{H'}_{\mathbb{L}\leftrightarrow\mathbb{R}} = (-1)^n J_n\left(\frac{V_{\mathrm{AC}}}{\hbar\omega}\right)\sum_{\sigma}\left(t_{\mathbb{LR}}e^{in\omega t}\hat{c}^{\dagger}_{\mathbb{L}\sigma}\hat{c}_{\mathbb{R}\sigma} + \mathrm{H.c.}\right). \tag{D.1.12}$$

One can also define the Rabi frequency for an electron oscillating back an forth between the two quantum dots [217] as

$$\Omega_n = 2J_{-n}\left(\frac{V_{\mathrm{AC}}}{\hbar\omega}\right)t_{\mathbb{LR}}. \tag{D.1.13}$$

In order to study the electron dynamics of the DQD system, the non-diagonal elements of the reduced density matrix has to be considered so that both terms of Eq. (4.3.51) are used, *i.e.*

$$\begin{aligned}\dot{\rho}(t)_{m'm} = &-\frac{i}{\hbar}\omega_{m'm}\rho_{m'm}(t) - \frac{i}{\hbar}[\hat{H'}_{\mathbb{L}\leftrightarrow\mathbb{R}}(t), \hat{\rho}(t)]_{m'm} \\ &+\begin{cases}\sum_{k\neq m}\Gamma^{km}\rho_{kk} - \sum_{k\neq m}\Gamma^{mk}\rho_{mm} & (m = m') \\ -\Upsilon_{m'm}\rho_{m'm} & (m \neq m'),\end{cases}\end{aligned} \tag{D.1.14}$$

where $\omega_{m'm}$ is the energy difference between the eigenstates ($|m\rangle$ and $|m'\rangle$) of the isolated DQD. The first two terms of Eq. (D.1.14) describe the reversible or coherent dynamics between the two quantum dots. The third term describes the irreversible dynamics due to the coupling with the electrodes. Γ^{km} is the transition rates for electrons tunneling between the quantum dots and the electrodes when making a transition from the charging state $|k\rangle$ to the charging state $|m\rangle$. These transition rates are given by Eq. (8.1.3) and Eq. (8.1.4). Finally, the last term describes the decoherence due to the interaction with the electrodes following the relation $\mathrm{Re}\{\Upsilon_{m'm}\} = \frac{1}{2}\left(\sum_{l\neq m'}\Gamma^{m'l} + \sum_{l\neq m}\Gamma^{ml}\right)$. We define the basis set to constructing the reduced density operator. If we consider up to two electrons in the DQD system (up to one electron on each quantum dot), the charging states are: $|0\rangle$ for no electron in the DQD, $|\mathbb{L}\rangle$ for one electron in the left dot, $|\mathbb{R}\rangle$ for one electron in the right dot and $|2\rangle$ for one electron in each dot.

In the case of no-PAT, the current through the DQD is strongly suppressed when the detuning parameter, ϵ, is large, *i.e.* the energy levels do not have similar energies. In contrast, with PAT there are two main regimes considered when studying DQD systems, namely, the high-bias [218] and pumping regimes [219, 217, 220]. In the high-bias regime, the single energy levels of the DQD lay inside the bias window. In this case, as schematically shown in Fig. D.2(a), PAT between the dots and the electrodes can be disregarded because an electron in the left dot would need to absorb a large number of photons to jump to the left electrode. Similarly, for an electron in the right electrode to enter the right quantum dot. However, if the frequency of the AC potential matches the energy difference between the two quantum dots, $\epsilon_{\mathbb{L}} - \epsilon_{\mathbb{R}} \sim \hbar\omega$, the electron can absorb [Fig. D.2(a)] or emit [Fig. D.2(b)] photons to jump between the two dots with Rabi oscillations with frequency equal to $\Omega_1 = 2J_1\left(\frac{V_{\mathrm{AC}}}{\hbar\omega}\right) t_{\mathbb{LR}}$.

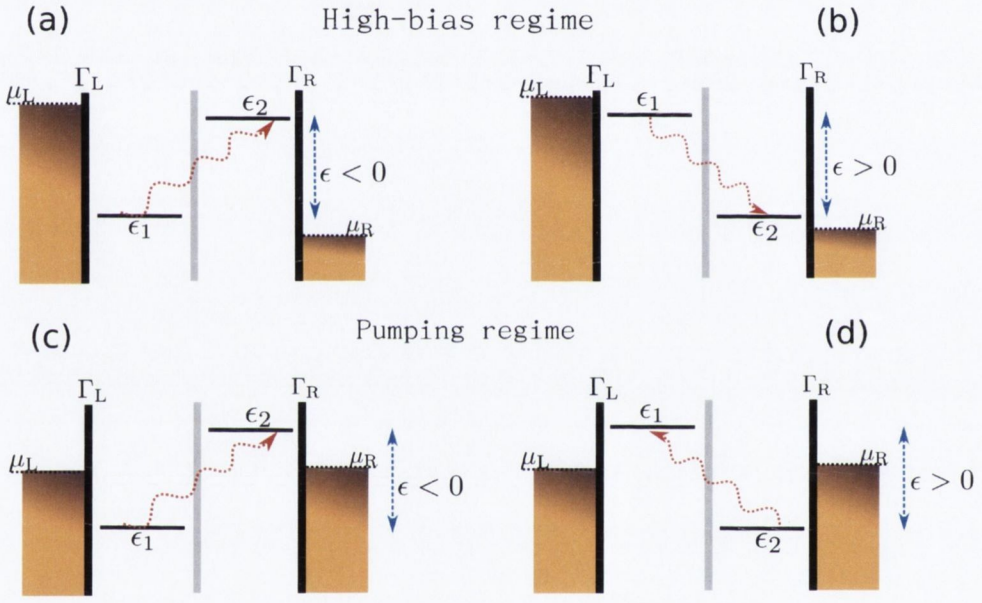

Figure D.2: Energy level diagram of absorbtion (a) and emission (b) of photons for the high-bias regime, respectively. (c) and (d) show the two possible pumping configurations in which just absorption of photons is possible.

In the pumping regime ($V_{\mathrm{sd}} \to 0$), the electrodes chemical potentials lay between the two energy levels, as shown in Fig. D.2(c-d). For no-PAT, there is no current following through the device[1], since the electron does not have energy to jump out of the dot to the electrodes or to perform interdot transitions. In order to observe electrical current, PAT is needed and also a spatial asymmetry between the energy levels, *i.e.* the detuning parameter has to be $\epsilon \neq 0$. With PAT, if $\epsilon_{\mathbb{L}} - \epsilon_{\mathbb{R}} \sim \hbar\omega$, an electron in the left dot [Fig. D.2(c)] can absorb one photon to make a transition to the right dot and eventually be extracted to the right electrode. Therefore, in case of up to one electron in the DQD

[1]Strictly speaking there is a residual current even for $V_{\mathrm{sd}} \to 0$ and we leave the discussion to the end of the section.

system ($\mathcal{U}_i$, $\mathcal{U}_{\mathbb{LR}} \to \infty$), the electrical current flowing from left to right can be expressed as $|\mathbb{L}\rangle \rightsquigarrow |\mathbb{R}\rangle \to |0\rangle \to |\mathbb{L}\rangle$. Similarly, an electron in the right electrode can absorb photon and jump to the right dot and subsequently emit a photon and jump to the left dot. Then, the contribution to the current from right to left can be represented by $|\mathbb{R}\rangle \rightsquigarrow |\mathbb{L}\rangle \to |0\rangle \to |\mathbb{R}\rangle$. The same reasoning can be applied for the case of $\epsilon > 0$ [Fig. D.2(d)]. If we allow up to two electrons in the DQD ($\mathcal{U}_i \to \infty$, $\mathcal{U}_{\mathbb{LR}} \to 0$), one can have other transition possibilities. For instance, if an excitation $|\mathbb{R}\rangle \rightsquigarrow |\mathbb{L}\rangle$ has taken place, an electron jumps from the right electrode to the right dot and then the excited electron on the left dot leaves through the left barrier following the sequence of transitions $|\mathbb{R}\rangle \rightsquigarrow |\mathbb{L}\rangle \to |2\rangle \to |\mathbb{R}\rangle$. These sequences will depend on the energy of the intermediate states $|0\rangle$ and $|2\rangle$ that can be controlled by the gate voltage applied to the dots.

From Eq. (D.1.14), the master equation can be written in a more explicit way as

$$\dot{\rho}_{00} = \Gamma_{0\mathbb{R}}\rho_{\mathbb{RR}} + \Gamma_{0\mathbb{L}}\rho_{\mathbb{LL}} - (\Gamma_{\mathbb{L}0} + \Gamma_{\mathbb{R}0})\rho_{00} \tag{D.1.15}$$

$$\dot{\rho}_{\mathbb{LL}} = \Gamma_{\mathbb{L}0}\rho_{00} + \Gamma_{\mathbb{L}2}\rho_{22} - (\Gamma_{0\mathbb{L}} + \Gamma_{2\mathbb{L}})\rho_{\mathbb{LL}} + \frac{i}{2}\Omega_1(\rho_{\mathbb{LR}} - \rho_{\mathbb{RL}}) \tag{D.1.16}$$

$$\dot{\rho}_{\mathbb{RR}} = \Gamma_{\mathbb{R}0}\rho_{00} + \Gamma_{\mathbb{R}2}\rho_{22} - (\Gamma_{0\mathbb{R}} + \Gamma_{2\mathbb{R}})\rho_{\mathbb{RR}} + \frac{i}{2}\Omega_1(\rho_{\mathbb{RL}} - \rho_{\mathbb{LR}}) \tag{D.1.17}$$

$$\dot{\rho}_{22} = \Gamma_{2\mathbb{L}}\rho_{\mathbb{LL}} + \Gamma_{2\mathbb{R}}\rho_{\mathbb{RR}} - (\Gamma_{\mathbb{L}2} + \Gamma_{\mathbb{R}2})\rho_{22} \tag{D.1.18}$$

$$\dot{\rho}_{\mathbb{LR}} = -i(\epsilon - \hbar\omega)\rho_{\mathbb{LR}} - \frac{i}{2}\Omega_1(\rho_{\mathbb{RR}} - \rho_{\mathbb{LL}}) - \frac{1}{2}(\Gamma_{0\mathbb{L}} + \Gamma_{2\mathbb{L}} + \Gamma_{0\mathbb{R}} + \Gamma_{2\mathbb{R}})\rho_{\mathbb{LR}} \tag{D.1.19}$$

$$\dot{\rho}_{\mathbb{RL}} = i(\epsilon - \hbar\omega)\rho_{\mathbb{RL}} + \frac{i}{2}\Omega_1(\rho_{\mathbb{RR}} - \rho_{\mathbb{LL}}) - \frac{1}{2}(\Gamma_{0\mathbb{L}} + \Gamma_{2\mathbb{L}} + \Gamma_{0\mathbb{R}} + \Gamma_{2\mathbb{R}})\rho_{\mathbb{RL}}, \tag{D.1.20}$$

where we used the ansatz $\rho'_{\mathbb{LR}}(t) = e^{-i\nu\hbar\omega t}\rho_{\mathbb{LR}}(t)$ to remove the time-dependence from the differential equations coefficients. Along with the normalization condition for the occupations, $\rho_{00} + \rho_{\mathbb{LL}} + \rho_{\mathbb{RR}} + \rho_{22} = 1$, one can write these equation as a product of matrices and solve the linear problem to determine the occupations for the steady state case, $\dot{\rho}_{ij} = 0$,

$$\begin{pmatrix} \dot{\rho}_{00} \\ \dot{\rho}_{\mathbb{LL}} \\ \dot{\rho}_{\mathbb{RR}} \\ \dot{\rho}_{22} \\ \dot{\rho}_{\mathbb{LR}} \\ \dot{\rho}_{\mathbb{RL}} \end{pmatrix} = \begin{pmatrix} -(\Gamma_{\mathbb{L}0} + \Gamma_{\mathbb{R}0}) & \Gamma_{0\mathbb{L}} & \Gamma_{0\mathbb{R}} & 0 & 0 & 0 \\ \Gamma_{\mathbb{L}0} & -(\Gamma_{0\mathbb{L}} + \Gamma_{2\mathbb{L}}) & 0 & \Gamma_{\mathbb{L}2} & i\frac{\Omega_1}{2} & -i\frac{\Omega_1}{2} \\ \Gamma_{\mathbb{R}0} & 0 & -(\Gamma_{0\mathbb{R}} + \Gamma_{2\mathbb{R}}) & \Gamma_{\mathbb{R}2} & -i\frac{\Omega_1}{2} & i\frac{\Omega_1}{2} \\ 0 & \Gamma_{2\mathbb{L}} & \Gamma_{2\mathbb{R}} & -(\Gamma_{\mathbb{L}2} + \Gamma_{\mathbb{R}2}) & 0 & 0 \\ 0 & i\frac{\Omega_1}{2} & -i\frac{\Omega_1}{2} & 0 & -i(\epsilon - \hbar\omega) - \Upsilon & 0 \\ 0 & i\frac{\Omega_1}{2} & -i\frac{\Omega_1}{2} & 0 & 0 & +i(\epsilon - \hbar\omega) - \Upsilon \end{pmatrix} \times \begin{pmatrix} \rho_{00} \\ \rho_{\mathbb{LL}} \\ \rho_{\mathbb{RR}} \\ \rho_{22} \\ \rho_{\mathbb{LR}} \\ \rho_{\mathbb{RL}} \end{pmatrix}, \tag{D.1.21}$$

with $\Upsilon = \frac{1}{2}(\Gamma_{0\mathbb{L}} + \Gamma_{2\mathbb{L}} + \Gamma_{0\mathbb{R}} + \Gamma_{2\mathbb{R}})$. The current through the right barrier is given by $I_{\mathrm{R}} = e(\Gamma_{0\mathbb{R}}\rho_{\mathbb{RR}} - \Gamma_{\mathbb{R}0}\rho_{00})$. Fig. D.3 shows the $I \times V_{\mathrm{sd}}$ characteristics for no-PAT and with

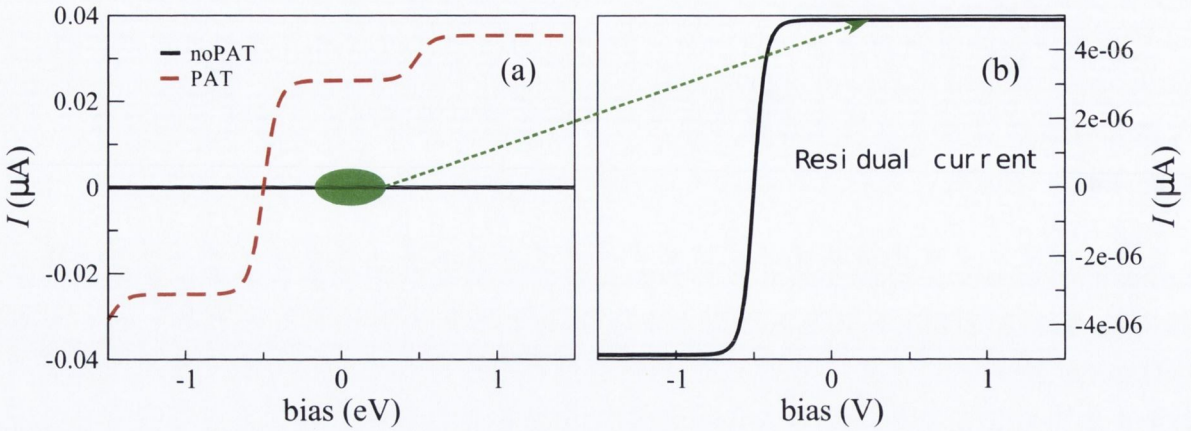

Figure D.3: (a) Current as a function of the dc bias with and without PAT. (b) Residual current as a function of bias for no-PAT. Parameters used are $\xi = 1$, $k_B\Theta = 0.025$ eV, $\Gamma_{L,R} = 0.005$ eV, $\Gamma_{int} = 0.001$ eV, $\mathcal{U} = 0$ eV.

PAT on the DQD. The energy of the left dot is 0.25 eV above E_F whereas for the right dot the energy is at -0.25 eV. The energy of the photons is chosen in such a way to match the difference between the energy of the dots, *i.e.* $\hbar\omega = 0.5$ eV. Now, for $V_{sd} \to 0$ we can already observe a dc current flowing in the system when PAT is allowed, as shown in Fig. D.3(a).

An important limitation of this formulation when considering the localized basis set to derive the master equations is that it may lead to results that apparently violate thermodynamic properties of equilibrium [221]. For instance, Fig. D.3(b) shows a residual current even when there is no applied bias in the system. This is always observed when $\epsilon_{\mathbb{L}} \neq \epsilon_{\mathbb{R}}$. This apparent violation of thermodynamics properties was discussed by Novotný [221] and its roots are in the fact that just first-order tunneling events were considered in the derivation of the transition rates. In fact, higher order processes, such as coherent transport or cotunneling would cancel this spurious current at zero bias. Indeed, in Sec. 7.2.2 we have shown that second order terms in the tunneling Hamiltonian reduces the sequential tunneling current.

Appendix E

Constrained-DFT

E.1 Implementation details

Our implementation of the constrained DFT approach within SIESTA follows the prescription of Wu *et al.* described in Ref. [222]. Accordingly, we begin by defining a set of constraints on the electronic spin density of the form

$$\sum_{\sigma} \int w_{\mathrm{k}}^{\sigma}(\mathbf{r}) \rho^{\sigma}(\mathbf{r}) d\mathbf{r} = N_{\mathrm{k}} \,, \tag{E.1.1}$$

wherein $\sigma = \uparrow, \downarrow$ represents the spin index, $w_{\mathrm{k}}^{\sigma}(\mathbf{r})$ is a weight function corresponding to the constraint k, defining the property being constrained and N_{k} is the constraint value. The total electron density is given by

$$\rho(\mathbf{r}) = \sum_{\sigma} \rho^{\sigma}(\mathbf{r}) = \sum_{\sigma} \sum_{i}^{N_{\sigma}} |\phi_i^{\sigma}(\mathbf{r})|^2 \,, \tag{E.1.2}$$

where N_{σ} is the number of occupied Kohn-Sham (KS) orbitals $\phi_i^{\sigma}(\mathbf{r})$. A Lagrange multiplier, V_{k}, is associated to each constraint specified in Eq. (E.1.1). This allows the following modified energy functional to be defined

$$W[\rho, \{V_{\mathrm{k}}\}] = E[\rho] + \sum_{\mathrm{k}} V_{\mathrm{k}} \left[\sum_{\sigma} \int w_{\mathrm{k}}^{\sigma}(\mathbf{r}) \rho^{\sigma}(\mathbf{r}) d\mathbf{r} - N_{\mathrm{k}} \right] , \tag{E.1.3}$$

with $E[\rho]$ being the standard Kohn-Sham energy functional given by

$$E[\rho] = \sum_{\sigma} \sum_{i}^{N_{\sigma}} \langle \phi_i^{\sigma} | -\frac{1}{2} \nabla^2 | \phi_i^{\sigma} \rangle + \int v_{ext}(\mathbf{r}) \rho(\mathbf{r}) + \\ + J[\rho] + E_{\mathrm{xc}}[\rho^{\uparrow}, \rho^{\downarrow}] \,. \tag{E.1.4}$$

In Eq. (E.1.4) the first term is the kinetic energy, $v_{ext}(\mathbf{r})$ is the external potential, $J[\rho]$ is the classical Coulomb energy and $E_{\rm xc}[\rho^{\uparrow},\rho^{\downarrow}]$ is the exchange-correlation energy. The variational principle yields the stationary condition for the functional W with respect to the normalized orbitals ϕ_i^{σ}, which leads to the following modified Kohn-Sham equations

$$\left[-\frac{1}{2}\nabla^2 + v_{ext}(\mathbf{r}) + \int d\mathbf{r}'\frac{\rho(\mathbf{r}')}{|\mathbf{r}-\mathbf{r}'|} + v_{\rm xc}^{\sigma}(\mathbf{r}) + \right. \qquad \text{(E.1.5)}$$
$$\left. + \sum_{\rm k} V_{\rm k} w_{\rm k}^{\sigma}(\mathbf{r})\right]\phi_i^{\sigma}(\mathbf{r}) = \epsilon_i^{\sigma}\phi_i^{\sigma}(\mathbf{r})\,.$$

Thus, the constraints enter the effective KS Hamiltonian in the form of an additional external potential $\sum_{\rm k} V_{\rm k} w_{\rm k}^{\sigma}(\mathbf{r})$. The ground-state of the constrained KS system is obtained by solving Eq. (E.1.5) in conjunction with Eq. (E.1.1). Wu *et al.* have shown [222] that the functional W is concave with respect to the parameters $V_{\rm k}$ and that by optimizing W through varying $\{V_{\rm k}\}$, one can find the constraint potential that yields the ground-state of the constrained system. In order to optimize W, we utilize its first derivate with respect to $\{V_{\rm k}\}$ given by

$$\frac{dW}{dV_{\rm k}} = \sum_{\sigma}\sum_{i}^{N_{\sigma}}\left(\frac{\delta W}{\delta\phi_i^{\sigma}}\frac{\partial\phi_i^{\sigma}}{\partial V_{\rm k}} + c.c\right) + \frac{\partial W}{\partial V_{\rm k}} \qquad \text{(E.1.6)}$$
$$= \sum_{\sigma}\int w_{\rm k}^{\sigma}(\mathbf{r})\rho^{\sigma}(\mathbf{r})d\mathbf{r} - N_{\rm k},$$

where the stationary condition $\frac{\delta W}{\delta\phi_i^{\sigma}} = 0$ implied by Eq. (E.1.5) is used. Thus we see that the derivative $\frac{dW}{dV_{\rm k}}$ vanishes automatically when Eq. (E.1.1) is satisfied. We now outline the implementation of this formalism for the simulation of the electron transfer processes within SIESTA. In a typical electron transfer problem one has to partition the system into a donor region (D) and an acceptor region (A). Within SIESTA, this is done by specifying a certain group of atoms as belonging to D and a second group of atoms as belonging to A. The constrained calculation then involves the transfer of a specified amount of charge from D to A. In order to partition the continuous electron density in real space between the A and D regions, we choose an appropriate population analysis scheme, which in turn determines the form of the weight function $w_{\rm k}$ in Eq. (E.1.1). The localized numerical orbital basis set within SIESTA is particularly suitable for atomic orbital based population analysis schemes such as the ones due to Löwdin [97] and Mülliken [98]. We have implemented weight functions corresponding to both the Löwdin and Mülliken schemes within SIESTA. For Löwdin populations, the number of electrons on a group of atoms C is given

by

$$N_C = \sum_{\mu \in C} (\mathbf{S}^{\frac{1}{2}} \mathbf{D} \mathbf{S}^{\frac{1}{2}})_{\mu\mu} = \tag{E.1.7}$$
$$= \sum_{\nu\lambda} D_{\nu\lambda} \sum_{\mu \in C} S^{\frac{1}{2}}_{\lambda\mu} S^{\frac{1}{2}}_{\mu\nu} =$$
$$= \mathrm{Tr}(\mathbf{D}\mathbf{w}^L_C) \,,$$

where $\mathbf{D}$ and $\mathbf{S}$ are the density and overlap matrices respectively and $\mathbf{w}^L_{C\lambda\nu} = \sum_{\mu \in C} S^{\frac{1}{2}}_{\lambda\mu} S^{\frac{1}{2}}_{\mu\nu}$ defines the Löwdin weight matrix. Similarly, with a Mülliken population analysis, the number of electrons on a group of atoms C is

$$N_C = \sum_{\mu \in C} (\mathbf{DS})_{\mu\mu} = \mathrm{Tr}(\mathbf{DS}) \tag{E.1.8}$$

with the corresponding weight matrix given by

$$w^M_{C\mu\nu} = \begin{cases} S_{\mu\nu} & \text{if } \mu \in C \text{ and } \nu \in C \\ \frac{1}{2} S_{\mu\nu} & \text{if } \mu \in C \text{ or } \nu \in C \\ 0 & \text{if } \mu \ni C \text{ and } \nu \ni C \end{cases}$$

For charge transfer problems, Wu *et al.* recommend a partitioning of the charge density based on the Löwdin scheme.

The self consistent field (SCF) procedure for obtaining the constrained DFT ground-state within the current implementation consists of an inner and outer loop. The outer loop is similar to a conventional SCF cycle wherein the orbitals obtained by solving the KS equations and the associated self-consistent density are updated. The inner loop consists of optimizing the V_k multipliers to ensure that the constraint condition given in Eq. (E.1.1) is satisfied at each step of the outer loop. By Eq. (E.1.6), this is equivalent to find the extremes of W. Since the derivative of W with respect to the V_k is readily available from Eq. (E.1.6), we employ a conjugate gradients (CG) optimization procedure to ensure that Eq. (E.1.1) is satisfied. Subsequently, the KS equations are solved and the resulting orbitals are used to update the KS density and Hamiltonian in the outer loop. We note that Wu *et al.* also calculate the second derivative (Hessian matrix) of W with respect to the V_k parameters and employ the Newton's method to optimize $\{V_\mathrm{k}\}$. However, the expression for the second derivatives $\frac{\partial W}{\partial V_\mathrm{k} \partial V_\mathrm{l}}$ depends explicitly on the KS orbitals, whereas the first derivative [Eq. (E.1.6)] involves only the density [222]. We therefore prefer to work with the gradient alone and employ a CG optimization scheme for the $\{V_\mathrm{k}\}$. Thus the overall SCF procedure consists of the following sequence of steps: (i) Construct the standard KS Hamiltonian $\mathbf{H}$ for the current guess density. (ii) Obtain the constrained KS Hamiltonian $\mathbf{H}_C = \mathbf{H} + \sum_\mathrm{k} V_\mathrm{k} w^\sigma_\mathrm{k}(\mathbf{r})$ by adding the constraint potential $\sum_\mathrm{k} V_\mathrm{k} w^\sigma_\mathrm{k}(\mathbf{r})$ from

the previous iteration. (iii) Using the Pulay scheme, mix $\mathbf{H}_C$ with Hamiltonians from previous iterations to obtain $\mathbf{H}'_C$. (iv) By keeping $\mathbf{H}'_C$ fixed, optimize $\{V_\mathrm{k}\}$ so that the constraints in Eq. (E.1.1) are satisfied. (v) Solve the KS equations for the Hamiltonian combining $\mathbf{H}'_C$ and the optimized $\{V_\mathrm{k}\}$. The new density matrix $\mathbf{D}$ thus obtained and the optimized $\{V_\mathrm{k}\}$ are used in the next iteration. (vi) Repeat steps (i) through (v) until self-consistency is achieved.

Appendix F

List of Publications

- A. M. Souza, I. Rungger, C. D. Pemmaraju, U. Schwingenschlögl, and S. Sanvito. "Constrained-DFT method for accurate energy-level alignment of metal/molecule interfaces". Phys. Rev. B, **88**, 165112, 2013.
- W. R. French, C. R. Iacovella, I. Rungger, A. M. Souza, S. Sanvito and P. T. Cummings. "Atomistic simulations of highly conductive molecular transport junctions under realistic conditions". Nanoscale, **5**, 3654, 2013.
- W. R. French, C. R. Iacovella, I. Rungger, A. M. Souza, S. Sanvito and P. T. Cummings. "Structural Origins of Conductance Fluctuations in Gold-Thiolate Molecular Transport Junctions". J. Phys. Chem. Lett., **4**, 887, 2013.
- A. M. Souza, I. Rungger, R. B. Pontes, A. R. Rocha, A. J. R. da Silva, U. Schwingenschlögl and S. Sanvito. "Stretching of BDT-gold molecular junctions: thiol or thiolate termination?". Nanoscale, **6**, 14495, 2014.
- A. M. Souza, I. Rungger, U. Schwingenschlögl, and S. Sanvito. "Image charge effect and phonon-assisted processes in coulomb blockade transport." (in preparation).

Bibliography

[1] M. L. Perrin, E. Burzur, and H. S. J. van der Zant, "Single-molecule transistors", *Chem. Soc. Rev.* **44**, pp. 902–919 (2015).

[2] M. A. Ratner A. Aviran, "Molecular rectifiers", *Chem. Phys. Lett.* **29**, pp. 277–283 (1974).

[3] C. R. Arroyo, E. Leary, A. Castellanos-Gómez, G. Rubio-Bollinger, M. T. González, and N. Agraït, "Influence of binding groups on molecular junction formation.", *J. Am. Chem. Soc.* **133**, pp. 14313–14319 (2011).

[4] C. Bruot, J. Hihath, and N. Tao, "Mechanically controlled molecular orbital alignment in single molecule junctions", *Nat. Nanotechnol.* **7**, pp. 35–40 (2012).

[5] K. Baheti, J. A. Malen, P. Doak, P. Reddy, Sung-Yeon Jang, T. D. Tilley, A. Majumdar, and R. A Segalman, "Probing the chemistry of molecular heterojunctions using thermoelectricity.", *Nano Lett.* **8**, pp. 715–719 (2008).

[6] V. Fatemi, M. Kamenetska, J. B. Neaton, and L. Venkataraman, "Environmental control of single-molecule junction transport.", *Nano Lett.* **11**, pp. 1988–1992 (2011).

[7] M. Kiguchi, H. Nakamura, Y. Takahashi, T. Takahashi, and T. Ohto, "Effect of anchoring group position on formation and conductance of a single disubstituted benzene molecule bridging Au electrodes: change of conductive molecular orbital and electron pathway", *J. Phys. Chem. C* **114**, pp. 22254–22261 (2010).

[8] P. Reddy, Sung-Yeon Jang, R. A. Segalman, and A. Majumdar, "Thermoelectricity in molecular junctions.", *Science* **315**, pp. 1568–1571 (2007).

[9] H. Vazquez, R. Skouta, S. Schneebeli, M. Kamenetska, R. Breslow, L. Venkataraman, and M. S. Hybertsen, "Probing the conductance superposition law in single-molecule circuits with parallel paths.", *Nat. Nanotechnol.* **7**, pp. 663–670 (2012).

[10] L. Venkataraman, J. E. Klare, I. W. Tam, C. Nuckolls, M. S. Hybertsen, and M. L. Steigerwald, "Single-molecule circuits with well-defined molecular conductance.", *Nano Lett.* **6**, pp. 458–462 (2006).

[11] D. J. Wold, R. Haag, M. A. Rampi, and C. D. Frisbie, "Distance dependence of electron tunneling through self-assembled monolayers measured", *J. Phys. Chem. B* **106**, pp. 10–13 (2002).

[12] B. Xu, X. Xiao, and N. J. Tao, "Measurement of single molecule conductance: benzenedithiol and benzenedimethanethiol", *Nano Lett.* **4**, pp. 267–271 (2004).

[13] B. Xu and N. J. Tao, "Measurement of single-molecule resistance by repeated formation of molecular junctions.", *Science* **301**, pp. 1221–1224 (2003).

[14] M. A. Reed, C. Zhou, C. J. Muller, T. P. Burgin, and J. M. Tour, "Conductance of a molecular junction", *Science* **278**, pp. 252–254 (1997).

[15] E. Lörtscher, H. Weber, and H. Riel, "Statistical approach to investigating transport through single molecules", *Phys. Rev. Lett.* **98**, pp. 12–15 (2007).

[16] M. T. Gonzalez, S. Wu, R. Huber, S. J. van der Molen, C. Schönenberger, and M. Calame, "Electrical conductance of molecular junctions by a robust statistical analysis.", *Nano Lett.* **6**, pp. 2238–2242 (2006).

[17] Y. Kim, T. Pietsch, A. Erbe, W. Belzig, and E. Scheer, "Benzenedithiol: a broad-range single-channel molecular conductor.", *Nano Lett.* **11**, pp. 3734–3738 (2011).

[18] M. Taniguchi, M. Tsutsui, K. Yokota, and T. Kawai, "Mechanically-controllable single molecule switch based on configuration specific electrical conductivity of metal-moleculemetal junctions", *Chem. Sci.* **1**, pp. 247–253 (2010).

[19] Jing-Hua Tian, B. Liu, X. Li, Zhi-Lin Yang, B. Ren, Sun-Tao Wu, N. J. Tao, and Zhong-Qun Tian, "Study of molecular junctions with a combined surface-enhanced Raman and mechanically controllable break junction method.", *J. Am. Chem. Soc.* **128**, pp. 14748–14757 (2006).

[20] Jing-Hua Tian, Y. Yang, Xiao-Shun Zhou, B. Schöllhorn, E. Maisonhaute, Zhao-Bin Chen, Fang-Zu Yang, Y. Chen, C. Amatore, Bing-Wei Mao, and Zhong-Qun Tian, "Electrochemically assisted fabrication of metal atomic wires and molecular junctions by MCBJ and STM-BJ methods.", *Chemphyschem* **11**, pp. 2745–55 (2010).

[21] M. Tsutsui, M. Taniguchi, K. Shoji, K. Yokota, and T. Kawai, "Identifying molecular signatures in metal-molecule-metal junctions.", *Nanoscale* **1**, pp. 164–170 (2009).

[22] M. Tsutsui, Y. Teramae, S. Kurokawa, and A. Sakai, "High-conductance states of single benzenedithiol molecules", *Appl. Phys. Lett.* **89**, pp. 163111–163114 (2006).

[23] M. Tsutsui, M. Taniguchi, and T. Kawai, "Atomistic mechanics and formation mechanism of metal - molecule - metal", *Nano Lett.* **9**, pp. 2433–2439 (2009).

[24] F. Demir and G. Kirczenow, "Inelastic tunneling spectroscopy of gold-thiol and gold-thiolate interfaces in molecular junctions: the role of hydrogen", *J. Chem. Phys.* **137**, pp. 94703–94714 (2012).

[25] R. B. Pontes, F. D. Novaes, A. Fazzio, and A. J. R. da Silva, "Adsorption of benzene-1, 4-dithiol on the Au (111) surface and its possible role in molecular conductance", *J. Am. Chem. Soc.* **128**, pp. 8996–8997 (2006).

[26] R. B. Pontes, A. R. Rocha, S. Sanvito, A. Fazzio, and A. J. R. da Silva, "Ab initio calculations of structural evolution and conductance of benzene-1,4-dithiol on gold leads", *ACS Nano* **5**, pp. 795–804 (2011).

[27] C Toher and S Sanvito, "Effects of self-interaction corrections on the transport properties of phenyl-based molecular junctions", *Phys. Rev. B* **77**, pp. 1–12 (2008).

[28] M. Strange and K. S. Thygesen, "Towards quantitative accuracy in first-principles transport calculations: the GW method applied to alkane/gold junctions", *arXiv:cond-mat/1108-3687v1* , pp. 1–7 (2011).

[29] W. R. French, C. R. Iacovella, I. Rungger, A. M. Souza, S. Sanvito, and P. T. Cummings, "Structural origins of conductance fluctuations in gold/thiolate molecular transport junctions", *J. Phys. Chem. Lett.* **4**, pp. 887–891 (2013).

[30] W. R. French, C. R. Iacovella, I. Rungger, A. M. Souza, S. Sanvito, and P. T. Cummings, "Atomistic simulations of highly conductive molecular transport junctions under realistic conditions.", *Nanoscale* **5**, pp. 3654–3659 (2013).

[31] A. M. Souza, I. Rungger, R. B. Pontes, A. R. Rocha, A. J. R. da Silva, U. Schwingenschloegl, and S. Sanvito, "Stretching of BDT-gold molecular junctions : thiol or thiolate termination?", *Nanoscale* **6**, pp. 14495–507 (2014).

[32] Jiwoong Park, *Electron Transport in Single Molecule Transistors*, PhD thesis University of California, Berkeley (2003).

[33] R. Hesper, L. H. Tjeng, and G. A. Sawatzky, "Strongly reduced band gap in a correlated insulator in close proximity to a metal", *Eur. Lett.* **40**, pp. 177–182 (1997).

[34] J. Repp, G. Meyer, S. Stojković, A. Gourdon, and C. Joachim, "Molecules on insulating films: scanning-tunneling microscopy imaging of individual molecular orbitals", *Phys. Rev. Lett.* **94**, pp. 1–4 (2005).

[35] X. Lu, M. Grobis, K. H. Khoo, S. G. Louie, and M. F. Crommie, "Charge transfer and screening in individual C60 molecules on metal substrates: a scanning tunneling spectroscopy and theoretical study", *Phys. Rev. B* **70**, pp. 115418–115426 (2004).

[36] M. T. Greiner, M. G. Helander, Wing-Man Tang, Zhi-Bin Wang, J. Qiu, and Zheng-Hong Lu, "Universal energy-level alignment of molecules on metal oxides", *Nat. Mater.* **11**, pp. 76–81 (2011).

[37] M. L. Perrin, C. J. O. Verzijl, Christian a. Martin, A. J. Shaikh, R. Eelkema, J. H. van Esch, J. M. van Ruitenbeek, J. M. Thijssen, H. S. J. van der Zant, and D. Dulić, "Large tunable image-charge effects in single-molecule junctions", *Nat. Nanotechnol.* **8**, pp. 282–287 (2013).

[38] S. Battacharyya, A. Kibel, G. Kodis, P. A. Liddell, M. Gervaldo, D. Gust, and S. Lindsay, "Optical modulation of molecular conductance.", *Nano Lett.* **11**, pp. 2709–2714 (2011).

[39] D. R. Ward, N. J. Halas, J. W. Ciszek, J. M. Tour, P. Nordlander, and D. Natelson, "Simultaneous measurements of electronic conduction and raman response in molecular junctions", *Nano Lett.* **8**, pp. 919–924 (2008).

[40] Z. Ioffe, T. Shamai, A. Ophir, G. Noy, I. Yutsis, K. Kfir, O. Cheshnovsky, and Y. Selzer, "Detection of heating in current-carrying molecular junctions by Raman scattering.", *Nat. Nanotechnol.* **3**, pp. 727–732 (2008).

[41] D. R. Ward, D. A. Corley, J. M. Tour, and D. Natelson, "Vibrational and electronic heating in nanoscale junctions.", *Nat. Nanotechnol.* **6**, pp. 33–38 (2011).

[42] M. Galperin and A. Nitzan, "Molecular optoelectronics: the interaction of molecular conduction junctions with light.", *Phys. Chem. Chem. Phys.* **14**, pp. 9421–9438 (2012).

[43] A. H. Dayem and R. J. Martin, "Quantum interaction of microwave radiation with tunneling between superconductors", *Phys. Rev. Lett.* **8**, pp. 246–249 (1961).

[44] P. K. Tien and J. P. Gordon, "Multiphoton process observed in the interaction of microwave fields", *Phys. Rev.* **129**, pp. 647–653 (1963).

[45] M. Riede, T. Mueller, W. Tress, R. Schueppel, and K. Leo, "Small-molecule solar cells-status and perspectives.", *Nanotechnology* **19**, pp. 424001–424013 (2008).

[46] M. Graetzel, "Photoelectrochemical cells", *Nature* **414**, pp. 338–344 (2001).

[47] B. O'Regan and M. Graetzel, "A low-cost, high-efficiency solar cell based on dye-sensitized colloidal TiO_2 fims", *Nature* **353**, pp. 737–739 (1991).

[48] A. Kojima, K. Teshima, Y. Shirai, and T. Miyasaka, "Organometal halide perovskites as visible-Light sensitizers for photovoltaic", *J. Am. Chem. Soc.* **131**, pp. 6050–6051 (2009).

[49] C. Foden and D. Whittaker, "Quantum electrodynamic treatment of photon-assisted tunneling", *Phys. Rev. B* **58**, pp. 12617–12620 (1998).

[50] Tae-Ho Park and M. Galperin, "Charge-transfer contribution to surface-enhanced Raman scattering in a molecular junction: time-dependent correlations", *Phys. Rev. B* **84**, pp. 075447–075458 (2011).

[51] M. Galperin and A. Nitzan, "Current-induced light emission and light-induced current in molecular-tunneling junctions", *Phys. Rev. Lett.* **95**, pp. 206802–206806 (2005).

[52] M. Galperin, A. Nitzan, and M. Ratner, "Molecular transport junctions: current from electronic excitations in the leads", *Phys. Rev. Lett.* **96**, pp. 166803–166807 (2006).

[53] M. Galperin and A. Nitzan, "Optical properties of current carrying molecular wires.", *J. Chem. Phys.* **124**, pp. 234709–234726 (2006).

[54] X. H. Qiu, G. V. Nazin, and W. Ho, "Vibrationally resolved fluorescence excited with submolecular precision", *Science* **299**, pp. 542–546 (2003).

[55] G. Tian and Y. Luo, "Electroluminescence of molecules in a scanning tunneling microscope: Role of tunneling electrons and surface plasmons", *Phys. Rev. B* **84**, pp. 205419–205428 (2011).

[56] B. Fainberg, M. Jouravlev, and A. Nitzan, "Light-induced current in molecular tunneling junctions excited with intense shaped pulses", *Phys. Rev. B* **76**, pp. 245329–245341 (2007).

[57] J. Koch and F. von Oppen, "Franck-Condon blockade and giant fano factors in transport through single molecules", *Phys. Rev. Lett.* **94**, pp. 206804–206808 (2005).

[58] H. Park, J. Park, A. K. L. Lim, E. H. Anderson, A. P. Alivisatos, and P. L. Mceuen, "Nanomechanical oscillations in a single-C 60 transistor", *Nature* **407**, pp. 57–60 (2000).

[59] L. Wang and V. May, "Optical switching of charge transmission through a single molecule: effects of contact excitations and molecule heating", *J. Phys. Chem. C* **114**, pp. 4179–4185 (2010).

[60] V. May and O. Kühn, "Photoinduced removal of the Franck - Condon blockade in single-electron inelastic charge transmission", *Nano Lett.* **8**, pp. 1095–1099 (2008).

[61] V. May and O. Kühn, "Optical field control of charge transmission through a molecular wire. I. generalized master equation description", *Phys. Rev. B* **77**, pp. 115439–115451 (2008).

[62] V. May and O. Kühn, "Optical field control of charge transmission through a molecular wire. II. photoinduced removal of the Franck-Condon blockade", *Phys. Rev. B* **77**, pp. 115440–115451 (2008).

[63] M. Di Ventra, *Electrical transport in nanoscale systems*, Cambridge University Press, New York (2008).

[64] R. S. Rodrigo, *Spin and charge transport through driven quantum dot systems and their fluctuations*, PhD thesis Universidad Autonoma de Madrid (2007).

[65] P. Hohemberg and W. Kohn, "Inhomogeneus electron gas", *Phys. Rev.* **136**, pp. B864–B871 (1964).

[66] W. Kohn and L. J. Sham, "Self-consistent equations including exchange and correlation effects", *Phys. Rev.* **385**, pp. A 1133–A 1138 (1965).

[67] K. Capelle, "A birds eye view of density-functional theory", *arXiv:cond-mat/0211443v5* , pp. 1–69 (2002).

[68] E. Fermi, "Un metodo statistico per la determinazione di alcune prioprietà dell'atomo", *Rend. Accad. Naz. Lincei* **6**, pp. 602–607 (1927).

[69] L. H. Thomas, "The calculation of atomic fields", *Math. Proc. Cambridge Philos. Soc.* **23**, pp. 542–548 (1927).

[70] Y. Tomishima, "Thomas-Fermi-Dirac Theory with Correlation Correction", *Prog. Theor. Phys.* **22**, pp. 1–11 (1959).

[71] Edward Teller, "On the stability of molecules in the Thomas-Fermi theory", *Rev. Mod. Phys.* **34**, pp. 627–631 (1962).

[72] D. M. Ceperley and B. J. Alder, "Ground state of the electron gas by a stochastic method", *Phys. Rev. Lett.* **45**, pp. 566–569 (1980).

[73] J. P. Perdew, K. Burke, and M. Ernzerhof, "Generalized gradient approximation made simple", *Phys. Rev. Lett.* **77**, pp. 3865–3868 (1996).

[74] J. Heyd, G. E. Scuseria, and M. Ernzerhof, "Hybrid functionals based on a screened Coulomb potential", *J. Chem. Phys.* **118**, pp. 8207–8215 (2003).

[75] A. D. Becke, "Density-functional thermochemistry. III. The role of exact exchange", *J. Chem. Phys.* **98**, pp. 5648–5652 (1993).

[76] J. P. Perdew and A. Zunger, "Self-interaction correction to density-functional approximations for many-electron systems", *Phys. Rev. B* **23**, pp. 5048–5080 (1981).

[77] J. P. Perdew and M. Levy, "Physical content of the exact Kohn-Sham orbital energies: band baps and derivative discontinuities", *Phys. Rev. Lett.* **51**, pp. 1884–1887 (1983).

[78] J. F. Janak, "Proof that dE/dn=e in density-functional theory", *Phys. Rev. B* **18**, pp. 7165–7168 (1978).

[79] J. P. Perdew, R. G. Parr, M. Levy, and J. L. Balduz, "Density-functional theory for fractional particle number: derivative discontinuities of the energy", *Phys. Rev. Lett.* **49**, pp. 1691–1694 (1982).

[80] L. J. Sham and M. Schluter, "Density-functional theory of the energy gap", *Phys. Rev. Lett.* **51**, pp. 1888–1891 (1983).

[81] T. Tsuneda and K. Hirao, "Self-interaction corrections in density functional theory.", *J. Chem. Phys.* **140**, pp. 18A513–18A526 (2014).

[82] H. B. Shore, J. H. Rose And, and E. Zaremba, "Failure of the Local Exchange Approximation in the Evaluation of the H- ground State", *Phys. Rev. B* **15**(6), pp. 2858–2861 (1977).

[83] K. Terakura, T. Oguchi, A. R. W. And, and J. Kubler, "Band theory of insulating transition-metal monoxides: band-structure calculations", *Phys. Rev. B* **30**, pp. 4734–4747 (1984).

[84] M. R. Pederson, A. Ruzsinszky, and J. P. Perdew, "Communication: self-interaction correction with unitary invariance in density functional theory.", *J. Chem. Phys.* **140**, pp. 121103–121107 (2014).

[85] C. Pemmaraju, T. Archer, D. Sánchez-Portal, and S. Sanvito, "Atomic-orbital-based approximate self-interaction correction scheme for molecules and solids", *Phys. Rev. B* **75**, pp. 45101–45117 (2007).

[86] J. Pollmann, D. Vogel, and P. Kru, "Self-interaction and relaxation-corrected pseudopotentials for II-VI semiconductors", **54**, pp. 5495–5511 (1996).

[87] J. Pollmann, D. Vogel, and P. Kru, "Structural and electronic properties of group-III nitrides", **55**, pp. 836–839 (1997).

[88] J. Pollmann, D. Vogel, and P. Kru, "Ab initio electronic structure of silver halides calculated with self-interaction and relaxation-corrected pseudopotentials", *Phys. Rev. B* **58**, pp. 3865–3869 (1998).

[89] A. Zunger, "Spin-dependent correlated atomic pseudopotentials", *Phys. Rev. B* **22**, pp. 649–662 (1980).

[90] H. Dederichs and H. Akai, "Ground-State of constrained systems: application to Cirium impurities", *Phys. Rev. Lett.* **53**, pp. 2512–2515 (1984).

[91] B. Kaduk, T. Kowalczyk, and T. V. Voorhis, "Constrained Density Functional Theory", *Chem. Rev.* **112**, pp. 321–370 (2012).

[92] Q. Wu and T. V. Voorhis, "Direct optimization method to study constrained systems within density-functional theory", *Phys. Rev. A* **72**, pp. 7–10 (2005).

[93] Q. Wu and T. V. Voorhis, "Direct calculation of electron transfer parameters through constrained density functional theory.", *J. Phys. Chem. A* **110**, pp. 9212–9218 (2006).

[94] Q. Wu and T. V. Voorhis, "Extracting electron transfer coupling elements from constrained density functional theory", *J. Chem. Phys.* **125**, pp. 164105–164114 (2006).

[95] S. Yeganeh and T. V. Voorhis, "Triplet excitation energy transfer with constrained density functional theory", *J. Phys. Chem. C* **114**, pp. 20756–20763 (2010).

[96] M. Soler, E. Artacho, J. D. Gale, A. Garc, J. Junquera, P. Ordej, and S. Daniel, "The SIESTA method for ab initio order- N materials", *J. Phys. Condens. Matter* **14**, pp. 2745–2779 (2002).

[97] Per-Olov Löwdin, "On the non-orthogonality problem connected with the use of atomic wave functions in the theory of molecules and crystals", *J. Chem. Phys.* **18**, pp. 365–375 (1950).

[98] R. S. Mülliken, "Electronic population analysis on LCAO[single bond]MO molecular wave functions", *J. Chem. Phys.* **23**, pp. 1833–1840 (1955).

[99] R. Landauer, "Spatial variation of currents and fields due to localized scatterers in metallic conduction", *IBM J. Res. Develop.* **1**, pp. 223–231 (1957).

[100] R. Landauer, "Electrical resistance of disordered one-dimentional lattices", *Phil. Mag.* **21**, pp. 863–867 (1970).

[101] M. Büttiker, "Four-terminal phase-coherent conductance", *Phys. Rev. Lett.* **57**, pp. 1761–1765 (1986).

[102] M. Büttiker, "Symmetry of electrical condution", *IBM J. Res. Develop.* **32**, pp. 306–317 (1988).

[103] S. Datta, *Quantum transport : atom to transistor*, Cambridge University Press, cambridge (2005).

[104] D. S. Fisher and P. A. Lee, "Relation between conductivity and transmission matrix", *Phys. Rev. B* **23**, pp. 6851–6854 (1981).

[105] E. N. Economou, *Green's functions in quantum physics*, Springer, Crete, 3rd edition (2005).

[106] F. Bloch, "Generalized theory of relaxation", *Phys. Rev.* **411**, pp. 1206–1222 (1957).

[107] R. K. Wangsness and F. Bloch, "The dynamical theory of nuclear induction", *Phys. Rev.* **1948**, pp. 728–739 (1953).

[108] C. Timm, "Tunneling through molecules and quantum dots: master-equation approaches", *Phys. Rev. B* **77**, pp. 195416–195434 (2008).

[109] S. Nakajima, "On quantum theory of transport phenomena", *Prog. Theor. Phys.* **20**, pp. 948–959 (1958).

[110] J. Koenig, J. Schmid, and H. Schoeller, "Resonant tunneling through ultrasmall quantum dots: zero-bias anomalies, magnetic-field dependence, and boson-assisted transport ", *Phys. Rev. B* **54**, pp. 820–837 (1996).

[111] J. Koenig, H. Schoeller, and G. Schoen, "Cotunneling at resonance for the single-electron transistor", *Phys. Rev. Lett.* **78**, pp. 4482–4485 (1997).

[112] J. Koenig, H. Schoeller, and G. Schoen, "Cotunneling and renormalization effects for the single-electron transistor ", *Phys. Rev. B* **58**, pp. 7882–7892 (1998).

[113] K. Blum, *Density matrix theory and applications*, Springer, Muenster, 3th edition (2011).

[114] F. Elste and C. Timm, "Cotunneling and nonequilibrium magnetization in magnetic molecular monolayers", *Phys. Rev. B* **75**, pp. 195341–1953419 (2007).

[115] J. Koch, F. von Oppen, Y. Oreg, and E. Sela, "Thermopower of single-molecule devices", *Phys. Rev. B* **70**, pp. 195107–195119 (2004).

[116] J. Koch, F. von Oppen, and A. Andreev, "Theory of the Franck-Condon blockade regime", *Phys. Rev. B* **74**, pp. 205438–205447 (2006).

[117] B. Muralidharan, A. W. Ghosh, S. K. Pati, and S. Datta, "Theory of high bias Coulomb blockade in ultrashort molecules Theory of High bias Coulomb blockade in ultrashort molecules", *IEEE Trans. Nanotechnol.* **6**, pp. 536–544 (2007).

[118] T. Hansen, V. Mujica, and M. A. Ratner, "Cotunneling model for current-induced events in molecular wires", *Nano Lett.* **8**, pp. 3525–3531 (2008).

[119] G. Begemann, S. Koller, M. Grifoni, and J. Paaske, "Inelastic cotunneling in quantum dots and molecules with weakly broken degeneracies", *Phys. Rev. B* **82**, pp. 045316–045327 (2010).

[120] J. N. Pedersen and A. Wacker, "Modeling of cotunneling in quantum dot systems", *Phys. E* **42**, pp. 595–599 (2010).

[121] M. Turek and K. Matveev, "Cotunneling thermopower of single electron transistors", *Phys. Rev. B* **65**, pp. 115332–115341 (2002).

[122] H. Bruus and K. Flensberg, *Introduction to many-body quantum theory in condensed matter physics*, Number August. Oxford University Press, Oxford, (2004).

[123] S. Koller, M. Grifoni, M. Leijnse, and M. R. Wegewijs, "Density-operator approaches to transport through interacting quantum dots: simplifications in fourth order perturbation theory", *arXiv:1008.0347v3* , pp. 1–29 (2012).

[124] V. N. Golovach and D. Loss, "Transport through a double quantum dot in the sequential tunneling and cotunneling regimes", *Phys. Rev. B* **69**, pp. 245327–245343 (2004).

[125] A. Filippetti, C. Pemmaraju, S. Sanvito, P. Delugas, D. Puggioni, and V. Fiorentini, "Variational pseudo-self-interaction-corrected density functional approach to the ab initio description of correlated solids and molecules", *Phys. Rev. B* **84**, pp. 195127–195149 (2011).

[126] J. B. Neaton, M. S. Hybertsen, and S. G. Louie, "Renormalization of Molecular electronic levels at metal-molecule interfaces", *Phys. Rev. Lett.* **97**, pp. 216405–216409 (2006).

[127] J. C. Inkson, "Many-body effects at metal-semiconductor junctions : 11 . The self energy and band structure distortion", *J. Phys. C Solid State Phys.* **6**, pp. 1350–1362 (1973).

[128] M. S. Hybertsen and S. G. Louie, "Electron correlation in semiconductors and insulators: Band gaps and quasiparticle energies.", *Phys. Rev. B* **34**, pp. 5390–5413 (1986).

[129] G. Onida, L. Reining, and A. Rubio, "Electronic excitations : density-functional versus many-body Green s-function approaches", *Rev. Mod. Phys.* **74**, pp. 601–659 (2002).

[130] J. M. Garcia-Lastra and K. S. Thygesen, "Renormalization of optical excitations in molecules near a metal surface", *Phys. Rev. Lett.* **106**, pp. 216405–216409 (2011).

[131] J. M. Garcia-Lastra, C. Rostgaard, A. Rubio, and K. S. Thygesen, "Polarization-induced renormalization of molecular levels at metallic and semiconducting surfaces", *Phys. Rev. B* **80**, pp. 245427–245434 (2009).

[132] I. Tamblyn, P. Darancet, S. Y. Quek, S. A. Bonev, and J. B. Neaton, "Electronic energy level alignment at metal-molecule interfaces with a GW approach", *Phys. Rev. B* **84**, pp. 201402–201406 (2011).

[133] G.-M. Rignanese, X. Blase, and S. G. Louie, "Quasiparticle effects on tunneling currents: a study of C2H4 adsorbed on the Si(001)-(2 x 1) surface", *Phys. Rev. Lett.* **86**, pp. 2110–2113 (2001).

[134] M. Strange and K. S. Thygesen, "Image-charge-induced localization of molecular orbitals at metal-molecule interfaces: Self-consistent GW calculations", *Phys. Rev. B* **86**, pp. 195121–195127 (2012).

[135] A. Ferretti, A. Calzolari, R. Di Felice, and F. Manghi, "First-principles theoretical description of electronic transport including electron-electron correlation", *Phys. Rev. B* **72**, pp. 125114–125127 (2005).

[136] S. Y. Quek, H. J. Choi, S. G. Louie, and J. B. Neaton, "Thermopower of amine - gold-linked principles", *ACS Nano* **5**, pp. 551–557 (2011).

[137] V. M. García-Suárez and C. J. Lambert, "First-principles scheme for spectral adjustment in nanoscale transport", *New J. Phys.* **13**, pp. 53026–53043 (2011).

[138] S. Y. Quek, L. Venkataraman, H. J. Choi, S. G. Louie, M. S. Hybertsen, and J. B. Neaton, "Amine-gold linked single-molecule circuits: experiment and theory.", *Nano Lett.* **7**, pp. 3477–3482 (2007).

[139] D. J. Mowbray, G. Jones, and K. S. Thygesen, "Influence of functional groups on charge transport in molecular junctions.", *J. Chem. Phys.* **128**, pp. 111103–111108 (2008).

[140] E. Abad, J. Ortega, Y. J. Dappe, and F. Flores, "Dipoles and band alignment for benzene/Au(111) and C60/Au(111) interfaces", *Appl. Phys. A* **95**, pp. 119–124 (2008).

[141] J. Gavnholt, T. Olsen, M. Engelund, and J. Schiotz, "Δ Self-consistent field method to obtain potential energy surfaces of excited molecules on surfaces", *Phys. Rev. B* **78**, pp. 07544–075451 (2008).

[142] J. Sau, J. B. Neaton, H. J. Choi, S. G. Louie, and M. L. Cohen, "Electronic Energy Levels of Weakly Coupled Nanostructures: C60-Metal Interfaces", *Phys. Rev. Lett.* **101**, pp. 026804–026808 (2008).

[143] N. Troullier and J. L. Martins, "Efficient pseudopotentials for plane-wave calculations", *Phys. Rev. B* **15**, pp. 43–57 (1991).

[144] G. Makov and M. C. Payne, "Periodic boundary conditions in ab initio calculations", *Phys. Rev. B* **51**, pp. 4014–4022 (1995).

[145] K. Kokko, P. T. Salo, R. Laihia, and K. Mansikka, "Work function and surface energy of optimized lithium slabs", *Phys. Rev. B* **52**, pp. 1536–1539 (1995).

[146] N. D. Lang and W. Kohn, "Theory of metal surfaces: work function", *Phys. Rev. B* **3**, pp. 1215–1223 (1971).

[147] L. A. Chewter, M. Sander, K. Muller-Dethlefs, and E. W. Schlag, "High resolution zero kinetic energy photoelectron spectroscopy of benzene and determination of the ionization potential", *J. Chem. Phys.* **86**, pp. 4736–4744 (1987).

[148] J. C. Rienstra-Kiracofe, G. S. Tschumper, H. F. Schaefer, S. Nandi, and G. B. Ellison, "Atomic and molecular electron affinities: photoelectron experiments and theoretical computations.", *Chem. Rev.* **102**, pp. 231–282 (2002).

[149] J. C. Rienstra-kiracofe, C. J. Barden, S. T. Brown, and H. F. Schaefer III, "Electron affinities of polycyclic aromatic hydrocarbons", *J. Phys. Chem. A* **105**, pp. 524–528 (2001).

[150] Huy-Viet Nguyen, T. A. Pham, D. Rocca, and G. Galli, "Improving accuracy and efficiency of calculations of photoemission spectra within the many-body perturbation theory", *Phys. Rev. B* **85**, pp. 081101–081106 (2012).

[151] G. Samsonidze, M. Jain, J. Deslippe, M. L. Cohen, and S. G. Louie, "Simple approximate physical orbitals for GW quasiparticle calculations", *Phys. Rev. Lett.* **107**, pp. 186404–186409 (2011).

[152] N. D. Lang and W. Kohn, "Theory of metal surfaces: induced surface charge and image potential", *Phys. Rev. B* **7**, pp. 3542–3552 (1973).

[153] A. M. Souza, I. Rungger, C. D. Pemmaraju, U. Schwingenschloegl, and S. Sanvito, "Constrained-DFT method for accurate energy level alignment of metal / molecule interfaces", *Phys. Rev. B* **88**, pp. 165112–165121 (2013).

[154] J. Tomfohr and O. F. Sankey, "Theoretical analysis of electron transport through organic molecules.", *J. Chem. Phys.* **120**, pp. 1542–1554 (2004).

[155] K. Stokbro, J. Taylor, M. Brandbyge, J.-L. Mozos, and P. Ordejón, "Theoretical study of the nonlinear conductance of di-thiol benzene coupled to Au(111) surfaces via thiol and thiolate bonds", *Comput. Mater. Sci.* **27**, pp. 151–160 (2003).

[156] P. Maksymovych and J. T. Yates Jr., "Au adatoms in self-assembly of benzenethiol on the Au(111) surface.", *J. Am. Chem. Soc.* **130**, pp. 7518–7520 (2008).

[157] W. Andreoni, Al. Curioni, and H. Groenbeck, "Density functional theory approach to thiols and disulfides on gold: Au(111) surface and clusters", *Int. J. Quantum Chem.* **80**, pp. 598–608 (2000).

[158] Qing Pu, Yongsheng Leng, Xiongce Zhao, and Peter T Cummings, "Molecular Simulation Studies on the Elongation of Gold Nanowires in Benzenedithiol", *J. Phys. Chem. C* **114**, pp. 10365–10372 (2010).

[159] M. Strange, C. Rostgaard, H. Häkkinen, and K. S. Thygesen, "Self-consistent GW calculations of electronic transport in thiol- and amine-linked molecular junctions", *Phys. Rev. B* **83**, pp. 115108–115120 (2011).

[160] H. Grönbeck, A. Curioni, and W. Andreoni, "Thiols and disulfides on the Au(111) surface: the headgroup gold interaction", *J. Am. Chem. Soc.* **122**, pp. 3839–3842 (2000).

[161] J. Nara, S. Higai, Y. Morikawa, and T. Ohno, "Density functional theory investigation of benzenethiol adsorption on Au(111).", *J. Chem. Phys.* **120**, pp. 6705–6711 (2004).

[162] Z. Ning, W. Ji, and H. Guo, "Role of contact formation process in transport properties of molecular junctions: conductance of Au/BDT/Au molecular wires", *arXiv:cond-mat/0907467v2* , pp. 1–5 (2010).

[163] F. Flores, J. Ortega, and H. Vázquez, "Modelling energy level alignment at organic interfaces and density functional theory.", *Phys. Chem. Chem. Phys.* **11**, pp. 8658–8675 (2009).

[164] Jian-Ge Zhou and F. Hagelberg, "Do methanethiol adsorbates on the Au(111) surface dissociate?", *Phys. Rev. Lett.* **97**, pp. 045505–045509 (2006).

[165] I. I. Rzeznicka, L. Junseok, P. Maksymovych, and J. T. Yates Jr., "Nondissociative chemisorption of short chain alkanethiols on Au(111)", *J. Phys. Chem. B* **109**, pp. 15992–15996 (2005).

[166] R. G. Nuzzo, Zegarski B. R., and Dubois L. H., "Fundamental studies of the chemisorption of organosulfur compounds on gold(111). Implications for molecular self-assembly on gold surfaces", *J. Am. Chem. Soc.* **109**, pp. 733–740 (1987).

[167] G. Henkelman and H. Jonsson, "Improved tangent estimate in the nudged elastic band method for finding minimum energy paths and saddle points", *J. Chem. Phys.* **113**, pp. 9978–9985 (2000).

[168] G. Henkelman and H. Jonsson, "A dimer method for finding saddle points on high dimensional potential surfaces using only first derivatives", *J. Chem. Phys.* **111**, pp. 7010–7022 (1999).

[169] G. Henkelman, B. P. Uberuaga, and H. Jonsson, "A climbing image nudged elastic band method for finding saddle points and minimum energy paths", *J. Chem. Phys.* **113**, pp. 9901–9904 (2000).

[170] M. Frei, S. V. Aradhya, M. S. Hybertsen, and L. Venkataraman, "Linker dependent bond rupture force measurements in single-molecule junctions", *J. Am. Chem. Soc.* **134**, pp. 4003–4006 (2012).

[171] S. V. Aradhya, M. Frei, M. S. Hybertsen, and L. Venkataraman, "Van der Waals interactions at metal/organic interfaces at the single-molecule level.", *Nat. Mater.* **11**, pp. 872–876 (2012).

[172] Z. Huang, B. Xu, Y. Chen, and M. Di Ventra, "Measurement of current-induced local heating in a single molecule junction", *Nano Lett.* **6**, pp. 1240–1244 (2006).

[173] X. Li, J. He, J. Hihath, B. Xu, and S. M. Lindsay, "Conductance of single alkanedithiols: conduction mechanism and effect of molecule - electrode contacts", *J. Am. Chem. Soc.* **128**, pp. 2135–2141 (2006).

[174] M. Strange, O. Lopez-acevedo, and H. Hannu, "Oligomeric gold-thiolate units define the properties of the molecular junction between gold and benzene dithiols", *J. Phys. Chem. Lett.* **1**, pp. 1528–1532 (2010).

[175] L. Romaner, G. Heimel, M. Gruber, Jean-Luc Brédas, and E. Zojer, "Stretching and breaking of a molecular junction.", *Small* **2**, pp. 1468–1475 (2006).

[176] N. Sergueev, L. Tsetseris, K. Varga, and S. Pantelides, "Configuration and conductance evolution of benzene-dithiol molecular junctions under elongation", *Phys. Rev. B* **82**, pp. 073106–073110 (2010).

[177] Y. Qi, J. Qin, G. Zhang, and T. Zhang, "Breaking mechanism of single molecular junctions formed by octanedithiol molecules and Au electrodes", *J. Am. Chem. Soc.* **131**, pp. 16418–16422 (2009).

[178] W. Haiss, C. Wang, R. Jitchati, I. Grace, S. Martín, A. S. Batsanov, S. J. Higgins, M. R. Bryce, C. J. Lambert, P. S. Jensen, and R. J. Nichols, "Variable contact gap single-molecule conductance determination for a series of conjugated molecular bridges.", *J. Phys. Condens. Matter* **20**, pp. 374119–374128 (2008).

[179] W. R. French, *Computer simulations for improved atomic-level control and understanding of molecular electronic devices*, PhD thesis Vanderbilt University (2013).

[180] C. Li, I. Pobelov, T. Wandlowski, A. Bagrets, A. Arnold, and F. Evers, "Charge transport in single Au/Alkanedithiol/Au junctions: coordination geometries and conformational degrees of freedom", *J. Am. Chem. Soc.* **130**, pp. 318–326 (2008).

[181] S. Y. Quek, M. Kamenetska, M. L. Steigerwald, H. J. Choi, S. G. Louie, M. S. Hybertsen, J. B. Neaton, and L. Venkataraman, "Mechanically controlled binary conductance switching of a single-molecule junction", *Nat. Nanotechnol.* **4**, pp. 230–234 (2009).

[182] A. I. Yanson, G. R. Bollinger, H. E. van den Brom, N. Agraiet, and J. M. van Ruitenbeek, "Formation and manipulation of a metallic wire of single gold atoms", *Nature* **214**, pp. 783–785 (1998).

[183] F. Tavazza, L. E. Levine, and A. M. Chaka, "Structural changes during the formation of gold single-atom chains: Stability criteria and electronic structure", *Phys. Rev. B* **81**, pp. 235424–235436 (2010).

[184] Y. Meir and S. W. Ned, "Landauer formula for the current through an interacting electron region", *Phys. Rev. Lett.* **68**, pp. 2512–2515 (1992).

[185] M. Brandbyge, José-Luis Mozos, P. Ordejón, J. Taylor, and K. Stokbro, "Density-functional method for nonequilibrium electron transport", *Phys. Rev. B* **65**, pp. 165401–165418 (2002).

[186] C. Toher, A. Filippetti, S. Sanvito, and K. Burke, "Self-Interaction Errors in Density-Functional Calculations of Electronic Transport", *Phys. Rev. Lett.* **95**, pp. 146402–146406 (2005).

[187] A. R. Rocha, V. García-Suárez, S. Bailey, C. J. Lambert, J. Ferrer, and S. Sanvito, "Spin and molecular electronics in atomically generated orbital landscapes", *Phys. Rev. B* **73**, pp. 85414–85435 (2006).

[188] I. Rungger and S. Sanvito, "Algorithm for the construction of self-energies for electronic transport calculations based on singularity elimination and singular value decomposition", *Phys. Rev. B* **78**, pp. 035407–035420 (2008).

[189] D. C. Langreth, "Singularities in the X-Ray spectra of metals", *Phys. Rev. B* **108**, pp. 471–477 (1970).

[190] A. Mitra, I. Aleiner, and A. J. Millis, "Phonon effects in molecular transistors: quantal and classical treatment", *Phys. Rev. B* **69**, pp. 245302–245323 (2004).

[191] A. J. Cohen, P. Mori-Sánchez, and W. Yang, "Insights into current limitations of density functional theory.", *Science* **321**, pp. 792–794 (2008).

[192] E. Burzur, Y. Yamamoto, M. Warnock, X. Zhong, K. Park, A. Cornia, and H. S. J. van der Zant, "Franck-Condon blockade in a single-molecule transistor", *Nano Lett.* **14**, pp. 3191–3196 (2014).

[193] M. Berritta, D. Z. Manrique, and C. J. Lambert, "Interplay between quantum interference and conformational fluctuations in single-molecule break junctions", *Nanoscale* **7**, pp. 1096–1101 (2014).

[194] C. Jin and K. S. Thygesen, "Dynamical image-charge effect in molecular tunnel junctions: Beyond energy level alignment", *Phys. Rev. B* **89**, pp. 041102–041107 (2014).

[195] J. Viljas, F. Pauly, and J. Cuevas, "Modeling elastic and photoassisted transport in organic molecular wires: Length dependence and current-voltage characteristics", *Phys. Rev. B* **77**, pp. 155119–155123 (2008).

[196] J. Viljas, F. Pauly, and J. Cuevas, "Photoconductance of organic single-molecule contacts", *Phys. Rev. B* **76**, pp. 033403–033407 (2007).

[197] J. Viljas and J. Cuevas, "Role of electronic structure in photoassisted transport through atomic-sized contacts", *Phys. Rev. B* **75**, pp. 075406–075412 (2007).

[198] M. Büttiker and R. Landauer, "Traversal time for tunneling", *Phys. Rev. Lett.* **49**, pp. 1739–1742 (1982).

[199] L. P. Kouwenhoven, S. Jauhar, J. Orenstein, P. L. McEuen, Y. Nagamune, J. Motohisa, and H. Sakaki, "Observation of photon-assisted tunneling through a quantum dot", *Phys. Rev. Lett.* **73**, pp. 3443–3446 (1994).

[200] C. W. J. Beenakker, "Theory of Coulomb-blockade oscillations in the conductance of a quantum dot", *Phys. Rev. B* **44**, pp. 1646–1656 (1991).

[201] T. H. Oosterkamp, L. P. Kouwenhoven, A. E. A. Koolen, N. C. van der Vaart, and C. J. P. M. Harmans, "Photon sidebands of the ground state and first excited state of a quantum dot", *Phys. Rev. Lett.* **78**, pp. 1536–1539 (1997).

[202] C. Bruder and H. Schoeller, "Charging effects in ultrasmall quantum dots in the presence of time-varying field", *Phys. Rev. Lett.* **72**, pp. 1076–1079 (1994).

[203] L. P. Kouwenhoven, S. Jauhar, K. MacCormick, D. Dixon, P. L. McEuen, Y. V. Nazarov, N. C. van der Vaart, and C. T. Foxon, "Photon-assisted tunneling through a quantum dot", *Phys. Rev. B* **50**, pp. 2019–2022 (1994).

[204] E. M. Weig, R. H. Blick, T. Brandes, J. Kirschbaum, W. Wegscheider, M. Bichler, and J. P. Kotthaus, "Single-electron-phonon interaction in a suspended quantum dot phonon cavity", *Phys. Rev. Lett.* **92**, pp. 046804–046808 (2004).

[205] S. Sapmaz, P. Jarillo-Herrero, Y. M. Blanter, C. Dekker, and H. S. J. van der Zant, "Tunneling in suspended carbon nanotubes assisted by longitudinal phonons", *Phys. Rev. Lett.* **96**, pp. 026801–026805 (2006).

[206] L. Wang and V. May, "Charge transmission through single molecules: effects of nonequilibrium molecular vibrations and photoinduced transitions", *Chem. Phys.* **375**, pp. 252–264 (2010).

[207] F. Chen, J. He, C. Nuckolls, T. Roberts, J. E. Klare, and S. Lindsay, "A molecular switch based on potential-induced changes of oxidation state.", *Nano Lett.* **5**, pp. 503–509 (2005).

[208] U. Aeberhard and R. H. Morf, "Microscopic nonequilibrium theory of quantum well solar cells", *Phys. Rev. B* **77**, pp. 125343–125352 (2008).

[209] U. Aeberhard, "Theory and simulation of quantum photovoltaic devices based on the non-equilibrium Greens function formalism", *J. Comput. Electron.* **10**, pp. 394–413 (2011).

[210] O. Kurniawan, P. Bai, and E. P. Li, "Non-equilibrium Greens function calculation of optical absorption in nano optoelectronic devices", *IEEE* , pp. 1–4 (2009).

[211] U. Aeberhard, "Photon Greens functions for a consistent theory of absorption and emission in nanostructure-based solar cell devices", *Opt. Quantum Electron.* **46**, pp. 791–796 (2013).

[212] W. G. van der Wiel, S. De Franceschi, J. M. Elzerman, T. Fujisawa, S. Tarucha, and L. P. Kouwenhoven, "Electron transport through double quantum dots", *Rev. Mod. Phys.* **75**, pp. 1–22 (2003).

[213] C. Wang, J. Ren, B. W. Li, and Q. H. Chen, "Quantum transport of double quantum dots coupled to an oscillator in arbitrary strong coupling regime", *Eur. Phys. J. B* **85**, pp. 1–10 (2012).

[214] E. Cota, R. Aguado, and G. Platero, "Ac-driven double quantum dots as spin pumps and spin filters", *Phys. Rev. Lett.* **94**, pp. 1–4 (2005).

[215] G. S. Agarwal, "Rotating-wave approximation and spontaneous emission", *Phys. Rev. A* **7**, pp. 1195–1197 (1972).

[216] P. L. Knight and L. Allen, "Rotating-wave approximation in coherent interactions", *Phys. Rev. A* **7**, pp. 368–370 (1973).

[217] C. A. Stafford and N. S. Wingreen, "Resonant photon-assisted tunneling through a double quantum dot: an electron pump from spatial Rabi oscillations.", *Phys. Rev. Lett.* **76**, pp. 1916–1919 (1996).

[218] T. H. Stoof and Y. V. Nazarov, "Time-dependent resonant tunneling via two discrete states", *Phys. Rev. B* **53**, pp. 1050–1053 (1996).

[219] W. G. van der Wiel, T. Fujisawa, T. H. Oosterkamp, and L. P. Kouwenhoven, "Microwave spectroscopy of a double quantum dot in the low- and high-power regime", *Phys. B* **272**, pp. 31–35 (1999).

[220] C. Bruder and H. Schoeller, "Photon-assisted transport through ultrasmall quantum dots: Influence of intradot transitions", *Phys. Rev. B* **56**, pp. 4730–4736 (1997).

[221] T. Novotny, "Investigation of apparent violation of the second law", *Europhys. Lett.* **648**, pp. 648–654 (2002).

[222] Q. Wu and T. Van Voorhis, "Constrained density functional theory and Its application in long-range electron transfer", *J. Chem. Theory Comput.* **2**, pp. 765–774 (2006).